

Synthetic Molecular Approaches for Artificial Anion Transport Systems and their Bio-Applicability

A Thesis
Submitted in Partial Fulfillment of the Requirements
for the Degree of

Doctor of Philosophy

by

Tanmoy Saha

ID: 20113149



Indian Institute of Science Education and Research, Pune

2017

Dedicated

those who dreamt for me...



भारतीय विज्ञान शिक्षा एवं अनुसंधान संस्थान, पुणे
INDIAN INSTITUTE OF SCIENCE EDUCATION AND RESEARCH (IISER) PUNE
(An Autonomous Institution of Ministry of Human Resource Development, Govt. of India)
Dr. Homi Bhabha Road, Pune - 411008.

Dr. Pinaki Talukdar
Associate Professor
Department of Chemistry,
IISER Pune

CERTIFICATE

Certified that the work incorporated in the thesis entitled “*Synthetic Molecular Approaches for Artificial Anion Transport Systems and their Bio-applicability*” submitted by **Mr. Tanmoy Saha** was carried out by the candidate, under my supervision. The work presented here or any part of it has not been included in any other thesis submitted previously for the award of any degree or diploma from any other university or institution.

Date: 29th Nov 2016

Dr. Pinaki Talukdar
(Research Supervisor)



DECLARATION

I declare that this written submission represents my ideas in my own words and wherever other's ideas have been included; I have adequately cited and referenced the original sources. I also declare that I have adhered to all principles of academic honesty and integrity and have not misrepresented or fabricated or falsified any idea / data / fact / source in my submission. I understand that violation of the above will cause for disciplinary action by the Institute and can also evoke penal action from the sources which have thus not been properly cited or from whom proper permission has not been taken when needed.

Date: 29th Nov 2016

Mr. Tanmoy saha
I.D.: 20113149

Acknowledgement

The tenure of my Ph.D. degree was an incredible journey for me. There are a few personalities who always stood with me at every stage during the voyage. The journey could not be so magnificent; moreover, it could have appeared till the finish line without their unconditional help and support. So before stating the narration of my journey, I would like to thank them for bearing with me...

I sincerely thank my thesis supervisor Dr. Pinaki Talukdar for his suggestion, supports, and encouragements during the last five years. Though it was a slow start, as I was assigned to set up a new arena of research in our lab, he always stood behind me in my failures and successes and helped me to achieve the acceleration. With his practical guidance, I learned designing and successful execution of research projects. On above of everything he always encouraged me to have free thinking which helped me draw my own path in research. Additionally, I should acknowledge for the training related to preparing and delivering a presentation.

I would like to express my profound gratitude to my Research Advisory Committee (RAC) members, Dr. Sayam Sengupta and Dr. Jeet Kalia for their valuable suggestion during the RAC meetings. They are such personalities whose frequency perfectly aligns with mine and our ideas always coincide while designing new experiments, interpretation of results and the discussion of future directions. Moreover, they always pushed the boundary according to my experience during my presentations which helped me to gain the confidence of standing on the dais.

I feel honored to be a part of Indian Institute of Science Education and Research (IISER), Pune. I would like to spread my gratitude to each and everybody related IISER Pune, in particular, to them who offered their endless effort to build such a wonderful institute with world-class research facilities. I thank Prof. K. N. Ganesh, director IISER Pune for hosting this institution during its earlier days to the world's leading scientific communities. The friendly atmosphere of research at IISER Pune always amazed me. I strongly feel that the accessibility of easy discussion among faculty members and students is the key feature of the successful interdisciplinary research at this institute.

I am incredibly grateful to Dr. Mayurika Lahiri for allowing me to perform all biological experiments in her laboratory. It was a great pleasure of feeling to have a second

lab at IISER. I always enjoyed the working freedom, and always been treated as a member of this group. The entire biological knowledge and skills, which I can gather in last few years, are only because of the discussion and support from her lab members. I also thank Mitali, Satish, Libi, Vaishali, Ashiq, Aishwarya, Virender and Rintu for teaching and helping me in all biological experiments. Moreover, it was a great fun of working with the Lahiri lab team and I would carry a lot of fun memories with me.

I want to say about two persons who have a significant impact on my early research life. Dr. Dnyaneshwar Kand (DK), who was apparently the senior most member in our lab, and I got my preliminary research training with him. He influenced my mind to have dedication, patience, and attitude in research. Dr. Abhigyan Sengupta (Abhigyan da) is a friend philosopher and guide of mine; he taught me the free thinking regarding the problem and way to find the solution.

I am thankful to get the opportunity of working with Dr. Arnab Mukherjee, Dr. Sujit K. Ghosh, Dr. Partha Hazra, Dr. Amal K. Bera, Dr. K. M. Sureshan and Prof. Nikolay E. Nifantiev in various collaborative projects. The guidance and suggestions in diverse fields of research endowed me a wider working experience and knowledge. I would like to thank other faculty members for helping me in various aspects of research. I never hesitate to knock their door for any assistance regarding research. Particularly, my deep gratitude goes to Dr. Harinath Chakrapani, Dr. Sudipta Basu, Dr. Jeetender Chugh, Dr. S.G. Srivatsan, Dr. Thomas Pucadyil, Dr. Sudha Rajamani, Dr. Richa Ricky, Dr. Kundan Sengupta, Dr. Nirmalya Ballav, Dr. H. N. Gopi, Dr. Anirban Hazra, Dr. Arnab Mukherjee, Prof. Srinivas Hotha, Prof. M. Jayakannan and Prof. B.S.M. Rao. I thank all non-teaching and technical staffs for their support, particularly, Mr. Mayuresh, Mr. Mahesh, Mr. Nitin, Ms. Nayna (HRMS), Ms. Swati (MALDI), Ms. Dipali and Mr. Chinmay (NMR), Ms. Mrinalini (biology), Mr. Vijay (microscopy), and Mr. Tushar.

It's my pleasure to thank all the lab members; Sharad, Dinesh, Arundhati, Sopan, Sanjit, Javid, Sreejit, Pratyush, Manjeet, Gourab, Prashant, Sahid, Debasish, Anjana, Rashmi, Avishikta, Nihar and Manzoor for making my journey wonderful. It was indeed a great experience of working with them.

I thank Dr. Amal Kanti Bera and his lab members, Debanjan da (Dr. Debanjan Tewari) and Sucheta for helping me to learn BLM instrument and to acquire knowledge

about basic electrophysiology. I also thank Dr. Gil Toombes for helping me to standardize BLM instrument.

I am thankful to Biplab da, Sagar, Partha, and Sohini, for their constant support in all odd and even events in past few years. Specially, I should thank Sagar and Partha for staying beside during the final year of Ph.D. Apart from them, I must thank my friends, seniors, and juniors; Moumita di, Abhik (Mota), Avishek (Golu), Soumya, Barun, Rajkumar, Sayma, Partha da, Sudeb da, Kaushik da, Manna da...

Apart from the IISER community, few persons have a great influence on my success. Though, it is not possible to summaries their contributions here, I am thankful to Pronob da (Prof. Pranab Sarkar), Kattick Da (Dr. Kattick Bhoumik), Tatha, Rudra, Santu, Susanta da, Atryee, Sugoto, Tina, Arpita, Debu, Pintu, Suomen (Boss), Debdyuti, Tumpa, Anwasha...

No words can ever convey my sense of gratitude for my parents (Mr. Tapan Saha and Ms. Sonali Saha) and my uncle (Mr. Uttam Saha). It is due to their unconditional trust, timely encouragement, endless patience and unstinting sacrifice; I am able to reach this position. It is also a pleasure to acknowledge my grandma Late. Kusum Saha, who had expressed the first wish to get the prefix of 'Dr.' on my name. I also express my gratitude and love to my grandfather, Mr. Gour Saha, my aunt, Ms. Sadhana Saha, my sister Tanima and brother Tapas.

I am thankful to University Grant Commission (UGC), Government of India, for my research scholarship the financial support during the course of Ph.D. I thank Science and Engineering Research Board (SERB) for funding me to attend Biointerface Science Conference in Switzerland. Moreover, I like to thank American Chemical Society (ACS), Royal Society of Chemistry (RSC), John Wiley & Sons, Elsevier Science Ltd., for publishing several research articles produced during the course of my research as well as for giving the permission for a reprint of copyrighted materials.

Finally, I express my profound gratitude to them, whose names are missed out in this section, despite their unconditional support to make my journey successful. I would like to end up by saying... It was indeed a great and wonderful journey...

Tanmoy

Synopsis

The fundamental objective of this thesis is to introduce artificial ion transport systems and to explore its application in the biomedical arena. The research during my doctoral study was mainly focused on design, synthesis, and characterization of biomimetic artificial ion channels and ion carriers which have shown a remarkable biological application in the line of future therapeutics. In particular, this thesis mainly deals with the unimolecular or supramolecular architecture of artificial ion channels for selective transport of chloride ions. Accessibility for tunable ion transport by controlling the pore diameter, and better ion selectivity by incorporating multiple selectivity filters had been addressed. Furthermore, an interesting correlation of ion transport activity and lipophilicity was achieved by anion transport systems. Apoptosis inducing activity because of chloride ion transport in live cells by ion carrier and ion channel was evaluated, which could be a potential therapeutic tool for cancer treatment in the next generation.

Chapter 1: Introduction

Transport of solute molecules across the cellular membrane is extremely crucial to perform fundamental biological processes such as cell to cell communication, energy production, biosynthesis, and metabolism. However, the transmembrane transport of solutes is restricted because of the thermodynamic barrier imposed by the hydrophobic domain of the membrane. Certain classes of membrane proteins perform the task of controlling the exchange of meticulous solutes (such as ions), by overcoming the thermodynamic barrier. Chloride is the most abundant anion in the physiological system. Selective transport of chloride ions, usually facilitated by chloride selective ion transporters, has pivotal implication in diverse biological processes, e.g. transepithelial salt transport, acidification of internal and extracellular compartments, cell volume regulation, cell cycle, and apoptosis. Dysfunction of ion transport proteins may lead to various life threatening diseases such as myotonia congenita, cystic fibrosis, Bartter syndrome, Gitelman syndrome, Dent's diseases, renal tubular acidosis, deafness, etc. Hence, transparent knowledge about the function and workability of chloride transport systems is a burgeoning field for researchers of biochemistry and biotechnology field.

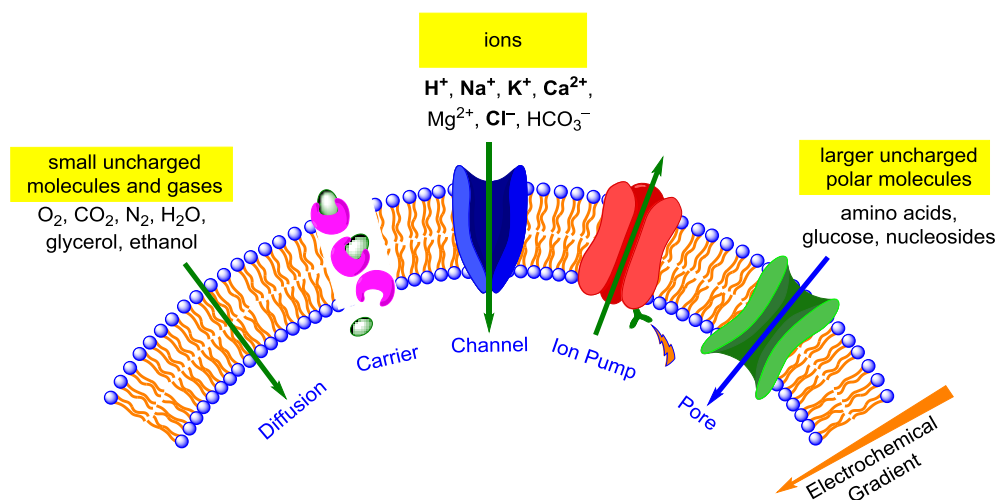


Figure 1. Schematic representation of solute transport through the membrane.

Chapter 2: Unimolecular Anion-Selective Artificial Ion Channel

Unimolecular ion channels were designed by functionalization of a new type of cyclic oligosaccharides, the cyclo-oligo-(1→6)- β -D-glucosamines, connected to lipophilic membrane-spanning tails. Transport activities of these glycoconjugates were manipulated by altering oligomericity of macrocycles, and the number of the attached tails. Ion transport activity increased from dimeric to tetrameric glucosamine macrocycle but, decreased further when a flexible pentameric glucosamine was introduced. The importance of the number of membrane-spanning tails was also evaluated for controlling the ion transport activity. All glucosamines derivatives exhibited anion selectivity due to hydrogen bonding between the macrocycle and the water molecules solvating the anion. Ion selectivity of synthesized derivatives displayed a uniform $\text{Cl}^- > \text{Br}^- > \text{I}^-$ selectivity sequence.

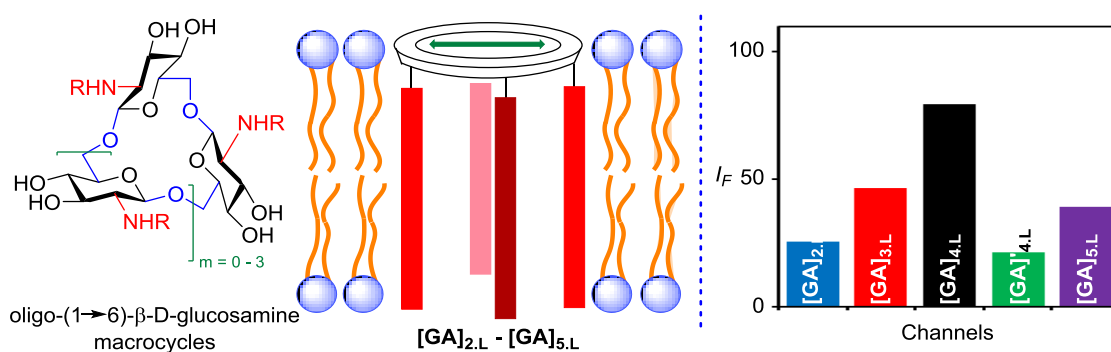


Figure 2. The design strategy for glucosamine based ion channel and variation of ion transport activity.

Chapter 3: Supramolecular Approach for Barrel-Hoop Ion Channel

Supramolecular approach for constructing nanotubular structure having adaptable lipophilicity is a well acceptable method for artificial ion channel construction. In this chapter, an amphiphilic macrocycle was introduced, which can self-assemble to form a barrel-hoop based artificial ion channel structure by sharing the intermolecular hydrogen bonding interaction via the di-oxalyl amide moieties. The efficient ion transport through the channel and anion selectivity was proved by fluorescence-based assays using large unilamellar vesicle. The confirmation of ion channel formation was achieved by conductance measurement in the planar lipid bilayer. The supramolecular approach of introducing synthetic ion channel opens up the possibilities for further modification related to ion transport property and could be a potent pioneer for biotechnological application.

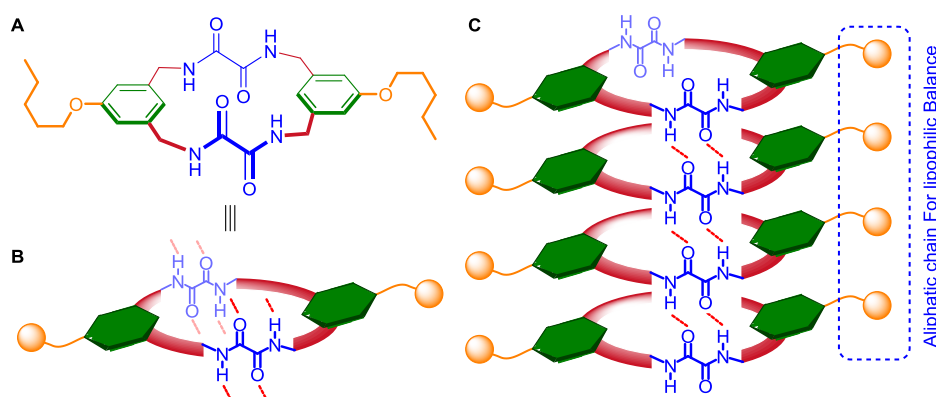


Figure 3. Structure and design of the rigid macrocyclic building unit having hydrogen bonding moiety and aliphatic chains for lipophilic balance.

Chapter 4: Hopping Mediated Anion Transport through a Mannitol-Based Rosette Ion Channel

Imposition of exclusive ion selectivity of the natural ion channel is associated with the presence of multiple numbers of ion-recognition sites. Small molecules were designed that can self-organized to form a barrel-rosette ion channel in the lipid membrane to offer a single-file multiple anion-recognition sites. Diketal protected mannitol derivative can form nanotubes through intermolecular hydrogen bond formation, while its hydrophobic counterpart is stabilized by the hydrophobic interaction in the membrane. Anion selectivity of the supramolecular ion channel was confirmed by ion transport experiments across the vesicular lipid bilayers, and planar

lipid bilayers. Molecular dynamics (MD) simulations indicate the formation of a trimeric rosette which self-assembled to form a channel, and the $\text{OH}\cdots\text{Cl}^-$ hydrogen bonding interaction for successive anion transport by hopping mechanism.

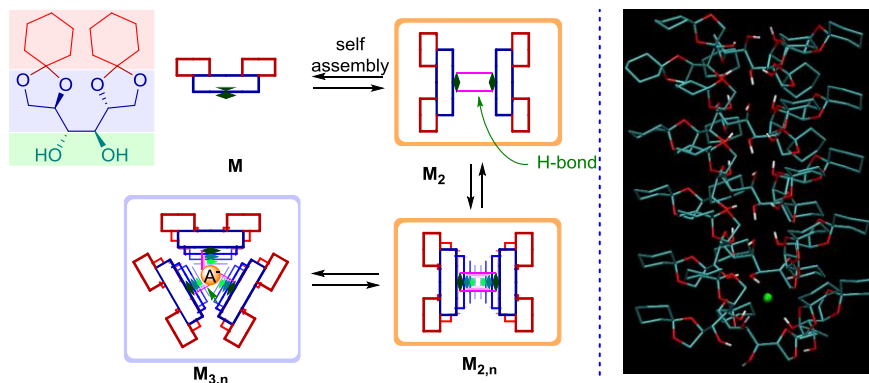


Figure 4. The structure of the building unit of barrel-rosette ion channel and mode of self-assembly to form the nanochannel structure.

Chapter 5: Chloride Transport through Supramolecular Barrel-Rosette Ion Channels: Lipophilic Control and Apoptosis-Inducing Activity

Despite the great interest in the artificial ion channel design, only a small number of channel forming molecules are currently available for addressing challenging problems, particularly in the biological systems. The present work describes vicinal diols, tethered to a rigid 1,3-diethynylbenzene core, as pivotal moieties for the barrel-rosette ion channel formation. Ion transport across vesicles revealed an excellent alliance of lipophilicity with the transport activity.

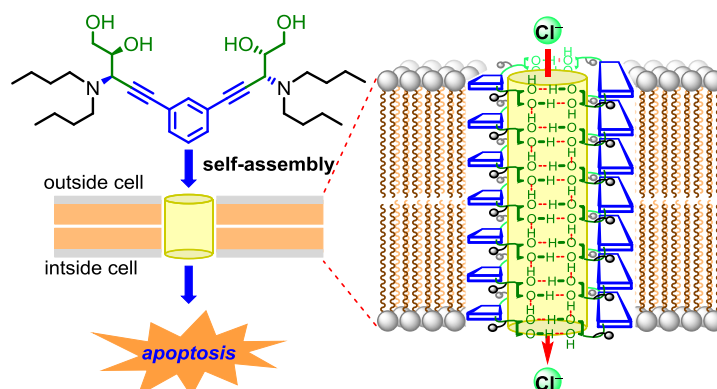


Figure 5. Structure and design strategy of the barrel-rosette ion channel.

The bis(diols) system favoured anion transport with prominent chloride ion selectivity. The bis(diols) system was efficient in delivering Cl^- ions into cells, and the process also

resulted in perturbation of intracellular ionic homeostasis. The perturbation of chloride homeostasis in cell instigates cell death by inducing caspase-mediated intrinsic pathway of apoptosis. This ion transport mediated apoptosis inducing activity can be a potential approach for anticancer therapy.

Chapter 6: Chloride-Mediated Apoptosis-Inducing Activity of Bis(sulfonamide) Anionophores

Ion carriers are relatively small biomolecules, which can travel across the membrane after successive complexation with ions followed by the release of the same on the opposite side of the membrane. Here we show bis(sulfonamides) as efficient receptors for selective Cl^- ion binding and transport across lipid bilayer membranes. Anion binding studies by ^1H NMR indicate a logical correlation between the acidity of sulfonamide N–H proton and binding strength. Such recognition is influenced further by the lipophilicity of a receptor during the ion transport process. Fluorescent-based assays confirm the Cl^- /anion antiport as the operational mechanism of the ion transport by bis(sulfonamides). MTT assay indicated an inverse correlation between cell viability and ion transport activity of bis(sulfonamides) derivatives. The elevated intracellular Cl^- ion level and the Cl^- mediated cell death were also confirmed because of the disruption of ionic homeostasis of cells. Induction of caspase-dependent intrinsic pathway of apoptosis was established by a number of experiments. Hence, artificial Cl^- transporters as apoptotic inducing agents, via disrupting ionic homeostasis of the cell, could be a potential therapeutic tool for cancer treatment in next generation.

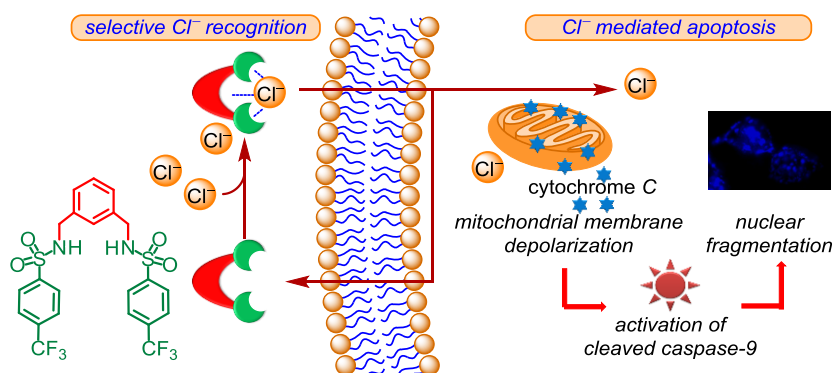


Figure 6. Structure and design strategy of the ion carrier and induction of apoptosis.

Contents

Contents	i
List of Symbols and Abbreviations	v
Chapter 1. Introduction	1
1.1. Introduction of Cell Membrane	2
1.2. Membrane Transport	3
1.3. Ion Transport	3
1.4. Membrane Potential and Ion Transport	5
1.5. Characteristics of Ion Transport Systems	6
1.6. Natural Ion Transport Systems	7
1.7. Significance of Ion Transport	9
1.8. Design Principle of Artificial Ion Transport System	10
1.9. Artificial Ion Channels	11
1.10. Artificial Ion Carriers	14
1.11 Artificial Ion Transport Systems in the Light of Next Generation Therapeutics	15
1.12. Techniques Used in Ion Channel Studies	17
1.12.1. Ion Transport Study in Spherical Lipid Bilayer	17
1.12.2. Ion Transport Study in Planar Lipid Bilayer	19
1.12. Reference	20
Chapter 2. Unimolecular Anion-Selective Artificial Ion Channel	25
2.1. Introduction	26
2.2. Result and Discussion	29
2.2.1. Synthesis	29
2.2.2. Ion Transport Activity	29
2.2.3. Ion Selectivity Studies	32
2.3. Conclusion	35
2.4. Experimental Section	36
2.4.1. General Methods	36
2.4.2. Physical measurements	36

2.4.3. Synthesis	36
2.4.4. Ion Transport Activity	36
2.4.5. Ion Selectivity Studies	37
2.4.6. Molecular Dynamics Simulation	38
2.5. Reference	39
Chapter 3: Self-Assembly of Bis(oxalyl amide) Macrocycles as Transmembrane Barrel-Hoop Anion Channel	41
3.1. Introduction	42
3.2. Result and Discussion	44
3.2.1. Synthesis	44
3.2.2. Ion Transport Activity	45
3.2.3. Ion Selectivity	46
3.2.4. Membrane Disruption Assay by CF	47
3.2.5. Planar Lipid Bilayer Conductance Measurements	48
3.3. Conclusion	49
3.4. Experimental Section	50
3.4.1. General Methods	50
3.4.2. Physical measurements	50
3.4.3. Synthesis	51
3.4.4. Ion Transport Activity	52
3.4.5. CF Assay	52
3.4.6. Planar Bilayer Conductance Measurements	53
3.4.7. NMR Spectra	54
3.5. Reference	58
Chapter 4: Hopping Mediated Anion Transport through a Mannitol-Based Rosette Ion Channel	60
4.1. Introduction	61
4.2. Result and Discussion	65
4.2.1. Self-assembly of Mannitol Derivatives in Solid State	65
4.2.2. Ion Transport Activity by Vesicle Assay	66
4.2.3. Ion Selectivity Studies by Vesicle Assay	68

4.2.4. Mass-Spectrometric Evidence of Anion Binding	71
4.2.5. Single Channel Conductance Measurements	72
4.2.6. Molecular Model of Ion Channel	73
4.2.7. Free Energy Profile and Mechanism of Ion Transport	75
4.3. Conclusion	78
4.4. Experimental Section	79
4.4.1. General Methods	79
4.4.2. Physical measurements	79
4.4.3. Synthesis	79
4.4.4. Single Crystal X-ray Crystallography Study of 1 and 2	79
4.4.5. Ion Transport Activity	82
4.4.6. Mass-Spectrometric study for Anion Recognition	83
4.4.7. Planar Bilayer Conductance Measurements	83
4.5. Reference	83
Chapter 5: Chloride Transport through Supramolecular Barrel-Rosette Ion Channels: Lipophilic Control and Apoptosis-Inducing Activity	87
5.1. Introduction	88
5.2. Result and Discussion	90
5.2.1. Synthesis	90
5.2.2. Ion Transport Activity	91
5.2.3. Ion Selectivity Studies	93
5.2.4. Chloride Ion Transport Assay	94
5.2.5. Planar Lipid Bilayer Conductance Measurements	98
5.2.6. Molecular Modeling for the Ion Channel Formation	98
5.2.7. Effect of Ion Transport in Biological System	99
5.3. Conclusion	106
5.4. Experimental Section	107
5.4.1. General Methods	107
5.4.2. Physical measurements	108
5.4.3. Synthesis	108
5.4.4. Ion Transport Activity and Selectivity	113

5.4.5. Planar Bilayer Conductance Measurements	116
5.4.6. Molecular Modeling Studies	117
5.4.7. Biological Studies	117
5.4.8. NMR Spectra	120
5.5. Reference	128
Chapter 6: Chloride-Mediated Apoptosis-Inducing Activity of Bis(sulfonamide) Anionophores	132
6.1. Introduction	133
6.2. Result and Discussion	135
6.2.1. Synthesis	135
6.2.2. Anion Binding Studies	136
6.2.3. Anion Binding Model	139
6.2.4. Ion Transport Activity	142
6.2.5. Ion Selectivity Studies	144
6.2.6. Chloride Ion Transport Assay	145
6.2.7. Ion Transport Mechanism	147
6.2.8. Evidence of Carrier Mechanism	149
6.2.9. Effect of Ion Transport in Biological System	150
6.3. Conclusion	159
6.4. Experimental Section	160
5.4.1. General Methods	160
6.4.2. Physical measurements	160
6.4.3. Synthesis	161
6.4.4. Anion Recognition by ^1H -NMR Titration	164
6.4.5. Ion Transport Activity and Selectivity	165
6.4.6. Evidence of Carrier Mechanism	165
6.4.7. Biological Studies	165
6.4.8. NMR Spectra	169
6.5. Reference	177
Overall Conclusion	182
Research Publications	183

Abbreviations and Symbols

A

α	Alpha
Å	Angstrom
A	Absorbance
Ar	Aromatic
Ac	Acetyl
ANOVA	Analysis of Variance
ADP	Adenosine Di-Phosphate
ATP	Adenosine Tri-Phosphate

B

β	Beta
br	Broad singlet
BLM	Bilayer lipid membrane or Black lipid membrane

C

c	Concentration
cm	Centimeter
CD	Cyclodextrin
CF	Carboxyfluorescein
Cal	Calorie
Calc	Calculated
CPT	Camptothecin
CFTR	Cystic Fibrosis Transmembrane Conductance Regulator
CLC	Chloride Channel
CLIC	Chloride intracellular channel protein
CLNS1A	Chloride Nucleotide-Sensitive Channel 1A
CLCA	Calcium-activated chloride channel
CHCl_3	Chloroform
CDCl_3	Deuterated chloroform

CH ₃ CN	Acetonitrile
CsCl	Cesium chloride
CCDC	Cambridge Crystallographic Data Centre

D

δ	Delta (Chemical shift)
°C	Degree Celsius
<i>d</i>	Diameter
d	Doublet
dd	Doublet of doublet
DPhPC	2-diphytanoyl- <i>sn</i> -glycero-3-phosphocholine
DMSO	Dimethylsulfoxide
DMF	Dimethylformamide
DCM	Dichloromethane
D ₂ O	Deuterated water
DMEM	Dulbecco's Modified Eagle's Medium
DTT	Dithiothreitol

E

Energy	Energy
EYPC	L- α -phosphatidylcholine from egg-yolk
EC ₅₀	Effective concentration at half maximal activity
EtOAc	Ethylacetate
EtOH	Ethanol
Et ₃ N	Triethylamine
ESI	Electrospray ionization

F

F	Faraday's constant
F _{<i>t</i>}	Fluorescence intensity at time <i>t</i>
FCCP	Carbonyl cyanide- <i>p</i> -trifluoromethoxyphenylhydrazone

FBS	Fetal bovine serum
G	
g	corrected conductance
GA	Glucosamine
GAPDH	Glyceraldehyde 3-phosphate dehydrogenase
G1	Gap-1 phase in cell cycle
G	Free energy
G_{hyd}	Free energy of hydration
H	
Hz	Hertz
h	Hour
HPTS	8-Hydroxypyrene-1,3,6-trisulfonate trisodium salt
HBSS	Hanks balanced salt solution
HEPES	4-(2-hydroxyethyl)-1-piperazineethanesulfonic acid
HCl	Hydrochloric acid
HPLC	High performance liquid chromatography
HRMS	High Resolution Mass Spectrometry
I	
I_{F}	Normalized Fluorescence Intensity
IP ₃	Inositoltriphosphate
IR	Infrared spectroscopy
ISE	Ion selective electrode
J	
J	Coupling constant
J	Joule
K	
k	Kilo

k	Rate constant
K	Equilibrium constant
K_a	Association constant
K_d	Dissociation constant
K_2CO_3	Potassium carbonate
KCl	Potassium chloride
KBr	Potassium bromide
L	
λ	Lambda
Leu (L)	Leucine
Lys (K)	Lysine
LUV	Large unilamellar vesicle
logP	Partition Coefficient
LAH	Lithium aluminium hydride
LiCl	Lithium chloride
M	
m	Multiplet
M	Molar
μM	Micromolar
μL	Microliter
M.P.	Melting Point
MHz	Mega hertz
min	Minute(s)
max	Maximum
mg	Milligram(s)
mol	Mole
mmol	Millimole(s)
mM	Millimolar
mL	Milliliter
M. Wt.	Molecular weight

MQAE	<i>N</i> -(Ethoxycarbonylmethyl)-6-methoxyquinolinium bromide
MTT	3-(4,5-dimethylthiazol-2-yl)-2,5-diphenyltetrazolium bromide
MMP	Mitochondrial Membrane Potential
MALDI	Matrix Assisted Laser Desorption Ionization
MeOH	Methanol
Me	Methyl
MD	Molecular Dynamics

N

<i>n</i>	Hill coefficient
nm	Nanometer
NMR	Nuclear magnetic resonance
Na ₂ SO ₄	Sodium sulfate
NaF	Sodium fluoride
NaCl	Sodium chloride
NaBr	Sodium bromide
NaI	Sodium iodide
NaNO ₃	Sodium nitrate
NaClO ₄	Sodium perchlorate
NaSCN	Sodium thiocyanate
NaOAc	Sodium acetate
NaOH	Sodium hydroxide

O

obs	Observed
ORTEP	Oak Ridge Thermal Ellipsoid plot

P

pS	Picosiemens
pA	Picoampere
Ph	Phenyl
PTP	Permeability Transition Pore
PARP	Poly(ADP-ribose) polymerase
PBS	Phosphate-Buffered Saline

PEG	Polyethylene glycol
PAGE	Polyacrylamide Gel Electrophoresis
PVDF	Polyvinylidene fluoride
PPh ₃	Triphenylphosphine
PTSA	p-toluenesulfonic acid
Ph	Phenyl

R

<i>R</i>	Ideal gas constant
<i>r_i</i>	Initial rate
ρ	Resistivity
rt or RT	Room temperature
ROS	Reactive Oxygen Species
RbCl	Rubidium chloride

S

<i>s</i>	Second
Ser (S)	Serine
SDS	Sodium Dodecyl Sulfate
S	Synthesis phase in cell cycle

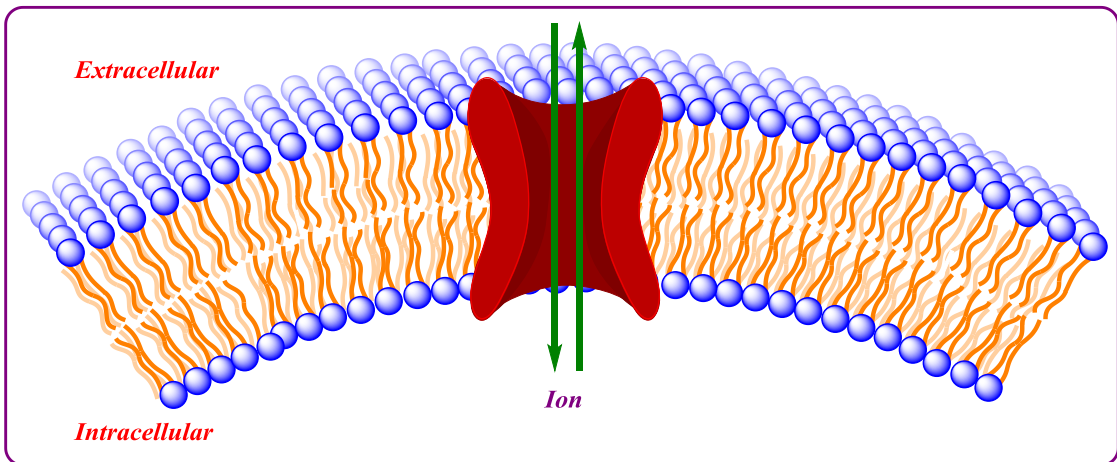
T

T	Temperature in Kelvin
t	Triplet
<i>t</i>	Time
Tx	Triton X-100
TLC	Thin Layer Chromatography
<i>t_{1/2}</i>	Half-life
TBS	Tris-Buffered Saline
THF	Tetrahydrofuran
TFA	Trifluoroacetic acid

TRPC6	Transient receptor potential cation channel, subfamily C, member 6
TBA	Tetrabutyl ammonium
TOF	Time of flight
Try (W)	Tryptophan
V	
V_m	Membrane Potential
V or Val	Valinomycin
VDAC	Voltage activated anion channel
Y	
Y	Fractional fluorescence intensity
Z	
z-DEVD-fmk	Benzyloxycarbonyl-Asp(OMe)-Glu(OMe)-Val-Asp(OMe)-fluoromethylketone
z-LEHD-fmk	Benzyloxycarbonyl-Leu-Glu(OMe)-His-Asp(OMe)-fluoromethylketone

Chapter 1

Introduction



1.1. Introduction of Cell Membrane:

The immense diversity of living organisms on the surface of the planet is based on a single basic building block: the cell, which is the basic structural, functional and biological unit of life. It performs the task of carrying genetic information, controlling physiological and biological activities, storing and producing energy. A eukaryotic cell consists of mainly two subunits, protoplasm, and the cell membrane. Protoplasm is comprised of several cell organelles like the nucleus, mitochondria, golgi body, endoplasmic reticulum, lysosome, and cytoplasm. The cell membrane is the lipid bilayer which confines and separates the protoplasm from the external environment. The internal cell organelles are also circumscribed by a single or multiple layers of the lipid bilayer. A lipid bilayer is nothing but the liquid crystalline state of the self-organized structure of millions of amphiphilic lipid molecules, maintaining a constant separation between intracellular and extracellular water pool. The key feature of the membrane is buried in the structure of the lipid molecule which comprises a hydrophilic head group connected to two hydrophobic tails. This unique structural feature imposes the self-organization of lipid molecules such a fashion that each leaf of the lipid bilayer comprises an array of the hydrophilic head groups while the other side consists of hydrophobic tails (Figure 1.1). In the presence of aqueous environment, the layers of hydrophobic groups come closer to form a bilayer where the hydrophilic head-groups are exposed to the aqueous environment.

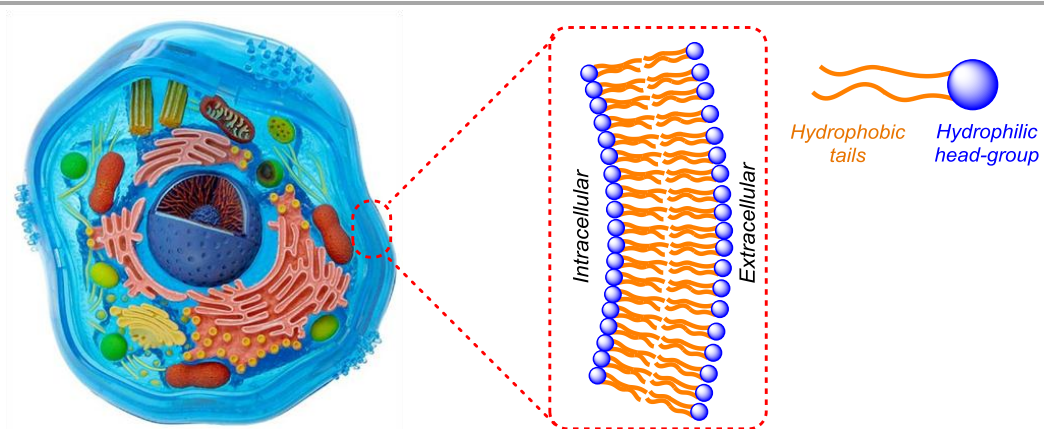


Figure 1.1: Schematic representation of eukaryotic cell and the structure of lipid bilayer. The diagram of cell has been adapted from www.thinglink.com/scene/648262315606540289.

1.2. Membrane Transport:

As the building block of life, every cell has to acquire some raw materials from the environment to perform the fundamental task of the cell to cell communication, energy production, and biosynthesis. Similarly, it must also release the byproduct of metabolism to the environment. But the semipermeable character of the membrane, because of a particular arrangement of hydrophobic and hydrophilic groups in the lipid bilayer, only permits a few selective solutes to pass through via simple diffusion process. Small uncharged molecules like natural gases (O_2 , CO_2 , and N_2), water, ethanol and small hydrophobic molecules can cross the membrane by diffusion process along the concentration gradient (Figure 1.2). But biologically significant polar organic molecules (glucose, nucleotides, etc.), large biomolecules (protein, DNA, etc.), and anions cannot penetrate through the lipid bilayer by simple diffusion method because of the large thermodynamic barrier enforced by hydrophobic region of the lipid bilayer.

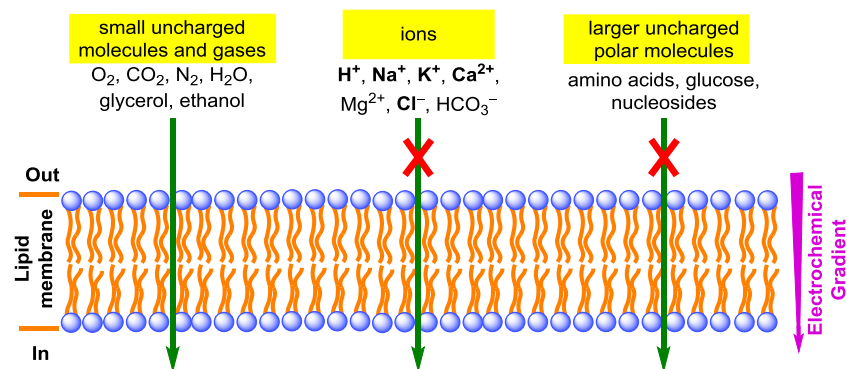


Figure 1.2: Transport of solute through a semipermeable membrane.

1.3. Ion Transport:

Ion transport across the cell membrane operates fundamental tasks of sensory transduction, cell proliferation, and regulation of pH and osmotic stress. The biomembrane present on the cell surface is intercalated with a wide variety of biomolecules, such as proteins, carbohydrates, and their complexes which are responsible for transmembrane transport of biologically active ions. A certain class of membrane proteins performs the crucial task of ion transport via the channel or carrier formation by overcoming the large thermodynamic barrier imposed by phospholipids bilayer. A significant amount of activation energy is being involved in the breaking of hydration shell for an ionic species while entering into the lipid bilayer. An equal amount of energy can be regained by the charged species upon reaching to the water pool on the

opposite side of the membrane. As a result of the hydrophobic environment of the lipid bilayer, at the intermediate path (near about 35 Å), an ion experiences a high-energy state. The transport of ions (or other solutes) through membrane proteins, in a dehydrated or partially hydrated form, is facilitated by the favorable binding interactions with the functionalities present in the hydrophilic channel lumen. These binding interactions impose extra thermodynamic stability to the ions by lowering the energy barrier during transport through the membrane (Figure 1.3).

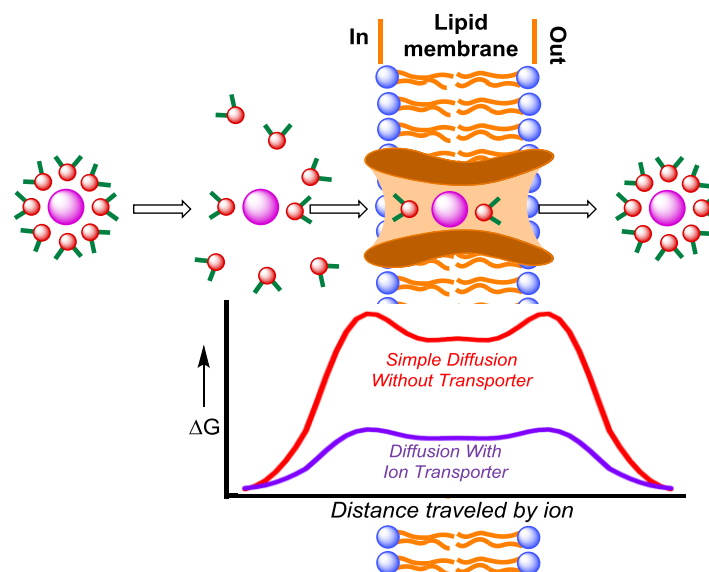


Figure 1.3: Free energy profile of ions in the absence and presence of ion channels.

Ion transport systems are mainly classified into two broad categories, ion carriers, and ion channels. Relatively small biomolecules, which can shuttle across the membrane by engulfing an ion from one side of the membrane and subsequently releases it to the other side are known as ion carriers (Figure 1.4). On the other hand, the large membrane proteins structures, whose transmembrane domain can form a lipophilic path for ions, are called ion channels. The ion transport is further classified into two major categories, active and passive transport. The movement of ions following the concentration gradient across the membrane is called passive transport, and the transport opposite to the concentration gradient is known as active transport. The ion channels involved in active transport mainly belong to the category of ligand-gated ion channel and often called as the ion pump. These gated ion pumps mostly triggered by ligand like ATP which supplies the excess energy required to perform the ion transport against the concentration gradient. The transmembrane proteins which can form a bigger cavity for successive

transport of larger biomolecules (sugar, nucleotide, etc.) are known as transmembrane pore (Figure 1.4).

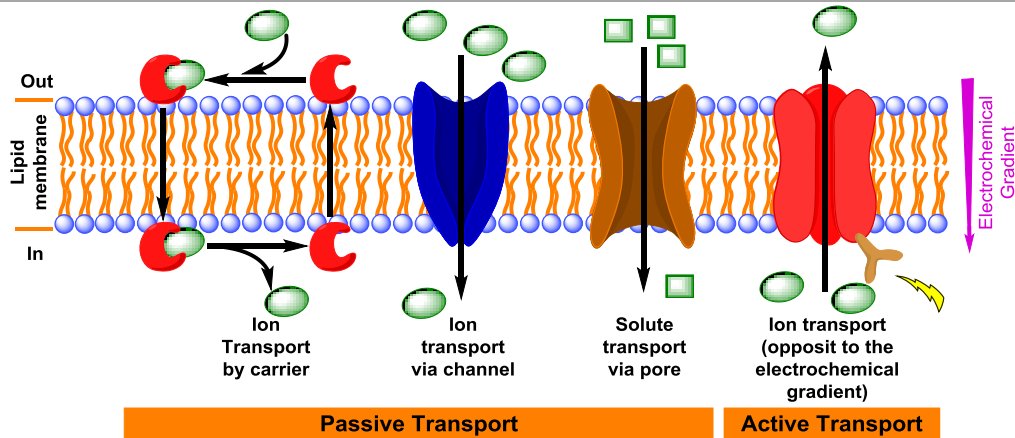


Figure 1.4: Different modes of membrane transport via carrier, channel, and pore.

1.4. Membrane Potential and Ion Transport:

The specific concentration of ions on either side of the lipid membrane comprises the particular membrane potential to the cell membrane as well as to the membranes present in each cell organelle. The equilibrium membrane potential for a particular ion can be calculated according to the Nernst equation,

$$V_m = \frac{RT}{F} \ln \frac{[ion]_{out}}{[ion]_{in}}$$

Equation 1.1

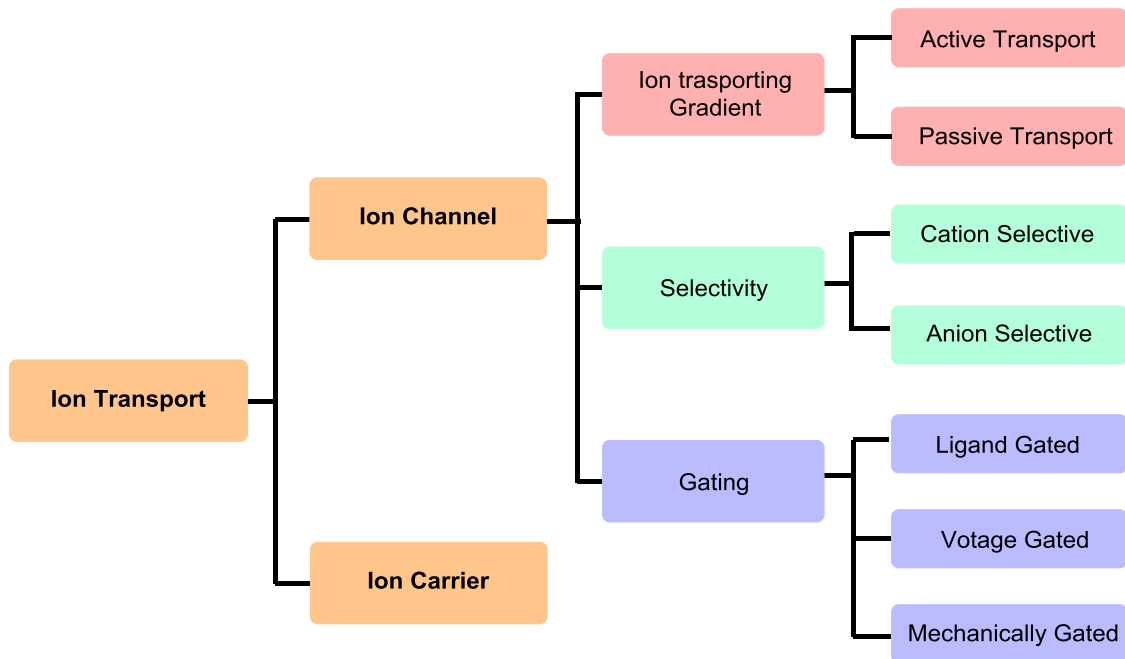
where, V_m = membrane potential; R = ideal gas constant (joules/kelvin/mole); T = temperature (kelvin); F = Faraday's constant (coulombs per mole); $[ion]_{out}$ = ion concentration outside the cell; $[ion]_{in}$ = ion concentration inside the cell.

The specific membrane potential across any particular biological lipid membrane is controlled by ion channels and the particular potential at which ion channels does not conduct any ion is called resting potential. For example, the chloride channels present at the eucaryotic cell membrane maintain the desired membrane potential of 30–60 mV by regulating the particular chloride gradient across the membrane (5–10 mM inside and 110–150 mM outside). On the other hand, the ion channels present at mitochondrial membrane maintains a potential of 180–220 mV.

1.5. Characteristic of Ion Transport Systems:

Ion transport systems mainly belong to two categories depending on the mode of transport, ion channel, and ion carrier. Ion channels are further categorized in various classes depending on their directionality of ion flow, selectivity and gating activity.

Table 1.1: Characteristic of Ion Transport Systems.



Active and passive transport of ion channels have been already discussed. The selectivity of the ion being transported through the channel brings it to two different categories of anion and cation selective ion channels. Among the natural ion channel examples, voltage-dependent anion channel (VDAC) appeared to be anion selective channel whereas, gramicidin A and KcsA are cation selective. On the other hand, the ease of opening and closing of pore depending on particular external stimuli is termed as gating activity of the ion channel. The gating, ease of opening and closing, activity of channel brings it to subcategories of voltage-gated, ligand-gated and mechanically-gated channels.

A. Voltage-Gated Ion Channels: When the opening and closing of ion channels are driven by depolarization and hyperpolarization of the membrane is called voltage-gated ion channel (Figure 1.5A). VDAC and KcsA channels are voltage-gated ion channels, whose transport activities depend on their respective membrane potential.

B. Ligand-Gated Ion Channels: Change in the structural conformation of a channel forming protein upon binding with specific ligand results in either opening or closing of a ligand-gated ion channel (Figure 1.5B). For example, the release of Ca^{2+} ions from the endoplasmic reticulum to the cytoplasm occurs through a calcium channel whose activity is controlled by the inositol triphosphate (IP_3) ligand.^{1,2}

C. Mechanically Gated Ion Channels: The opening and closing property of such kind of ion channels depend on the mechanical stress on the membrane (Figure 1.5C). They can also be termed as stress-activated ion channels. TRPC6 is a cation channel, mainly expressed in the cardiovascular system and is gated by mechanical stress on the membrane.^{3,4}

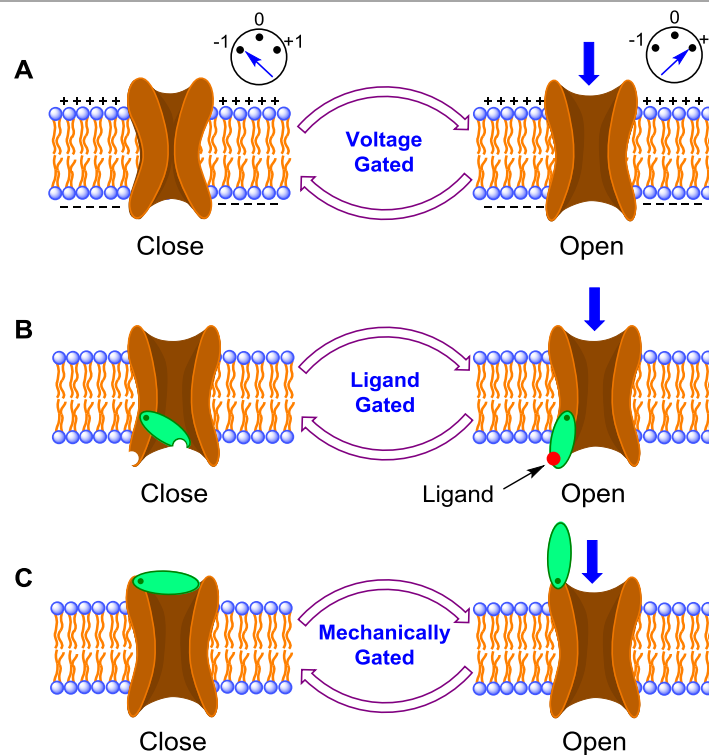


Figure 1.5: Representation of voltage (A), ligand (B) and mechanically (C) gated ion channels.

1.6. Natural Ion Transport Systems:

Diverse categories of ion channels have been observed in nature mainly made up of single or multiple subunits of proteins. The voltage-dependent anion channel (VDAC), is made up of single protein unit and known to be a unimolecular ion channel (Figure 1.6A).⁵ The channel can adopt specific on-off state depending on the potential of the membrane. Gramicidin A, a dimeric ion channel, which is formed by self-assembly of

two identical helical peptides and the channel structure is selective mostly towards cations.⁶ Similarly, the highly potassium selective KcsA channel is comprised of four identical α -helical peptide units, self-assemble to form an hour glass shape channel structure.⁷ The natural antibiotic, amphotericin-B is an example of the amphiphilic non-peptide molecule, which forms an oligomeric cation-selective ion channel. The self-assembly of amphotericin-B possesses a hydrophilic pore made up of the hydroxyl functionalities, and a hydrophobic outer-surface constituted from polyene moieties.⁸ On the other hand, prodigiosin⁹ and valinomycin¹⁰ are two naturally occurring ion carriers which can transport Cl^- and K^+ , respectively (Figure 1.5B). The giant heptameric structure of α -hemolysin, found in *Staphylococcus aureus*, forms a bigger size pore in the membrane for the transport of solutes e.g, water, DNA, toxins (Figure 1.5C).¹¹

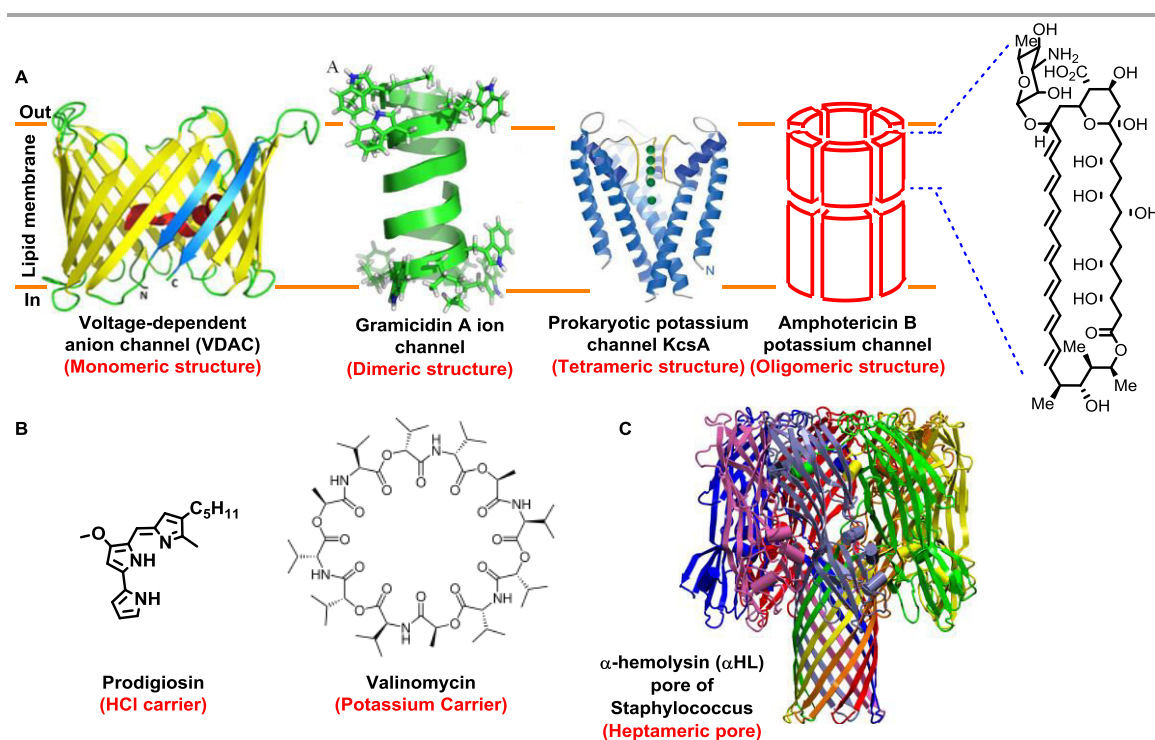


Figure 1.6: Schematic representation of monomeric or oligomeric structures of naturally occurring ion channels (A), ion carriers (B), and a pore (C).

1.7. Significance of Ion Transport:

The transmembrane transport of ions is responsible for fundamental biological functions such as sensory transduction,¹² cell proliferation,^{13,14} osmotic stress response,¹⁵ etc. Natural ion channels allow the passage of a particular ion and the selectivity is primarily governed by the strengths of ion binding at these sites.¹⁶⁻²² Depending on the ion selectivity, natural ion channels are classified into different categories, Na⁺, K⁺, Ca²⁺ and Cl⁻ ion channels. Among them, the cation selective channels are studied from 1950-60s decade but, the study of Cl⁻ channels started from the early 1990s. Therefore, the chloride channels are not much explored compared to cation channels. Being enthusiastic about Cl⁻ channels we have begun to evaluate its importance in the biological world.

Chloride channels are found to be the most abundant anion channels in the physiological system. Selective transport of chloride ion is pivotal in maintaining a desired potential gradient across the bilayer membranes *e.g.* 30–60 mV for eukaryotic cell membrane.²³⁻²⁵ The naturally occurring Cl⁻ ion transporting agents are CFTR, CLC, CLIC, CLNS1A, CLCA, etc. Diverse biological processes, *e.g.* transepithelial salt transport, acidification of internal and extracellular compartments, maintenance of membrane potential, cell volume regulation, cell cycle, and apoptosis^{15,26,27} are related to the selective transport of the ion. A brief discussion of the importance of Cl⁻ ion transporting agents can be illuminated by considering a model system of cancer cells. Here, the activity of CLC-3, a member of voltage-gated chloride channel superfamily, has been taken into account which is mainly expressed in cancer cells. The overexpression of CLC-3 may contribute to cell proliferation, apoptosis and drug resistance of cancer cells. The intracellular concentration of Cl⁻ gets enhanced because of the overexpression of CLC-3 channel which results in the increase in cell volume to maintain a constant osmolarity value. The increase in cell volume facilitates the transition from G1 to S phase in the cell cycle which accelerates the rate of cell proliferation. Hence, overexpressed CLC-3 in cancer cells can enhance the growth rate of tumors. In contrast to that, the activation of the CLC-3 channels in nasopharyngeal carcinoma cells inhibits the particular cell signaling pathway PI3K/Akt/mTOR, resulting in induction of apoptosis. On the other hand, overexpressed CLC-3 in the late endosomes and lysosomes increases the internal acidity, which confers chemical sequestration of basic chemotherapeutic drugs, leading to drug resistance to the cancer cells. Hence, the function of CLC-3 channels, *i.e.*, the concentration of Cl⁻ in the cytoplasm as well as in the internal

cell organelles is very crucial to maintain a normal physiological behavior in living organisms.

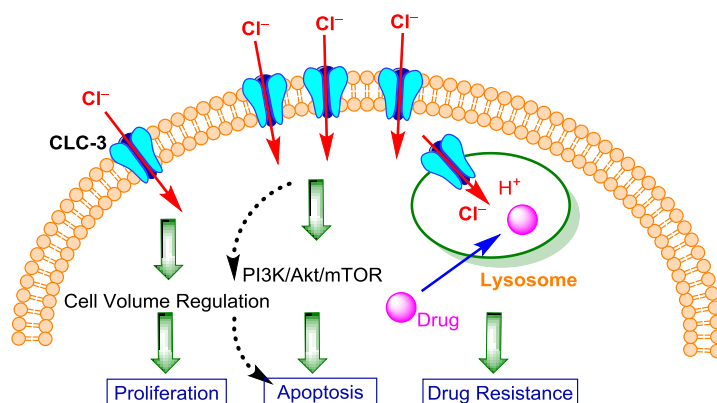


Figure 1.7: Schematic representation of the effect of CLC-3 channel dysfunction in cancer cells.

Additionally, the dysfunction of Cl⁻ ion channels or mutations of specific genes responsible for expressing Cl⁻ transport proteins may lead to various life-threatening diseases. Dysfunction in CFTR ion channel causes loss of the innate immune system of the lung, resulting lung infection, known as cystic fibrosis.²⁸ Myotonia congenita, a type of skeletal muscle disorder, has been found in the case of a mutation in the CLC-1 channel.^{29,30} Apart from that, malfunction of various chloride transporters and CLC family proteins may cause acute renal disorders including Bartter syndrome, Gitelman syndrome, Dent's diseases, etc.³¹ Hence, because of the overwhelming importance of Cl⁻ transport, acquiring a thorough knowledge about the function and workability of chloride transport systems is a burgeoning field for researchers in the biochemistry and biotechnology fields.

1.8. Design Principle of Artificial Ion Transport Systems:

Over the years, scientists have shown immense attention for introducing artificial ion transport systems to mimic diverse properties of natural ion channels and acquire a better understanding of supramolecular interactions. The ease of modulation of ion transport properties in natural ion transport systems is somehow restricted because of their complex structure. Whereas, chemically robust nature and adaptable modulation of ion transport characteristics, gating activity, and selectivity have led artificial ion transport systems as a convenient subject of research. Also, the rich collection of structural and functional motifs have appealed the broad interest of organic chemists to

construct unimolecular or self-assembled abiotic scaffolds which can transport ion either forming membrane-spanning channels, relay systems or mobile carriers. The basic principle of ion transporter design has been buried in the fundamental structural features of natural ion transport systems. Regardless of the structural variation of ion channels or ion carriers (e.g., gramicidin A, prodigiosin, and valinomycin, respectively), these systems always composed of a hydrophobic exterior, to have favorable interaction with lipid molecules, and a hydrophilic interior to recognize the ions (exceptions for water channel). Artificial ion transporting molecules or supramolecules are feature the fundamental concept of hydrophilic interior and hydrophobic exterior.

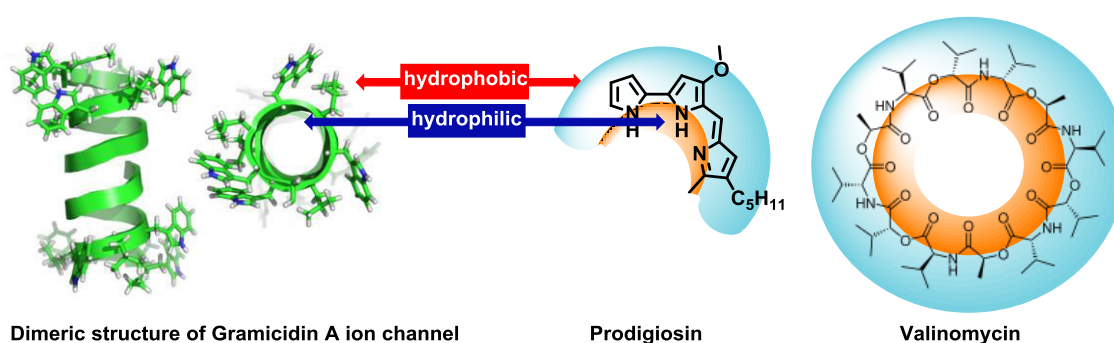


Figure 1.8: Representation of the hydrophilic interior and hydrophobic surface of natural ion transporting agents.

1.9. Artificial Ion Channels:

Various design strategies have been introduced for constructing unimolecular or self-assembled architectures as artificial ion channels. These strategies include unimolecular, barrel-hoop, barrel-stave, barrel-rosette, β -barrel, etc. (Figure 1.9). A brief discussion of reported ion channels following those design principles is presented here.

A. Unimolecular Ion Channels: Unimolecular ion channels are comprised of a single molecule which may contain a macrocyclic unit as a rigid abiotic scaffold, to sustain the membrane pressure, and covalently linked tails for spanning the lipid membrane. Cyclodextrins and

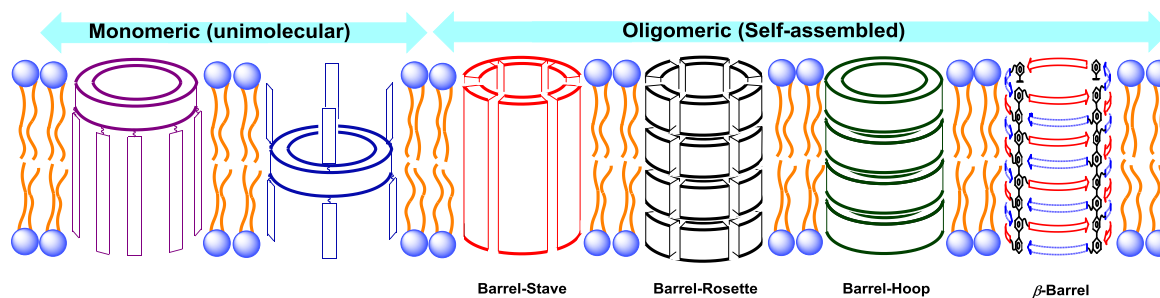


Figure 1.9: Schematic representation of various ion channel design.

calixarene derivatives connected with pentabutylenglycol and cholic acid tails are widely used (**1** and **2**).³²⁻³⁵ On the other hand, azacrown ethers, decorated with an α -helical peptide backbone have been used to maintain a hollow pore along the channel direction (**3**).³⁶

B. Barrel Stave Ion Channels: Cylindrical self-assembly of stave-like monomers has been found to form barrel-stave type self-assembled artificial ion channel. Diarylaminebased stave like molecule can self-assemble via the diamide functionality present at the center of the molecule (**4**).³⁷ Similarly, dimeric steroids have been found to form barrel-stave channels because of its matched length with the thickness of lipid bilayer (**5**).³⁸

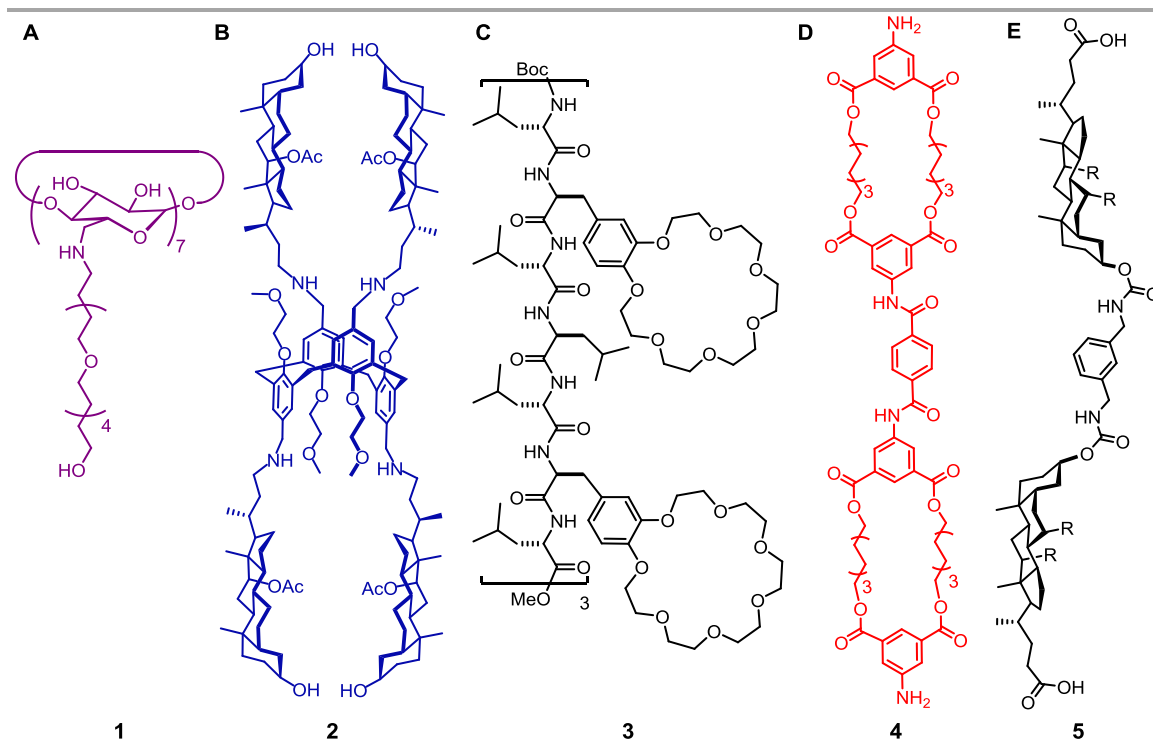


Figure 1.10: Structure of unimolecular (A-C) and barrel stave (C and D) ion channels.

C. Barrel Hoop Ion Channels: Ion channel formation by columnar self-assembly of amphiphilic macrocycles known as barrel-hoop structures. Ghadiri and coworkers have reported a cyclic peptide based on alternate D- and L-amino acids for forming barrel-hoop ion channels (**6**).³⁹⁻⁴⁴

D. Barrel Rosette Ion Channels: Interestingly, circular self-assembly of tiny molecules can result in rosette structures which can be interpreted as self-assembled macrocycles. These macrocyclic structures can further self-assemble in the columnar fashion to create the barrel-rosette type of ion channels. Hydroxy acid derivative reported by Martin and coworkers is known to form self-assembled barrel rosette structures in lipid membrane, and such self-assembly is driven by lipophilic and hydrogen bonding interactions (**7**).⁴⁵ Similarly, substituted guanosine units can form a rosette structure via G-quartets formation then two G-quartets can be brought together by a sandwiched K^+ ion to form G_8-K^+ octamers. Further columnar aggregation of G_8-K^+ octamers can create a channel structure in the lipid membrane (**8**).^{46,47}

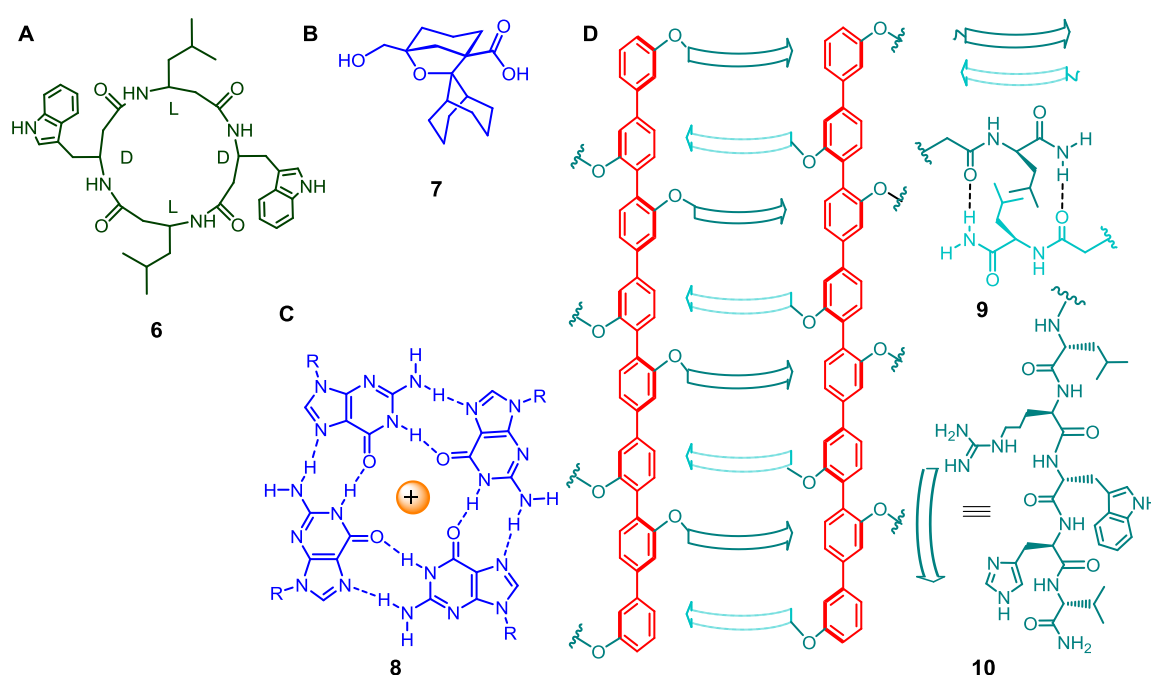


Figure 1.11: Structure of barrel-hoop (A), barrel rosette (B and C), and β -barrel (D) ion channels.

E.β-barrel Ion Channels: The β-barrel ion channel construction closely resembled with the barrel-stave like structure where each stave is further functionalized with a specific hydrogen bonding moieties. These functionalized side arms can undergo self-assembly with complementary candidate present in the adjacent stave. Matile and coworkers have reported molecules composed of rigid octaphenylrods and hydrogen bond forming units. Either a vicinal diol or short peptide connected to each phenyl ring of the Stave facilitated hydrogen bonding with the same moiety from the next molecule (**9** and **10**). Overall, supramolecular process from these hydrogen bond forming units resulted in the β-barrel formation.^{48,49}

1.10. Artificial Ion Carriers:

In past several years, a number of strategies have been incorporated in the construction of ion carriers for selective recognition and transmembrane transport of anions. The design strategies for artificial ion carriers are much simpler, and most of them are inspired from their natural analogs, like valinomycin and prodigiosin. These carriers are comprised of a rigid scaffold having hydrophobic external surface and a hydrophilic ion recognition motif. The rigid scaffold acts as a platform to hold the ion binding functionalities into the inner cavity of the ion receptor. Synthetic macrocyclic structures are widely used as ion receptors which can engulf an ion into their hydrophilic cavity (Figure 1.12). On the other hand, semicircular receptors containing multiple ion binding sites are also a well acceptable scaffold in ion carrier designs. The lipophilic scaffolds commonly so far used are, cholapods (**11**),⁵⁰⁻⁵³ *trans*-decaline (**12**),⁵⁴ calix[4]pyrrole (**13**), its fluorinated (**14**), and triazole analogues,⁵⁵⁻⁵⁷ tripodal tris(aminoethyl)amine (tren) (**15**),⁵⁸ squaramides (**16**),^{23,59} cyclohexane (**17**),⁶⁰ and cyanoguanidines (**18**).⁶¹ Few examples of scaffolds related to prodigiosin structure are also found in the literature (**18**).^{62,63} Various functional motifs have been used for coordinating anions with a host via hydrogen bonding interactions, among them urea, thiourea,^{54,59,64-71} amide groups,^{72,73} etc. are the most acceptable approaches for anion transporters. In addition to that, few examples of anion transporters involving anion-π interactions (**22**)^{74,75} and dipole anion interactions (**21**)^{74,76,77} are also present in literature.

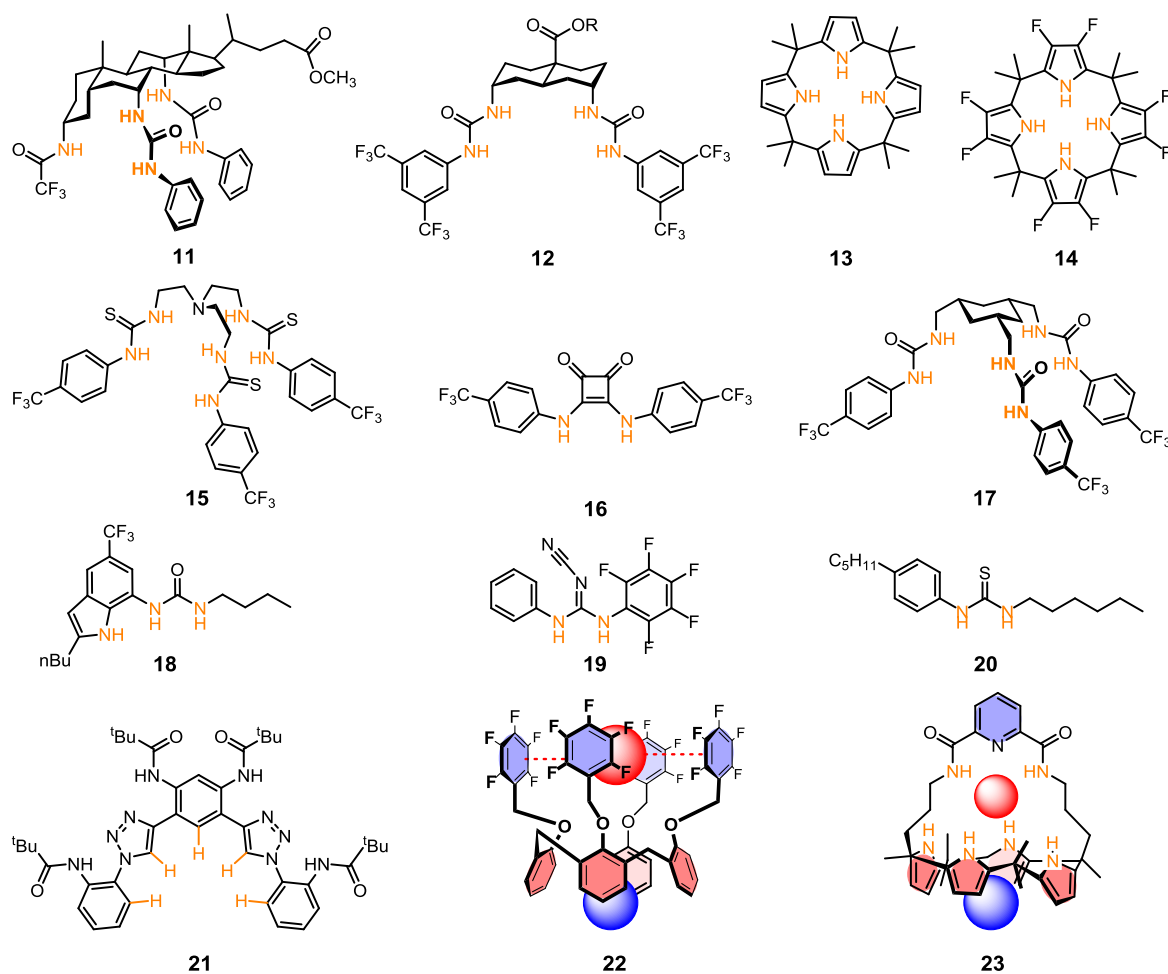


Figure 1.12: Design principle of artificial ion carriers and examples of the ion transporter based on various rigid scaffold and ion binding motifs.

1.11. Artificial Ion Transport Systems in the Light of Next Generation Therapeutics:

The application of artificial ion transport systems has been found in wide range of biotechnology and nanotechnology fields, which include, use in sensing, catalysis, fluidic diodes, etc.^{78,79} For example, a C-terminally modified derivative of gramicidin-A has been reported by Yang and coworkers, which can be employed in the sensing application.⁸⁰ Recently, the introduction of artificial ion channels as the “channel replacement therapy,” has instigated as a novel combination treatment modality for targeting diseases associated with ion channel dysfunction.^{81,82} Channel-forming peptides, which can involve in selective transport of chloride, are employed to restore the Cl⁻ transport in the cells responsible for cystic fibrosis. The addition of these channel forming peptides on the apical surface of cystic fibrosis airway tissues promotes anion

secretion and surface hydration resulting therapeutic benefit for the diseases.⁸¹ Therefore synthetic ion transport systems have immense potential in integrating a palliative care approach into several life-threatening diseases, including cystic fibrosis, cancer, etc. However, the research related to the use of artificial ion channels and carriers are still at the threshold level. In the context of artificial ion channels, crown ether based unimolecular hydrophilic channels (**24**, **25**), reported by Gokel^{83,84} and cyclic peptide (**26**) based self-assembled ion channel reported by

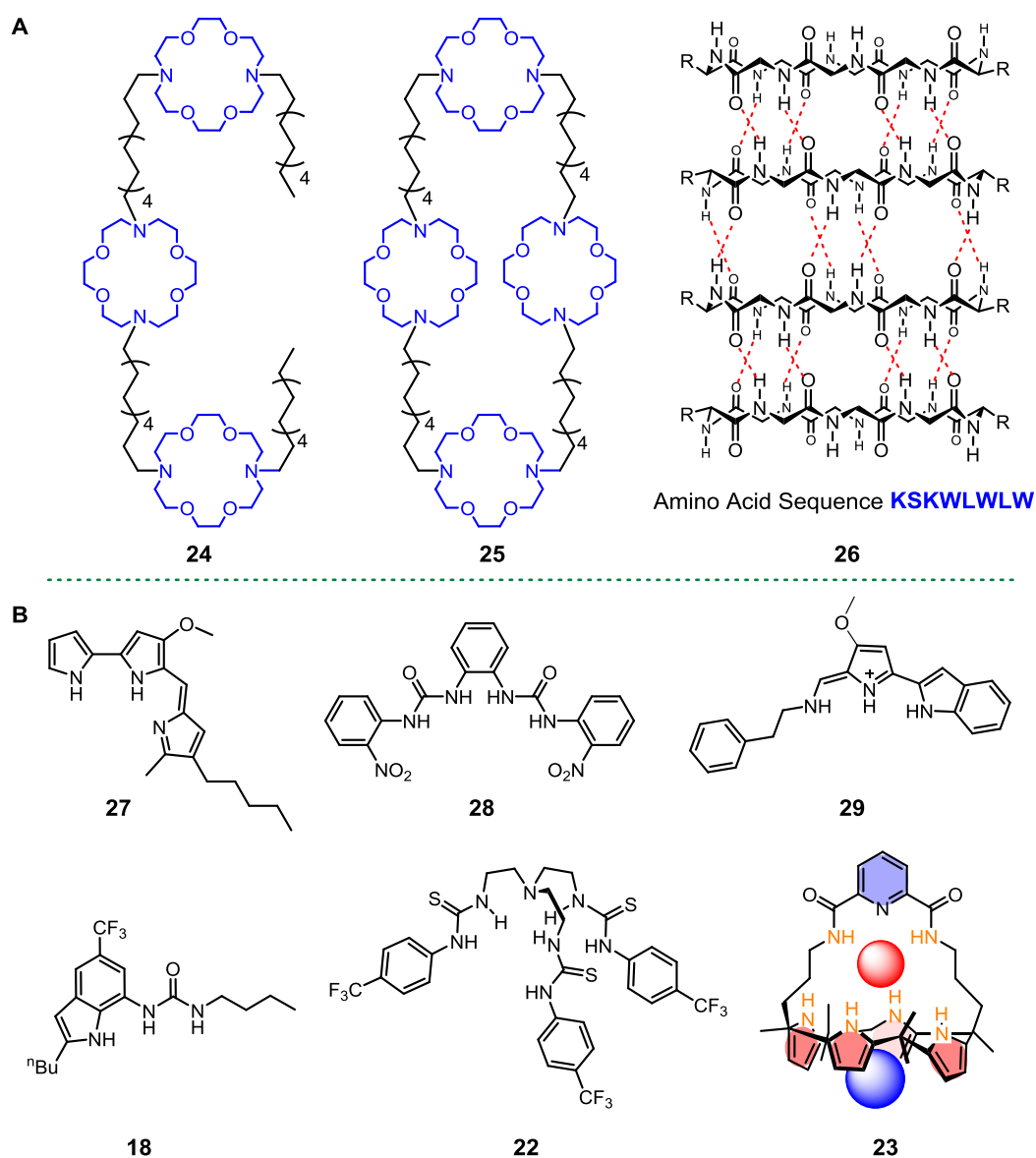


Figure 1.13: Structures of bioactive artificial ion channels (A) and carriers (B).

Ghadiri⁸⁵ have promising antibacterial activity against gram negative and gram positive bacteria. These synthetic ion channels undergo a rapid and selective cell death of bacteria by collapsing the transmembrane ion potential by transporting cations. Few crown ether

based hydrophilic channels, reported by Gokel and Voyer, facilitate cation transport into cells resulting in the cancer cell death via necrotic pathway.⁸⁶⁻⁸⁸ However, apoptotic cell death is preferred for the therapeutic development as the necrotic cell death pathway is associated with possibilities of toxicity in the living organs. On the other hand, anion carriers have revealed the apoptosis-inducing activity in cancer cells by either changing the pH or destroying the ionic homeostasis of cells (Figure 1.13).^{65,69,71,72,89,90} Prodigiosin⁶² is a natural Cl^- carrier that can function as an anion exchanger via either H^+/Cl^- symport or Cl^-/anion antiport mechanism.⁹ Ion transport properties of prodigiosin and its synthetic analogs are also linked to their anticancer activities (27).^{91,92} A classes of urea/thiourea (18, 22, 28),^{65,69,71} and tambjamine analogs (29)⁶³ have shown anticancer activity upon changing the pH of the intracellular matrix. However, the mechanism of apoptosis-inducing activity is not studied in detail for aforementioned ion carriers. The detailed study of apoptosis-inducing activity by calix[4]pyrrole⁷² derivatives (23), upon changing ionic homeostasis of the cell, has been reported by Sessler and coworkers. Hence, the introduction of modern ion transporting agents for palliative care of transport related diseases is a promising field of study.

1.12. Techniques Used in Ion Channel Studies:

Cell membrane mimics, e.g., spherical lipid bilayers (i.e., vesicles) and planar lipid bilayers, made up of commercially available lipids, are used in the evolution of ion transport via synthetic systems. Brief discussion about various ion transport techniques are provided here.

1.12.1. Transport Study in a Spherical Lipid Bilayer: Vesicles are prepared with either EYPC or POPC lipid by the standard freeze-thaw method. Vesicles are subjected to extrude with the polycarbonate membrane of the specific pore size to obtain unilamellar vesicles of uniform diameter ranging from 100-200 nm. Various analytical techniques are used to study the ion transport through liposomal membranes which include fluorescence, ion selective electrode, and ²³Na-NMR titration.

A. Fluorescence Method: Vesicles are prepared by encapsulating 8-hydroxypyrene-1,3,6-trisulfonate (HPTS), a pH sensitive dye. A pH gradient is applied by the addition of NaOH at extravesicular buffer, and the fluorescence intensity of HPTS is monitored with time

(Figure 1.14). The change in pH of the intravesicular buffer, i.e., the change in HPTS emission intensity is only possible when any ion transporting agent is present in the system. Hence, the change in emission intensity can deliver the information of ion transport ability of particular compound. Similarly, lucigenin, a chloride selective dye can be used to monitor the Cl^- ion transport through any ion transporting agent. Additionally, carboxyfluorescein, ANTS-DPX and calcein dyes are also used according to the experimental requirement. Carboxyfluorescein and ANTS-DPX dyes can be used to check the membrane perturbation property and the dye leakage properties of ion transporter molecule. The calcein dye, a Ca^{2+} selective dye, is used to evaluate the Ca^{2+} ion transport by the ion transporting agent.

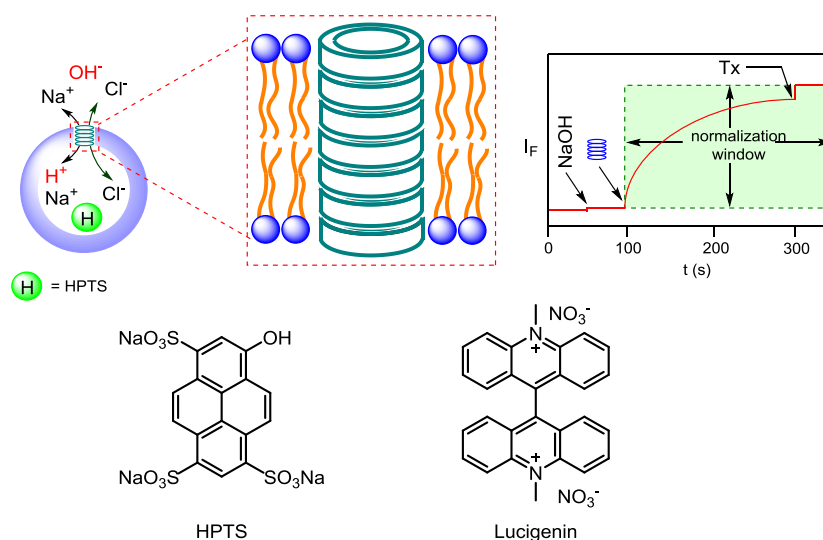


Figure 1.14: Representation of fluorescence-based ion transport assay using vesicles. The structure of fluorescent dyes used in ion transport assay.

B. Ion Selective Electrode: Efflux of ions from vesicles can be monitored by recording the conductivity of particular ion in solution using ion selective electrode. Vesicles loaded with high concentration of NaCl can be suspended in NaNO_3 solution and the rate of Cl^- efflux, after addition of ion transporting agent, can be monitored via chloride selective electrode (Figure 1.15A).

C. ^{23}Na -NMR Titration: In this method, unilamellar vesicles are prepared with NaCl salt, and dysprosium triphosphate salt is added to the extravesicular buffer. The Dy^{3+} salt acts as a shift reagent in the ^{23}Na -NMR study which results in the shifting and broadening of the peak for extravesicular Na^+ . The presence of Dy^{3+} discriminates the ^{23}Na -NMR signal of intra and extravesicular buffer (Figure 1.15B). Hence, the line

broadening of the peak for extravesicular Na^+ can be monitored to check the rate of Na^+ transport across the membrane, in the presence of ion transporting agent.

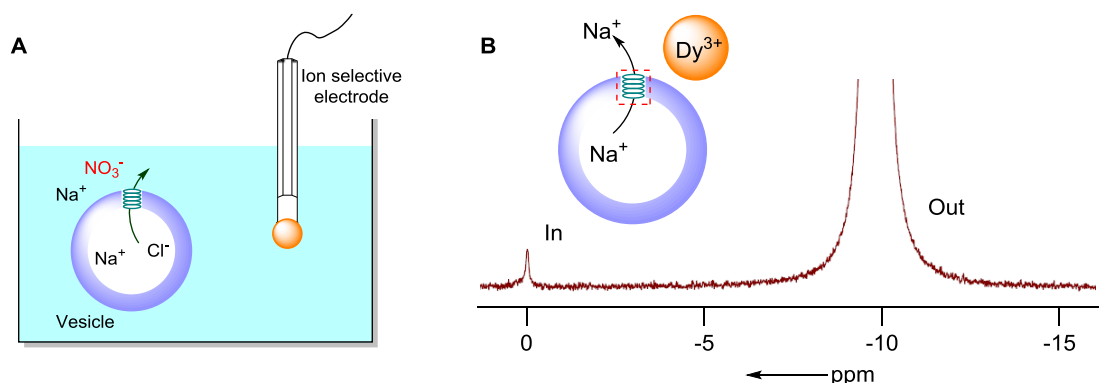


Figure 1.15: Schematic representation of ion transport study using ion selective electrode (A) and ^{23}Na -NMR technique (B).

1.12.2. Ion Transport Study in Planar Lipid Bilayer:

This technique is used to distinguish ion channels from ion carriers by measuring the ion conductance across planar bilayer lipid membrane (BLM). According to this technique, an electrolyte chamber is compartmentalized into two by a Teflon barrier, which contains a tiny hole (of 150–250 μm diameter) to maintain the communication between the electrolyte present in either chamber. A planar lipid bilayer can be readily formed in the micropore to create a semipermeable barrier between electrolyte chambers (Figure 1.16). This planar lipid bilayer restricts the electrical conductance along the nanopore because of blocking the ion flow. The electrical communication between the electrolyte chambers can be restored upon employing an ion channel into the planar lipid bilayer. Therefore, the electrical conductance along the nanopore can provide the information about ion channel formation and properties of ion transport across the lipid bilayer.³⁹ In principle, the electrolyte chamber connected with the ground electrode is known as the *cis* chamber, and the one with measuring electrode is referred to as the *trans* chamber. A small salt bridge is used to connect the chamber and electrode.

The formation of the planar lipid bilayer on the orifice can be justified from the parallel plate capacitor behavior upon applying an exact amount of voltage. The current flow across the membrane is the measure of ion channel behavior. The periodic fluctuation of the current value (generally in pA level) is the signature signal of opening

and closing of the channel on the membrane. Detail of the data analysis and outcome of this experiment is discussed in chapter 3 and 4.

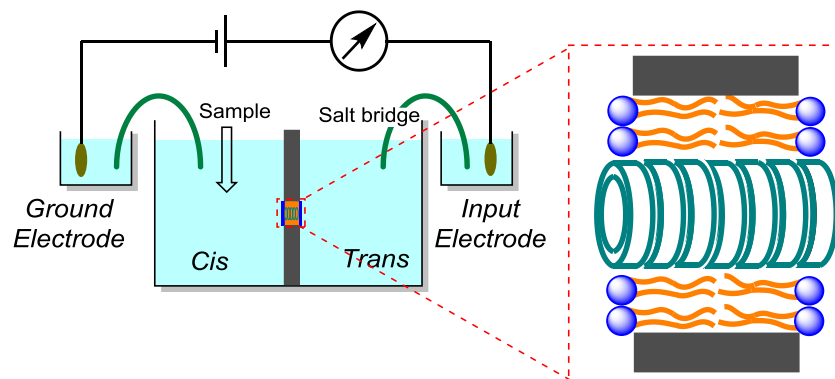


Figure 1.16: Schematic representation of the planar bilayer conductance measurements technique.

1.13. Reference:

- (1) Boulay, G.; Brown, D. M.; Qin, N.; Jiang, M.; Dietrich, A.; Zhu, M. X.; Chen, Z.; Birnbaumer, M.; Mikoshiba, K.; Birnbaumer, L. *Proc. Nat. Acad. Sci.* **1999**, *96*, 14955.
- (2) Hucho, F.; Weise, C. *Angew Chem, Int. Ed.* **2001**, *40*, 3100.
- (3) Sackin, H. *Kidney Int.* **1995**, *48*, 1134.
- (4) Odell, G. M.; Oster, G.; Alberch, P.; Burnside, B. *Dev. Biol.* **1981**, *85*, 446.
- (5) Bayrhuber, M.; Meins, T.; Habeck, M.; Becker, S.; Giller, K.; Villinger, S.; Vornhein, C.; Griesinger, C.; Zweckstetter, M.; Zeth, K. *Proc. Nat. Acad. Sci.* **2008**, *105*, 15370.
- (6) Roux, B.; Karplus, M. *Biophys. J.* **1991**, *59*, 961.
- (7) Doyle, D. A.; Cabral, J. M.; Pfuetzner, R. A.; Kuo, A.; Gulbis, J. M.; Cohen, S. L.; Chait, B. T.; MacKinnon, R. *Science* **1998**, *280*, 69.
- (8) Fujii, G.; Chang, J.-E.; Coley, T.; Steere, B. *Biochemistry* **1997**, *36*, 4959.
- (9) Seganish, J. L.; Davis, J. T. *Chem. Commun.* **2005**, 5781.
- (10) Stark, G.; Ketterer, B.; Benz, R.; Lauger, P. *Biophys. J.* **1971**, *11*, 981.
- (11) Song, L.; Hobaugh, M. R.; Shustak, C.; Cheley, S.; Bayley, H.; Gouaux, J. E. *Science* **1996**, *274*, 1859.
- (12) Legutko, B.; Staufenbiel, M.; Krieglstein, K. *Int. J. Dev. Neurosci.* **1998**, *16*, 347.
- (13) Chiu, S. Y.; Wilson, G. F. *J. Physiol.* **1989**, *408*, 199.
- (14) DeCoursey, T. E.; Chandy, K. G.; Gupta, S.; Cahalan, M. D. *Nature* **1984**, *307*, 465.
- (15) Lange, K. *J. Cell. Physiol.* **2000**, *185*, 21.
- (16) Hille, B.; Schwarz, W. *J. Gen. Physiol.* **1978**, *72*, 409.
- (17) Miller, C. *J. Gen. Physiol.* **1999**, *113*, 783.

- (18) Hille, B. *Ionic Channels of Excitable Membranes, 3rd Edition*, 2001.
- (19) Keramidas, A.; Moorhouse, A. J.; Schofield, P. R.; Barry, P. H. *Prog. Biophys. Mol. Biol.***2004**, *86*, 161.
- (20) Gouaux, E.; MacKinnon, R. *Science***2005**, *310*, 1461.
- (21) Corry, B.; Chung, S. H. *Cell. Mol. Life Sci.***2006**, *63*, 301.
- (22) Tsien, R. W.; Hess, P.; McCleskey, E. W.; Rosenberg, R. L. *Annu. Rev. Biophys. Biophys. Chem.***1987**, *16*, 265.
- (23) Santacroce, P. V.; Davis, J. T.; Light, M. E.; Gale, P. A.; Iglesias-Sanchez, J. C.; Prados, P.; Quesada, R. *J. Am. Chem. Soc.* **2007**, *129*, 1886.
- (24) Jentsch, T. J.; Stein, V.; Weinreich, F.; Zdebik, A. A. *Physiol. Rev.***2002**, *82*, 503.
- (25) Duran, C.; Thompson, C. H.; Xiao, Q.; Hartzell, H. C. *Annu. Rev. Physiol.***2010**, *72*, 95.
- (26) Hong, S.; Bi, M.; Wang, L.; Kang, Z.; Ling, L.; Zhao, C. *Oncology Rep.***2015**, *33*, 507.
- (27) Benz, R.; Hancock, R. E. W. *J. Gen. Physiol.* **1987**, *89*, 275.
- (28) Quinton, P. M. *Nature***1983**, *301*, 421.
- (29) Hutter, O. F.; Noble, D. *J. Physiol.***1960**, *151*, 89.
- (30) Pusch, M.; Steinmeyer, K.; Koch, M. C.; Jentsch, T. J. *Neuron***1995**, *15*, 1455.
- (31) Jentsch, T. J.; Maritzen, T.; Zdebik, A. A. *J. Clin. Inv.***2005**, *115*, 2039.
- (32) Tabushi, I.; Kuroda, Y.; Yokota, K. *Tetrahedron Lett.***1982**, *23*, 4601.
- (33) Madhavan, N.; Robert, E. C.; Gin, M. S. *Angew. Chem., Int. Ed.* **2005**, *44*, 7584.
- (34) Madhavan, N.; Gin, M. S. *ChemBioChem***2007**, *8*, 1834.
- (35) Maulucci, N.; De Riccardis, F.; Botta, C. B.; Casapullo, A.; Cressina, E.; Fregonese, M.; Tecilla, P.; Izzo, I. *Chem. Commun.***2005**, 1354.
- (36) Biron, E.; Otis, F.; Meillon, J.-C.; Robitaille, M.; Lamothe, J.; Van Hove, P.; Cormier, M.-E.; Voyer, N. *Bioorg. Med. Chem.***2004**, *12*, 1279.
- (37) Eggers, P. K.; Fyles, T. M.; Mitchell, K. D. D.; Sutherland, T. *J. Org. Chem.***2003**, *68*, 1050.
- (38) Yoshii, M.; Yamamura, M.; Satake, A.; Kobuke, Y. *Org. Biomol. Chem.***2004**, *2*, 2619.
- (39) Ishida, H.; Qi, Z.; Sokabe, M.; Donowaki, K.; Inoue, Y. *J. Org. Chem.* **2001**, *66*, 2978.
- (40) Bong, D. T.; Clark, T. D.; Granja, J. R.; Ghadiri, M. R. *Angew. Chem., Int. Ed.* **2001**, *40*, 988.
- (41) Sánchez-Quesada, J.; Isler, M. P.; Ghadiri, M. R. *J. Am. Chem. Soc.* **2002**, *124*, 10004.
- (42) Fernandez-Lopez, S.; Kim, H.-S.; Choi, E. C.; Delgado, M.; Granja, J. R.; Khasanov, A.; Kraehenbuehl, K.; Long, G.; Weinberger, D. A.; Wilcoxon, K. M.; Ghadiri, M. R. *Nature***2001**, *412*, 452.
- (43) Clark, T. D.; Buehler, L. K.; Ghadiri, M. R. *J. Am. Chem. Soc.* **1998**, *120*, 651.
- (44) Ghadiri, M. R.; Granja, J. R.; Buehler, L. K. *Nature* **1994**, *369*, 301.
- (45) Pérez, C.; Espínola, C. G.; Foces-Foces, C.; Núñez-Coello, P.; Carrasco, H.; Martín, J. D. *Org. Lett.***2000**, *2*, 1185.

- (46) Forman, S. L.; Fettinger, J. C.; Pieraccini, S.; Gottarelli, G.; Davis, J. T. *J. Am. Chem. Soc.* **2000**, *122*, 4060.
- (47) Sakai, N.; Kamikawa, Y.; Nishii, M.; Matsuoka, T.; Kato, T.; Matile, S. *J. Am. Chem. Soc.* **2006**, *128*, 2218.
- (48) Sakai, N.; Majumdar, N.; Matile, S. *J. Am. Chem. Soc.* **1999**, *121*, 4294.
- (49) Talukdar, P.; Sakai, N.; Sordé, N.; Gerard, D.; Cardona, V. M. F.; Matile, S. *Bioorg. Med. Chem.* **2004**, *12*, 1325.
- (50) McNally, B. A.; Koulov, A. V.; Smith, B. D.; Joos, J.-B.; Davis, A. P. *Chem. Commun.* **2005**, 1087.
- (51) Davis, A. P.; Joos, J.-B. *Coord. Chem. Rev.* **2003**, *240*, 143.
- (52) Davis, A. P. *Coord. Chem. Rev.* **2006**, *250*, 2939.
- (53) McNally, B. A.; Koulov, A. V.; Lambert, T. N.; Smith, B. D.; Joos, J.-B.; Sisson, A. L.; Clare, J. P.; Sgarlata, V.; Judd, L. W.; Magro, G.; Davis, A. P. *Chem. Eur. J.* **2008**, *14*, 9599.
- (54) Hussain, S.; Brotherhood, P. R.; Judd, L. W.; Davis, A. P. *J. Am. Chem. Soc.* **2011**, *133*, 1614.
- (55) Tong, C. C.; Quesada, R.; Sessler, J. L.; Gale, P. A. *Chem. Commun.* **2008**, 6321.
- (56) Gale, P. A.; Tong, C. C.; Haynes, C. J. E.; Adeosun, O.; Gross, D. E.; Karnas, E.; Sedenberg, E. M.; Quesada, R.; Sessler, J. L. *J. Am. Chem. Soc.* **2010**, *132*, 3240.
- (57) Fisher, M. G.; Gale, P. A.; Hiscock, J. R.; Hursthouse, M. B.; Light, M. E.; Schmidtchen, F. P.; Tong, C. C. *Chem. Commun.* **2009**, 3017.
- (58) Busschaert, N.; Gale, P. A.; Haynes, C. J. E.; Light, M. E.; Moore, S. J.; Tong, C. C.; Davis, J. T.; Harrell, W. A., Jr. *Chem. Commun.* **2010**, *46*, 6252.
- (59) Busschaert, N.; Kirby, I. L.; Young, S.; Coles, S. J.; Horton, P. N.; Light, M. E.; Gale, P. A. *Angew. Chem., Int. Ed.* **2012**, *51*, 4426.
- (60) Cooper, J. A.; Street, S. T. G.; Davis, A. P. *Angew. Chem., Int. Ed.* **2014**, *53*, 5609.
- (61) Wenzel, M.; Light, M. E.; Davis, A. P.; Gale, P. A. *Chem. Commun.* **2011**, *47*, 7641.
- (62) Fuerstner, A. *Angew. Chem., Int. Ed.* **2003**, *42*, 3582.
- (63) Soto-Cerrato, V.; Manuel-Manresa, P.; Hernando, E.; Calabuig-Fariñas, S.; Martínez-Romero, A.; Fernández-Dueñas, V.; Sahlholm, K.; Knöpfel, T.; García-Valverde, M.; Rodilla, A. M.; Jantus-Lewintre, E.; Farràs, R.; Ciruela, F.; Pérez-Tomás, R.; Quesada, R. *J. Am. Chem. Soc.* **2015**, *137*, 15892.
- (64) Andrews, N. J.; Haynes, C. J. E.; Light, M. E.; Moore, S. J.; Tong, C. C.; Davis, J. T.; Harrell Jr, W. A.; Gale, P. A. *Chem. Sci.* **2011**, *2*, 256.
- (65) Moore, S. J.; Wenzel, M.; Light, M. E.; Morley, R.; Bradberry, S. J.; Gomez-Iglesias, P.; Soto-Cerrato, V.; Perez-Tomas, R.; Gale, P. A. *Chem. Sci.* **2012**, *3*, 2501.
- (66) Valkenier, H.; Judd, L. W.; Li, H.; Hussain, S.; Sheppard, D. N.; Davis, A. P. *J. Am. Chem. Soc.* **2014**, *136*, 12507.

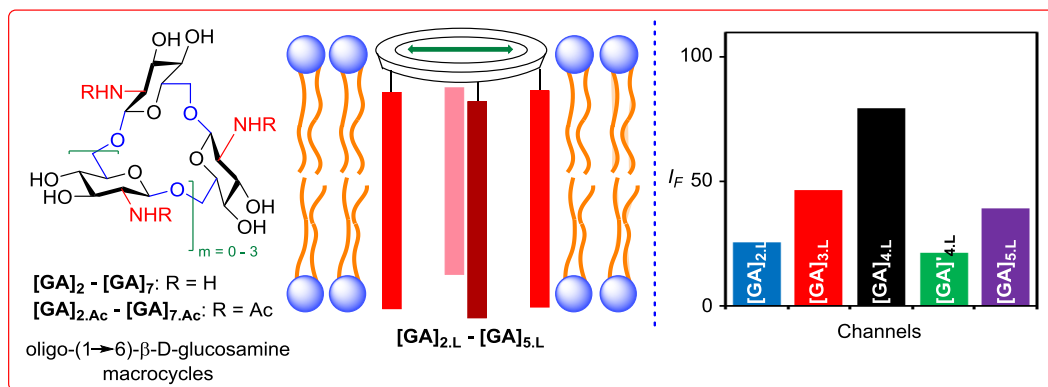
- (67) Busschaert, N.; Bradberry, S. J.; Wenzel, M.; Haynes, C. J. E.; Hiscock, J. R.; Kirby, I. L.; Karagiannidis, L. E.; Moore, S. J.; Wells, N. J.; Herniman, J.; Langley, G. J.; Horton, P. N.; Light, M. E.; Marques, I.; Costa, P. J.; Felix, V.; Frey, J. G.; Gale, P. A. *Chem. Sci.***2013**, *4*, 3036.
- (68) Valkenier, H.; Haynes, C. J. E.; Herniman, J.; Gale, P. A.; Davis, A. P. *Chem. Sci.***2014**, *5*, 1128.
- (69) Busschaert, N.; Wenzel, M.; Light, M. E.; Iglesias-Hernández, P.; Pérez-Tomás, R.; Gale, P. A. *J. Am. Chem. Soc.* **2011**, *133*, 14136.
- (70) Lee, J. H.; Lee, J. H.; Choi, Y. R.; Kang, P.; Choi, M.-G.; Jeong, K.-S. *J. Org. Chem.***2014**, *79*, 6403.
- (71) Moore, S. J.; Haynes, C. J. E.; Gonzalez, J.; Sutton, J. L.; Brooks, S. J.; Light, M. E.; Herniman, J.; Langley, G. J.; Soto-Cerrato, V.; Perez-Tomas, R.; Marques, I.; Costa, P. J.; Felix, V.; Gale, P. A. *Chem. Sci.***2013**, *4*, 103.
- (72) Ko, S.-K.; Kim, S. K.; Share, A.; Lynch, V. M.; Park, J.; Namkung, W.; Van Rossom, W.; Busschaert, N.; Gale, P. A.; Sessler, J. L.; Shin, I. *Nature Chem.***2014**, *6*, 885.
- (73) Winstanley, K. J.; Allen, S. J.; Smith, D. K. *Chem. Commun.***2009**, 4299.
- (74) Vargas Jentsch, A.; Emery, D.; Mareda, J.; Metrangolo, P.; Resnati, G.; Matile, S. *Angew Chem, Int. Ed.* **2011**, *50*, 11675.
- (75) Lin, N.-T.; Vargas Jentsch, A.; Guenee, L.; Neudorfl, J.-M.; Aziz, S.; Berkessel, A.; Orentas, E.; Sakai, N.; Matile, S. *Chem. Sci.***2012**, *3*, 1121.
- (76) Shang, J.; Si, W.; Zhao, W.; Che, Y.; Hou, J.-L.; Jiang, H. *Org. Lett.***2014**, *16*, 4008.
- (77) Lisbjerg, M.; Valkenier, H.; Jessen, B. M.; Al-Kerdi, H.; Davis, A. P.; Pittelkow, M. *J. Am. Chem. Soc.* **2015**, *137*, 4948.
- (78) Wang, D.; Guo, L.; Zhang, J.; Roeske, R. W.; Jones, L. R.; Chen, Z.; Pritchard, C. J. *Peptide Res.***2001**, *57*, 301.
- (79) Steller, L.; Kreir, M.; Salzer, R. *Anal. Bioanal. Chem.***2012**, *402*, 209.
- (80) Blake, S.; Capone, R.; Mayer, M.; Yang, J. *Bioconjugate Chem.***2008**, *19*, 1614.
- (81) Broughman, J. R.; Shank, L. P.; Takeguchi, W.; Schultz, B. D.; Iwamoto, T.; Mitchell, K. E.; Tomich, J. M. *Biochemistry***2002**, *41*, 7350.
- (82) Tomich, J. M.; Bukovnik, U.; Layman, J.; Schultz, B. D. *Cystic Fibrosis: Renewed Hopes through Research***2012**, 291.
- (83) Leevy, W. M.; Donato, G. M.; Ferdani, R.; Goldman, W. E.; Schlesinger, P. H.; Gokel, G. W. *J. Am. Chem. Soc.* **2002**, *124*, 9022.
- (84) Leevy, W. M.; Gokel, M. R.; Hughes-Strange, G. B.; Schlesinger, P. H.; Gokel, G. W. *New J. Chem.***2005**, *29*, 205.

- (85) Fernandez-Lopez, S.; Kim, H.-S.; Chol, E. C.; Delgado, M.; Granja, J. R.; Khasanov, A.; Kraehenbuehl, K.; Long, G.; Weinberger, D. A.; Wilcoxon, K. M.; Ghadiri, M. R. *Nature* **2001**, *414*, 329.
- (86) Leevy, W. M.; Gammon, S. T.; Levchenko, T.; Daranciang, D. D.; Murillo, O.; Torchilin, V.; Piwnica-Worms, D.; Huettner, J. E.; Gokel, G. W. *Org. Biomol. Chem.* **2005**, *3*, 3544.
- (87) Boudreault, P.-L.; Arseneault, M.; Otis, F.; Voyer, N. *Chem. Commun.* **2008**, 2118.
- (88) Smith, B. A.; Daschbach, M. M.; Gammon, S. T.; Xiao, S.; Chapman, S. E.; Hudson, C.; Suckow, M.; Piwnica-Worms, D.; Gokel, G. W.; Leevy, W. M. *Chem. Commun.* **2011**, *47*, 7977.
- (89) Soto-Cerrato, V.; Manuel-Manresa, P.; Hernando, E.; Calabuig-Fariñas, S.; Martinez-Romero, A.; Fernandez Dueñas, V.; Sahlholm, K.; Knopfel, T.; Garcia-Valverde, M.; Rodilla, A. M.; Jantus-Lewintre, E.; Farras, R.; Ciruela, F.; Perez-Tomas, R.; Quesada, R. *J. Am. Chem. Soc.* **2015**, *137*, 15892.
- (90) Saha, T.; Hossain, M. S.; Saha, D.; Lahiri, M.; Talukdar, P. *J. Am. Chem. Soc.* **2016**, *138*, 7558.
- (91) Sessler, J. L.; Eller, L. R.; Cho, W.-S.; Nicolaou, S.; Aguilar, A.; Lee, J. T.; Lynch, V. M.; Magda, D. J. *Angew. Chem., Int. Ed.* **2005**, *44*, 5989.
- (92) Marchal, E.; Rastogi, S.; Thompson, A.; Davis, J. T. *Org. Biomol. Chem.* **2014**, *12*, 7515.

End of Chapter 1

Chapter 2

Unimolecular Anion-Selective Artificial Ion Channel





2.1. INTRODUCTION:

Biomimetic artificial ion transport systems have gained a prime interest of research from last two decades because of their fundamental biological activity. Various synthetic or semisynthetic compounds were studied as potential building blocks to design artificial ion transport systems which can either form unimolecular or self-assembled membrane-spanning channels for transmembrane transport of ions. Use of macrocyclic organic compounds (mostly, cyclic oligosaccharides) connected to membrane spanning tails is a well acceptable approach for designing artificial unimolecular ion channels. Those cyclic oligosaccharides provide the rigid platform to withstand the implosion caused by lipid pressure, and membrane spanning tails are used to allow the hydrophilic passage for conduction of ion.¹⁻¹⁰ Cyclodextrins (CDs) have been widely used as a rigid macrocyclic scaffold to construct artificial ion transport systems.¹¹⁻¹⁶ The connection of membrane spanning linkers to the CDs led to the formation of ion channels displaying either cation or anion selectivity. The pioneering work by Tabushi and coworkers highlighted the A,C,D,F,-tetra-6-(6-n-butyrylamino-n-hexylsulfenyl)- β -cyclodextrin as a half-channel dimer that displayed cation transport across lipid membranes.¹¹ Fyles and coworkers reported triazole-linked β -CD derivatives as half-channel dimers, and cation transport through these channels was established.^{14,16} The per-(2,3-di-O-heptyl)-6-methoxyPEG-6-(1,2,3-triazole)- β -CDs were also tested for their pH-dependent aggregation characteristics in the lipid membranes.¹⁵ Despite, most of the CD based unimolecular ion channels are cation-selective, anion selective unimolecular artificial ion channel consisting of aminocyclodextrin derivative was reported by Gin and co-workers (Figure 2.1A).^{12,13} Under physiological conditions, the β -CD derivative exhibited anion transport with selectivity sequence of $I^- > Br^- > Cl^-$. In contrast with the selectivity sequence, Cl^- is the most abundant anion in physiological systems; therefore, artificial ion channel having Cl^- selectivity is always preferable. However, the design of a Cl^- selective ion channel based on CDs (α -, β - and γ -CD) is challenging because of large cavities of these cyclic oligosaccharides (Figure 2.1B). The inner diameters of common CDs ($d_{\alpha-CD} = 0.45 - 0.57$ nm, $d_{\beta-CD} = 0.62 - 0.78$ nm and $d_{\gamma-CD} = 0.79 - 0.95$ nm) are very large compared to the diameter of Cl^- ion ($d_{Cl^-} = 0.36$ nm). Unfortunately, smaller analogs of CDs are

Synthetically inaccessible because of strain imposed in the inter-saccharidic bond angle on the diminution of cyclodextrin macrocycle from six glucose units.¹⁷ On the other hand, molecular recognition studies and theoretical calculation revealed that the cavity present in β -CD is mostly hydrophobic which is not preferable for ion recognition (Figure 2.1C).^{18,19} Furthermore, the modulation of ion transport activity was not explored in the case of CD based ion transport systems. Hence, the introduction of a new sugar-based artificial Cl^- selective unimolecular ion channel having a hydrophilic cavity and tuneable transport activity was of prime importance.

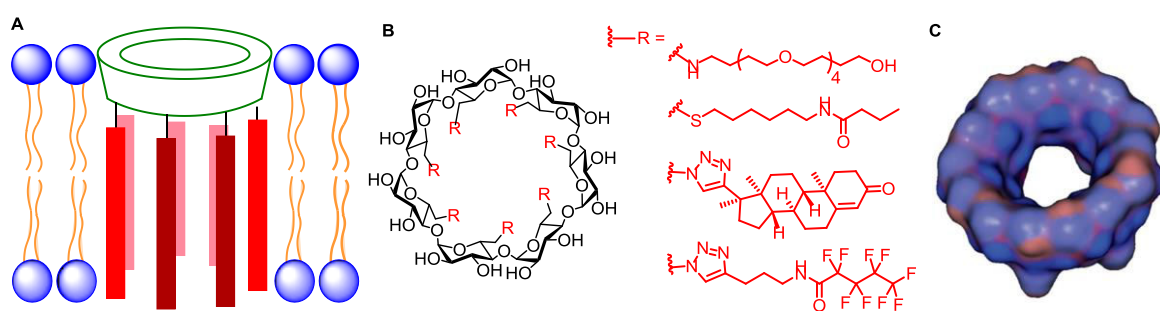


Figure 2.1. Schematic representation of cyclodextrin-based ion channels (A), structures of β -cyclodextrin-based reported ion channels (B), Representation of the hydrophilic (blue) and hydrophobic (red) indentation in β -CD (C).

In the year 2011, Nifantiev and coworkers had reported an efficient synthetic strategy for easy access to a series of individual cyclo oligo-(1 \rightarrow 6)- β -D-glucosamine (GA) derivatives $[\text{GA}]_2 - [\text{GA}]_7$ consisted from two up to seven glucosamine units (Figure 2.2A).²⁰⁻²² The pore diameter of the macrocycles follows an increasing order from dimeric to tetrameric cyclo-(1 \rightarrow 6)- β -D-glucosamines $[\text{GA}]_{2,\text{Ac}} - [\text{GA}]_{4,\text{Ac}}$ (0.35 to 0.58 nm) (Figure 2.2D). The variable diameter of GA macrocycles offers a scaffold to construct artificial ion transport systems with tunable pore diameter. However, an interesting correlation between oligomericity and rigidity of these macrocycles was observed from molecular dynamics (MD) simulation studies.^{21,23} In the context of larger macrocycles $[\text{GA}]_{5,\text{Ac}} - [\text{GA}]_{7,\text{Ac}}$, the effective pore diameter fluctuates because of the complicated shape and conformational disorder of macrocycles (Figure 2.2B). Hence, a contraction of effective pore diameter of was predicted, for macrocycles with more than four glucosamine units.

Moreover, theoretical calculations revealed the presence of defined hydrophilic cavities within these macrocycles (Figure 2.2E).²¹ This characteristic can be regarded as an essential parameter for constructing the polar pore for recognizing hydrophilic anions. Additionally, recognition of ions within the GA cavities would contribute to the lower free energy loss due to dehydration of ion in comparison to the CD cavities. The presence of free amino groups in the macrocycles facilitates the attachment of lipophilic tails required to produce an active transmembrane pore.²³

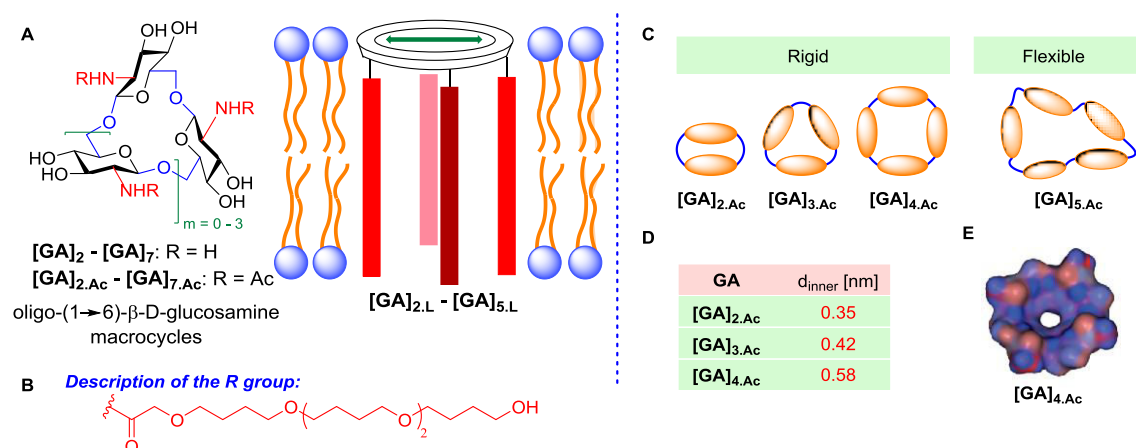


Figure 2.2. The structure of glucosamine macrocycle and proposed a model of ion transport systems with tunable pore diameter (A). Description of lipophilic tail linked to designed macrocycles (B). Representation of oligomericity versus rigidity (C). Representation of the hydrophilic (blue) and hydrophobic (red) indentation in $[\text{GA}]_{4,\text{Ac}}$ (D). Inner diameters of $[\text{GA}]_{2,\text{Ac}} - [\text{GA}]_{4,\text{Ac}}$ (E).

Therefore, the design of new synthetic ion channels was proposed based on macrocycles $[\text{GA}]_2 - [\text{GA}]_5$. Lipophilic tails were connected to the glucosamine macrocycle for spanning through the phospholipid bilayer and providing a hydrophilic path for ions. A pentabutylene glycol-based chain was selected¹² as a long tail (Figure 2.2B) to match the thickness of phospholipid membranes (thickness = 0.35 – 0.40 nm). Furthermore, a “hybrid” tetrasaccharide-based macrocycle $[\text{GA}]'_4$ ^{21,22} (Figure 2.3) was also introduced to address the effect of the number of membrane spanning tails on the ion transport activity. This class of hybrid ion channel $[\text{GA}]'_{4,\text{L}}$ was accessible for covalent linking of only two tails in diagonally opposite glucosamine unit in the macrocycle. Hence we expected to have a bimodal control on ion transport activity; by varying (a) ring size of glucosamine macrocycle, and (b) number of membrane spanning tails.

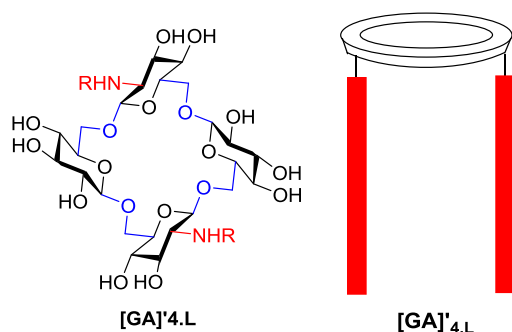


Figure 2.3. The structure of “Hybrid” cyclic tetrasaccharide based channel with fewer membrane spanning tails.

2.2. RESULT AND DISCUSSION:

2.2.1. Synthesis:

Synthesis of the long tail was done by reported procedure.²⁴ The conjugation of tails with the glucosamine macrocycles was performed in the laboratory of Prof. Nifantiev, and received by us as a part of the collaboration.

2.2.2. Ion Transport Activity:

The ion-transporting activity of the synthesized compounds was evaluated in the spherical lipid bilayer of large unilamellar vesicles (LUVs). Unilamellar vesicles of uniform size (~ 100 nm) were used as the mimic of the cell membrane to get a model system of ion transport study. The LUVs are prepared by EYPC (L- α -Phosphatidylcholine from egg yolk) lipid with entrapped 8-hydroxypyrene-1,3,6-trisulfonate (HPTS), a pH-sensitive dye, to get EYPC-LUVs \supset HPTS (Figure 3a).^{25,26} The fluorescence intensity of HPTS dye is found to get increased with increasing intravesicular pH. A pH gradient of $\Delta\text{pH} = 0.8$ ($\text{pH}_{\text{in}} = 7.0$ and $\text{pH}_{\text{out}} = 7.8$) was applied by addition of 0.5 M NaOH to the extravesicular buffer. The fluorescence intensity of HPTS was monitored to get the extent of ion transport across the membrane, i.e., the amount enhancement of intravesicular pH. No significant enhancement in fluorescence was expected as the ion transport through the membrane is restricted in the absence of ion channel. The ion transport was evident from enhanced fluorescence intensity of HPTS only after addition of channel forming molecules. Finally, vesicles were lysed by adding 10% Triton X-100 (Tx) to achieve the maximum possible fluorescence intensity (Figure 2.4). The addition of ion transporting compounds resulted in the destruction of

pH gradient via either OH^- influx or H^+ efflux, leading to an increase in intravesicular pH.

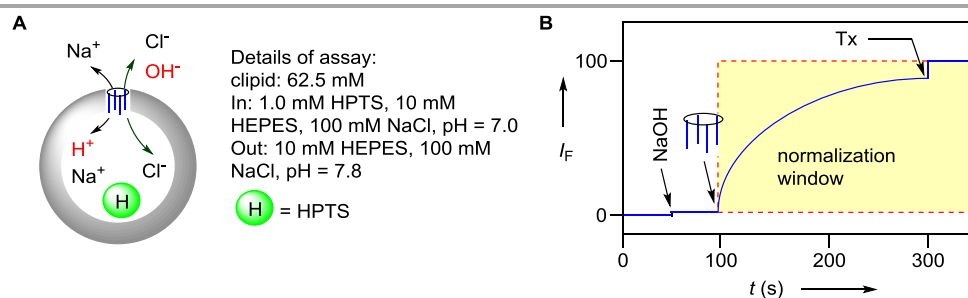


Figure 2.4. Representation of ion transport activity assay using EYPC vesicles (A); representation of ion transport kinetics experiment using fluorescence (B).

Ion transport activity of each glycoconjugate was recorded at monomer concentration 0 – 10 μM indicating concentration-dependent responses during the transport process (Figure 2.5). Each plot was normalized into the normalization window according to Figure 2.4B. This normalization represents the time of neoglycolipid addition as $t = 0$ s and time of Triton-X 100 addition as $t = 200$ s. Each fluorescence intensity course was normalized to obtain the percentage emission intensity I_F using Equation 2.1:

$$I_F = [(F_t - F_0) / (F_\infty - F_0)] \times 100 \quad \text{Equation 2.1}$$

where, F_t = fluorescence intensity at time t , F_0 = fluorescence intensity 2 s before the [GA] derivative addition and F_∞ = fluorescence intensity at saturation after lysis of vesicles (at 220 s).

The direct comparison of the ion transport activity for all glycoconjugates was obtained from the bar diagram (Figure 2.6), generated by considering the transport efficiency at 1.5 μM concentration (recorded after 100 s of compound addition). Enhancement in the extent of ion transport with the increase in effective diameter of macrocycle was encountered $[\text{GA}]_{2,\text{L}} < [\text{GA}]_{3,\text{L}} < [\text{GA}]_{4,\text{L}}$, which further diminished in the case of $[\text{GA}]_{5,\text{L}}$ (Figure 2.6). This outcome was in accordance with the assumption of an increment in transport rate with increase in oligomericity of glucosamines. Lower activity of $[\text{GA}]_{5,\text{L}}$ compared to $[\text{GA}]_{4,\text{L}}$ can be explained regarding conformational freedom of the glucosamine macrocycles and such loss of ring structure because of implosion caused by lipid pressure.

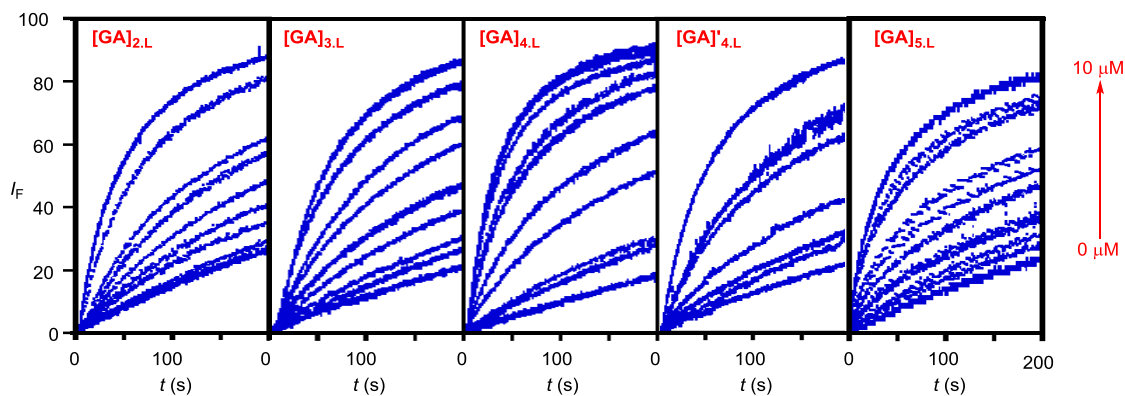


Figure 2.5. Ion transport assay of neoglycolipid derivatives using EYPC LUVs Δ HPTS, where the time of compound addition was taken as 0 s and Triton X-100 was added at 200 s. Compound number was indicated in the plot.

The difference in activity depending on the number of membrane-spanning tails, connected to a glucosamine macrocycle also suggest its importance in ion transport activity. Four-membered glucosamine macrocycle offers better activity when connected to four membrane spanning tails $[GA]_{4,L}$ with respect to those connected to two tails $[GA]'_{4,L}$ (Figure 2.6).

A comparison of dose-response curve (0 – 5 μ M) of all long tail connected compounds ($[GA]_{2,L}$ – $[GA]_{5,L}$, and $[GA]'_{4,L}$) was plotted, by recording the normalized fluorescence intensity values at $t = 100$ s. Hill analysis was performed by fitting of respective curves in equation 2.2.

$$Y = Y_{\infty} + (Y_0 - Y_{\infty}) / [1 + (c / EC_{50})^n] \quad \text{Equation 2.2}$$

where, Y_0 = fractional fluorescence intensity at $c = 0$, Y_{∞} = fractional fluorescence intensity for $c = c_{\max}$ and Y = fractional fluorescence intensity at a particular concentration c .

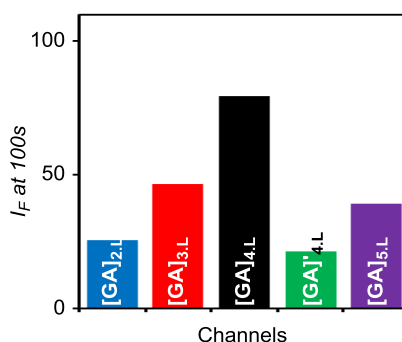


Figure 2.6. Comparison of ion transporting activity of $[GA]_{2,L}$ – $[GA]_{5,L}$ and $[GA]'_{4,L}$ at 1.5 μ M concentrations .

From Hill analysis, the effective concentration of half maximal activity (EC_{50}) was obtained for each compound (Figure 2.7B). The EC_{50} values, $[GA]_{4,L} > [GA]_{3,L} > [GA]_{5,L} > [GA]_{2,L} > [GA]'_{4,L}$, also indicates similar ion transport activity as observed in Figure 2.6. The Hill coefficient for $[GA]_{4,L}$, $n = 1.2$ stands for the unimolecularity of the channel structure. The Hill coefficient for other active compounds $[GA]_{3,L}$ and $[GA]_{5,L}$ also displays the behavior of the unimolecular ion channel. A slight variation of Hill coefficient in case of $[GA]_{2,L}$ can be explained by the negligible activity followed by improper fitting of the Hill plot. The compound $[GA]'_{4,L}$ also offers the Hill coefficient, $n = 2$, which confers the information of dimeric channel formation. The presence of half number of membrane tails in case of $[GA]'_{4,L}$ in comparison to the normal analogue $[GA]_{4,L}$ is responsible for the dimeric structure of the successful formation of channel structure.

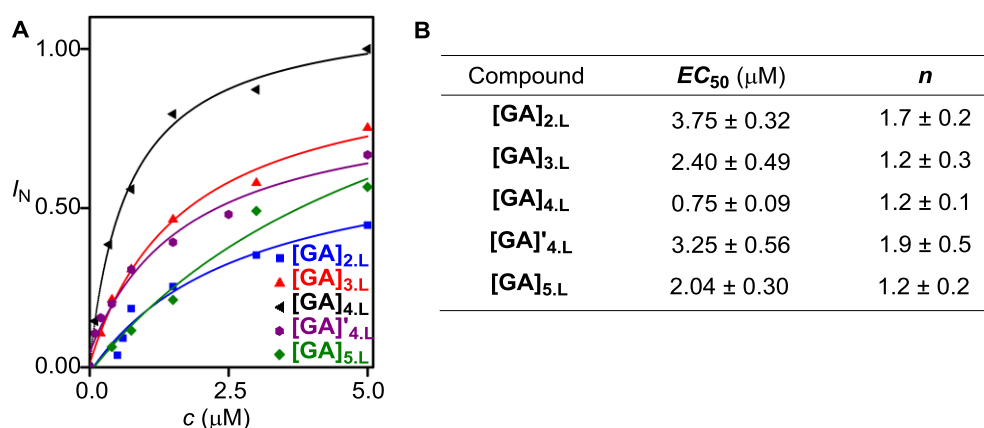


Figure 2.7. The dose-dependent activity of $[GA]_{2,L}$ – $[GA]_{5,L}$ and $[GA]'_{4,L}$ at in EYPC-LUV \supset HPTS (**B**) table of EC_{50} values and Hill coefficient obtained for $[GA]_{2,L}$ – $[GA]_{5,L}$ and $[GA]'_{4,L}$ at in EYPC-LUV \supset HPTS.

2.2.3. Ion Selectivity:

The significant ion transport activity of long tail connected neoglycolipid derivatives inspired us to investigate the ion selectivity. Fluorescence-based competitive assay for ion transport was applied to EYPC-LUVs \supset HPTS to evaluate ion selectivity. The rate of change of ion transport activity was monitored by altering the extravesicular buffer with various cations, MCl by keeping the constant iso-osmolar intravesicular NaCl to obtain the cation selectivity. On the other hand, extravesicular anions NaX can be varied to obtain anion selectivity (Figure 2.8).

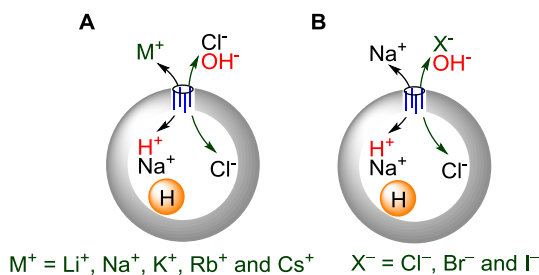


Figure 2.8. Schematic representations of the fluorescence-based ion selectivity assay. Vesicle leakage assay for cation selectivity (A) and anion selectivity (B).

ion transport activity was monitored by altering the extravesicular buffer with various cations, MCl by keeping the constant iso-osmolar intravesicular NaCl to obtain the cation selectivity. On the other hand, extravesicular anions NaX can be varied to obtain anion selectivity (Figure 2.8).

Variation of cations in the extravesicular buffer (MCl; $M^+ = \text{Li}^+, \text{Na}^+, \text{K}^+, \text{Rb}^+$ and Cs^+) did not offer any significant change in the rate of ion transport which signifies the absence of

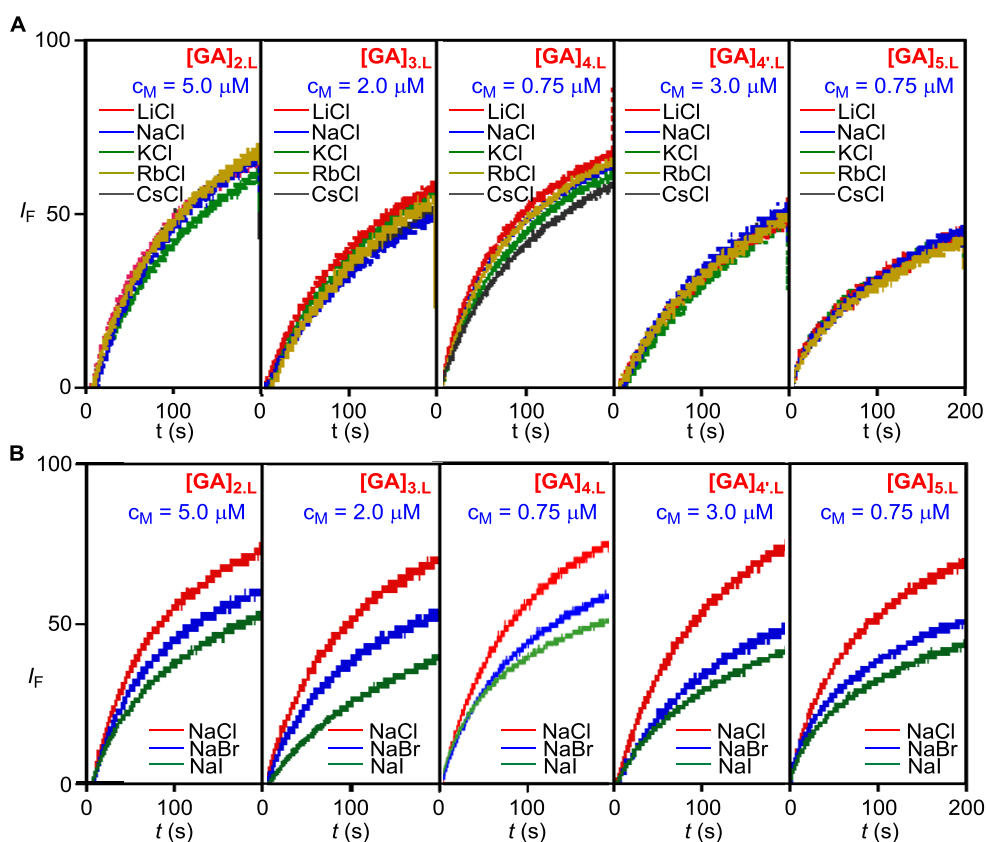


Figure 2.9. Cation (A) and anion (B) selectivity of long tail connected compounds across EYPC-LUV Δ HPTS.

cation transport through the pore (Figure 2.8A). On the other hand, a significant and uniform trend in anion selectivity, $\text{Cl}^- > \text{Br}^- > \text{I}^-$, was observed for all compounds when, extravesicular (Figure 2.8B). The uniform anion selectivity sequence, $\text{Cl}^- > \text{Br}^- > \text{I}^-$, was observed for all tested compounds, which follows the reverse trend of common Hofmeister halide sequence. Therefore, proposed Cl^- selectivity during ion transport was achieved based on designed oligo-(1 \rightarrow 6)- β -D-glucosamine derivatives.

To rationalize the observation related to anion selectivity, the dependence of the ion selectivities of $[\text{GA}]_{2,\text{L}} - [\text{GA}]_{5,\text{L}}$ and $[\text{GA}]'_{4,\text{L}}$ on either reciprocal anion radius r^{-1} (Figure 2.10A) or the free energy of anion hydration ΔG_{hyd} (Figure 2.10.B) were plotted. For each compound, better ion transport was observed with the increase in r^{-1} (*i.e.* for smaller halide). On the other hand, the ion transport activity decreased with the decrease in ΔG_{hyd} , confirming that the dehydration process had less contribution to the observed selectivity. Therefore, it can be believed that anions are recognized by the macrocycle in their partially hydrated state. Based on this result, the contribution of hydrogen bonding between water molecules and the macrocycle could be proposed for anion selectivity.^{27,28} The observed halide topology is unusually rare and can be correlated to either of halide V, VI, or VII Eisenman series.²⁹⁻³¹ However, the outcome (*i.e.* better Cl^- ion selectivity) can be related to the potential application of these synthetic molecules in the replacement therapy for diseases related to misregulated Cl^- ion transport.

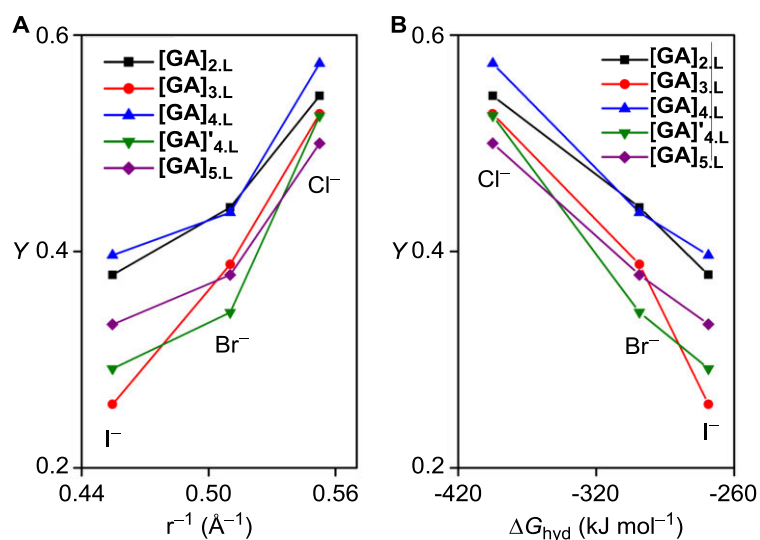


Figure 2.10. Normalized emission intensity I_F as a function of the reciprocal anion radius (**A**), and as a function of corresponding anion hydration energy (**B**).

To confirm the above assumptions, computer modeling of different halides (Cl^- , Br^- and I^-) passing through the pore of $[\text{GA}]_{4,\text{Ac}}$ cyclo-oligosaccharide in water solutions was carried out by Dr. Alexey G. Gerbst in the collaboration of Prof. Nikolay E. Nifantiev. TINKER software v. 5.0 was employed for this purpose (for full details see the ESI). A halide particle was placed at the distance of 5 Å from the potential pore first on one side, and then on the other. These structures after energy minimization were used as models for the starting and the final state. SADDLE procedure was employed to locate the transition state between these two points. After this, transition state structures were soaked into the droplet of 2200 water molecules with the radius of 25 Å. The halide anions and the saccharide were frozen while water molecules were allowed to move. Systems were minimized and subjected to MD simulations with structural snapshots being saved every 2 ps. Visual analysis of the transitional structures showed that in all cases, the halide inside the pore was solvated by two or three water molecules (Figure 2.11). Thus, the study supported the idea of the polar pore and the movement of halide ion through the cavity in a partly dehydrated form.

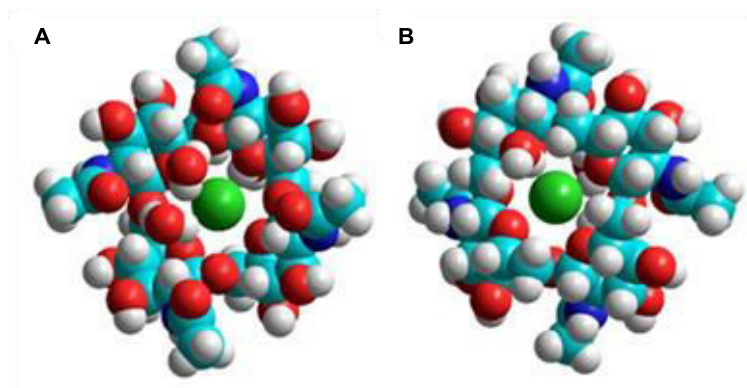


Figure 2.11. Complex formed during MD simulation between $[\text{GA}]_{4,\text{Ac}}$, a Cl^- ion and water molecules inside its inner cavity. Upside (A) and downside (B) views are shown. Redundant waters are removed.

2.3. CONCLUSION:

In conclusion, a new family of artificial ion transport systems was designed based on the functionalization of the oligo-(1→6)- β -D-glucosamine macrocycles by membrane-spanning tails. These macrocycles possess smaller and more hydrophilic cavities compared to cyclodextrins, and these features provided a rational tool to address Cl^- selectivity during ion transport across unilamellar vesicles. Modulation of ring size

and rigidity by changing oligomericity of these macrocycles provided a handle to control ion transport activity. The ring size dependent rigidity of these macrocycles was also important to withstand the lateral pressure of the phospholipids bilayer. The long tail capable of spanning the bilayer membrane was used; the active supramolecule was formed by a monomer. The importance of the number of membrane-spanning tails was also evaluated. The transport activity decreased dramatically when a lesser number of tails were connected to the glucosamine macrocycle.

All cyclo-oligo-(1→6)- β -D-glucosamines exhibited anion selectivity due to hydrogen bonding between the macrocycle and water molecules solvating the anion. Ion selectivity of synthesized derivatives displayed a uniform $\text{Cl}^- > \text{Br}^- > \text{I}^-$ selectivity sequence. Dependence towards ionic size over dehydration process confirmed the presence of polar pore with better selectivity towards Cl^- ion. These glucosamine-based biomolecular systems^{32,33} can be considered for replacement therapy for diseases caused by misregulated Cl^- ion transport.

2.4. EXPERIMENTAL SECTION:

2.4.1. General Methods.

Egg-yolk phosphatidylcholine (EYPC) was purchased from Avanti Polar Lipids as a solution in chloroform (25 mg/mL). HEPES buffer, HPTS, Triton X-100, NaOH and inorganic salts of molecular biology grade were purchased from Sigma. Gel-permeation chromatography was performed on a column of Sephadex LH-20 gel (25 × 300 mm, $V_0 = 25$ mL) in $\text{CHCl}_3/\text{MeOH}$ (1:1, v/v). Large unilamellar vesicles (LUV) were prepared by using mini extruder, equipped with a polycarbonate membrane of 100 nm pore size, obtained from Avanti Polar Lipids.

2.4.2. Physical Measurements.

Fluorescence spectra were recorded by using Fluoromax-4 from Jobin Yvon Edison equipped with an injector port and a magnetic stirrer. 10 mM HEPES (with 100 mM NaCl) buffer solution used for fluorescence experiment and the pH of the buffer was adjusted to 7.0 with NaOH using Helmer pH meter. All data of fluorescence studies were processed either by Origin 8.5 or KaleidaGraph.

2.4.3. Synthesis.

Synthesis of alcohol L: Alcohol L was synthesized according to the published procedure³⁴ and the analytical data were in accordance with those reported.

All macrocycles were synthesised by our collaborator (Prof. Nikolay E. Nifantiev group) and those are connected with the alcohol **L**. All final compounds were obtained from our collaborator in purified form.

2.4.4. Ion Transport Activity.^{23,35}

Buffer and stock solution preparation: HEPES buffer was prepared by dissolving solid HEPES (10 mM) and NaCl (100 mM) in autoclaved water, followed by adjustment of pH = 7.0 by adding NaOH solution. Stock solutions of all glucosamine molecules were prepared in HPLC grade DMSO.

Preparation of EYPC-LUVs Δ HPTS: A transparent thin film of egg yolk phosphatidylcholine (EYPC) was prepared by drying 1 mL of EYPC (25 mg/mL in CHCl₃) with the purging of nitrogen and continuous rotation in a clean and dry small round-bottomed flask. The resulting transparent film was kept under high vacuum for 3 h to remove all trace of CHCl₃ for drying. The transparent film was then hydrated with 1 mL of HEPES buffer (1 mM HPTS, 10 mM HEPES, 100 mM NaCl, pH = 7.0) for 1 h with occasional vortexing of 4-5 times and then subjected to freeze-thaw cycle (≥ 15 times). Extrusions were done 19 times (must be an odd number) by a Mini-extruder with a polycarbonate membrane having a pore diameter of 100 nm. Extravesicular dyes were removed by gel filtration (by Sephadex G-50) with buffer (10 mM HEPES, 100 mM NaCl, pH = 7.0) and obtained vesicle was diluted to 6 mL to get EYPC-LUVs Δ HPTS: ~ 5.0 mM EYPC, inside: 1 mM HPTS, 10 mM HEPES, 100 mM NaCl, pH = 7.0, outside: 10 mM HEPES, 100 mM NaCl, pH = 7.0.

Ion transport activity: 1975 μ L of HEPES buffer (10 mM HEPES, 100 mM NaCl, pH = 7.0) was placed in a clean and dry fluorescence cuvette followed by addition of 25 μ L vesicle (EYPC-LUVs Δ HPTS). The cuvette was placed on a fluorescence instrument equipped with a magnetic stirrer. Fluorescence emission intensity of pH sensitive dye HPTS was monitored at $\lambda_{em} = 510$ nm ($\lambda_{ex} = 450$ nm). After starting each experiment (at $t = 0$), a pH gradient between the intra and extra-vesicular system were created at $t = 20$ s by adding 20 μ L of 0.5 M NaOH. Different concentrations (0–10 μ M) of glucosamine derivatives were added at $t = 100$ s. Finally, vesicles were lysed at $t = 300$ s by adding 25 μ L Triton X-100 (10%) to achieve complete destruction of the pH gradient and saturation in fluorescence emission intensity.

The concentration of 5 μ M of channel forming compound corresponds to the 0.068 mol% of the lipid in the assay medium.

Hill analysis:

From the fluorescence kinetics plots of each derivative (Figure S2), the normalized fluorescence intensity values at $t = 100$ s were noted. The normalized fluorescence intensities

were then subtracted from the intensity value of background data so that the background intensity was then adjusted to 0. The normalized fluorescence intensity at excess monomer concentration was then adjusted to 1. All other data were adjusted accordingly to get fractional fluorescence intensities. A new graph was generated by plotting fractional fluorescence intensity values (represented as Y) against corresponding concentration (c) values (the background data set was excluded). Each plot was then analyzed by Hill Equation (Equation 2.2) to obtain the effective concentration (EC_{50}) and Hill coefficient (n).

2.4.5. Ion Selectivity Studies:

Buffer and stock solution preparation: HEPES buffer was prepared by dissolving solid HEPES (10 mM) and appropriate salt (100 mM) in autoclaved water, followed by adjustment of pH = 7.0 by adding NaOH solution. A stock solution of each glycoconjugate was prepared in HPLC grade DMSO.

Preparation of EYPC-LUVs \Rightarrow HPTS: Vesicle was prepared according to the same procedure as stated above.

Ion selectivity assay: In a dry and clean fluorescence cuvette, 1975 μ L HEPES buffer (10 mM HEPES, 100 mM of either MCl or NaX, pH = 7.0) and 25 μ L of EYPC-LUVs \Rightarrow HPTS vesicle were added. The mixture was placed on a fluorimeter equipped with a magnetic stirrer. Fluorescence emission intensity of pH sensitive dye HPTS was monitored at $\lambda_{em} = 510$ nm ($\lambda_{ex} = 450$ nm). After starting each experiment (at $t = 0$), a pH gradient between the intra and extra-vesicular systems was created at $t = 20$ s by adding 20 μ L of 0.5 M NaOH. Glucosamine derivatives were added at $t = 100$ s at a particular concentration. Finally, vesicles were lysed at $t = 300$ s by adding 25 μ L Triton X-100 (10%) to achieve complete destruction of the pH gradient and saturation in fluorescence emission intensity. Each data was normalized according to Equations 2.1.

Cation selectivity experiments were carried out by varying the extravesicular chloride salts (MCl) of different alkali metal cations ($M^+ = Li^+, Na^+, K^+, Rb^+$ and Cs^+). For each glycoconjugate, the normalized fluorescence intensity values at $t = 100$ s for different metal ions were compared.

Anion selectivity experiments were carried out by varying the halides ($X^- = Cl^-, Br^-$ and I^-) of extravesicular sodium salts (NaX). For each glycoconjugate, the normalized fluorescence intensity values at $t = 100$ s for different sodium halides were compared.

2.4.6. Molecular Dynamics Simulations.

Calculations were carried out using TINKER software v. 5.0.³⁶ Cyclo-oligosaccharide matrix together with the chloride anion in the pore, preliminary found as transition state using SADDLE procedure, was soaked into the previously equilibrated droplet of 2300 TIP3P³⁷ water molecules with the radius of 25 Å using a built-in routine. The energy of the resulting system was minimized until the RMS gradient of 0.1 kcal/mol·Å. After that the system was subjected to the MD equilibration for 500 ps and the MD simulation was run for 10000 ps with the structural snapshots being written every 2 ps. The simulations were run in the constant temperature mode at 300 K. Only water molecules were allowed to move, positions of all atoms constituting the matrix and the chloride were frozen. All bonds involving hydrogen atoms were constrained using RATTLE version of SHAKE algorithm.³⁸ All interactions were cut off at 5.

2.5. REFERENCE:

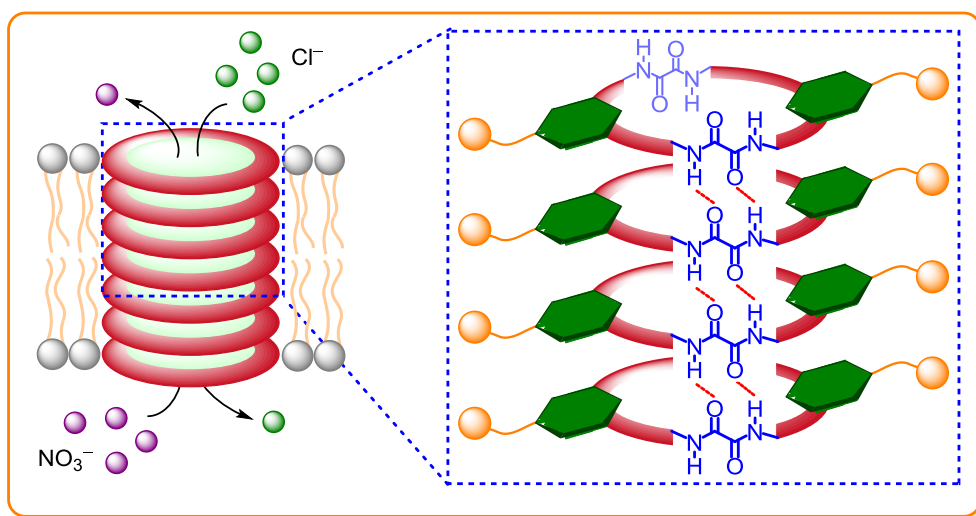
- (1) Matile, S.; Vargas Jentzsch, A.; Montenegro, J.; Fin, A. *Chem. Soc. Rev.* **2011**, *40*, 2453.
- (2) Fyles, T. M. *Chem. Soc. Rev.* **2007**, *36*, 335.
- (3) Sisson, A. L.; Shah, M. R.; Bhosale, S.; Matile, S. *Chem. Soc. Rev.* **2006**, *35*, 1269.
- (4) Matile, S.; Som, A.; Sorde, N. *Tetrahedron* **2004**, *60*, 6405.
- (5) Maulucci, N.; De Riccardis, F.; Botta, C. B.; Casapullo, A.; Cressina, E.; Fregonese, M.; Tecilla, P.; Izzo, I. *Chem. Commun.* **2005**, 1354.
- (6) Iqbal, K. S. J.; Cragg, P. J. *Dalton Trans.* **2007**, 26.
- (7) Leevy, W. M.; Gokel, M. R.; Hughes-Strange, G. B.; Schlesinger, P. H.; Gokel, G. W. *New J. Chem.* **2005**, *29*, 205.
- (8) Wright, A. J.; Matthews, S. E.; Fischer, W. B.; Beer, P. D. *Chem. Eur. J.* **2001**, *7*, 3474.
- (9) Murray, C. L.; Gokel, G. W. *J. Supramol. Chem.* **2001**, *1*, 23.
- (10) Fernandez-Lopez, S.; Kim, H.-S.; Choi, E. C.; Delgado, M.; Granja, J. R.; Khasanov, A.; Kraehenbuehl, K.; Long, G.; Weinberger, D. A.; Wilcoxon, K. M.; Ghadiri, M. R. *Nature* **2001**, *412*, 452.
- (11) Tabushi, I.; Kuroda, Y.; Yokota, K. *Tetrahedron Lett.* **1982**, *23*, 4601.
- (12) Madhavan, N.; Robert, E. C.; Gin, M. S. *Angew. Chem., Int. Ed.* **2005**, *44*, 7584.
- (13) Madhavan, N.; Gin, M. S. *ChemBioChem* **2007**, *8*, 1834.
- (14) Chui, J. K. W.; Fyles, T. M. *Chem. Commun.* **2010**, *46*, 4169.
- (15) El Ghouli, Y.; Renia, R.; Faye, I.; Rassou, S.; Badi, N.; Bennevault-Celton, V.; Huin, C.; Guegan, P. *Chem. Commun.* **2013**, *49*, 11647.
- (16) Chui, J. K. W.; Fyles, T. M. *Org. Biomol. Chem.* **2014**, *12*, 3622.
- (17) Immel, S.; Brickmann, J.; Lichtenthaler, F. W. *Liebigs Annalen* **1995**, 929.
- (18) Szejtli, J. *Chem. Rev.* **1998**, *98*, 1743.
- (19) Del Valle, E. M. M. *Process Biochem.* **2004**, *39*, 1033.

- (20) Gening, M. L.; Titov, D. V.; Grachev, A. A.; Gerbst, A. G.; Yudina, O. N.; Shashkov, A. S.; Chizhov, A. O.; Tsvetkov, Y. E.; Nifantiev, N. E. *Eur. J. Org. Chem.* **2010**, 2465.
- (21) Saha, T.; Roy, A.; Gening, M. L.; Titov, D. V.; Gerbst, A. G.; Tsvetkov, Y. E.; Nifantiev, N. E.; Talukdar, P. *Chem. Commun.* **2014**, 50, 5514.
- (22) Titov, D. V.; Gening, M. L.; Gerbst, A. G.; Chizhov, A. O.; Tsvetkov, Y. E.; Nifantiev, N. E. *Carbohydrate Res.* **2013**, 381, 161.
- (23) Gening, M. L.; Titov, D. V.; Grachev, A. A.; Gerbst, A. G.; Yudina, O. N.; Shashkov, A. S.; Chizhov, A. O.; Tsvetkov, Y. E.; Nifantiev, N. E. *Eur. J. Org. Chem.* **2010**, 2010, 2465.
- (24) Hoffmann, B.; Bernet, B.; Vasella, A. *Helvetica Chimica Acta* **2002**, 85, 265.
- (25) Talukdar, P.; Bollot, G.; Mareda, J.; Sakai, N.; Matile, S. *J. Am. Chem. Soc.* **2005**, 127, 6528.
- (26) Sakai, N.; Matile, S. *J. Am. Chem. Soc.* **2003**, 125, 14348.
- (27) Gorteau, V.; Bollot, G.; Mareda, J.; Perez-Velasco, A.; Matile, S. *J. Am. Chem. Soc.* **2006**, 128, 14788.
- (28) Gorteau, V.; Bollot, G.; Mareda, J.; Matile, S. *Org. Biomol. Chem.* **2007**, 5, 3000.
- (29) Hille, B.; Schwarz, W. *J. Gen. Physiol.* **1978**, 72, 409.
- (30) Miller, C. *J. Gen. Physiol.* **1999**, 113, 783.
- (31) Eisenman, G.; Horn, R. *J. Membr. Biol.* **1983**, 76, 197.
- (32) Ananikov, V. P.; Khokhlova, E. A.; Egorov, M. P.; Sakharov, A. M.; Zlotin, S. G.; Kucherov, A. V.; Kustov, L. M.; Gening, M. L.; Nifantiev, N. E. *Mendeleev Commun.* **2015**, 25, 75.
- (33) Dudin, O.; Bendezú, F. O.; Groux, R.; Laroche, T.; Seitz, A.; Martin, S. G. *J. Cell Biol.* **2015**, 208, 897.
- (34) Knuf, E. C.; Jiang, J.-K.; Gin, M. S. *J. Org. Chem.* **2003**, 68, 9166.
- (35) Saha, T.; Dasari, S.; Tewari, D.; Prathap, A.; Sureshan, K. M.; Bera, A. K.; Mukherjee, A.; Talukdar, P. *J. Am. Chem. Soc.* **2014**, 136, 14128.
- (36) <http://dasher.wustl.edu/tinker..>
- (37) Jorgensen, W. L.; Chandrasekhar, J.; Madura, J. D.; Impey, R. W.; Klein, M. L. *J. Chem. Phys.* **1983**, 79, 926.
- (38) Leimkuhler, B. J.; Skeel, R. D. *J. Comput. Phys.* **1994**, 112, 117.

End of Chapter 2

Chapter 3

Self-Assembly of Bis(oxalyl amide) Macrocycles as Transmembrane Barrel-Hoop Anion Channel



3.1. INTRODUCTION:

Supramolecular approaches for constructing nanotubular structure having adaptable lipophilicity is a well acceptable strategy for ion channel construction. Mutual recognition of identical protein components are widely found in naturally existing ion channels and pores, which includes dimeric structure of gramicidin, tetrameric structure of KcsA and heptameric structure of α -hemolysin (Figure 3.1A).¹⁻⁸ The design related to a unimolecular artificial ion channel, described in the previous chapter, suffers the drawback related to the selectivity because of the presence of single selectivity filter in entire transmembrane structure. On the other hand, the supramolecular architecture of channel constructed from the self-aggregation of small building units serves the purpose rigidity and selectivity of the nanochannel structure. The design principle consists of the crucial requirement of multiple selectivity filters in each representative building unit. Synthetic macrocyclic scaffold containing strong hydrogen bonding motif can be introduced into self-assembled nanochannel structure to form a barrel-hoop type of artificial ion channel. A few examples of barrel hoop model of artificial ion channels have been found in literature, which consists of cyclic peptide structures as the repetitive building unit (Figure 3.1B).⁹⁻¹⁴ Those cyclic peptides can adopt lateral self-assembly by sharing strong hydrogen bonding among amide functionalities (Figure 3.1C). The amide moiety contributes to the required hydrophilicity in the channel lumen and the hydrophobic amino-acid residues, exposed to the external surface participating in the membrane penetration and stability in the lipid bilayer.

In the present chapter, we had reported a non-peptide based macrocyclic building block which is capable of forming self-assembled nanotubular architecture. We got inspired from the strong and extended hydrogen bonding present in Kevlar and translated into the designed molecule in the form of oxalyl amide. Each macrocycle had been decorated with two oxalyl amide units which are capable of participating in intermolecular hydrogen bonding interaction to create a nanotubular structure (Figure 3.2). The alkyl chains were connected to each molecule for maintaining proper lipophilic balance for successful membrane translocation. The rate of membrane translocation and stability in phospholipid bilayer primarily depends on the lipophilicity of a particular

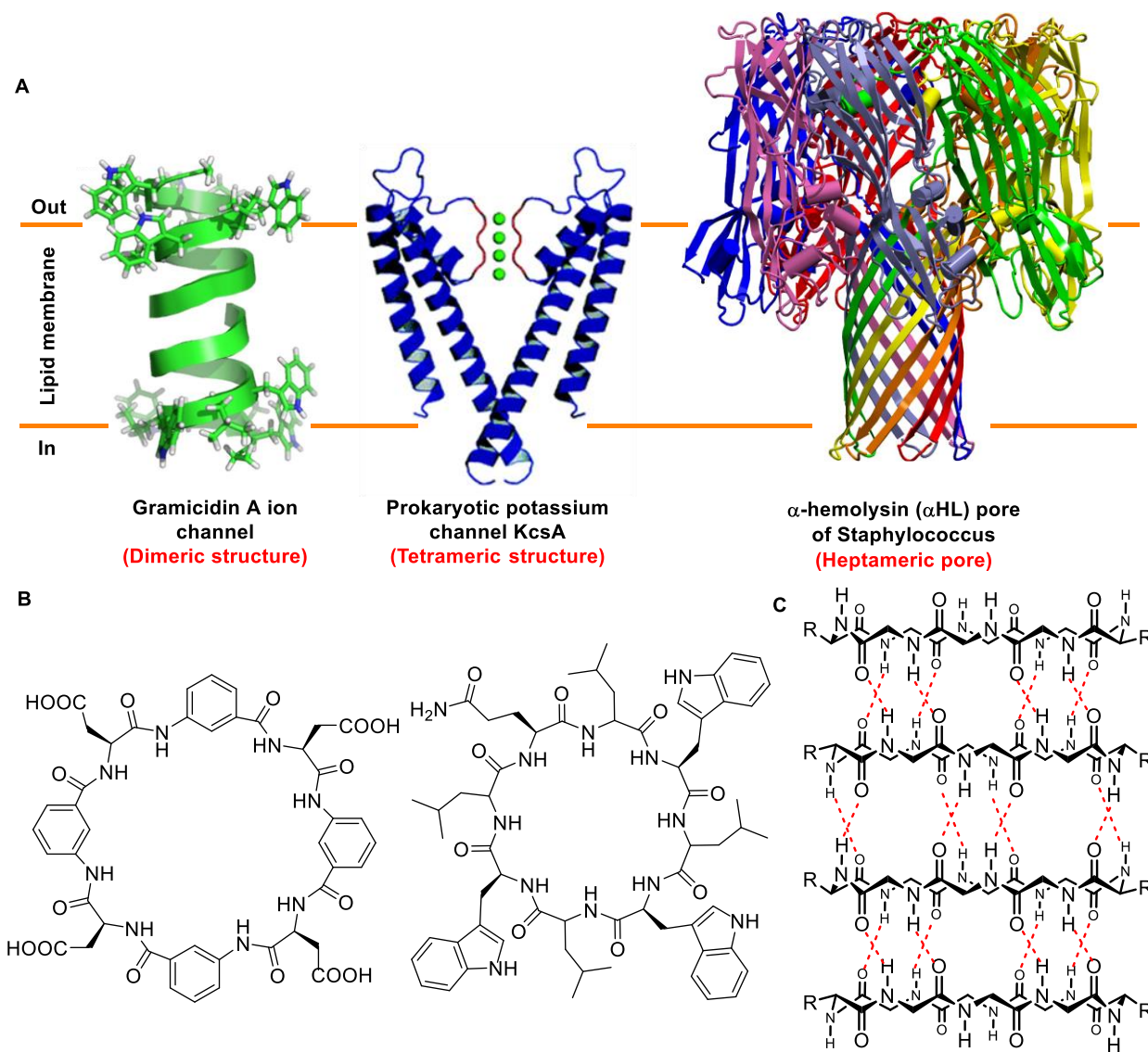


Figure 3.1: Self-assembled structure of natural ion channels and pore (**A**); cyclic peptides for barrel-hoop ion channel construction (**B**); self-assembly of cyclic peptides for nanochannel formation (**C**).

distributes in aqueous media than of getting inserted into the bilayer. In contrast to that, a strong hydrophobic molecule suffer's problem related to aqueous solubility. Hence, the optimum lipophilicity is suggested for an ion transporting agent. In addition to the alkyl chain, extended towards the external surface of macrocycles, can involve in favourable van der waal's interaction with the hydrophobic domain of lipid bilayer. We assumed that the macrocycle connected to two diagonally oriented *n*-pentyl groups offered the optimum lipophilicity, to perform the task of successful membrane penetration (Figure 3.2). Additionally, the macrocyclic building units

offers a sufficient rigidity to restrict the contraction of the diameter of the channel because of the lateral pressure induced by lipid bilayers.

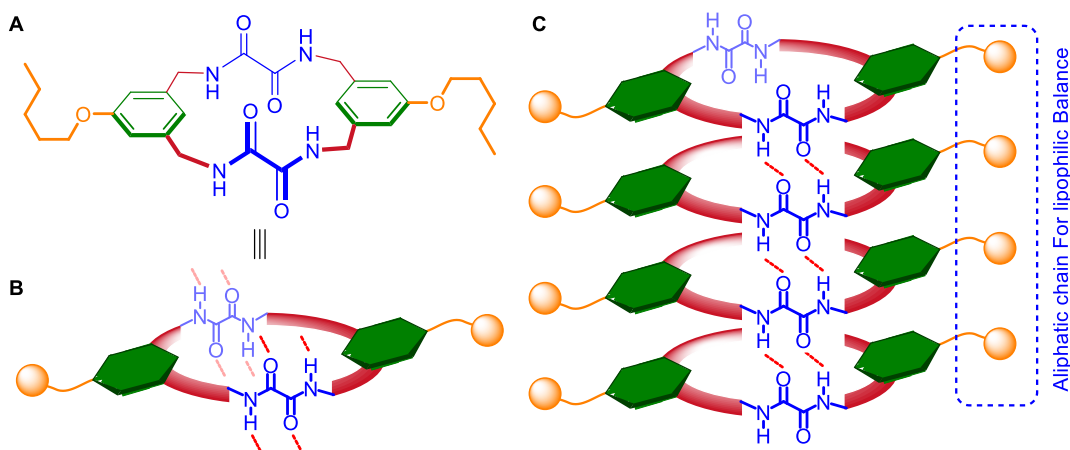
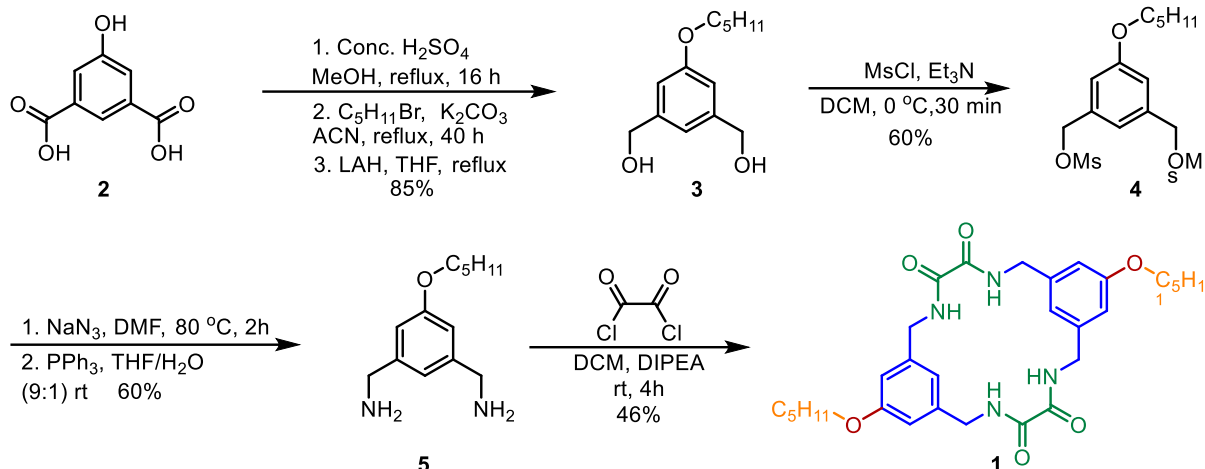


Figure 3.2: Design of the rigid macrocyclic building unit having hydrogen bonding moiety and aliphatic chains for lipophilic balance (A). The structure of macrocycle (B). Mode of self-assembly for barrel-hoop type ion channel (C).

3.2. RESULT AND DISCUSSION:

3.2.1. Synthesis:

Synthesis of the designed macrocycle was initiated from the commercially available 5-hydroxyisophthalic acid **2**. The acid **2** was subjected to esterification followed by n-pentylation of the phenolic moiety (Scheme 3.1). Subsequent reduction of ester groups with LiAlH_4 provided compound **3** in overall 85% yield.¹⁸ Compound **3** was further reacted with MsCl to obtain bis(mesylated) compound **4** in 60% yield. Treatment of compound **4** with NaN_3 followed by reduction in the presence of PPh_3 provided bis(amine) in 60% yield. Finally, the macrocycle **1** was obtained in 46% yield by coupling of **5** with oxalyl chloride under high dilution condition. All compounds were purified by column chromatography and structures were confirmed adequately (See experimental section for detailed reaction procedure and characterization data).



Scheme 3.1: Synthesis of macrocycle **1**.

3.2.2. Ion Transport Activity:

The ion transport activity of compound **1** was evaluated using EYPC-LUVs \Rightarrow HPTS. Large unilamellar vesicles were prepared by using EYPC lipid upon entrapping a pH sensitive fluorescent dye HPTS, as discussed in the previous chapter.^{19,20,21} The destruction of pH gradient upon addition of compound **1** was monitored to investigate the ion transport activity. A remarkable increase in fluorescence intensity, observed immediately after addition of compound **1**, signified the ion transport activity of designed macrocycle (Figure 3.3A). The abrupt

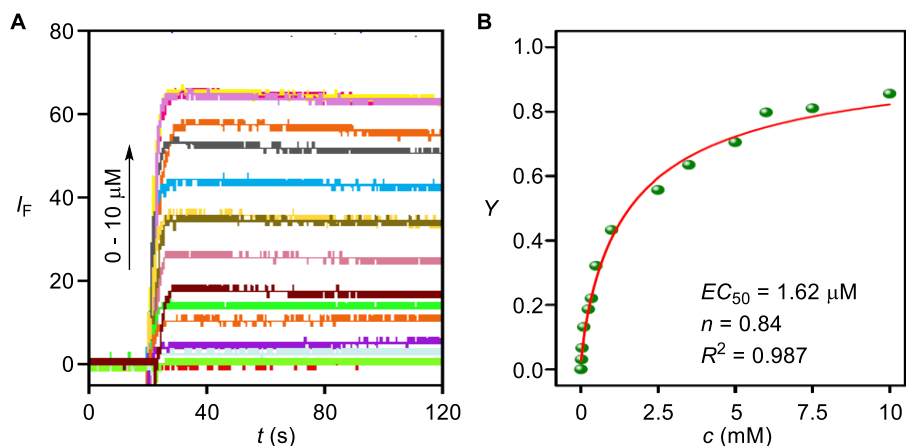


Figure 3.3. Dose-dependent ion transporting activity of macrocycle **1** EYPC-LUV \Rightarrow HPTS, presented in normalized emission intensity I_F as a function of time t (**A**), and Hill plot of **1** generated from the fractional fluorescence intensity (Y) of **1** at $t = 50$ s versus concentration (**B**).

enhancement in fluorescence intensity upon addition of **1** to EYPC-LUVs Δ HPTS, indicates the pre-assembled nanochannel architecture, i.e., the strong hydrogen bonding interaction among the macrocyclic building units. This was further supported by the Hill coefficient, $n = 0.84$ obtained from the fitting of the dose response plot of **1** to Hill equation.²² The EC_{50} (1.62 μ M) value, obtained from the dose response plot of compound **1**, in the lower range indicates the excellent efficiency of macrocycle **1** as an ion transporting agent.

3.2.3. Ion Selectivity:

The ion transport activity of compound **1** prompted us to investigate the ion selectivity in EYPC-LUVs Δ HPTS. Ion selectivity of **1** ($c = 3 \mu$ M) was screened with EYPC-LUVs Δ HPTS by varying either the cation, M^+ (where $M^+ = Li^+, Na^+, K^+, Rb^+, \text{ and } Cs^+$) or the anion, A^- (where $A^- = F^-, Cl^-, Br^-, I^-, NO_3^-, \text{ and } ClO_4^-$) in the extravesicular buffer. Variation of cations provided a negligible difference in the amount of ion transport suggesting no contribution of cations in the transport process (Figure 3.4A). However, the change of anion resulted in the activity sequence: $Cl^- > ClO_4^- > Br^- \sim NO_3^- > SO_4^{2-} > I^- > OAc^-$ (Figure 3.4B). A significant difference in the amount of ion transport activity signifies the involvement of anion in the transport process. It was assumed, that the anion selectivity of the supramolecular ion channel is being governed by the aromatic $C-H \cdots X^-$ and amide $N-H \cdots X^-$ interactions.

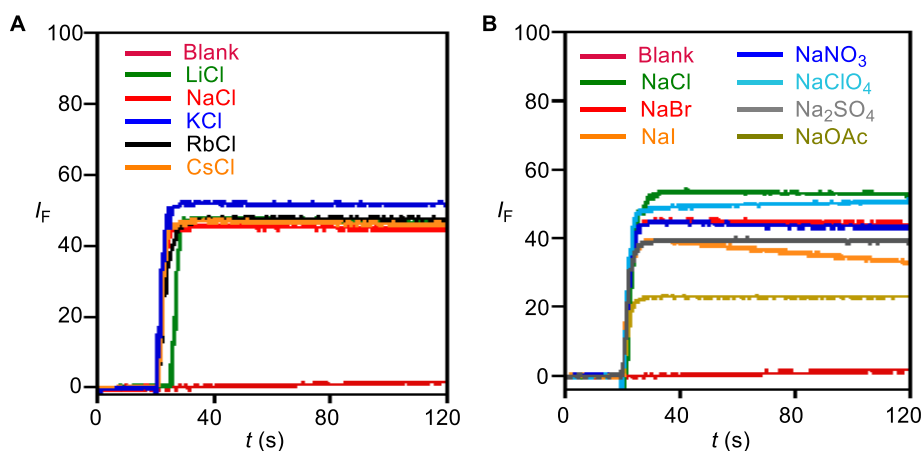


Figure 3.4: Cation selectivity of **1** (3 μ M) determined with the HPTS assay with intravesicular Na^+ ion and varied external cations M^+ (A), anion selectivity of compound **1** with intravesicular Cl^- and varied extravesicular A^- (B).

3.2.4. Membrane Disruption Assay by CF:

The sudden enhancement in ion transport activity, upon addition of compound **1**, also indicates to the possibility of membrane disruption followed by exposing of HPTS dye to the extravesicular buffer because of compound **1**. To investigate the possibility of membrane disruption, CF (carboxyfluorescein) assay had been carried out. EYPC vesicles were prepared by entrapping excess amount of 5-carboxyfluorescein (50 mM) dye. The fluorescence emission of 5-carboxyfluorescein suffered from collisional quenching because of high intravesicular dye concentration.^{23,24} Upon discharging the CF dye to the extravesicular buffer, the fluorescence intensity can restore because of lack of collisional self-quenching. Hence, the extent of membrane disruption can be measured by monitoring the enhancement in fluorescence intensity of CF dye (Figure 3.5A). At the end of the experiment, Triton X-100 was added to get the maximum possible intensity for CF dye. No enhancement in emission intensity was observed upon addition of compound **1** (3 μM) into EYPC-LUVs \supset CF, and this excludes the membrane disrupting possibility of compound **1** (Figure 3.5B). This experiment also eliminates the possibility of dye leakage from the vesicle through the channel formed by compound **1**. Hence, the enhancement of fluorescence intensity obtained in EYPC-LUVs \supset HPTS is solely the result of ion transport through the nanochannel. Absence of dye leakage from vesicle also ruled out the formation of any large pore from **1**.

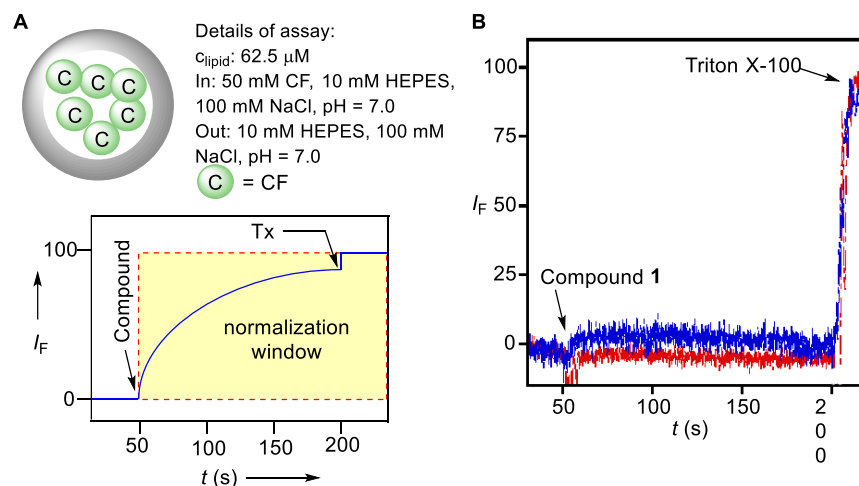


Figure 3.5: Representation of CF assays for EYPC-LUV (A); CF assay, in presence and absence of compound **1** (3 μM), showing no membrane disruption (B).

3.2.5. Planar Lipid Bilayer Conductance Measurements:

The confirmational study of successful ion transport via artificial ion channel formation, by compound **1**, was done by recording the conductance across planar bilayer membrane (BLM). A planar lipid bilayer can be readily formed to the micropore by 2-diphytanoyl-*sn*-glycero-3-phosphocholine (DPhPC) lipid to maintain a semipermeable barrier for electrolyte chambers (Figure 3.6A). The electrical communication between the electrolyte chambers can be restored upon employing an ion channel into the planar lipid bilayer.⁹ According to the experimental setup, compound **1** (20 μM) was added to the *cis* chamber containing 1 M KCl solution and stirred for 30 min. A significant amount of electrical conductance was observed in both positive and negative potential across the membrane (Figure 3.6B), which signifies the successful formation of the artificial ion channel by compound **1**. Furthermore, the periodic opening and closing of the channel, reflected in the conductance data, deliver the information related to opened and closed state of the ion channel. The single channel conductance of 38.85 ± 5.15 pS was obtained upon analyzing the data from the single channel recordings.

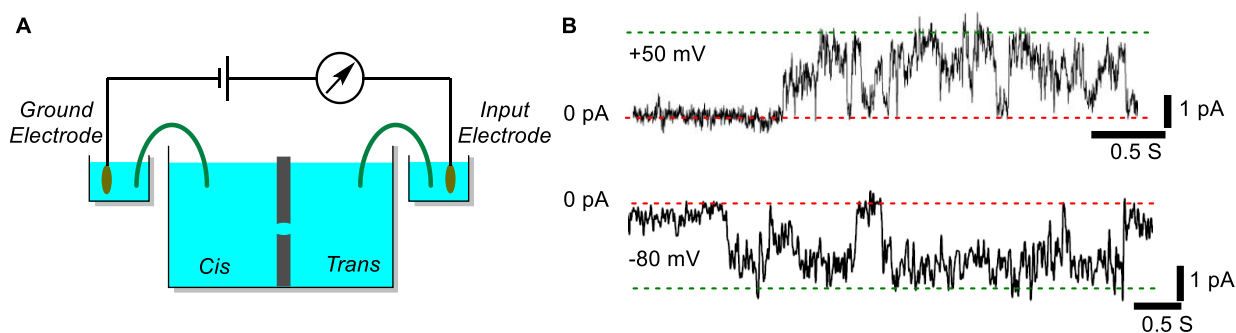


Figure 3.6: Schematic representation of experimental setup of planar lipid bilayer conductance measurements assay (A). Single channel current traces recorded at +50 mV and -80 mV holding potentials in 1 M symmetrical KCl solution. 0 pA at the right-hand side indicates base line current. The main conductance state is indicated by two green dotted lines.

The diameter of the artificial ion channel formed by compound **1** was calculated from the single channel conductance value by using the equation 3.1,²⁰ and the diameter appeared to be 3.19 ± 0.21 Å. The diameter obtained was closely resembled to the ionic diameter of Cl^- ion which confirms the unbeaten conduction of Cl^- ion through the channel lumen.

$$1/g = (l + \pi d/4) \times (4\rho/\pi d^2) \quad \text{Equation 3.1}$$

where, g = corrected conductance (obtained by multiplying measured conductance with the Sansom's correction factor), l = length of the ion channel (34 Å) and ρ = resistivity of the recording solution ($\rho = 9.44 \Omega \cdot \text{cm}$).

In addition to that, an I-V plot was generated in a symmetrical electrolyte solution of two chambers (1 M KCl in each chamber). The applied voltage was ramped from -80 mV to $+80$ mV for a definite time interval and the current were measured which follows an ohmic relationship. An equal amount of current was obtained irrespective of the direction of applied potential (Figure 3.7). The absence of hysteresis in the I-V plot indicates the voltage independent behavior of the synthetic ion channel.

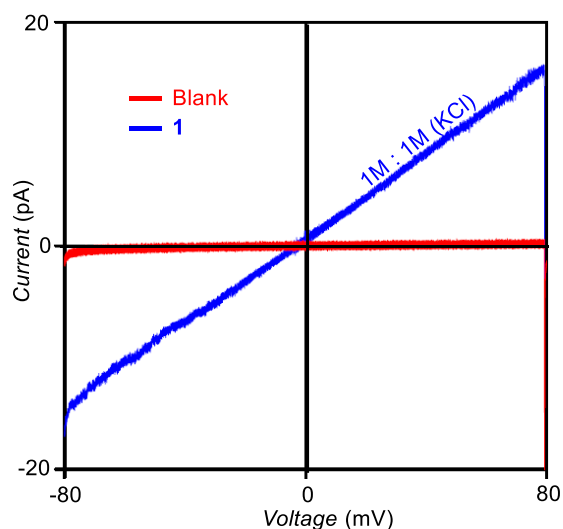


Figure 3.7: I-V plot using voltage ramp (-80 mV to $+80$ mV) in 1 M symmetrical KCl solution (blue line).

3.3. CONCLUSION:

In summary, a barrel-hoop based artificial ion channel was designed where small macrocyclic building units can self-assemble to form a nanochannel structure. A lipophilic macrocycle was synthesized which contains di-oxalyl amide moieties to form intermolecular hydrogen bonding for construction of the supramolecular entity. The inner lumen of the channel structure was found to be hydrophilic, because of the presence of oxalyl-amide moieties, which

can help in self-assembly as well as in ion transport. The presence of n-pentyl groups impose hydrophobicity to the external surface of the nanochannel. The efficient ion transport through the channel and anion selectivity was proved by fluorescence-based assays using large unilamellar vesicle. The confirmation of ion channel formation was achieved by conductance measurement in the planar lipid bilayer. The exclusive anion selectivity was imposed by the multiple selectivity filter, usually from the aromatic C–H \cdots X⁻ and amide N–H \cdots X⁻ interactions, present in the nanochannel. The supramolecular approach of introducing synthetic ion channel opens up the possibilities for further modification related to ion transport property and could be a potent pioneer for biotechnological application.

3.4. EXPERIMENTAL SECTION:

3.4.1. General Methods.

All reagents and solvents for synthesis were purchased commercially and used without further purification. Dichloromethane (CH₂Cl₂) was pre-dried over calcium hydride and then distilled. Column chromatographies were performed on Merck silica gel (100 – 200 mesh). Thin layer chromatographies (TLCs) were carried out with E. Merck silica gel 60-F254 plates. Egg yolk phosphatidylcholine (EYPC) and dipalmitoylphosphatidylcholine (DPPC) were obtained from Avanti Polar Lipids as a solution in CHCl₃ (25 mg/mL). HEPES buffer, HPTS, lucigenin, Triton X-100, NaOH and inorganic salts were purchased of molecular biology grade from Sigma. Large unilamellar vesicles (LUV) were prepared by using mini extruder, equipped with a polycarbonate membrane of 100 nm pore size, obtained from Avanti Polar Lipids.

3.4.2. Physical Measurements.

All NMR spectra were recorded either on 500 MHz Bruker, or 400 MHz Bruker Ascend™ 400 spectrometer using either residual solvent signals as an internal reference or from internal tetramethylsilane on the δ scale. The chemical shifts (δ) were reported in ppm and coupling constants (J) in Hz. The following abbreviations were used: m (multiplet), s (singlet), d (doublet), t (triplet) dd (doublet of doublet). High-resolution mass spectra were obtained on a MicroMass ESI-TOF MS spectrometer equipped with a Micromass Z-Spray electrospray ionization (ESI) source (Waters Co., Synapt G2, France). FT-IR spectra were obtained using NICOLET 6700 FT-IR spectrophotometer as KBr disc and reported in ν (cm⁻¹). Melting points were measured using a VEEGO Melting point apparatus. All melting points were measured in open glass capillary, and values are uncorrected. Fluorescence spectra were recorded from Fluoromax-4 from JobinYvon Edison-equipped with an injector port and a magnetic

stirrer. Measurements of pH were done using a Helmer pH meter. All data from fluorescence studies were processed either by KaleidaGraph 3.51 or Origin 8.5 program. ChemBio Draw 15 Ultra software was used for drawing structures and processing figures.

3.4.3. Synthesis:

Synthesis of (5-(pentyloxy)-1,3-phenylene)dimethanol (C₁₃H₂₀O₃) **3**:

In a 100 mL round bottom flask, 5-hydroxyisophthalic acid **2** (2.0 g, 10.9 mmol) was dissolved in 15 mL of methanol and 0.2 mL of H₂SO₄ was added to it dropwise. The reaction was monitored by thin layer chromatography (TLC) and washed with a saturated NaHCO₃ solution. The compound was collected by evaporating the solvent and proceeds to the next step without purification.

The compound was dissolved in 20 mL of ACN in a 100 mL round bottom flask. Bromopentane (1.6 gm, 10.9 mmol) and K₂CO₃ (3.7 gm, 27.3 mmol) were added to the solution and refluxed for 40 h. The reaction was monitored by TLC and washed with water. The compound was collected by evaporating the solvent and proceeds to the next step without purification.

Lithium aluminiumhydride (830mg, 19 mmol) was mixed with 12 mL of dry THF in a clean and dry round bottom flask and stirred for 30 min at rt. The compound was dissolved in 3 mL of dry THF and added to the mixture in dropwise manner. The reaction was monitored by TLC, and excess LAH was quenched by EtOAc and washed with saturate solution of Na₂SO₄. Compound was purified by a filter column using 100% DCM to yield 2.2 gm (92% overall yield) of **3** as white solid. **M.p.**: 74 – 76 °C; **¹H NMR (400 MHz, CDCl₃)**: δ 6.9 (s, 1H), 6.82 (s, 2H), 4.63 (s, 4H), 3.95 (t, *J* = 6.6 Hz, 2H), 2.05 (s, 2H), 1.83 – 1.73 (m, 2H), 1.50 – 1.26 (m, 4H), 0.93 (t, *J* = 7.1 Hz, 3H). **¹³C NMR (100 MHz, CDCl₃)**: δ 159.74, 142.84, 117.44, 112.25, 77.16, 68.19, 65.25, 29.08, 28.32, 22.58, 14.17; **IR (KBr)**: ν/cm⁻¹ 3340, 2932, 2868, 1599, 1455, 1294, 1161, 1023; **HRMS (ESI)**: Calc. for C₁₃H₂₀O₃Na⁺ [M+Na]⁺: 247.1309; Found: 247.1660.

Synthesis of (5-(pentyloxy)-1,3-phenylene)bis(methylene) dimethanesulfonate (C₁₅H₂₄O₇S₂) **4**:

In a 50 mL round bottom flask **3** (500 mg, 2.22 mmol) and Et₃N (0.75 mL, 5.34 mmol) were dissolved in dry CH₂Cl₂ (8 mL). To the reaction mixture, a solution of methane sulfonyl chloride in 2 mL of CH₂Cl₂ (0.42 mL, 2.4 mmol) was added dropwise at 0 °C. After 30 min of stirring at room temperature, the reaction mixture was washed with water and compound was purified by column chromatography which yielded 500 mg (60%) of **4** as colorless oil. **¹H NMR (400 MHz, CDCl₃)**: δ 7.01 (s, 7H), 6.95 (d, *J* = 4 Hz, 2H), 5.20 (s, 4H), 3.97 (t, *J* = 6.5 Hz, 2H), 2.98 (s, 6H), 1.78 (dd, *J* = 14, 6.6 Hz, 2H), 1.42 (ddd, *J* = 20.1, 11.1, 6.6 Hz, 4H), 0.94 (t, *J* = 7.1 Hz, 3H). **¹³C NMR (100 MHz, CDCl₃)**: δ 160.03, 135.73, 120.57, 115.55, 77.16, 70.77, 68.50, 38.46, 28.95, 28.27, 22.57, 14.16; **IR (KBr)**: ν/cm⁻¹ 2943, 2870,

1603, 1462, 1348, 1172, 930, 834; **HRMS (ESI):** Calc. for $C_{15}H_{24}O_7S_2Na^+$ $[M+Na]^+$: 403.086; Found: 403.0864.

Synthesis of (5-(pentyloxy)-1,3-phenylene)dimethanamine ($C_{13}H_{22}N_2O$) **5**:

In a 50 mL round bottom flask, **4** (880 mg, 2.52 mmol) was dissolved in dry DMF (8 mL). NaN_3 (500 mg, 7.6 mmol) was added to the reaction mixture and stir for 2 h at 80 °C. After completion of the reaction, the compound was collected by washing with water and brine.

The compound was taken in a 50 mL round bottomed flask and dissolved in 6 mL of THF/water (9:1). Solid triphenylphosphine (2.6 gm, 10.08 mmol) was added to the mixture and stirred for 15 h at room temperature. After completion of the reaction, compound was purified by column chromatography through neutral alumina which yield 230 mg of semisolid compound **5** (41%). **1H NMR (400 MHz, MeOD):** δ 6.85 (s, 1H), 6.78 (d, $J = 1.2$, 2H), 3.98 (t, $J = 6.5$ Hz, 2H), 3.73 (s, 4H), 1.77 (dd, $J = 8.0$, 6.6 Hz, 2H), 1.51 – 1.34 (m, 4H), 0.95 (t, $J = 7.2$ Hz, 3H). **^{13}C NMR (100 MHz, MeOD):** δ 161.10, 145.44, 119.52, 113.05, 68.98, 49.00, 46.73, 30.17, 29.43, 23.51, 14.38; **IR (KBr):** ν/cm^{-1} 3288, 2962, 2864, 2422, 1592, 1450, 1286, 1156, 992, 833; **HRMS (ESI):** Calc. for $C_{13}H_{23}N_2O$ $[M+H]^+$: 222.1805; Found: 222.1794.

Synthesis of 15,85-bis(pentyloxy)-3,6,10,13-tetraaza-1,8(1,3)-dibenzenacyclotetradecaphane-4,5,11,12-tetraone ($C_{30}H_{40}N_4O_6$) **1**:

In a 250 mL round bottom flask Oxalyl chloride (114 mg, 0.9 mmol) and diisopropylethylamine (0.7 mL, 4 mmol) were dissolved in dry CH_2Cl_2 (30 mL) and cooled to 0 °C. A solution of **5** (100 mg, 0.45 mmol) in 15 mL dry CH_2Cl_2 was added to the ice-cooled mixture, dropwise, over the period of 2 h and stir at rt for another 2 h. After that, another portion of **5** (100 mg in 15 mL CH_2Cl_2) was added to the mixture dropwise and stir for 24 h. Expected compound was purified by column chromatography 15% MeOH/ $CHCl_3$ which yield 115 mg of **1** as white solid. **M.p.:** 131 – 133 °C; **1H NMR (400 MHz, $CDCl_3$ /MeOD):** δ 6.88 (s, 2H), 6.81 (s, 4H), 3.96 (t, $J = 6.4$ Hz, 4H), 3.85 (s, 8H), 1.81 – 1.68 (m, 4H), 1.40 (ddd, $J = 20.1$, 11.1, 6.5 Hz, 8H), 0.91 (t, $J = 7.1$ Hz, 6H). **^{13}C NMR (101 MHz, $CHCl_3$ /MeOD)** δ 160.52, 140.81, 119.90, 114.15, 68.72, 49.00, 45.13, 29.44, 28.72, 22.90, 14.20; **IR (KBr):** ν/cm^{-1} 2930, 2864, 1596, 1535, 1455, 1379, 1291, 1153, 1018, 932, 830; **HRMS (ESI):** Calc. $C_{30}H_{40}N_4O_6H^+$ $[M+H]^+$: 553.3026; Found: 553.3013.

IV. Ion transport activity and selectivity:

Ion transport activity and selectivity were screened in EYPC-LUVs \supset HPTS according to the similar procedure as described in the previous chapter.

3.4.5. CF Assay:

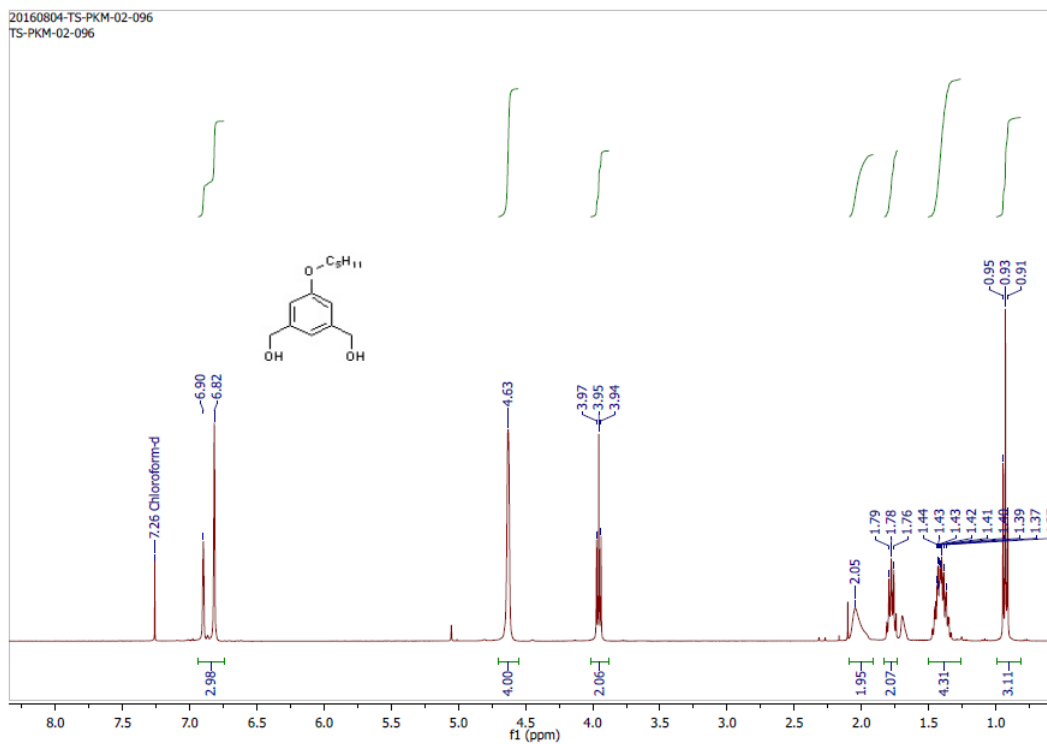
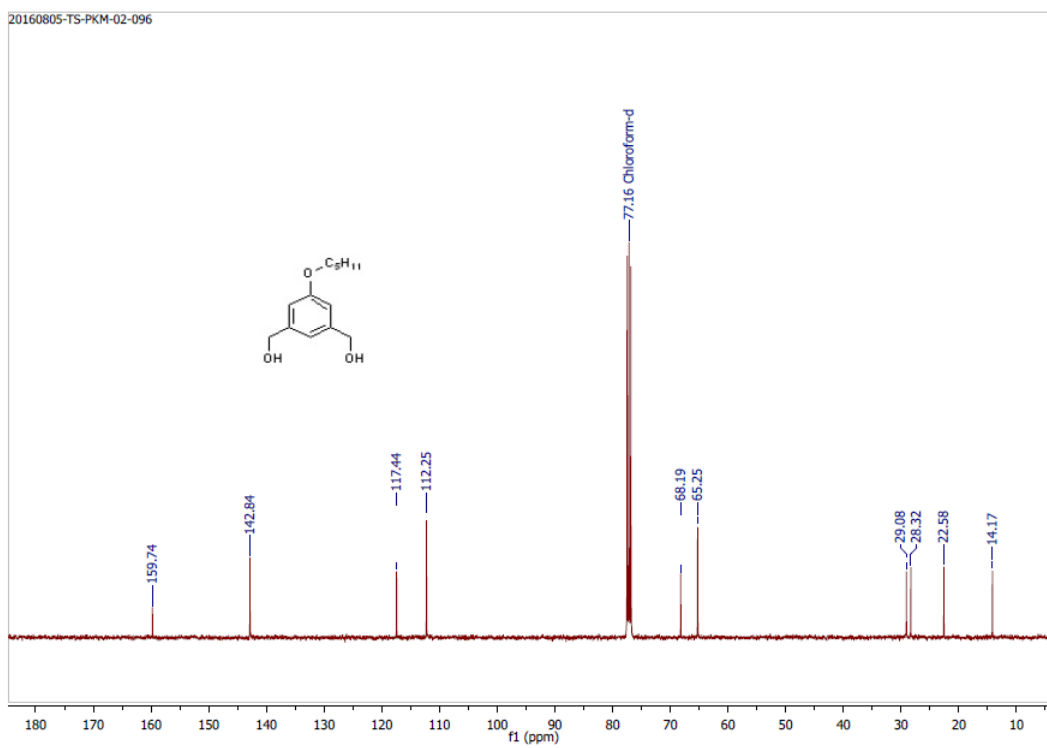
Preparation of EYPC-LUVs Δ CF: In a clean and dry small round bottomed flask 1 mL of egg yolk phosphatidylcholine (EYPC, 25 mg/mL in CHCl₃) was dried by purging nitrogen gas with continuous rotation to form a transparent thin film of EYPC. The transparent film was kept under high vacuum for 6 h to remove all trace of CHCl₃ at room temperature. The resulting film was hydrated with 1 mL buffer (50 mM CF, 10 mM HEPES, 10 mM NaCl, pH = 7.0) for 1 h with 4–5 times occasional vortexing and subjected to freeze-thaw cycle (≥ 15 times). Extrusions were done 21 times (must be an odd number) by a Mini-extruder with a polycarbonate membrane of pore size 100 nm (Avanti). Extravesicular dyes were removed by gel filtration (using Sephadex G-50) with buffer (10 mM HEPES, 100 mM NaCl, pH = 7.0) and diluted to 6 mL to get EYPC-LUVs Δ CF: ~ 5.0 mM EYPC; inside: 50 mM CF, 10 mM HEPES, 10 mM NaCl, pH = 7.0, outside: 10 mM HEPES, 100 mM NaCl, pH = 7.0.²⁵⁻²⁹

Ion transport activity: In a clean and dry fluorescence cuvette, 1975 μ L of HEPES buffer (10 mM HEPES, 100 mM NaCl, pH = 7.0) was added followed by addition of 25 μ L of EYPC-LUVs Δ HPTS. The cuvette was placed in the fluorescence instrument with slowly stirring condition by a magnetic stirrer equipped in the instrument (at $t = 0$ s). The time course of HPTS fluorescence emission intensity, F_t was observed at $\lambda_{em} = 517$ nm ($\lambda_{ex} = 492$ nm). Compound **1** (3 μ M) was added at $t = 50$ s, and finally, 25 μ L of 10% Triton X-100 was added at $t = 200$ s to lyse vesicles resulting destruction of the membrane.

3.4.6. Planar Bilayer Conductance Measurements:

Bilayer membrane (BLM) was formed across an aperture of 150 μ m diameter in a polystyrene cup (Warner Instrument, USA) with lipid diphytanoylphosphatidylcholine (DPhPC; Avanti Polar Lipids), dissolved in *n*-decane (20 mg/mL). Both *cis* and *trans* compartments were filled with symmetrical solution, containing 1 M KCl. The *cis* compartment was held at virtual ground, and the *trans* chamber was connected to the BC 535 head-stage (Warner Instrument, USA) via matched Ag-AgCl electrodes. Derivative **1** was added to the *cis* chamber, and the solution was stirred with magnetic stirrer. It formed channels within 5 minutes, as observed by the distinct channel opening and closing events at different voltages. Currents were low-pass filtered at 0.5 kHz and digitized at 1 kHz using pClamp9 software (Molecular Probes, USA) and an analog-to-digital converter (Digidata 1440A, Molecular Devices). Positive clamping potentials refer potentials with respect to the ground, and positive currents are presented as upward deflections from the base line (0 pA). The software pClamp 9 was used for data acquisition and analysis. I-V curve was generated from the BLM, containing multiple channels using a voltage ramp from -80 mV to $+80$ mV.

3.4.7. NMR Spectra:

Figure 3.7: ^1H NMR spectrum of **3**.Figure 3.8: ^{13}C NMR spectrum of **3**.

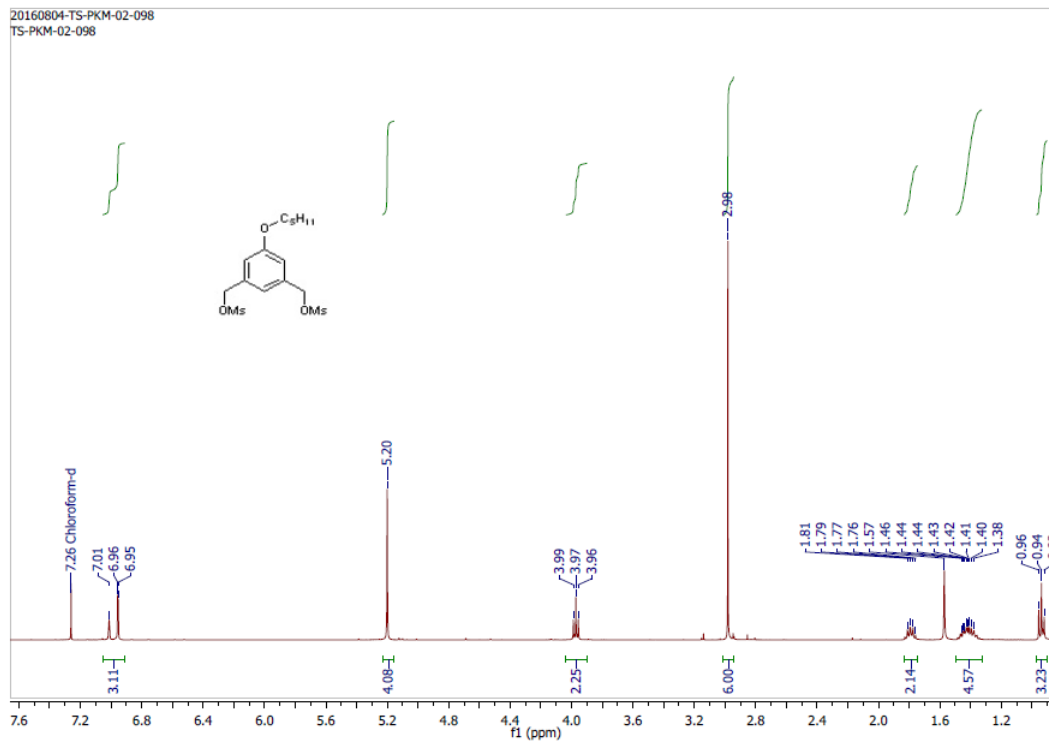


Figure 3.9: ^1H NMR spectrum of **4**.

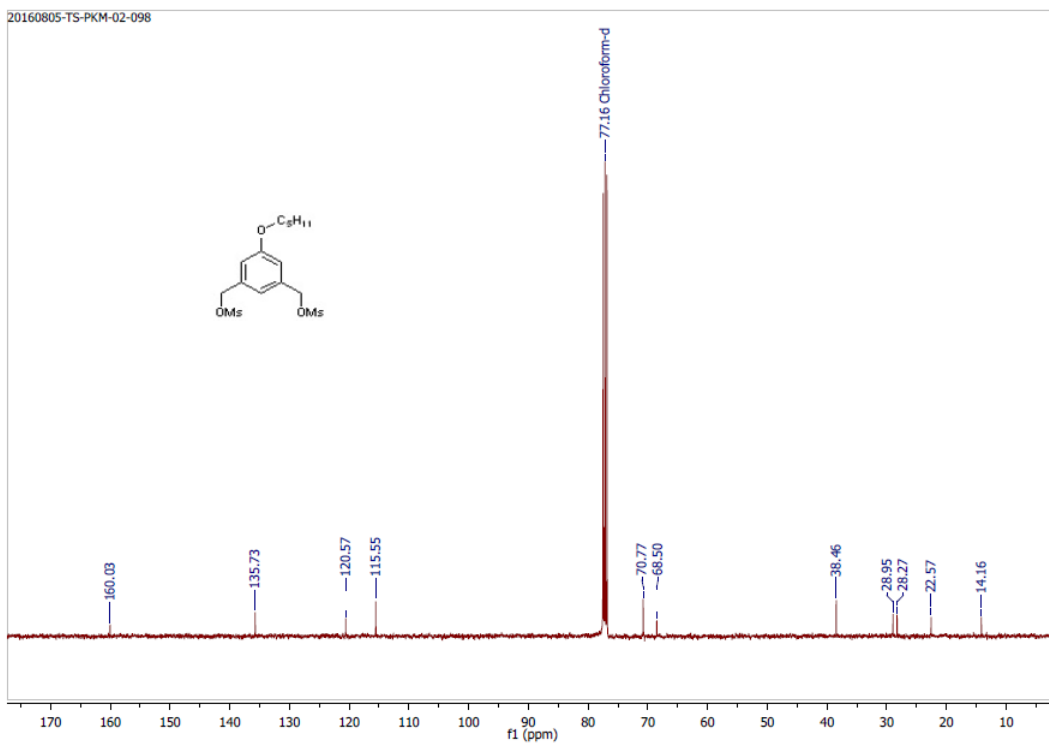


Figure 3.10: ^{13}C NMR spectrum of **4**.

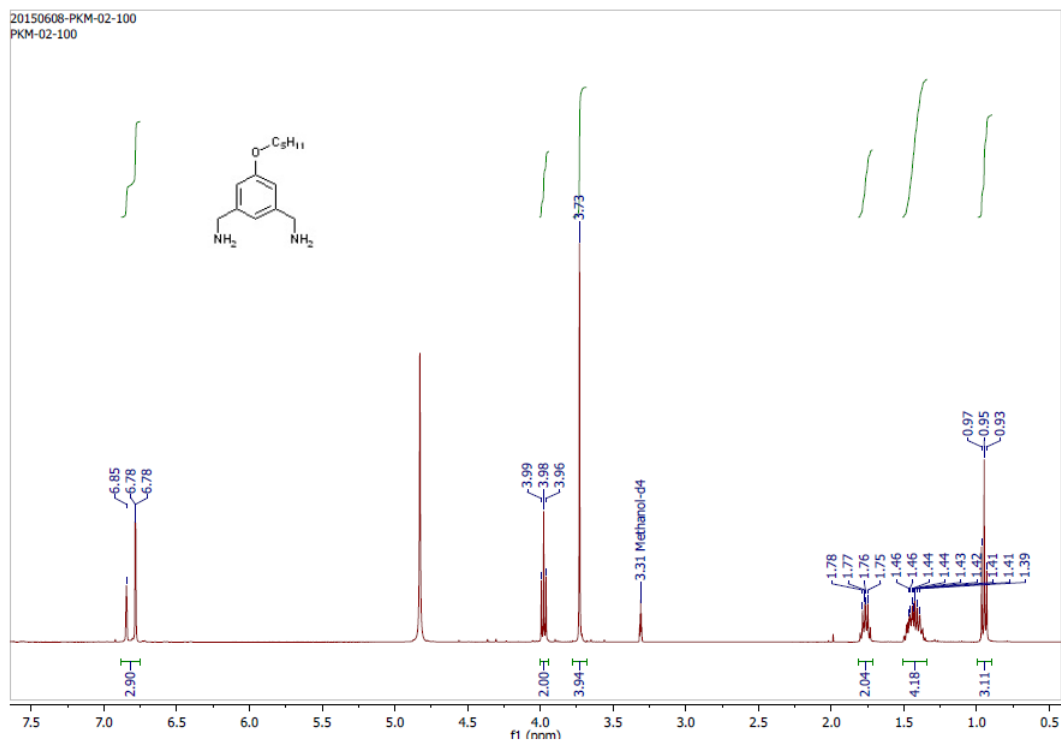


Figure 3.11: ^1H NMR spectrum of **5**.

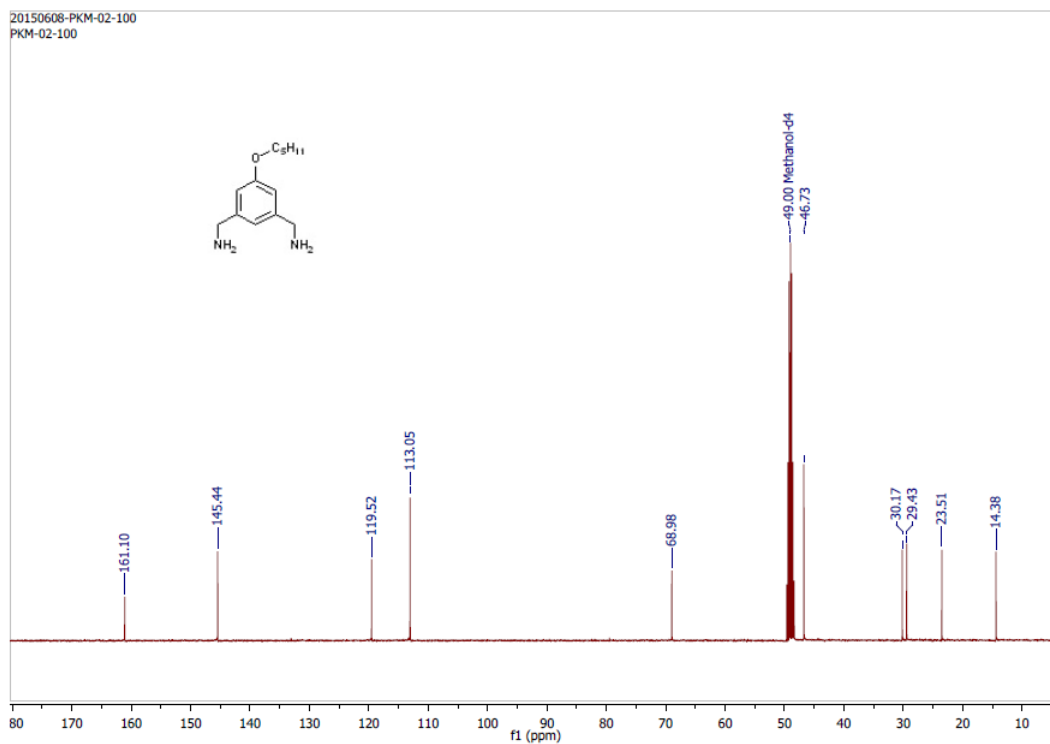


Figure 3.12: ^{13}C NMR spectrum of **5**.

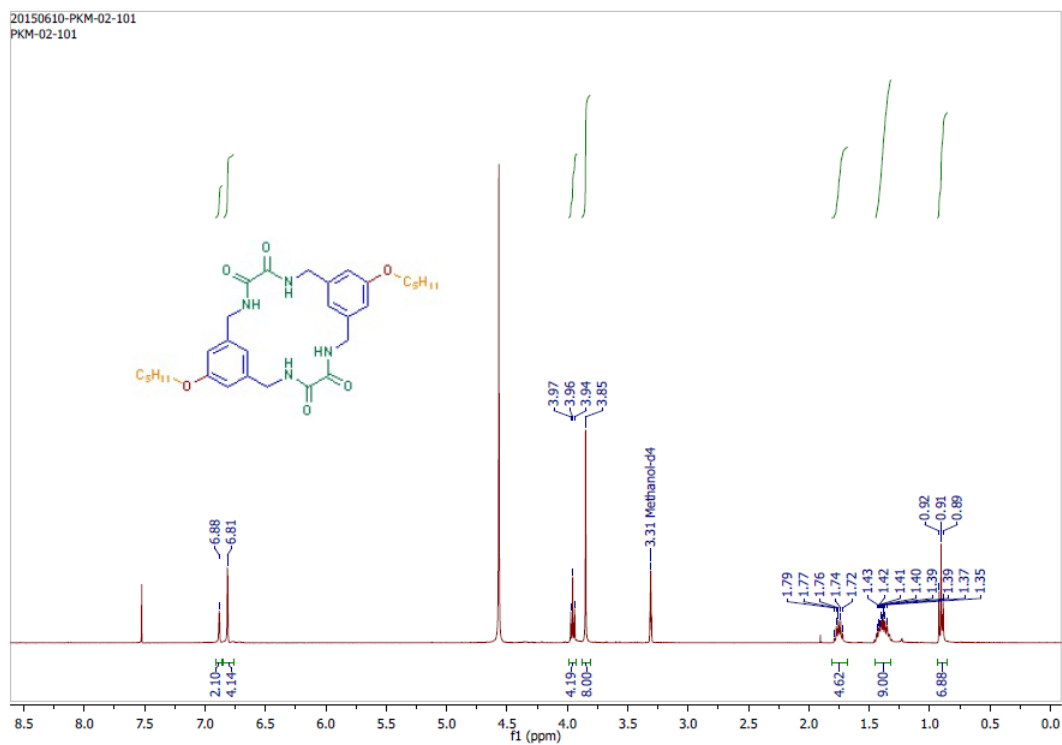


Figure 3.13: ^1H NMR spectrum of **1**.

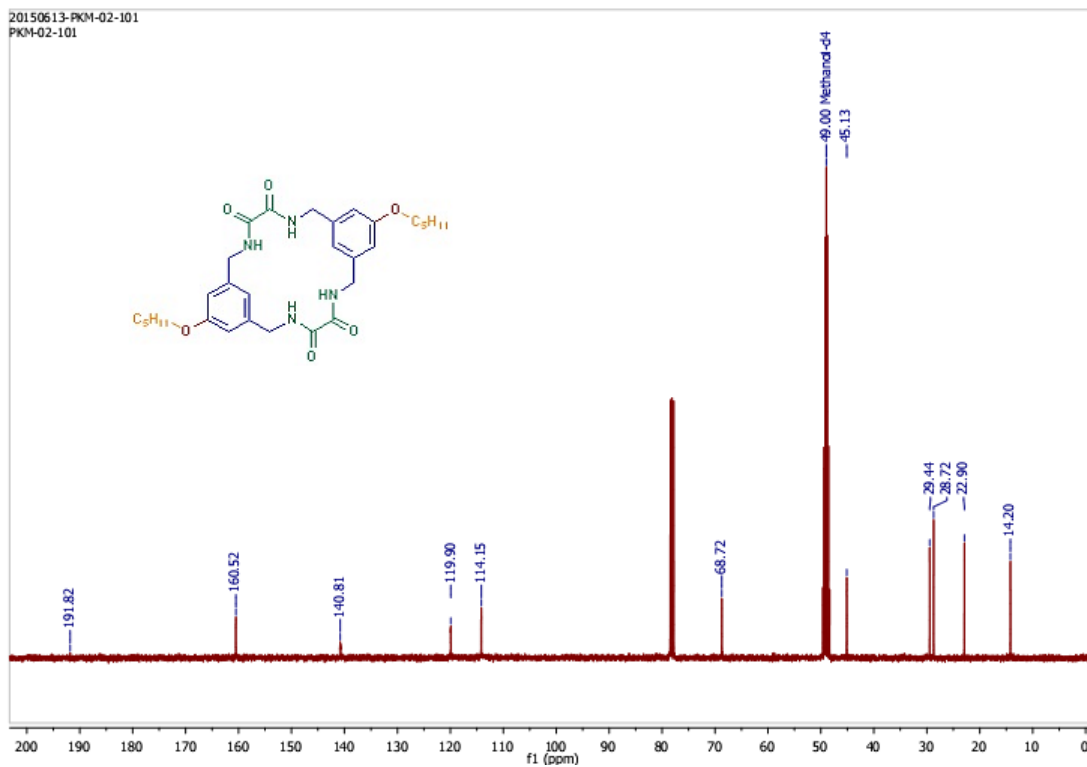


Figure 3.14: ^{13}C NMR spectrum of **1**.

3.5. REFERENCES:

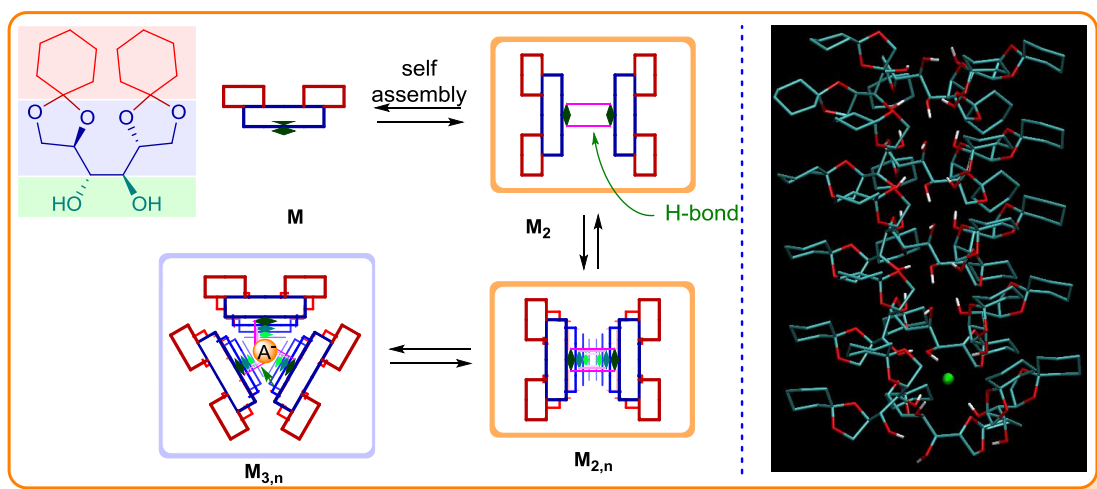
- (1) Hille, B.; Schwarz, W. *J. Gen. Physiol.* **1978**, *72*, 409.
- (2) Miller, C. *J. Gen. Physiol.* **1999**, *113*, 783.
- (3) Hille, B. *Ionic Channels of Excitable Membranes, 3rd Edition*, 2001.
- (4) Keramidas, A.; Moorhouse, A. J.; Schofield, P. R.; Barry, P. H. *Prog. Biophys. Mol. Biol.* **2004**, *86*, 161.
- (5) Gouaux, E.; MacKinnon, R. *Science* **2005**, *310*, 1461.
- (6) Corry, B.; Chung, S. H. *Cell. Mol. Life Sci.* **2006**, *63*, 301.
- (7) Tsien, R. W.; Hess, P.; McCleskey, E. W.; Rosenberg, R. L. *Ann. Rev. Biophys. Biophys. Chem.* **1987**, *16*, 265.
- (8) Song, L.; Hobaugh, M. R.; Shustak, C.; Cheley, S.; Bayley, H.; Gouaux, J. E. *Science* **1996**, *274*, 1859.
- (9) Ishida, H.; Qi, Z.; Sokabe, M.; Donowaki, K.; Inoue, Y. *J. Org. Chem.* **2001**, *66*, 2978.
- (10) Bong, D. T.; Clark, T. D.; Granja, J. R.; Ghadiri, M. R. *Angew. Chem., Int. Ed.* **2001**, *40*, 988.
- (11) Sánchez-Quesada, J.; Isler, M. P.; Ghadiri, M. R. *J. Am. Chem. Soc.* **2002**, *124*, 10004.
- (12) Fernandez-Lopez, S.; Kim, H.-S.; Choi, E. C.; Delgado, M.; Granja, J. R.; Khasanov, A.; Kraehenbuehl, K.; Long, G.; Weinberger, D. A.; Wilcoxon, K. M.; Ghadiri, M. R. *Nature* **2001**, *412*, 452.
- (13) Clark, T. D.; Buehler, L. K.; Ghadiri, M. R. *J. Am. Chem. Soc.* **1998**, *120*, 651.
- (14) Ghadiri, M. R.; Granja, J. R.; Buehler, L. K. *Nature* **1994**, *369*, 301.
- (15) Saggiomo, V.; Otto, S.; Marques, I.; Felix, V.; Torroba, T.; Quesada, R. *Chem. Commun.* **2012**, *48*, 5274.
- (16) Haynes, C. J. E.; Moore, S. J.; Hiscock, J. R.; Marques, I.; Costa, P. J.; Felix, V.; Gale, P. A. *Chem. Sci.* **2012**, *3*, 1436.
- (17) Busschaert, N.; Bradberry, S. J.; Wenzel, M.; Haynes, C. J. E.; Hiscock, J. R.; Kirby, I. L.; Karagiannidis, L. E.; Moore, S. J.; Wells, N. J.; Herniman, J.; Langley, G. J.; Horton, P. N.; Light, M. E.; Marques, I.; Costa, P. J.; Felix, V.; Frey, J. G.; Gale, P. A. *Chem. Sci.* **2013**, *4*, 3036.
- (18) Nakatake, D.; Yokote, Y.; Matsushima, Y.; Yazaki, R.; Ohshima, T. *Green Chem.* **2016**, *18*, 1524.
- (19) Sakai, N.; Matile, S. *J. Phys. Org. Chem.* **2006**, *19*, 452.
- (20) Talukdar, P.; Bollot, G.; Mareda, J.; Sakai, N.; Matile, S. *J. Am. Chem. Soc.* **2005**, *127*, 6528.
- (21) Sakai, N.; Matile, S. *J. Am. Chem. Soc.* **2003**, *125*, 14348.
- (22) Litvinchuk, S.; Bollot, G.; Mareda, J.; Som, A.; Ronan, D.; Shah, M. R.; Perrottet, P.; Sakai, N.; Matile, S. *J. Am. Chem. Soc.* **2004**, *126*, 10067.

- (23) Dawson, R. E.; Hennig, A.; Weimann, D. P.; Emery, D.; Ravikumar, V.; Montenegro, J.; Takeuchi, T.; Gabutti, S.; Mayor, M.; Mareda, J.; Schalley, C. A.; Matile, S. *Nat. Chem.* **2010**, *2*, 533.
- (24) Matile, S. & Sakai, N. in *Analytical Methods in Supramolecular Chemistry* (ed. Schalley, C. A.) 391–418 (Wiley, 2007).
- (25) Saha, T.; Dasari, S.; Tewari, D.; Prathap, A.; Sureshan, K. M.; Bera, A. K.; Mukherjee, A.; Talukdar, P. *J. Am. Chem. Soc.* **2014**, *136*, 14128.
- (26) Talukdar, P.; Bollot, G.; Mareda, J.; Sakai, N.; Matile, S. *J. Am. Chem. Soc.* **2005**, *127*, 6528.
- (27) Gorteau, V.; Bollot, G.; Mareda, J.; Perez-Velasco, A.; Matile, S. *J. Am. Chem. Soc.* **2006**, *128*, 14788.
- (28) Saha, T.; Roy, A.; Gening, M. L.; Titov, D. V.; Gerbst, A. G.; Tsvetkov, Y. E.; Nifantiev, N. E.; Talukdar, P. *Chem. Commun.* **2014**, *50*, 5514.
- (29) Roy, A.; Saha, T.; Gening, M. L.; Titov, D. V.; Gerbst, A. G.; Tsvetkov, Y. E.; Nifantiev, N. E.; Talukdar, P. *Chem. Eur. J.* **2015**, *21*, 17445.

End of Chapter 3

Chapter 4

Hopping Mediated Anion Transport through a Mannitol-Based Rosette Ion Channel



4.1. INTRODUCTION:

Imposition of exclusive ion selectivity of the natural ion channels is associated with the presence of multiple numbers of ion-recognition sites, inclined along the narrow pore of the channel.¹⁻³ The selectivity is primarily governed by the strength of ion binding at these sites, and the ion transport occurs via hopping from one binding site to the next in single-file direction.^{4,7} If we revisit to the KcsA channel for example, the exclusive K^+ selectivity is imposed by the single-file orientation of carbonyl units along the pore. In this naturally occurring potassium channel, present in *Streptomyces lividans*, four identical α -helical protein units are self-assembled to form a large water-filled channel where the ion selectivity was determined by the region called selectivity filter.⁸ Main chain carbonyl oxygen atoms, from each subunit of the channel, are exposed along the line of the selectivity filter, which helps to recognize K^+ ion exclusively. It can be

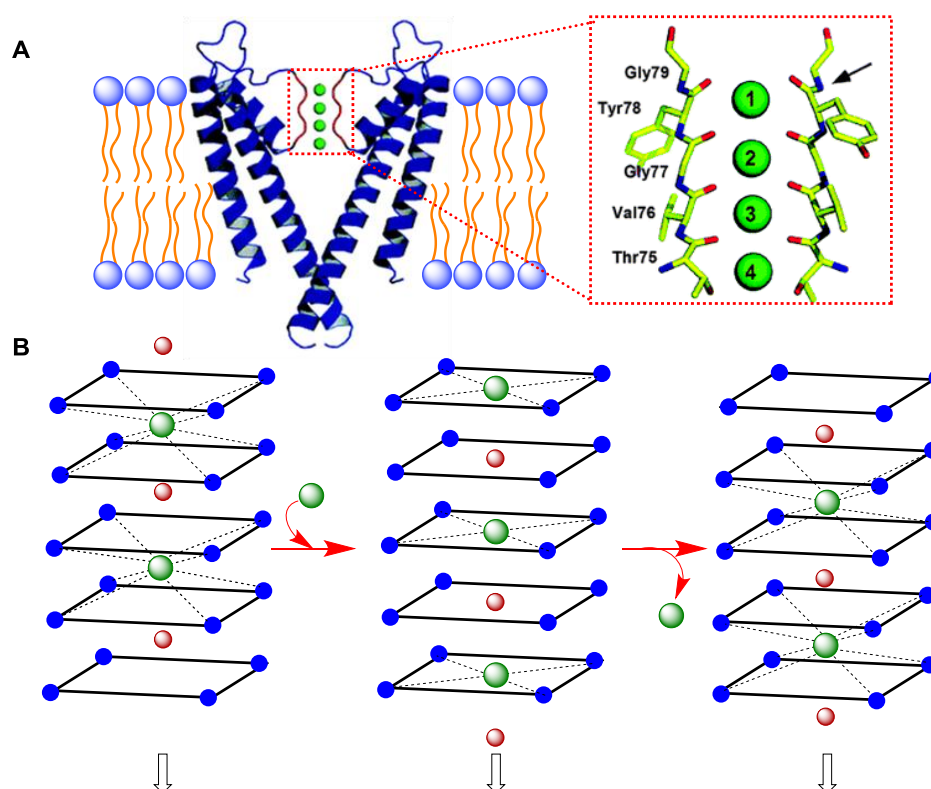


Figure 4.1. Structure of K^+ selective KcsA ion channel and representation of single file orientation of carbonyl units in selectivity filter (A); ion conduction through the channel via hopping mechanism (B).

considered that the carbonyl functionalities are arranged in five layers where each layer contains four carbonyl groups contributed from each α -helical subunit of the channel. The conduction of ions occurs via the hopping mechanism, in partially dehydrated form, with the help of periodic formation and breaking of hydrogen bond interactions from each layer. Similar multiple selectivity filters are also present in Na^+ binding sites in the LeuT Na ϕ -dependent pump,⁹ two Ca^{2+} binding sites in the Ca^{2+} ATPase pump,¹⁰ and the central Cl^- binding sites in CLC channel.¹¹

Therefore, introducing synthetic ion channels with replicative ion binding sites has been of significant interest. Design strategies reported for incorporating multiple ion-recognition sites have primarily resulted in cation selectivity. In 1999, Matile and coworkers reported a single file array of cation- π interaction motif, provided by two hepta(*p*-phenylene) units, in a ligand-assembled ion channel (Figure 4.2A).¹² In this ion channel, a sandwiched binding motif involving two phenyl rings and a cation is repeated along the channel direction, maintaining the cation- π interaction all over the channel. The carbonyl-cation interaction motif had been used widely in the design of cyclic peptide-based nanochannel (Figure 4.2B).¹³⁻¹⁸ An alternate strategy to capitalize the carbonyl-cation interaction was adapted in the construction of rosette type molecules (Figure 4.2C).¹⁹⁻²¹ Hydrophile-cation interaction, a common cation-recognition motif,^{22,23} was adapted by Matile,²⁴ Fyles²⁵ and Voyer²⁶ to construct single-file pores (Figure 4.2D). Self-assembled "barrel-stave" ion channels were constructed via the tethering of either vicinal diols or peptide side chains to a *p*-octiphenyl rod (Figure 4.2E).²⁷⁻³⁰ However, these supramolecules were also cation selective.

Only the successful design of transmembrane supramolecules with single-file multiple anion-recognition sites was demonstrated primarily by Matile and coworkers. Oligonaphthalenediimide^{31,32} and oligoperylenediimide³³ based rigid-rod molecules were reported to form π -slides in lipid vesicles. Selectivity of these supramolecules during ion transport studies was accounted by anion- π interactions at each recognition site along the channel direction (Figure 4.2F). However, single-channel conductance data of these molecules are not available. Therefore, the design of anion selective artificial ion channels with multiple ion-recognition sites is still a challenge. In the pursuit to develop a robust anion selective ion channel which can work in spherical as well as in planar lipid bilayers, we looked into different anion-recognition motifs routinely applied in anion binding and different strategy of self-assembly.

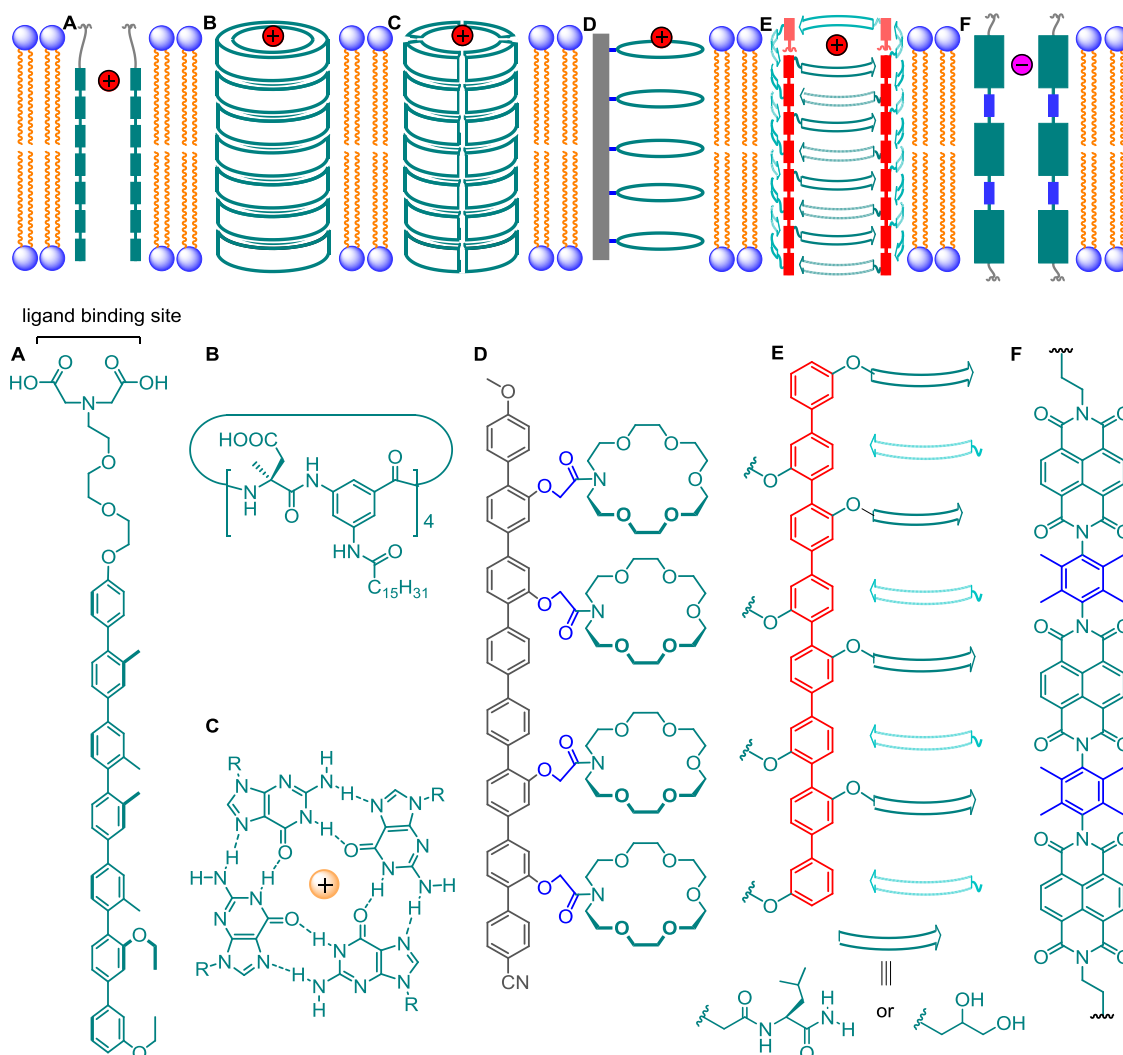


Figure 4.2. Synthetic ion channel designs with single-file multiple ion-recognition sites.

Abundance of use of hydroxyl ($-\text{OH}$) group in the anion binding sites encouraged us to consider it as the recognition motif.³⁴⁻⁴¹ However, such an idea is debatable because all reported synthetic ion channels involving $-\text{OH}$ group are cation selective.^{27-29,42} The cation recognition by the lone pair of oxygen atoms is responsible for the selectivity in these artificial channels.⁴³ However, $-\text{OH}$ group is also the best known of all hydrogen bond donor groups for recognition of anions^{39,44-46} The anion recognition ability of $-\text{OH}$ group had been demonstrated in cyclic cholaphanes⁴⁵ (Figure 4.3A) and colorimetric anion sensor by 3-hydroxy-1,4-naphthaquinone derivative³⁹ (Figure 4.3B). Therefore, the $-\text{OH}$ functionality can in principle be incorporated in the design of anion selective ion channels. In addition to that, in the line of channel architecture, we got inspired by the barrel rosette type of artificial ion channel formed by self-assembly of tiny molecules. An infinitesimal change in functionality in building unit of the channel actually

translated in a multiplicative effect in the self-assembled nanochannel structure. Hence, the modulation of ion selectivity would be much accessible in case of barrel rosette type of ion channel.

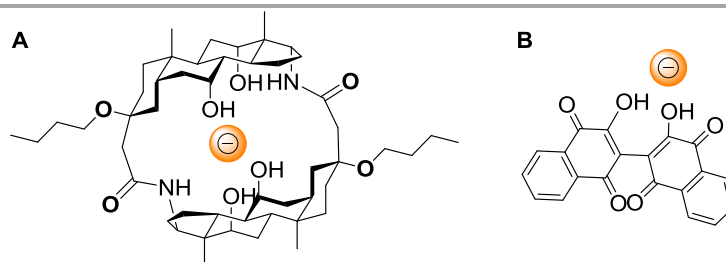


Figure 4.3. Anion recognition by $-OH$ group in cholaphanes (A) and naphthaquinone derivative (B).

In order to find a suitable molecule capable of providing multiple $-OH$ groups for self-assembly and anion recognition, mannitol derivatives **1** and **2** (Figure 4.4A), had drawn our attention.⁴⁷ According to Sureshan and co-workers, these compounds are capable of forming transparent gels in hydrocarbon solvents. We had anticipated that the $-OH$ groups facilitate self-assembly of the monomers **M** along one direction to form fibrils **M_n** (Figure 4.4B). Upon aggregation, these fibrils may form fibers, which entangle to form 3D fibrous spaghetti-like networks immobilizing the solvent via capillary force.⁴⁷ We anticipated that the aggregation of these fibrils **M_n** may provide a face-to-face assembly **M_{n,2}** which further expands to the fibers. The face-to-face assembly **M_{n,2}** aggregations are favourable in either gel or crystalline state. Therefore, the self-assembly provides negligible internal space. However, in the presence of an ion, in the lipid membrane, the interfibril hydrogen bonding can be shared to form self-assembled nanotubular structures **M_{n,3}**, **M_{n,4}**, etc. (Figure 4.4B). Overall, each nanotubular structure can also be viewed as layers of supramolecular rosettes formed by either three or four units of **M**, and each rosette would provide a recognition site for an anion A^- via multivalent $O-H\cdots A^-$ hydrogen bonding interactions. Transport of anion can be predicted through the nanotubular structure, facilitated by the movement of an anion from one rosette to the next in single-file. Cyclohexyl rings of mannitol **1** would be necessary for the better stability of channel structure due to strong Van der Waals interactions compared to **2**.

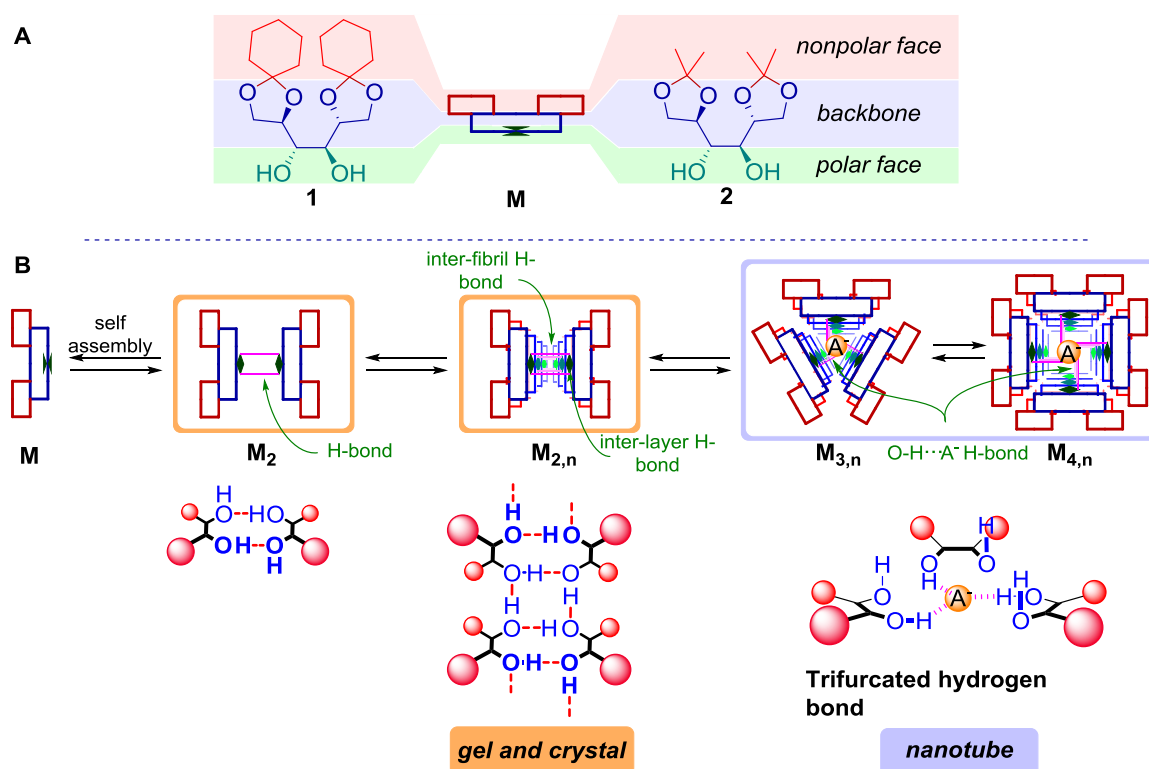


Figure 4.4. Structures of mannitol derivatives **1** and **2** (A) and schematic representation of self-assembly of these molecules in gel/crystalline state as well as in lipid membrane (B).

4.2. RESULT AND DISCUSSION:

4.2.1. Self-assembly of Mannitol Derivatives in the Solid State:

At first, the mode of hydrogen bonding in the solid state of compound **1** was evaluated to validate our anticipation of self-assembly. The mannitol derivative **1** was crystallized from a mixture of acetone and water, and the crystal structure was solved. From the crystal structure, it is evident that both the -OH groups are involved in face-to-face hydrogen bond ($\text{O}_3 \dots \text{O}_3 = 2.73 \text{ \AA}$; $\text{O}_4 \dots \text{O}_4 = 2.76 \text{ \AA}$) with identical -OH groups of a neighbouring molecule in the horizontal direction, which forms a dimer with hydrophilic core and hydrophobic periphery (Figure 4.5A). Such dimers are connected through strong inter-layer hydrogen bonds ($\text{O}_3 \dots \text{O}_4 = 2.76 \text{ \AA}$), forming infinite chains along 'b' direction. The distance between two molecules along this direction was found to be 5.49 \AA (Figure 4.5A). In other words, the hydrogen bonded infinite fibrils formed along 'b' direction are dimerized along 'a' direction through additional hydrogen bonds (Figure 4.5B). The formation of dimeric-fibrils through lateral hydrogen bonds suggests the possibility of formation of higher order structures (*e.g.* trimeric- or tetrameric-fibrils)

through such lateral hydrogen bonds. Also, it is possible to have dynamic interconversion of such higher order structures, especially in response to some stimulus, when the molecules are loosely bound (higher degrees of freedom of motion) unlike in crystals. The presence of an anion can be a stimulus for the formation of such higher order structures ($M_{n,3}$ or $M_{n,4}$) in the lipid membranes. In each lateral-layer (*i.e.* either trimeric or tetrameric rosette) of such structure, multivalent $O-H\cdots A^-$ hydrogen bond interactions is feasible for the anion recognition (Figure 4.4B) and the ion can hop from one rosette to the next in single-file to facilitate ion permeation. Crystal structure also predicts that minimum of seven monomer units (*i.e.* for $n = 7$, the distance between two exterior $O\cdots O = 35.7 \text{ \AA}$) are required to span the 37 \AA EYPC bilayer membranes (Figure 4.5B, C). Crystal structure and packing of **2** is also very similar to that of **1**. However, additional Van der Waals interactions between cyclohexyl groups were present in the solid state assembly of **1**.

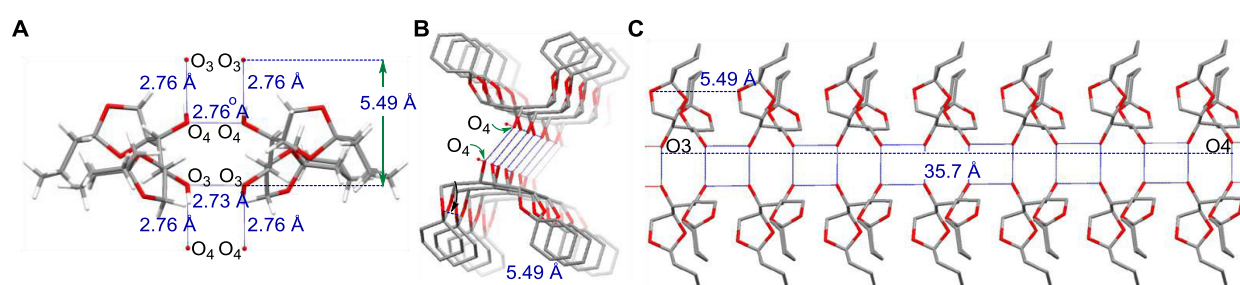


Figure 4.5. Single crystal structure of **1** showing (A) face-to-face and interlayer hydrogen bonding; top (B) and side views (C) of face-to-face aggregation of ladder like structures.

4.2.2. Ion-Transporting Activity by Vesicle Assay:

The ion-transporting activity of mannitol derivatives **1** and **2** was investigated in a spherical lipid bilayer using EYPC-LUV Δ HPTS as described in the previous chapters.^{48,49,50} The compound **1** (20 μM) exhibited high ion transporting activity while the derivative **2** (20 μM) was inactive (Figure 4.6A). Although the hydrogen bonded fibril motif is present in the crystal structure of amphiphile **2** (Figure 4.20), the inactivity could be due to the less stability of nanochannel structure. The instability could be due to missing Van der Waals interactions of cyclohexyl rings or inability of the molecules of **2** to get embedded in the lipid bilayer because of its less hydrophobic nature. The logP value calculated from MarvinSketch program for **1** and **2** appeared to be 2.18 and -0.33

respectively, which indicates the hydrophilic nature of compound **2** for favouring aqueous solubility rather than penetrating lipid bilayer. The inactivity of compound **2** was evident from its negligible transporting activity even at higher concentration (80 μM). In other words, a proper balance between hydrophobic and hydrophilic features in **1** ($\log P = 2.18$) allows its incorporation in the lipid layer.⁵¹ Self-assembly of **1** in the lipid membranes is facilitated by the network of hydrogen bonding interactions and Van der Waals interactions of cyclohexyl rings. Detailed examination of the ion transporting activity of compound **1** was then carried out by varying its concentrations from 0 to 60 μM (Figure 4.6B). A pseudo-first order in transport kinetics was observed for the compound. Rate constant (k_{obs}) values were plotted against respective monomer concentration (c_{M}) values for compound **1** (Figure 4.6C) and Hill analyses were performed by using Equation 4.1:^{26,52,53}

$$k_{\text{obs}} = k_0 + k_{\text{max}} \times [c_{\text{M}}]^n / ([c_{\text{M}}]^n + [EC_{50}]^n) \quad \text{Equation 4.1}$$

where, k_0 is the rate constant for the blank measurement, EC_{50} is the “effective” monomer concentration of each conjugate needed to reach 50% of the maximum activity (k_{max}) and n is the Hill coefficient that reveals the cooperatively of the transport process.

From the Hill analysis, an $EC_{50} = 42.5 \mu\text{M}$ and $n = 0.9$ was calculated which indicates a thermodynamically favourable self-assembly of **1** which appear as a mimic of the monomeric structure during permeation into the lipid membranes.

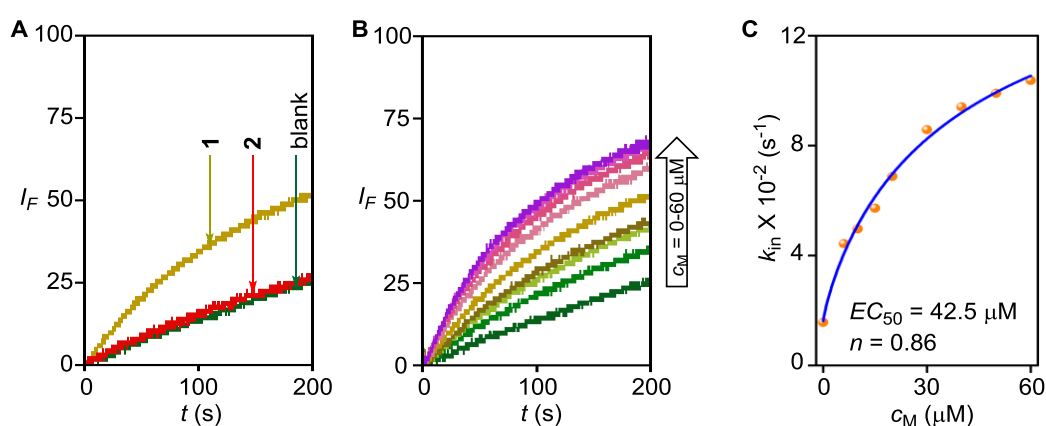


Figure 4.6. Comparison of ion transporting activity of mannitol derivatives **1** (20 μM) and **2** (20 μM) in EYPC vesicle, presented in normalized emission intensity I_F as a function of time t (A). Concentration profile (B) and Hill plot of **1** (C).

4.2.3. Ion Selectivity Studies by Vesicle Assays:

The transporting activity of **1** encouraged us to investigate its ion selectivity and the mechanism of ion transport. At first, the transporting activity was evaluated in the presence of a proton transporter, carbonyl cyanide-4-(trifluoromethoxy) phenylhydrazone (FCCP) to identify whether a H^+/M^+ antiport (M^+ = alkali metal cation) or OH^-/A^- (A^- = monovalent anion) antiport mechanism is dominant through the ion channel. FCCP allows selective efflux of H^+ ion from the intravesicular water pool to the extravesicular bulk water when a pH gradient is applied across the membrane.⁵⁴ Under the applied pH gradient, FCCP ($5\ \mu\text{M}$) exhibited negligible ion transport. On the other hand, the transporting activity of **1** enhanced by approximately 2-fold when studied in the presence of FCCP indicating the cooperative effect of **1** and FCCP (Figure 4.7A). From these data, a faster OH^-/A^- exchange compared to H^+/M^+ antiport across the EYPC membrane was confirmed for mannitol derivative **1**. This data is in accordance with our prediction of anion recognition within the channel structure.

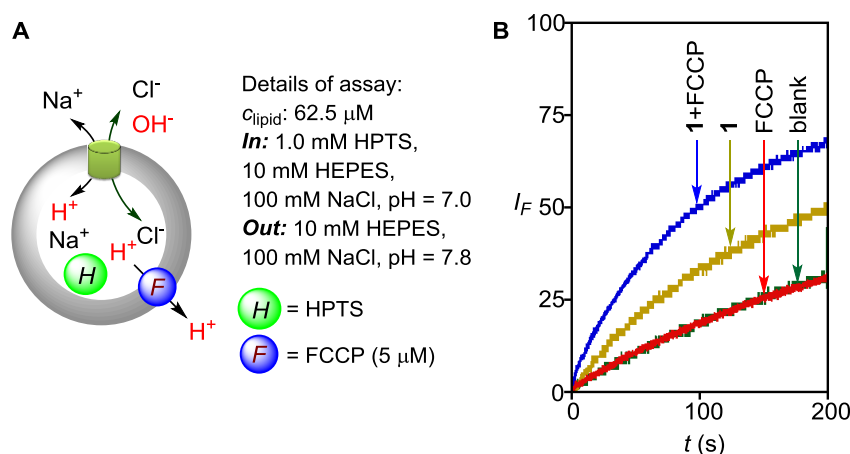


Figure 4.7. Representations of fluorescence based FCCP assay using EYPC vesicle (A) Ion transport activity of **1** ($20\ \mu\text{M}$) determined in the absence and presence of FCCP (B).

A further comparison of transport rate between OH^- and Cl^- was carried out with the help of valinomycin, a K^+ ion selective carrier.⁵⁵ In this assay (Figure 4.8A), a Na^+ versus K^+ gradient was applied between the interior and exterior of EYPC vesicles. The influx of K^+ ion by valinomycin is expected to be accompanied by the OH^-/Cl^- influx to maintain the charge equality. Valinomycin ($1\ \text{pM}$) alone did not display any transporting ability. Fluorescence enhancement of HPTS was nearly similar when **1** ($20\ \mu\text{M}$) was

tested in the absence and presence of valinomycin (Figure 4.8B). These results confirm preferential transport of Cl^- ion through the channel formed by **1** over OH^- ion. This effect implies that the channel formed by **1** acts as an OH^-/Cl^- exchanger with a faster rate of Cl^- ion transport compared to OH^- (*i.e.* a $\text{Cl}^- > \text{OH}^-$ selectivity).

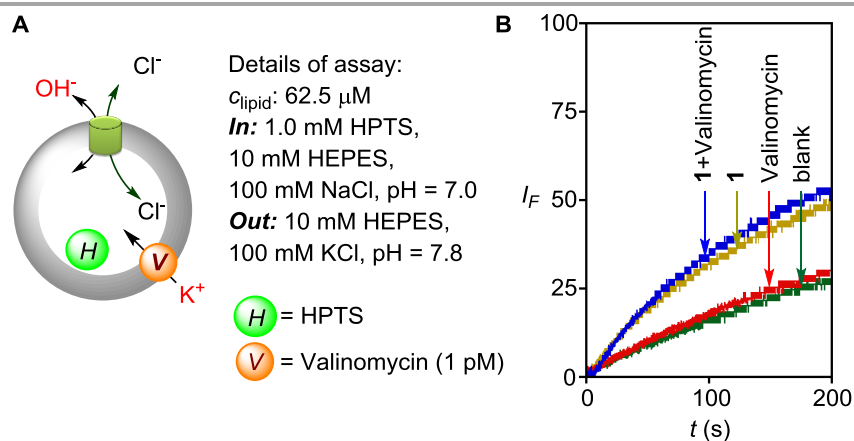


Figure 4.8. Representations of fluorescence based Valinomycin assay using EYPC vesicle (A), ion transport activity of **1** determined in the absence and presence of valinomycin (B).

Anion transport across the channel formed by **1** encouraged us to determine the selectivity sequences caused by iso-osmolar Cl^- (intravesicular) to the monovalent anion, A^- (extravesicular) exchange, a more complicated determination due to the transmembrane Cl^-/A^- gradients. Upon variation of extravesicular anions, a selectivity topology: $\text{Cl}^- > \text{NO}_3^- > \text{Br}^- > \text{SCN}^- > \text{ClO}_4^- \geq \text{I}^- > \text{OAc}^- \geq \text{F}^-$ was determined for **1** (Figure 4.9A). Variation of external cations ($\text{M}^+ = \text{Li}^+, \text{Na}^+, \text{K}^+, \text{Rb}^+, \text{and Cs}^+$) did not provide any difference in ion transporting behavior which further establishes that the rosette channel is specific to only anions (Figure 4.9B).

To rationalize the observation of ion selectivity, the dependence of the fractional activity Y on the reciprocal anion radius (Figure 4.10B) or the anion hydration energy (Figure 4.10C) was plotted. The fluorescence intensities at 100 s after addition of **1** in anion selectivity plot were recorded, and each value (emission intensity for different ion) was divided by the intensity value obtained from Cl^- ion plot to calculate the functional activity (Y). Poor transport of weakly basic anions such as OAc^- or F^- suggested that the origin of the derived Cl^- selectivity is mainly

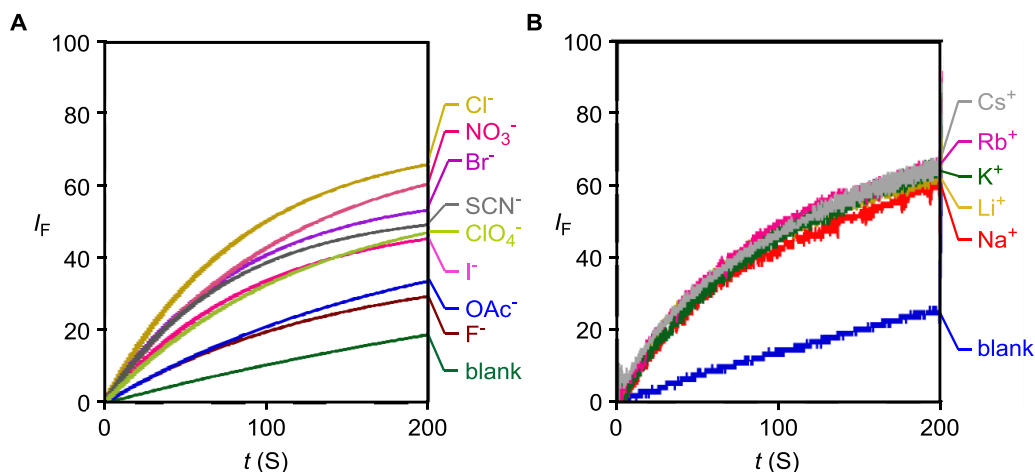


Figure 4.9. Anion selectivity of **1** (20 μM) determined with the HPTS assay with intravesicular Cl^- ion and varied external anions A^- (A), cation selectivity of compound **1** with intravesicular Na^+ and varied extravascular M^+ (B).

energetic, and contribution from anionic radii ($\text{OAc}^- \gg \text{F}^-$) can be excluded (Figure 4.10). The selectivity of mannitol derivative **1**, derived from HPTS assays decreased with increasing halide radius (*i.e.* $\text{Cl}^- > \text{Br}^- > \text{I}^-$). This halide topology is unusually rare (either of halide V, VI or VII Hofmeister series)^{8,9,42,66} and opposite to the common, dehydration-dominated Hofmeister series or halide I sequence. Binding of Cl^- ion by $\text{O}-\text{H}\cdots\text{Cl}^-$ interactions along the nanotube is responsible for the exceptional selectivity and is supported by Eisenman theory.^{56,57}

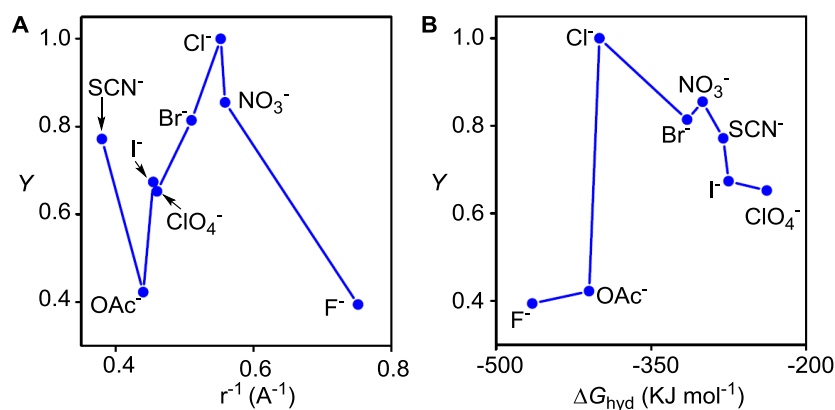


Figure 4.10. Anion selectivity of **1** determined with the HPTS assay with intravesicular Cl^- ion and varied external anions A^- . Anion selectivity presented in; fractional activity Y (relative to Cl^-) as a function of the reciprocal anion radius (A); and fractional activity Y (relative to Cl^-) as a function of the anion hydration energy (B).

4.2.4. Mass-Spectrometric Evidence of Anion Binding:

Electrospray ionization-mass spectrometric (ESI-MS) studies were carried out to obtain direct evidence of anion recognition by mannitol **1** because the technique is suitable to deliver the direct experimental evidence of weak supramolecular interactions.^{58,59} Samples were prepared in acetonitrile by mixing **1** with Me₄NCl in 2:1 molar ratio and then electrosprayed under as mild as possible ionization conditions. When data was recorded from the 2:1 molar solution, formation of the **1**₂•Cl⁻ and **1**₃•Cl⁻ adduct were detected (Figure 4.11). This results support Cl⁻ ion recognition by **1** by O–H···Cl⁻ interactions as the mannitol derivative contains no other moiety to bind the anion.

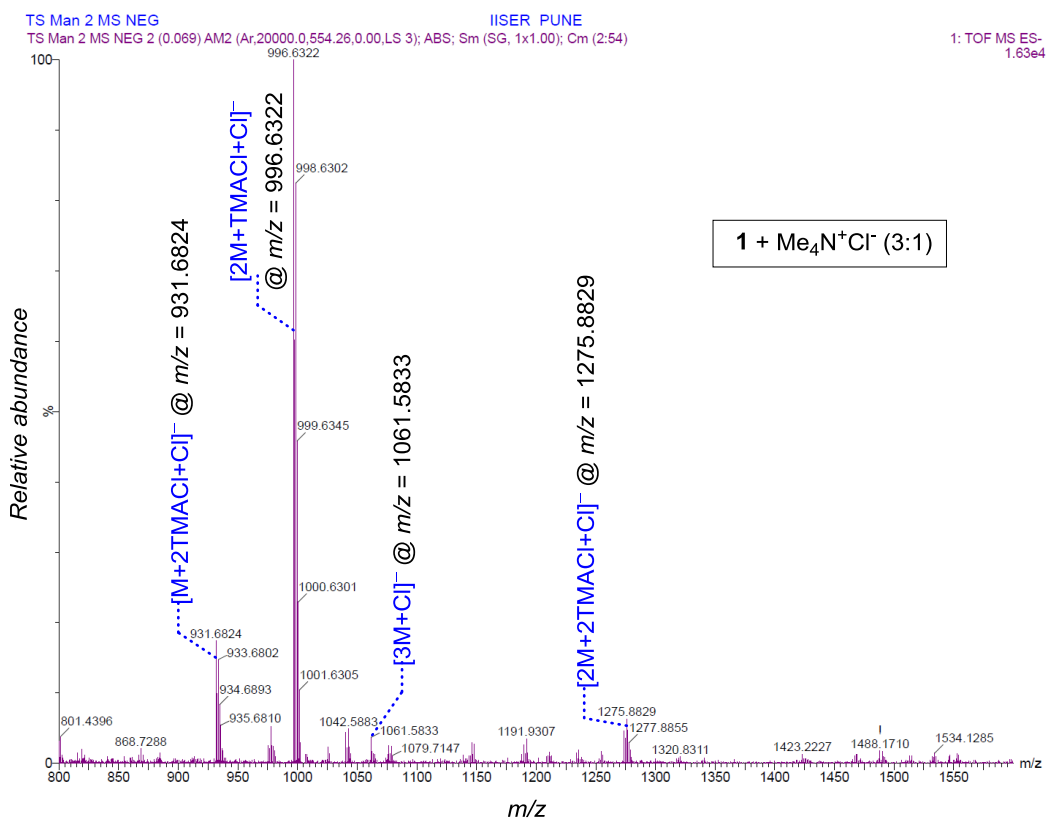


Figure 4.11. Expanded region (m/z 800 to 1600) of ESI-MS spectrum recorded from of 2:1 molar mixture of **1** and Me₄NCl prepared in acetonitrile.

4.2.5. Single Channel Conductance Measurements:

To validate the mode of ion transport of compound **1** via ion channel formation single channel conductance measurements were performed in planar lipid bilayer membrane (BLM). Distinct single channel opening and closing events were observed at different holding potentials when compound **1** was added to the *cis* chamber (Figure 4.12A and B). Single channel conductance, calculated from the all-point histogram (Figure 4.12C and D) is appeared to be about 38.1 ± 3 pS (in 1 M KCl). The diameter of artificial ion channel can also be determined by BLM measurements by applying equation 4.2, the diameter obtained is 3.06 Å. The calculated diameter is in accordance with the ionic diameter of Cl^- ion which indicates the pore diameter is sufficient for transport of Cl^- ion.

$$l / g = (l + \pi d / 4) \times (4\rho / \pi d^2) \quad \text{Equation 4.2}$$

where, g = corrected conductance (obtained by multiplying measured conductance with the Sansom's correction factor), l = length of the ion channel (34 Å) and ρ = resistivity of the recording solution ($\rho = 9.44 \Omega \cdot \text{cm}$).

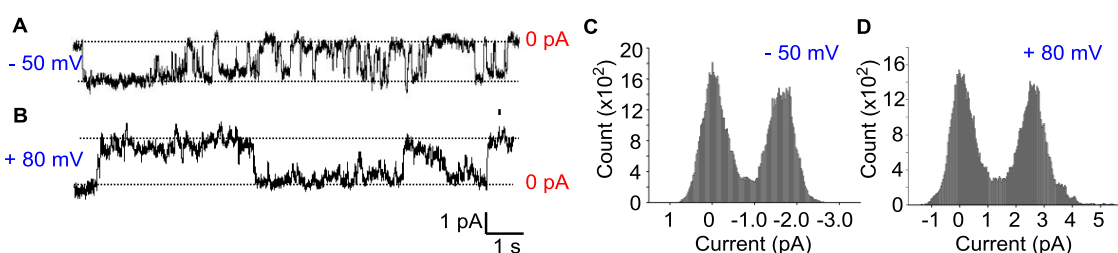


Figure 4.12. Single channel current traces recorded at -50 mV (**A**) and $+80$ mV (**B**) holding potentials in 1M symmetrical KCl solution. 0 pA at the right-hand side indicates base line current. The main conductance state is indicated by two dotted lines. All point histogram generated from the corresponding current traces at -50 mV (**C**) and $+80$ mV (**D**), respectively.

Current-voltage relationship plot (I-V plot) derived from the BLM, containing multiple channels is shown in Figure 4.13. I-V plot followed ohmic relation with symmetrical currents at negative and positive polarity when iso-osmolar concentrations of KCl were used in both the electrolyte chamber. The I-V plot was generated in asymmetrical bathing solution with a KCl gradient (1 M in *cis*: 0.5 M in *trans*) to check the ion selectivity. The +ve value of current obtained in the 0 mV applied potential in the asymmetrical electrolyte concentration, indicates the selective transport of Cl^- ion, i.e.,

anion selectivity. As shown in Figure 4.13, the reversal potential is -20 mV, which is close to the theoretically derived equilibrium potential of Cl^- (-17.8 mV), using Nernst equation. It confirms that the conducting ion is Cl^- .

$$V_r = \frac{RT}{F} \ln \frac{[\text{KCl}]_{out}}{[\text{KCl}]_{in}} \quad \text{Equation 4.3}$$

where, V_r = reversal potential; R = ideal gas constant (joules/kelvin/mole); T = temperature (kelvin); F = Faraday's constant (coulombs per mole).

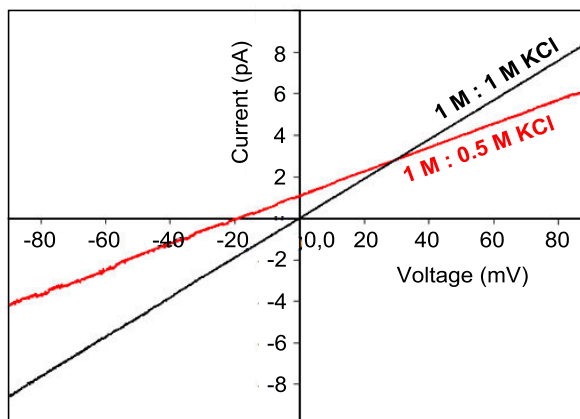


Figure 4.13. I-V plot using voltage ramp (-90 mV to $+90$ mV) in 1 M symmetrical KCl solution (black line) and in 1 M : 0.5 M KCl gradient (red line).

4.2.6. Molecular Model of ion channel:

Molecular level insight was further acquired from the computational study of the ion channel formation and passage of Cl^- ion. These studies were carried out in the laboratory of Dr. Arnab Mukherjee at IISER Pune. To create the model of the ion channel, the monomer **1** was first optimized quantum mechanically using Gaussian 09⁶⁰ software with wB97X-D⁶¹ functional and 6-31g(d) basis set. Further, a trimeric configuration was constructed from the optimized monomers. The trimeric structure was further optimized by using the same functional and basis set (Figure 4.14A). This optimized trimer was then used for the channel construction ($3 \times 3 = 3$ columns and 3 rows) by placing three trimers together followed by further optimization of the entire channel (9 monomeric unit) semi-empirically at PM6 level using MOPAC2009⁶² (Figure 4.14B). Further optimization of the trimeric channel was done with Cl^- incorporated as well (Figure 4.14C).

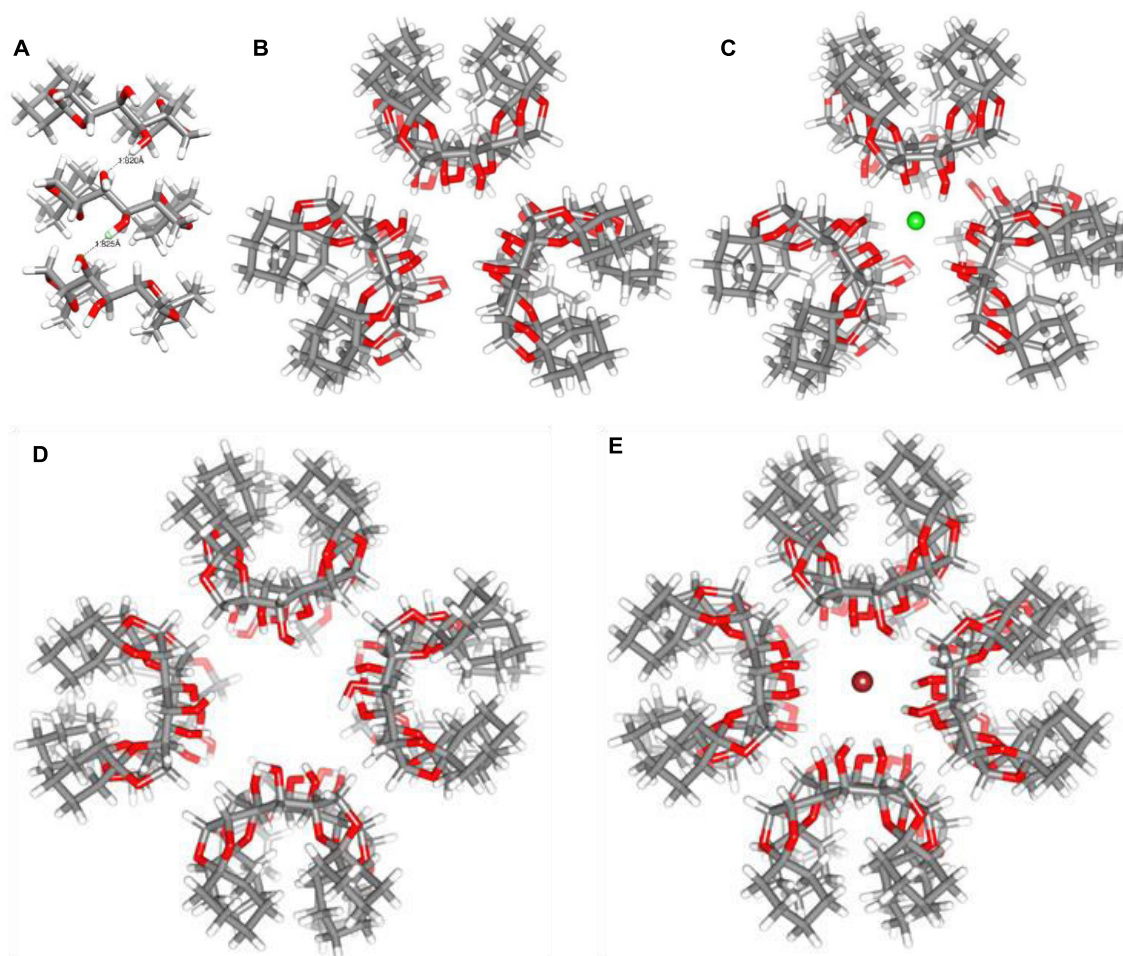


Figure 4.14. Optimized structure of trimeric fibril **1₃** using Chimera (A), optimized structures of ion channels containing nine monomers (3 × 3) without Cl⁻ ion (B) and with one Cl⁻ ion (C). Optimized structures of ion channels containing twelve monomers (4 × 3) without Br⁻ ion (D) and with one Br⁻ ion (E).

We also built a channel consisting of 12 monomeric units (4 × 3 = 4 columns and 3 rows) placing four trimers together, followed by optimization of the whole channel with (Figure 4.14E) and without (Figure 4.14D) an incorporated Br⁻ ion. The diameter of the 3 × 3 channel model was calculated to be 3.23 Å whereas the diameter of the 4 × 3 channel was 4.60 Å. The diameter of the model generated 3 × 3 channel (3.23 Å) agrees well with the channel diameter (3.06 Å) obtained from conductance measurement, which signifies the 3 × 3 channel as the active ion channel conformation in the planner lipid bilayer.

Therefore, we proceeded with 3×3 channel to construct 3×5 channel model and optimized using molecular mechanical force field of the monomer (described below). The structure of the optimized 3×5 channel with Cl^- ion is shown in Figure 4.15.

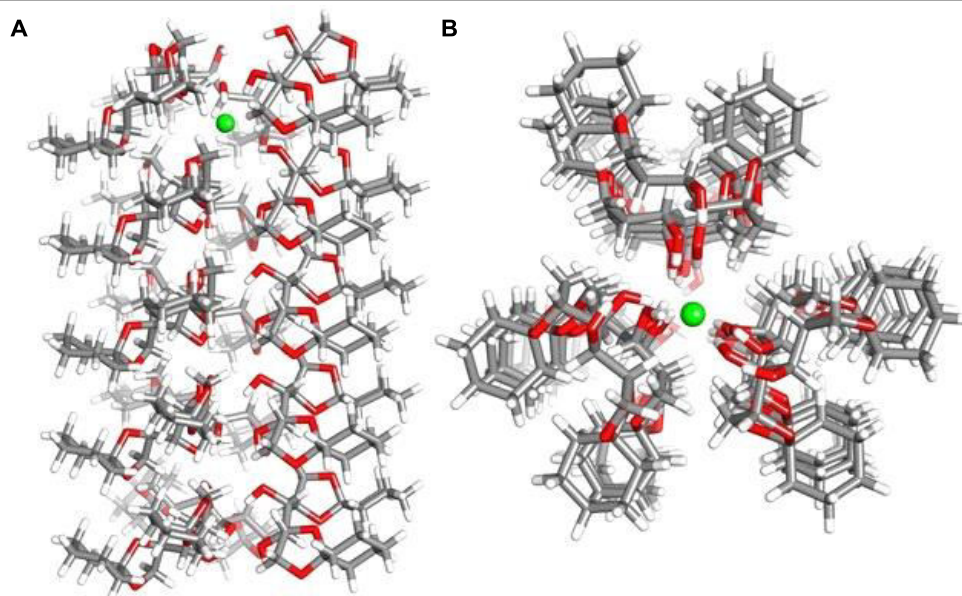


Figure 4.15. Lateral (A) and top (B) view of optimized structures of ion channels containing (3×5) monomers with Cl^- ion.

4.2.7. Free Energy Profile and Mechanism of Ion Transport:

After constructing the channel with the anion, we embedded it in a pre-equilibrated DPPC/water lipid bilayer⁶³ maintaining the ratio of the number of water molecules to the number of lipid molecules to be ~ 28 . The system consists of 94 lipid molecules and 2658 water molecules. GROMOS-53a6 united atom force field⁶⁴ was used for DPPC molecules, and SPC model⁶⁵ was used for water. The box dimension is $6.18 \times 6.18 \times 5.89 \text{ nm}^3$. One Na^+ ion was added to neutralize the system. The system was minimized and equilibrated for 500 ps restraining the channel. The equilibrated system is shown in Figure 4.16A. With the constructed and embedded channel, we performed umbrella sampling to calculate the free energy for the passage of the chloride ion through the channel. We used GROMACS⁶⁶ molecular dynamics software to carry out all the simulations. General AMBER Force-Field (GAFF)⁶⁷ for monomer was calculated by performing quantum calculation using Hartree-Fock theory and 6-31G(d) basis set using Gaussian 03.⁶⁸ AMBER tool⁶⁹ was used to construct the topology and RESP charges.

The coordinates and topology were converted to GROMACS format using amb2gmx.pl program.⁷⁰

To calculate the free energy of the ion movement along the channel, we performed a series of simulations with external harmonic potential ($1/2 k (Z - Z_0)^2$, where k is the force constant (25 kcal/mol) and Z_0 equilibrium point of the potential) to accelerate sampling of the barrier region (known as umbrella sampling simulations).⁷¹ Distance (Z) between the reference group and the chloride ion serves as the reaction coordinate. We had considered the center of mass of the bottom layer of the channel as the reference group. We performed 65 simulations by placing the center of the umbrella potential Z_0 at a separation of 0.3 Å. For each simulation, we started with the same initial configuration (Figure 4.16B), however, placing Cl^- closest to Z_0 . In each simulation, the system was simulated for 1.5 ns at constant temperature (300 K) and constant pressure (1 bar) using Nose-Hoover⁷² thermostat with a coupling constant of 0.5 ps and a Parrinello-Rahman⁷³ barostat with a coupling constant of 1 ps. The time step of each simulation was taken as 2 fs. The electrostatic interaction was treated using particle mesh Ewald⁷⁴ (PME) with a cut-off at 12 Å, and the van der Waals (vdW) cut-off was taken at 12 Å. GROMACS analysis program g_wham⁷⁵ was used to calculate the free energy using the final 1 ns simulation.

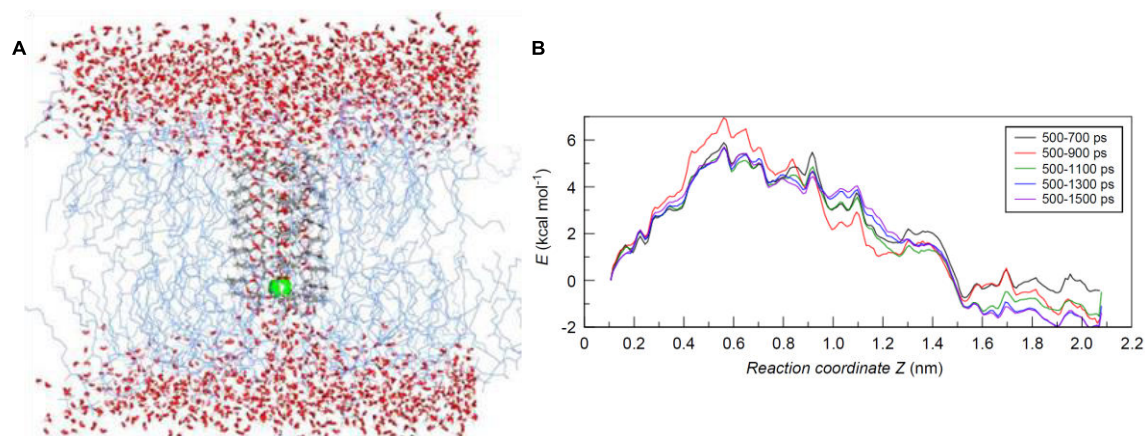


Figure 4.16. Equilibrated channel-DPPC/water system (A), free energy profile of a Cl^- ion while moving through the channel lumen (B).

Free energy profile along the channel is shown in Figure 16B. The convergence in the free energy profile is shown in Figure 16B. From the free energy profile, we conclude that the barrier to cross the channel is ~ 6.5 kcal/mol, which indicates that the rate of chloride ion passing will be in the range of ~ 10 ns to sub-microseconds. The free

energy profile is almost symmetric on both sides. Origin of the barrier is entropic because of the less mobility of the anion in the channel compared to the water layer. Moreover, less accessibility to hydrogen bonding to water also contributes to the barrier.

To understand the molecular mechanism of Cl^- ion transport across the membrane, we had calculated an average number of hydrogen bonds formed by the $-\text{OH}$ groups of each mannitol derivative with Cl^- ion from the above 65 simulations. Figure 4.17 shows the contour plot of the average value of the hydrogen bonds formed between the Cl^- and the $-\text{OH}$ group contributed by the mannitol derivatives at different layers along the reaction coordinate Z . As Z increases, Cl^- ion moves along the channel by breaking the multivalent $\text{O}-\text{H}\cdots\text{Cl}^-$ interaction in one layer and forming the same in the next, thus indicating that the transport is happening via transfer of hydrogen bonds from one rosette to the next. We observed that maximum four hydrogen bonds are made at any time. We had also noticed that the molecules are rather flexible even in the bilayer. However, each time Cl^- ion is surrounded by some monomers that primarily form hydrogen bonds to chloride through the hydroxyl group. In some cases, hydrogen bonds become less where some water molecules insert the layer and contribute to hydrogen bonding.

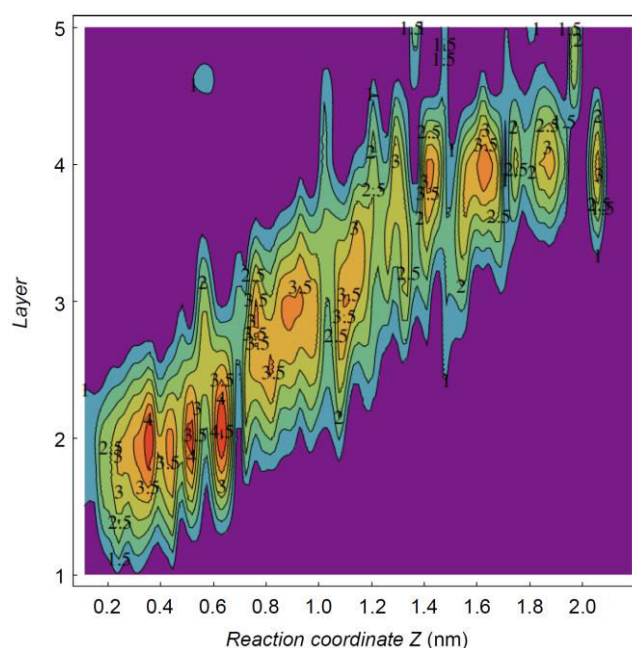


Figure 4.17. 2-D contour plot of Cl^- transport across the channel. Average number of hydrogen bonds to the Cl^- ion along the channel is shown.

However, we did not see any loss of hydrogen bonds along the path indicating that the monomers are flexible, and therefore, all along the channel they contribute to hydrogen bonding to the ion, defining a hopping mechanism at least in this case. This contour plot is in accordance with the hopping mechanism of ion transport as presented in Figure 4.1B. Whenever the Cl^- ion is in between the two consecutive rosettes of the channel, it forms a hydrogen bond with both rosettes, providing energetic stability. When the ion crosses one rosette, it comes close to the oxygen atoms of the hydroxyl groups which makes the system go through a barrier. The barrier is so small that the Cl^- ion can hop from one low energy state to another low energy state.

4.3. CONCLUSION:

In summary, artificial ion channels were designed from diketal protected mannitols **1** and **2**. Formation of a supramolecular ion channel was proposed in the lipid membranes via rosette-type self-assembly of either three or four units of the monomer and a subsequent single-file arrangement of these rosettes via hydrogen bonding interactions. Evidence of such hydrogen bonding interactions was obtained from the crystal structure of **1**, and subsequently, the possibility of anion recognition within the channel was predicted. The derivative **1**, containing cyclohexylidene groups, displayed ion transporting activity ($EC_{50} = 42.5 \mu\text{M}$) while derivative **2**, with isopropylidene groups, was inactive. A proper balance between hydrophobicity and hydrophilicity favored the incorporation of the ion channel formed by **1** into the lipid bilayer membranes. Fluorescence-based vesicle assay and planar bilayer conductance measurements confirmed selective transport of anions through the active channel. The observed selectivity was explained by the multivalent $\text{O-H}\cdots\text{A}^-$ hydrogen bonding interaction of an anion (A^-) with free $-\text{OH}$ groups of each rosette. Experimental evidence of anion recognition by **1** was also provided by mass spectrometry. Molecular dynamics (MD) simulations indicate that the trimeric channel with internal diameter 3.23 \AA is more feasible comparing with the experimental value 3.06 \AA obtained from single-channel conductance measurements. The study also indicated that the channel molecules present in a rosette surround and interact with the Cl^- ion via multiple $\text{O-H}\cdots\text{Cl}^-$ hydrogen bonding; and the movement of the ion occurs via an intermediate state where it forms hydrogen bonds with both layers, ensuring a relay mechanism.

4.4 EXPERIMENTAL SECTION:

4.4.1. General Methods.

All reagents for synthesis were commercial and used without further purification. Egg yolk phosphatidylcholine (EYPC) was obtained from Avanti Polar Lipids as a solution in CHCl_3 (25 mg/mL), HEPES buffer, HPTS, Triton X-100, NaOH and inorganic salts were of molecular biology grade from Sigma. Large unilamellar vesicles (LUV) were prepared by using mini extruder, equipped with a polycarbonate membrane of 100 nm pore size, obtained from Avanti Polar Lipids.

4.4.2. Physical Measurements.

Single Crystal X-Ray Diffraction (SCXRD) studies were done on a Bruker-KAPPA APEX II CCD diffractometer. Fluorescence spectra were recorded from Fluoromax-4 from JobinYvon Edison equipped with an injector port and a magnetic stirrer. Measurements of pH were done using a Helmer pH meter. All data from fluorescence studies were processed either by either of KaleidaGraph and Origin 8.0. Planar bilayer conductance (BLM) measurements were done on a BLM instrument from Warner Instrument, USA. High-resolution mass spectra were obtained on a MicroMass ESI-TOF MS spectrometer equipped with a Micromass Z-Spray electrospray ionization (ESI) source (Waters Co., Synapt G2, France).

4.4.3. Synthesis.

Compounds **1** and **2** were synthesized as reported.⁴⁷

4.4.4. Single Crystal X-Ray Diffraction Studies:

Crystallization of 1: To a solution of compound **1** (100 mg) in acetone (10 mL), distilled water was added in drops until the clear solution becomes slightly turbid at room temperature. The solution was left for five days undisturbed. After five days, very thin crystals (crystalline fibers) could be collected.

Crystallization of 2: 60 mg of compound **2** was dissolved in 1 mL of tetraethoxy silane (TEOS) by heating and the solution was left undisturbed for four days at room temperature. Thin fibrous crystals formed were analyzed in the single crystal XRD.

Single crystal X-ray crystallographic analysis of 1 and 2: X-ray intensity data measurements of freshly grown crystals of **1** and **2** were carried out at 298K on a Bruker-KAPPA APEX II CCD diffractometer with graphite-monochromatized ($\text{MoK} = 0.71073 \text{ \AA}$) radiation. The X-ray generator was operated at 50 kV and 30 mA. Data were collected with scan width of 0.3° at different settings of φ (0° , 90° and 180°) keeping the sample to detector distance fixed at 40 mm and the detector position (2θ) fixed at 24° . The X-ray data collection was monitored by SMART program (Bruker, 2003).^{S2} All data were corrected for Lorentzian, polarization and absorption effects using SAINT and SADABS programs (Bruker, 2003). SHELX-97 was used for structure

solution and full matrix least-squares refinement on F_2 .² All the hydrogen atoms were placed in geometrically idealized position and constrained to ride on their parent atoms [$U_{\text{iso}}(\text{H}) = 1.2U_{\text{eq}}(\text{C})$]. Molecular and packing diagrams were generated using ORTEP-3^{S3} and Mercury-3.^{S4} Geometrical calculations were performed using SHELXTL (Bruker, 2003) and PLATON.^{S5}

Crystal data of 1: CCDC 985014. $\text{C}_{18}\text{H}_{30}\text{O}_6$, $M = 342.42$, colorless blocks, $0.20 \times 0.15 \times 0.10 \text{ mm}^3$, Monoclinic, space group $C2$, $a = 21.660(2)$, $b = 5.4890(7)$, $c = 16.9869(18)\text{\AA}$, $V = 1857.9(4) \text{\AA}^3$, $Z = 4$, $T = 295(2) \text{ K}$, $2\theta_{\text{max}} = 50.00^\circ$, $D_{\text{calc}} (\text{g cm}^{-3}) = 1.224$, $F(000) = 744$, $\mu (\text{mm}^{-1}) = 0.091$, 7410 reflections collected, 3101 unique reflections ($R_{\text{int}} = 0.0389$), multi-scan absorption correction, $T_{\text{min}} = 0.9821$, $T_{\text{max}} = 0.9910$, number of parameters = 217, number of restraints = 1, $\text{GoF} = 1.068$, $R_1 = 0.0680$, $wR_2 = 0.1836$, R indices based on 2043 reflections with $I > 2s(I)$ (refinement on F_2). $\Delta\rho_{\text{max}} = 0.437$, $\Delta\rho_{\text{min}} = -0.360 (\text{e}\text{\AA}^{-3})$.

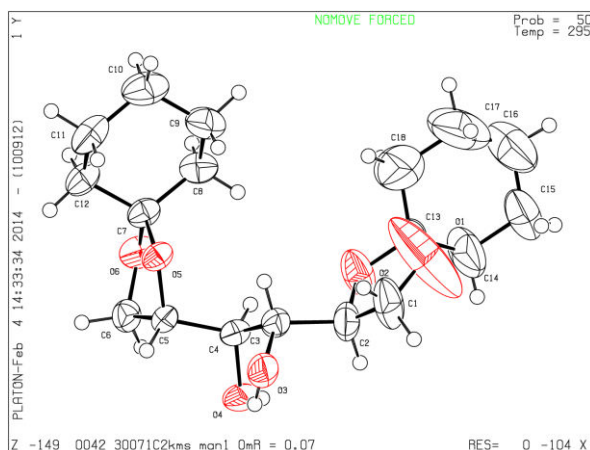


Figure 4.18. ORTEP diagram of mannitol derivative 1.

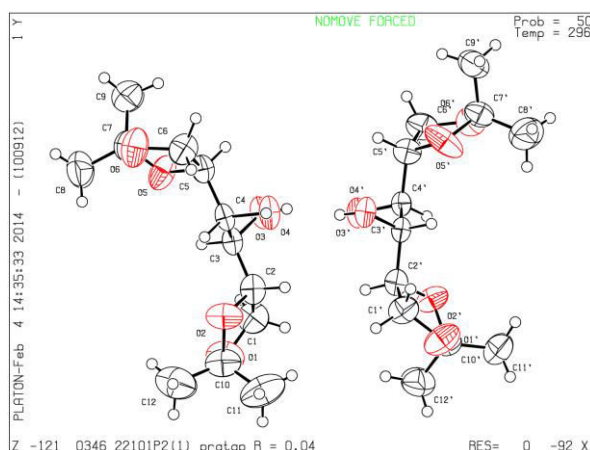


Figure 4.19. ORTEP diagram of mannitol derivative 2.

Crystal data of 2: CCDC 985015. $\text{C}_{12}\text{H}_{22}\text{O}_6$, $M = 262.30$, colorless blocks, $0.15 \times 0.15 \times 0.10 \text{ mm}^3$, Monoclinic, space group $P2(1)$, $a = 14.199(5)$, $b = 5.526(5)$, $c = 18.342(5)\text{\AA}$, $V =$

1436.5(14) Å³, $Z = 4$, $T = 293(2)$ K, $2\theta_{\max} = 50.00^\circ$, $D_{\text{calc}} (\text{g cm}^{-3}) = 1.213$, $F(000) = 568$, $\mu (\text{mm}^{-1}) = 0.097$, 11732 reflections collected, 4616 unique reflections ($R_{\text{int}} = 0.0389$), multi-scan absorption correction, $T_{\text{min}} = 0.9857$, $T_{\text{max}} = 0.9904$, number of parameters = 329, number of restraints = 1, $\text{GoF} = 1.113$, $R_1 = 0.0409$, $wR_2 = 0.1110$, R indices based on 4616 reflections with $I > 2s(I)$ (refinement on F^2). $\Delta\rho_{\max} = 0.292$, $\Delta\rho_{\min} = -0.273 (\text{e}\text{\AA}^{-3})$.

Illustration of O–H···A[−] (A[−] = anion) hydrogen bond possibilities within the nanotube: It is evident from the Figure 4.21A, that each ‘O’ atom participates in two O–H···O hydrogen bonds. If the atom $\text{O}_{4[\text{L},(i+1)]}$ (L = left M_3 unit and $i = i^{\text{th}}$ layer) is considered as the acceptor site for a hydrogen bond with the $\text{O}_{3[\text{L},(i)]}$ as donor, then it further participates as donor in the second hydrogen bond with the acceptor atom $\text{O}_{4[\text{R},(i+1)]}$ (Figure 4.21A). Similarly, the atom $\text{O}_{3[\text{R},(i+1)]}$ participates as a donor in the O–H···O hydrogen bond with $\text{O}_{3[\text{R},(i+1)]}$ and as an acceptor in the hydrogen bond with atom $\text{O}_{4[\text{R},(i+2)]}$.

As a component of the nanotubular structure, each unit of **1** offers one –OH group for provisional O–H···A[−] hydrogen bond (A[−] = anion) with an anion (Figure 4.21B). Therefore a rosette formed by three monomers can offer three –OH groups for accepting trifurcated O–H···A[−] hydrogen bonds with an anion. This types of hydrogen bond interactions can be repeated in each rosette of the $\text{M}_{n,3}$ nanotubes (Figure 4.4).

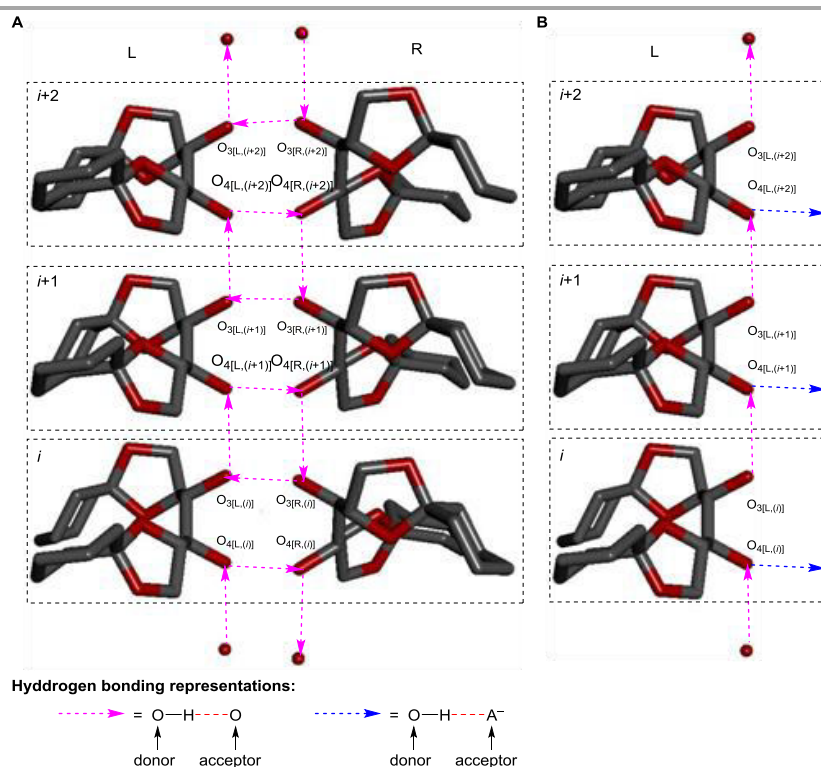


Figure 4.20. The $\text{M}_{3,2}$ (A) and M_3 (B) portions generated from the crystal structure of **1**. Here, all hydrogen atoms (C-H and O-H types) are omitted for clarity. Each O–H···O hydrogen bond

interaction is represented by pink dotted arrow and possibility of each $\text{O}-\text{H}\cdots\text{A}^-$ hydrogen bond interaction is represented by blue dotted arrow.

4.4.5. Ion Transport across Spherical Lipid Bilayer Membranes:

A. Ion transport activity through EYPC-LUVs \supset HPTS:

Study related to ion transport activity and analysis was done according to the procedure described in the previous chapter (unless mentioned in the current section).

B. Determination of Ion Selectivity by FCCP Assay:

Preparation of EYPC-LUVs \supset HPTS:

Preparation of EYPC-LUVs \supset HPTS is exactly same as mentioned above.

Selectivity study by using FCCP assay: In a clean and dry fluorescence cuvette 1975 μL of HEPES buffer (10 mM HEPES, 100 mM NaCl, pH = 7.0) was added followed by addition of 25 μL of EYPC-LUVs \supset HPTS in slowly stirring condition by a magnetic stirrer equipped with the fluorescence instrument (at $t = 0$). The time course of HPTS fluorescence emission intensity, F_t was observed at $\lambda_{\text{em}} = 510 \text{ nm}$ ($\lambda_{\text{ex}} = 450 \text{ nm}$). 20 μL of 0.5 M NaOH was added to the cuvette at $t = 20$ second to make the pH gradient between the intra and extra vesicular system. FCCP (5 μM) was added at $t = 50 \text{ s}$ (whenever necessary) and channel forming compound (20 μM) was added at $t = 100 \text{ s}$ (whenever necessary) and finally at $t = 300 \text{ s}$ 25 μL of 10% Triton X-100 was added to lyse those vesicles resulting destruction of pH gradient (Figure 4.7).

C. Determination of Ion Selectivity by Valinomycin assay:

In a clean and dry fluorescence cuvette 1975 μL of HEPES buffer (10 mM HEPES, 100 mM KCl, pH = 7.0) was added followed by addition of 25 μL of EYPC-LUVs \supset HPTS in slowly stirring condition by a magnetic stirrer equipped with the fluorescence instrument (at $t = 0$). The time course of HPTS fluorescence emission intensity, F_t was observed at $\lambda_{\text{em}} = 510 \text{ nm}$ ($\lambda_{\text{ex}} = 450 \text{ nm}$). 20 μL of 0.5 M NaOH was added to the cuvette at $t = 20$ second to make the pH gradient between the intra and extra vesicular system. Valinomycin (1 pM) was added at $t = 50 \text{ s}$ (whenever necessary) and channel forming molecule (20 μM) was added at $t = 100 \text{ s}$ (whenever necessary) and finally at $t = 300 \text{ s}$ 25 μL of 10% Triton X-100 was added to lyse those vesicles resulting destruction of pH gradient (Figure 4.8).

D. Ion selectivity studies:

Study related to ion transport activity and analysis was done according to the procedure described in the previous chapter.

4.4.6. Mass Spectrometric Studies for Anion Recognition:

The samples were prepared in acetonitrile by varying the ratio of **1** and Cl^- . Complexation of **1** and Cl^- was observed when **1** and Cl^- were mixed in 2:1 and 3:1 ratio. The samples were electrosprayed as 20 μM solutions of **1** and Me_4NCl (TMACl) in acetonitrile at flow rates of 0.4 mL/min. A constant spray and highest intensities were achieved with a capillary voltage of 3000 V at a source temperature of 80 °C. The parameters for sample cone (40 V) and extractor cone voltage (5 V) were optimized for maximum intensities of the desired complexes. Figure 4.11 represents the ESI-MS data recorded from acetonitrile solution of **1** with TMACl prepared in 2:1 molar ratio. From the spectrum, signals corresponding to $[\text{M}+\text{TMACl}+\text{Cl}]^-$, $[2\text{M}+\text{Cl}]^-$, $[\text{M}+2\text{TMACl}+\text{Cl}]^-$ and $[2\text{M}+\text{TMACl}+\text{Cl}]^-$ were detected (where, M = exact mol. weight of **1**).

4.4.7. Planar Bilayer Conductance Measurements:

Bilayer membrane (BLM) was formed across an aperture of 150 μM diameter in a polystyrene cup (Warner Instrument, USA) with lipid diphytanoylphosphatidylcholine (DPhPC; Avanti Polar Lipids), dissolved in *n*-decane (20 mg/mL). Both *cis* and *trans* compartments were filled with symmetrical solution, containing 1 M KCl, and 10 mM HEPES (pH 7.0). For ion selectivity experiment, a gradient of 1 : 0.5 M KCl was used. The *cis* compartment was held at virtual ground, and the *trans* chamber was connected to the PC 501A head-stage (Warner Instrument, USA) via matched Ag-AgCl electrodes. Mannitol derivative **1** was added to the *cis* chamber, and the solution was stirred with magnetic stirrer. It formed channels within 5 minutes, as observed by the distinct channel opening and closing events at different voltages. Currents were low-pass filtered at 1 kHz and digitized at 5 kHz using pClamp9 software (Molecular Probes, USA) and an analog-to-digital converter (Digidata 1322A, Molecular Probes). Positive clamping potentials refer potentials with respect to the ground, and positive currents are presented as upward deflections from the base line (0 pA). The software pClamp 9 was used for data acquisition and analysis. I-V curve was generated from the BLM, containing multiple channels using a voltage ramp from -90 mV to +90 mV. To check the ion selectivity, a KCl gradient of 1 M : 0.5 M (*cis*: *trans*) was used.

4.5 REFERENCE:

- (1) Hille, B.; Schwarz, W. J. *Gen. Physiol.* **1978**, 72, 409.
- (2) Miller, C. J. *Gen. Physiol.* **1999**, 113, 783.
- (3) Hille, B. *Ionic Channels of Excitable Membranes*, 3rd Edition, 2001.
- (4) Keramidas, A.; Moorhouse, A. J.; Schofield, P. R.; Barry, P. H. *Prog. Biophys. Mol. Biol.* **2004**, 86, 161.
- (5) Gouaux, E.; MacKinnon, R. *Science* **2005**, 310, 1461.
- (6) Corry, B.; Chung, S. H. *Cell. Mol. Life Sci.* **2006**, 63, 301.

- (7) Tsien, R. W.; Hess, P.; McCleskey, E. W.; Rosenberg, R. L. *Annu. Rev. Biophys. Biophys. Chem.* **1987**, *16*, 265.
- (8) Doyle, D. A.; Cabral, J. M.; Pfuetzner, R. A.; Kuo, A.; Gulbis, J. M.; Cohen, S. L.; Chait, B. T.; MacKinnon, R. *Science* **1998**, *280*, 69.
- (9) Yamashita, A.; Singh, S. K.; Kawate, T.; Jin, Y.; Gouaux, E. *Nature* **2005**, *437*, 215.
- (10) Toyoshima, C.; Nakasako, M.; Nomura, H.; Ogawa, H. *Nature* **2000**, *405*, 647.
- (11) Dutzler, R.; Campbell, E. B.; MacKinnon, R. *Science* **2003**, *300*, 108.
- (12) Tedesco, M. M.; Ghebremariam, B.; Sakai, N.; Matile, S. *Angew. Chem. Int. Ed.* **1999**, *38*, 540.
- (13) Ishida, H.; Qi, Z.; Sokabe, M.; Donowaki, K.; Inoue, Y. *J. Org. Chem.* **2001**, *66*, 2978.
- (14) Bong, D. T.; Clark, T. D.; Granja, J. R.; Ghadiri, M. R. *Angew. Chem., Int. Ed.* **2001**, *40*, 988.
- (15) Sánchez-Quesada, J.; Isler, M. P.; Ghadiri, M. R. *J. Am. Chem. Soc.* **2002**, *124*, 10004.
- (16) Fernandez-Lopez, S.; Kim, H.-S.; Choi, E. C.; Delgado, M.; Granja, J. R.; Khasanov, A.; Kraehenbuehl, K.; Long, G.; Weinberger, D. A.; Wilcoxon, K. M.; Ghadiri, M. R. *Nature* **2001**, *412*, 452.
- (17) Clark, T. D.; Buehler, L. K.; Ghadiri, M. R. *J. Am. Chem. Soc.* **1998**, *120*, 651.
- (18) Ghadiri, M. R.; Granja, J. R.; Buehler, L. K. *Nature* **1994**, *369*, 301.
- (19) Forman, S. L.; Fettingner, J. C.; Pieraccini, S.; Gottarelli, G.; Davis, J. T. *J. Am. Chem. Soc.* **2000**, *122*, 4060.
- (20) Sakai, N.; Kamikawa, Y.; Nishii, M.; Matsuoka, T.; Kato, T.; Matile, S. *J. Am. Chem. Soc.* **2006**, *128*, 2218.
- (21) Hennig, A.; Matile, S. *Chirality* **2008**, *20*, 932.
- (22) Pedersen, C. J. *J. Am. Chem. Soc.* **1967**, *89*, 2495.
- (23) Pedersen, C. J. *J. Am. Chem. Soc.* **1967**, *89*, 7017.
- (24) Winum, J.-Y.; Matile, S. *J. Am. Chem. Soc.* **1999**, *121*, 7961.
- (25) Cazacu, A.; Tong, C.; van der Lee, A.; Fyles, T. M.; Barboiu, M. *J. Am. Chem. Soc.* **2006**, *128*, 9541.
- (26) Boudreault, P.-L.; Voyer, N. *Org. Biomol. Chem.* **2007**, *5*, 1459.
- (27) Sakai, N.; Brennan, K. C.; Weiss, L. A.; Matile, S. *J. Am. Chem. Soc.* **1997**, *119*, 8726.
- (28) Weiss, L. A.; Sakai, N.; Ghebremariam, B.; Ni, C.; Matile, S. *J. Am. Chem. Soc.* **1997**, *119*, 12142.
- (29) Ni, C.; Matile, S. *Chem. Commun.* **1998**, 755.
- (30) Sakai, N.; Majumdar, N.; Matile, S. *J. Am. Chem. Soc.* **1999**, *121*, 4294.
- (31) Gorteau, V.; Bollot, G.; Mareda, J.; Perez-Velasco, A.; Matile, S. *J. Am. Chem. Soc.* **2006**, *128*, 14788.
- (32) Gorteau, V.; Bollot, G.; Mareda, J.; Matile, S. *Org. Biomol. Chem.* **2007**, *5*, 3000.

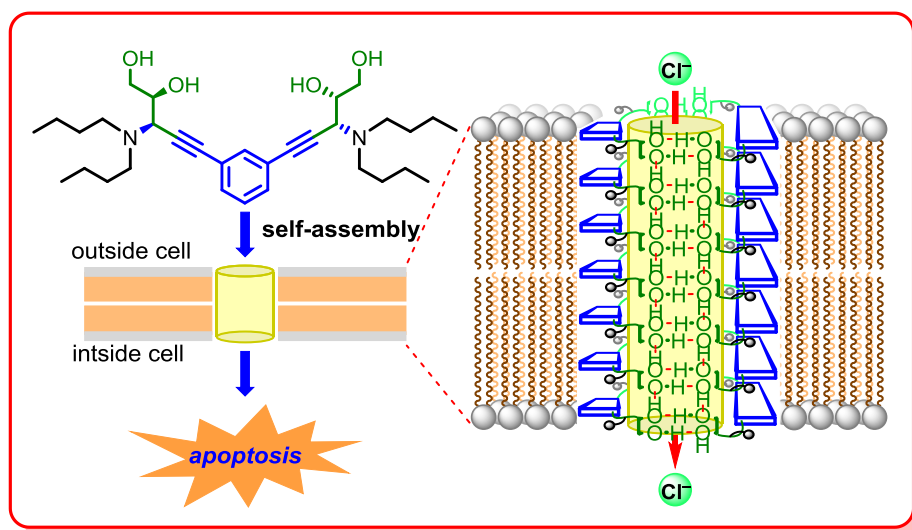
- (33) Perez-Velasco, A.; Gorteau, V.; Matile, S. *Angew. Chem., Int. Ed.* **2008**, *47*, 921.
- (34) Wojcik, J. F.; Rohrbach, R. P. *Journal of Physical Chemistry* **1975**, *79*, 2251.
- (35) Pelizzi, N.; Casnati, A.; Ungaro, R. *Chem. Commun.* **1998**, 2607.
- (36) Davis, A. P.; Perry, J. J.; Wareham, R. S. *Tetrahedron Lett.* **1998**, *39*, 4569.
- (37) Hayashida, O.; Kato, M.; Akagi, K.; Aoyama, Y. *J. Am. Chem. Soc.* **1999**, *121*, 11597.
- (38) Arduini, A.; Giorgi, G.; Pochini, A.; Secchi, A.; Ugozzoli, F. *J. Org. Chem.* **2001**, *66*, 8302.
- (39) Miyaji, H.; Sessler, J. L. *Angew. Chem., Int. Ed.* **2001**, *40*, 154.
- (40) Tong, H.; Zhou, G.; Wang, L.; Jing, X.; Wang, F.; Zhang, J. *Tetrahedron Lett.* **2003**, *44*, 131.
- (41) Sessler, J. L.; Gale, P. A.; Cho, W.-S. In *Anion Receptor Chemistry (Monographs in Supramolecular Chemistry)*; Stoddart, J. F., Ed.; RSC: Cambridge, 2006; pp 205–210.
- (42) Yamashita, K.; Janout, V.; Bernard, E.; Armstrong, D.; Regen, S. L. *J. Am. Chem. Soc.* **1995**, *117*, 6249.
- (43) Koenig, K. E.; Lein, G. M.; Stuckler, P.; Kaneda, T.; Cram, D. J. *J. Am. Chem. Soc.* **1979**, *101*, 3553.
- (44) Clare, J. P.; Ayling, A. J.; Joos, J.-B.; Sisson, A. L.; Magro, G.; Pérez-Payán, M. N.; Lambert, T. N.; Shukla, R.; Smith, B. D.; Davis, A. P. *J. Am. Chem. Soc.* **2005**, *127*, 10739.
- (45) Davis, A. P.; Gilmer, J. F.; Perry, J. J. *Angew. Chem., Int. Ed.* **1996**, *35*, 1312.
- (46) Ashokkumar, P.; Ramakrishnan, V. T.; Ramamurthy, P. *ChemPhysChem* **2011**, *12*, 389.
- (47) Vidyasagar, A.; Handore, K.; Sureshan, K. M. *Angew. Chem., Int. Ed.* **2011**, *50*, 8021.
- (48) Sakai, N.; Matile, S. *J. Phys. Org. Chem.* **2006**, *19*, 452.
- (49) Talukdar, P.; Bollot, G.; Mareda, J.; Sakai, N.; Matile, S. *J. Am. Chem. Soc.* **2005**, *127*, 6528.
- (50) Sakai, N.; Matile, S. *J. Am. Chem. Soc.* **2003**, *125*, 14348.
- (51) Lipinski, C. A.; Lombardo, F.; Dominy, B. W.; Feeney, P. J. *Adv. Drug Deliv. Rev.* **1997**, *23*, 3.
- (52) Qu, Z.; Hartzell, H. C. *J. Gen. Physiol.* **2000**, *116*, 825.
- (53) Sakai, N.; Gerard, D.; Matile, S. *J. Am. Chem. Soc.* **2001**, *123*, 2517.
- (54) Benz, R.; McLaughlin, S. *Biophys. J.* **1983**, *41*, 381.
- (55) Rose, L.; Jenkins, A. T. A. *Bioelectrochemistry* **2007**, *70*, 387.
- (56) Wright, E. M.; Diamond, J. M. *Physiol. Rev.* **1977**, *57*, 109.
- (57) Eisenman, G.; Horn, R. *J. Membrane Biol.* **1983**, *76*, 197.
- (58) Kogej, M.; Schalley, C. A. *Anal. Method. Supramol. Chem.* **2007**, 104.
- (59) Dawson, R. E.; Hennig, A.; Weimann, D. P.; Emery, D.; Ravikumar, V.; Montenegro, J.; Takeuchi, T.; Gabutti, S.; Mayor, M.; Mareda, J.; Schalley, C. A.; Matile, S. *Nat. Chem.* **2010**, *2*, 533.

- (60) Frisch M. J., Trucks G. W., Schlegel H. B., Scuseria G. E., Robb M. A., Cheeseman J. R., Scalmani G., Barone V., Mennucci B., Petersson G. A., Nakatsuji H., Caricato M., Li X., Hratchian H. P., Izmaylov A. F., Bloino J., Zheng G., Sonnenberg J. L., Hada M., Ehara M., Toyota K., Fukuda R., Hasegawa J., Ishida M., Nakajima T., Honda Y., Kitao O., Nakai H., Vreven T., Montgomery J. A., Jr., Peralta J. E., Ogliaro F., Bearpark M., Heyd J. J., Brothers E., Kudin K. N., Staroverov V. N., Keith T., Kobayashi R., Normand J., Raghavachari K., Rendell A., Burant J. C., Iyengar S. S., Tomasi J., Cossi M., Rega N., Millam J. M., Klene M., Knox J. E., Cross J. B., Bakken V., Adamo C., Jaramillo J., Gomperts R., Stratmann R. E., Yazyev O., Austin A. J., Cammi R., Pomelli C., Ochterski J. W., Martin R. L., Morokuma K., Zakrzewski V. G., Voth G. A., Salvador P., Dannenberg J. J., Dapprich S., Daniels A. D., Farkas O., Foresman J. B., Ortiz J. V., Cioslowski J., and Fox D. J. Gaussian 09, Revision B.01, Gaussian, Inc., Wallingford CT, **2010**.
- (61) Chai, J.-D.; Head-Gordon, M. *Phys. Chem. Chem. Phys.* **2008**, *10*, 6615.
- (62) Stewart J. J. P. MOPAC2009, Version 11.366L; Stewart Computational Chemistry, Colorado Springs, CO, 2009; <http://OpenMOPAC.net>.
- (63) Pandey, P. R.; Roy, S. *J. Phys. Chem. B* **2011**, *115*, 3155.
- (64) Oostenbrink, C.; Villa, A.; Mark, A. E.; van Gunsteren, W. F. *J. Comput. Chem.* **2004**, *25*, 1656.
- (65) Berendsen, H. J. C.; Postma, J. P. M.; van Gunsteren, W. F.; Hermans, J. Interaction Models for Water in Relation to Protein Hydration. In *Intermolecular Forces*; Pullman, B., Ed.; Reidel: Dordrecht, 1981; pp 331–342.
- (66) Hess, B.; Kutzner, C.; van der Spoel, D.; Lindahl, E. *J. Chem. Theory Comput.* **2008**, *4*, 435.
- (67) Wang, J.; Wolf, R. M.; Caldwell, J. W.; Kollman, P. A.; Case, D. A. *J. Comput. Chem.* **2004**, *25*, 1157.
- (68) Frisch, M. J. et al.. Gaussian 03, Revision E.01; Gaussian, Inc., Wallingford CT, 2004.
- (69) Case, D. A.; Cheatham, T. E., III; Darden, T.; Gohlke, H.; Luo, R.; Merz, K. M., Jr.; Onufriev, A.; Simmerling, C.; Wang, B.; Woods, R. J. *J. Comput. Chem.* **2005**, *26*, 1668.
- (70) Sorin, E. J.; Pande, V. S. *Biophys. J.* **2005**, *88*, 2472.
- (71) Torrie, G. M.; Valleau, J. P. *Chem. Phys. Lett.* **1974**, *28*, 578.
- (72) Nose, S. *Mol. Phys.* **1984**, *52*, 255.
- (73) Parrinello, M.; Rahman, A. *J. Appl. Phys.* **1981**, *52*, 7182.
- (74) Darden, T.; York, D.; Pedersen, L. *J. Chem. Phys.* **1993**, *98*, 10089.
- (75) Hub, J. S.; de Groot, B. L.; van der Spoel, D. *J. Chem. Theory Comput.* **2010**, *6*, 3713.

End of Chapter 4

Chapter 5

Chloride Transport through Supramolecular Barrel-Rosette Ion Channels: Lipophilic Control and Apoptosis-Inducing Activity



5.1. INTRODUCTION:

The robust chemical nature and adaptable ion transport behavior with the aid of structural manipulation have made artificial ion transport systems a convenient subject of research, compared to their natural congeners. Recently, the introduction of artificial ion channels as the “channel replacement therapy,” has instigated as a novel combination treatment modality for targeting diseases associated with ion channel dysfunction.^{1,2} However, the examples related to direct bio-applicability of synthetic ion channels are still rare. The crown ether based unimolecular hydrophile channels, reported by Gokel^{3,4} and cyclic peptide based self-assembled ion channels reported by Ghadiri⁵ had shown promising antibacterial activity by collapsing the transmembrane ion potential of bacteria by transporting cations. Few crown ether based hydrophile channels, reported by Gokel and Voyer, facilitate cation transport into cells resulting in the cancer cell death via necrotic pathway.⁶⁻⁸ Recent studies on synthetic chloride ion carriers reveal that selective transport of the ion induces apoptosis in cancer cells by either changing the pH or destroying the ionic homeostasis of cells.⁹⁻¹⁴ Therefore, an ion channel, selective for chloride ion transport, can be a judicious choice for apoptosis-inducing cell death studies.

Furthermore, the mannitol derivative based barrel-rosette ion channel, described in previous chapter, suffers the limitation related to selectivity because of dynamic self-assembly. Though the presence of multiple ion recognition sites induces the exclusive anion selectivity, the competitive transport among anion is somehow compromised as the channel can adopt a higher order structure in the presence of larger anion (Figure 5.1B). For example, the channel forming mannitol derivative **1**, described in the previous chapter can adopt the tetrameric structure $M_{4,n}$ in the presence of Br^- ion (Figure 5.1B). Herein, we had focused on modifying the mode of self-assembly to get a more rigid macromolecular structure, where self-assembly of the building unit became unaffected by the size of the anion. In addition to that, tuneable transport of anion was not achieved in the previous system. Barrel-rosette ion channel with tuneable ion transport activity would be a nice objective of the study. Therefore, combining all the requirements, the introduction of an artificial barrel-rosette type ion channel having distinct

bio-applicability by means of selective and tuneable transport of chloride ion is the prime importance of this chapter. Herein, we report a self-assembled barrel-rosette ion channel system constructed by hydrogen bonded network of vicinal diol moieties present at two termini of each monomer. The system portrays tuneable ion transport activity achieved by changing the lipophilicity of molecules. These ion channels exhibited Cl^- selective ion transport across lipid membranes, and such transport of Cl^- ion into the cells triggered the activation of caspase-dependent apoptotic pathways of cell death.

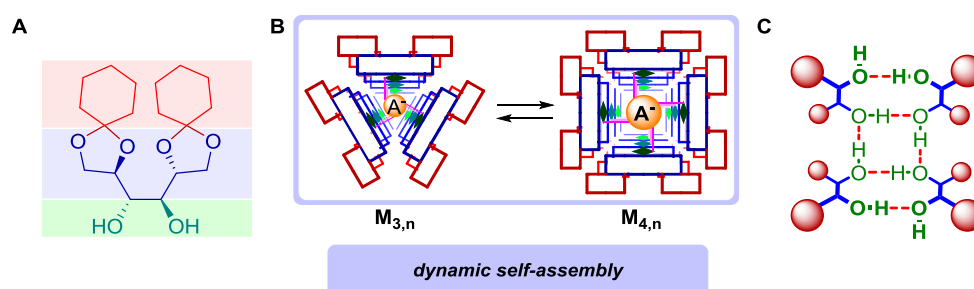


Figure 5.1. The structure of building unit of barrel-rosette ion channel described in the previous chapter (A), representation of dynamic self-assembly in the presence of anions of varying size (B), hydrogen bonding pattern of mannitol derivatives along the fibril structure (C).

The partitioning of ion transport systems into the lipid membranes and hence, the ion transport property, are affected significantly by their lipophilicity. Tuning of ion transport properties based on lipophilicity was extensively studied for ion carriers but neglected mostly in the synthetic ion channel design.¹⁵⁻¹⁷ Abide by the lipophilicity-permeability correlation; we designed monomers **1a** – **1d** for the barrel-rosette ion channel construction (Figure 5.2A). In each molecule, two vicinal diol groups were tethered at two alkyne ends of a central rigid 1,3-diethynylbenzene moiety, for avoiding intramolecular hydrogen bonding interactions and ensuring definite cavity. According to Lipinski's rule,¹⁸ the logP (*i.e.* partition coefficient in octanol-water) value of five is optimum for permeation in the lipid membranes. Therefore, a dialkylamino group was incorporated between each diol and alkyne moiety to vary the amphiphilicity of designed molecules. For monomers **1a** – **1d** logP = 16.25, 9.13, 5.53 and 1.71 were calculated using MarvinSketch program¹⁹ by varying R = $-\text{C}_{10}\text{H}_{21}$, $-\text{C}_6\text{H}_{13}$, $-\text{C}_4\text{H}_9$ and $-\text{C}_2\text{H}_5$, respectively (Figure 5.2B). To ensure the stereospecificity around each α -amino alcohol moiety, we planned the synthesis based on our previous report on diastereoselective aldehyde-amine-alkyne three-component (A^3 -coupling) reaction.^{20,21} The A^3 -coupling

reaction is also adaptable to the introduction of various $-NR_2$ groups in these molecules. We anticipated, in the line of our previous report (Figure 5.1C),²² that each terminal vicinal diol group of a monomer **M** would participate in hydrogen bonding interactions with a complementary vicinal diol group of a neighboring molecule to form a dimer **M**₂ as a representative of cyclic rosette structure (Figure 5.2C). Accessibility of interlayer hydrogen bonding interactions of consecutive **M**₂ dimers would engender to a higher order supramolecular nanotubular architecture **M**_{2,n} which upon permeation into the lipid bilayer membrane would form an ion channel. Overall the nanotubular structure can be viewed as a barrel structure formed by the stacking of dimeric rosettes providing a hydrophilic path for ion transport. The aliphatic chains at the external surface of the nanotubular architecture would impose additional thermodynamic stability to the channel structure for anchoring it at the hydrophobic layer of membrane.

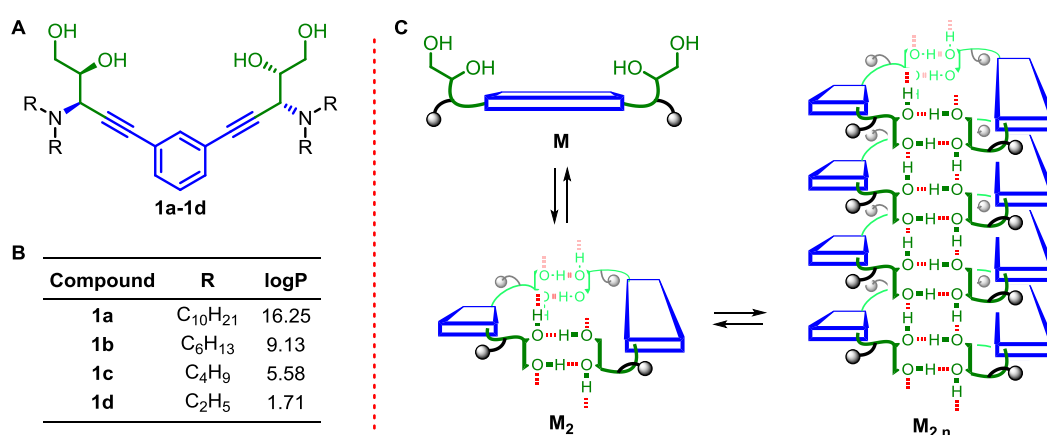


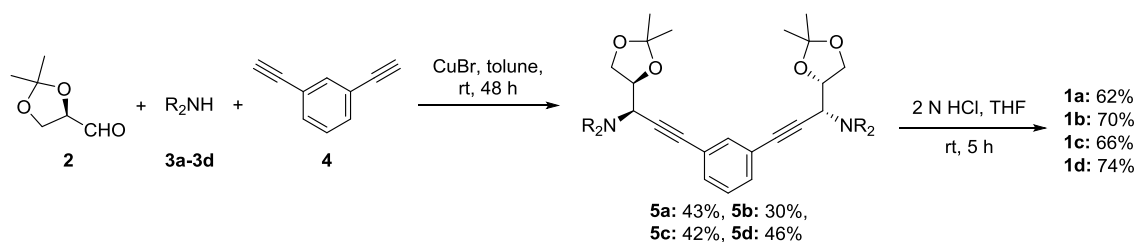
Figure 5.2. The structure of designed channel forming molecules **1a–1d** (A); lipophilicity (logP values) of the channel forming molecules with different alkyl substitution (B); mode of self-assembly of the channel forming molecules (C).

5.2 RESULTS AND DISCUSSIONS:

5.2.1. Synthesis:

Synthesis of compounds **1a – 1d** is described in Scheme 5.1. At first, the compound **2** was synthesized according to the reported procedure.²³ The subsequent multicomponent reaction of (*R*)-(+)-glyceraldehyde acetonide **2** with dialkylamines **3a–3d**, and 1,3-diethynylbenzene **4** in the presence of CuBr catalyst gave corresponding bis(acetonide) derivatives **5a–5d**. Acid catalyzed deportation of terminal acetonides provided final compounds **1a – 1d**. All compounds were purified by column

chromatography and characterized by $^1\text{H-NMR}$, $^{13}\text{C-NMR}$, HRMS, and IR (see experimental section for detailed experiments and characterization).



Scheme 5.1. Synthesis of derivative **1a–1d**.

5.2.2. Ion Transport Activity of **1a – 1d**:

The ion transport activity of bis(diol) derivatives **1a – 1d** across EYPC-LUVs \square HPTS was recorded by the fluorimetric method. Large unilamellar vesicles (LUVs) were prepared by entrapping the pH-sensitive dye, 8-hydroxypyrene-1,3,6-trisulfonate (HPTS, $pK_a = 7.2$) and a pH gradient was applied by the addition of NaOH (*i.e.* $\Delta\text{pH} = 0.8$) in the extravesicular buffer. The rate of change in the fluorescence intensity was monitored after addition of **1a – 1d** separately. Measurement of concentration dependent ion transport activity of compounds **1a – 1d** (Figure 5.3A–D) followed by Hill analyses also revealed the activity sequence of **1c** ($EC_{50} = 2.7 \pm 0.1 \mu\text{M}$) > **1b** ($EC_{50} = 3.3 \pm 0.3 \mu\text{M}$) > **1d** ($EC_{50} = 28.3 \pm 4.9 \mu\text{M}$) > **1a** ($EC_{50} = 38.5 \pm 4.9 \mu\text{M}$) (Figure 5.3E–H). The concentration dependent plot for all compounds also showed similar activity sequence as observed from EC_{50} values **1c** > **1b** > **1a** > **1d** (Figure 5.3I). The maximum activity of **1c** corroborated to its $\log P = 5.58$, the most optimum among designed bis(diol) derivatives, for efficient translocation of the molecule into phospholipids bilayer.¹⁸ The decreasing transport activity order **1c** > **1b** >> **1a** was associated with the increase in $\log P$ values upon increasing the length of alkyl chain contributing to the poorer water solubility of **1b** and **1a**. The lower activity of **1d**, on the other hand, was the result of a decrease $\log P$ value 1.71, which indicates to its higher water solubility compared to **1c**. The Hill coefficient $n \sim 2$, obtained for each compound, signified the dimer M_2 as the active rosette structure for the supramolecular nanochannel assembly.

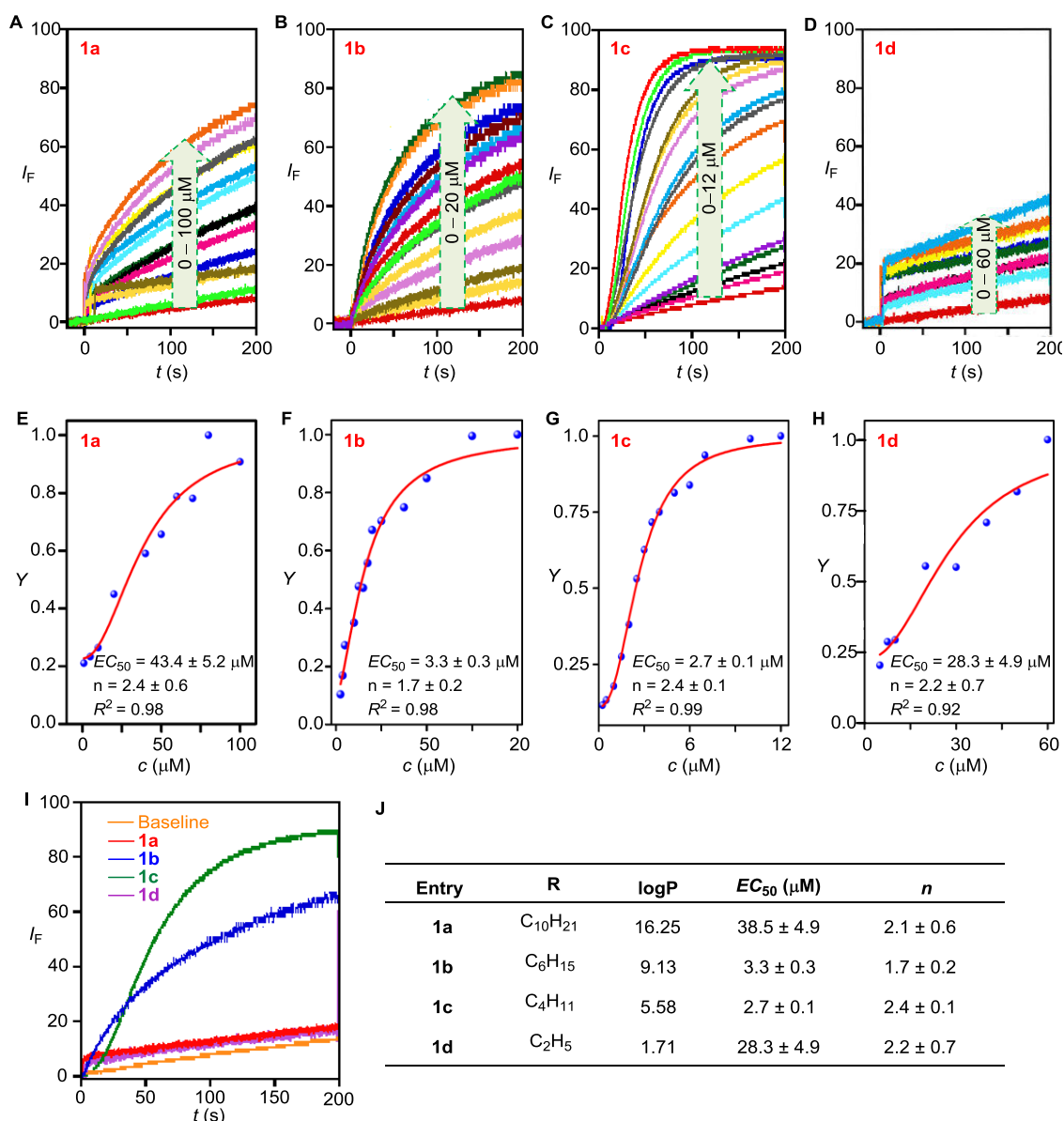


Figure 5.3. Concentration-dependent activity of **1a** (A), **1b** (B), **1c** (C), **1d** (D) across EYPC-LUVs>HPTS; Hill analysis of dose-response plot of **1a** (E), **1b** (F), **1c** (G), **1d** (H) at 100 s after addition of compound. Comparison of ion transport activities of derivatives **1a** – **1d** across EYPC-LUVs>HPTS at 5 μM concentration (I). Correlation table for calculated logP values with determined EC_{50} and Hill coefficients (n) values of **1a-1d** (J).

5.2.3. Ion Selectivity in EYPC-LUVs \supset HPTS:

The pronounced ion transport activity of **1c** prompted us to investigate the ion selectivity of this channel forming a molecule. Ion selectivity of **1c** ($c = 3 \mu\text{M}$) was screened with EYPC-LUVs \supset HPTS by varying either the cation, M^+ (where $\text{M}^+ = \text{Li}^+$, Na^+ , K^+ , Rb^+ , and Cs^+) or the anion, A^- (where $\text{A}^- = \text{F}^-$, Cl^- , Br^- , I^- , NO_3^- and ClO_4^-) in the extravesicular buffer. Variation of cations provided a little difference in the ion transport rate suggesting the minor contribution of cations in the transport process (Figure 5.4A). However, the change of anion resulted in the activity sequence: $\text{Cl}^- \gg \text{Br}^- \sim \text{ClO}_4^- > \text{F}^- \sim \text{NO}_3^- > \text{I}^-$ (Figure 4B). A significant difference in the rate of change of ion transport activity signifies the involvement of anion in the rate limiting step of the transport process. The observed increase of intravesicular pH upon addition of **1c** assumed either via antiport (*i.e.* either OH^-/A^- or H^+/M^+ where A^- and M^+ are cations and anions) or symport (*i.e.* either H^+/A^- or M^+/OH^-) as the ion transport mechanism. The anion selectivity of **1c** suggested to either OH^-/A^- antiport or H^+/A^- symport as the ion transport mechanism through the channel. Confirmation of anion selectivity was achieved by recording the ion transport activity of **1c** in presence and absence of a proton transporter, carbonyl cyanide-4-(trifluoromethoxy)-phenylhydrazone (FCCP).²⁴ Identification of the predominant mechanism of ion transport between H^+/M^+ antiport ($\text{M}^+ = \text{monovalent metal cation}$), OH^-/A^- ($\text{A}^- = \text{monovalent anion}$) or H^+/A^- symport can be determined by this experiment.²²

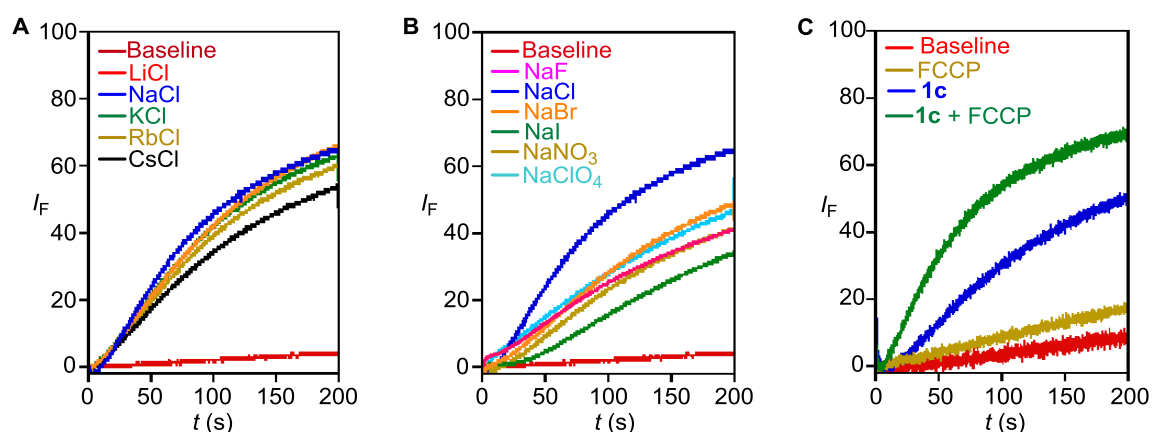


Figure 5.4. Ion transport activity of **1c** ($c = 3 \mu\text{M}$) across EYPC-LUVs \supset HPTS determined by varying cations (**A**) and anions (**B**) in the extravesicular buffer. Ion transport activity of **1c** ($2.5 \mu\text{M}$) in presence and absence of FCCP ($2 \mu\text{M}$) across EYPC-LUVs \supset HPTS (**C**).

The transport activity of **1c** was found to be enhanced almost two-fold in the presence of FCCP indicating the cooperative effect of **1c** and FCCP to enhance the intravesicular pH (Figure 5.4C). More efficient equilibration of the applied pH gradient by **1c**, in the presence of FCCP,²⁴ endorsed the OH^-/A^- antiport as the preferred ion transport mechanism (Figure 5.4C).

5.2.4. Chloride Ion Transport Assay:

Subsequently, the selective transport of Cl^- by **1c** across EYPC-LUVs was studied by monitoring the change in fluorescence of entrapped lucigenin, a Cl^- selective fluorescent dye at $\lambda_{\text{em}} = 535 \text{ nm}$ ($\lambda_{\text{ex}} = 450 \text{ nm}$). EYPC-LUVs \supset lucigenin were prepared by entrapping lucigenin dye (1 mM) in NaNO_3 solution (200 mM). Subsequently, a $\text{Cl}^-/\text{NO}_3^-$ gradient was applied by the addition of a concentrated solution of NaCl in the extravesicular buffer (Figure 5.5A). The quenching in fluorescence intensity of lucigenin by diffusion mediated collisional quenching method in the presence of Cl^- ion had been used in this study.²⁵ Quenching of lucigenin fluorescence due to the influx of Cl^- ion by ion channel was monitored with time. Finally, Triton X-100 was added to get the complete quenching of lucigenin fluorescence (Figure 5.5B).

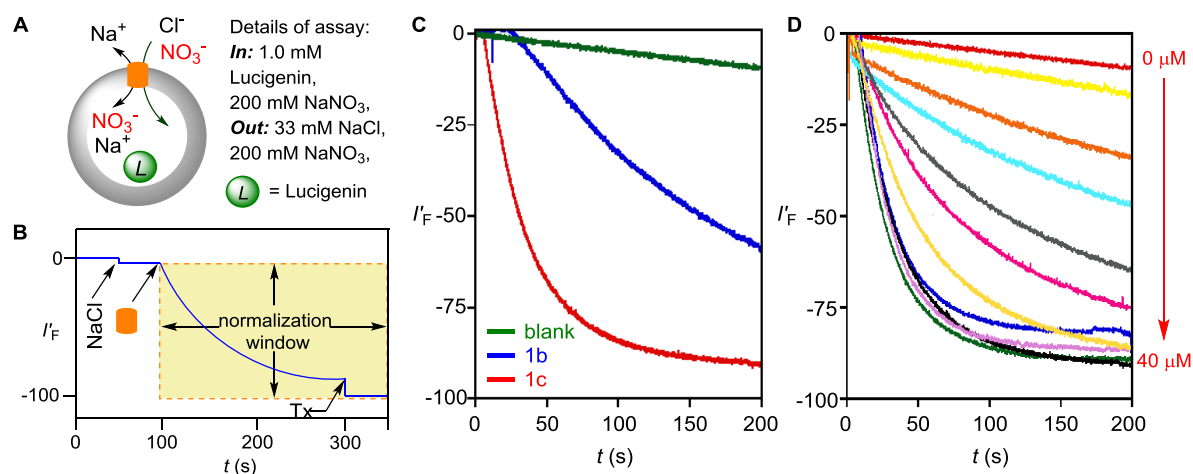


Figure 5.5. Representations of chloride transport activity across EYPC \supset lucigenin vesicles (**A**). Illustration of chloride transport kinetics showing the normalization window (**B**). Comparison of rate of Cl^- influx of **1b** and **1c** (30 μM each) in EYPC-LUVs \supset lucigenin (**C**). Dose-dependent influx of Cl^- ion across EYPC-LUVs \supset lucigenin upon addition of **1c** (0-40 μM).

Upon addition of **1b** and **1c**, a significant amount quenching of fluorescence was observed due to the influx of Cl^- into vesicles (Figure 5.5C). Compound **1c** was found to be much efficient Cl^- transporter with respect to **1b** in the identical condition (Figure 5.5C). The dose-dependent activity of Cl^- influx was obtained for compound **1c** (0 – 40 μM) in EYPC-LUVs \supset lucigenin (Figure 5.5D). The initial rate (r_i) and half-life ($t_{1/2}$) of the Cl^- transport were obtained upon applying numerical analysis in the fluorescence quenching curve (Table 5.1). A 66 times higher rate of Cl^- influx was obtained in case of **1c** than **1b** (at 30 μM concentration for each compound).

Half-lives ($t_{1/2}$) of transport activities were obtained by fitting of fluorescence quenching curves to a single exponential decay function (equation 5.1 and then calculating half-lives by use of equation 5.2).

$$I/I_0 = a + be^{-ct} \quad \text{Equation 5.1}$$

$$t_{1/2} = 0.693/c \quad \text{Equation 5.2}$$

To obtain the initial rate for the transport process differentiating equation 5.1 according to t gives:

$$\partial y/\partial t = a.b.e^{(-bt)} \quad \text{Equation 5.3}$$

The initial rate r_i (at $t = 0$ s) gives:

$$r_i = \partial y/\partial t_{t=0} = a.b \quad \text{Equation 5.4}$$

Table 5.1: Determination of half-lives ($t_{1/2}$) and initial rates (r_i) of Cl^- ion influx across EYPC-LUVs \supset lucigenin by **1b** and **1c** (30 μM each).

Compound	$t_{1/2}$ (s)	r_i (s^{-1})
1b	126.81 ± 0.96	0.0099 ± 0.0001
1c	22.48 ± 0.03	0.6560 ± 0.0048

The cationic composition of the extravesicular buffer was then varied to evaluate the contribution of cations in the $\text{Cl}^-/\text{NO}_3^-$ exchange. EYPC-LUVs \supset lucigenin were suspended in buffer containing MCl solution ($\text{M}^+ = \text{Li}^+, \text{Na}^+, \text{K}^+, \text{Rb}^+, \text{and Cs}^+$) and the rate of Cl^- influx was monitored through emission intensity of lucigenin (Figure 5.6A). No significant difference in the rate of Cl^- influx was encountered which implies that the lack of contribution of extravesicular cations in the rate limiting step of the ion transport process (Figure 5.6B).

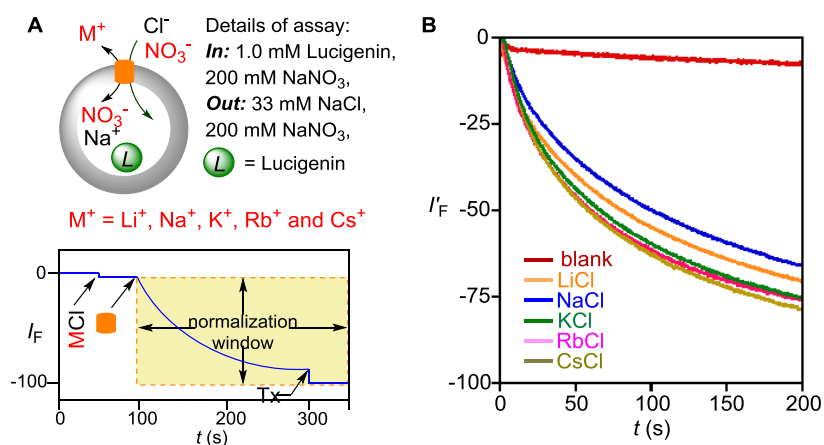


Figure 5.6. Representations chloride influx activity across EYPC-LUVs containing lucigenin by varying extravesicular cations (A). Influx of Cl⁻ ion across EYPC-LUVs containing lucigenin upon addition of **1c** (20 μM) with intravesicular NaNO₃ and extravesicular MCl (M⁺ = Li⁺, Na⁺, K⁺, Rb⁺ and Cs⁺) (C).

The contribution of extravesicular anions was evaluated by varying the anionic composition in the extravesicular buffer as Na_mA (A⁻ = F⁻, ClO₄⁻, NO₃⁻, SO₄²⁻, Cl⁻; m = valency of an anion) by keeping iso-osmolar NaCl as the intravesicular salt. In this assay EYPC- LUVs containing lucigenin were prepared with intravesicular NaCl (150 mM) and suspended in various extravesicular salt solution (Na_mA (A⁻ = F⁻, ClO₄⁻, NO₃⁻, SO₄²⁻, Cl⁻)). The rate of Cl⁻ efflux was monitored by the extent of the enhancement in emission intensity of entrapped lucigenin (Figure 5.7A). A remarkable difference in the rate of Cl⁻ efflux was observed which ascertains the involvement of the extravesicular anions in the rate of transport of Cl⁻ by antiport mechanism (Figure 5.7B). The combination outcome of the previous two experiment suggests the antiport mechanism (Cl⁻/A⁻) is being dominated over the symport mechanism (Cl⁻/M⁺) of ion transport.

The antiport mechanism was further confirmed by using valinomycin (V), a K⁺ selective transporter, in the extravesicular buffer (Figure 5.8A).¹⁴ KCl solution was added in the extravesicular buffer of EYPC-LUVs containing lucigenin keeping intravesicular NaNO₃, and rate of influx of Cl⁻ by **1c** (20 μM) was examined in absence and presence of valinomycin (2 μM). The synergistic effect of Cl⁻ influx by **1c** and K⁺ influx by valinomycin was evident from the

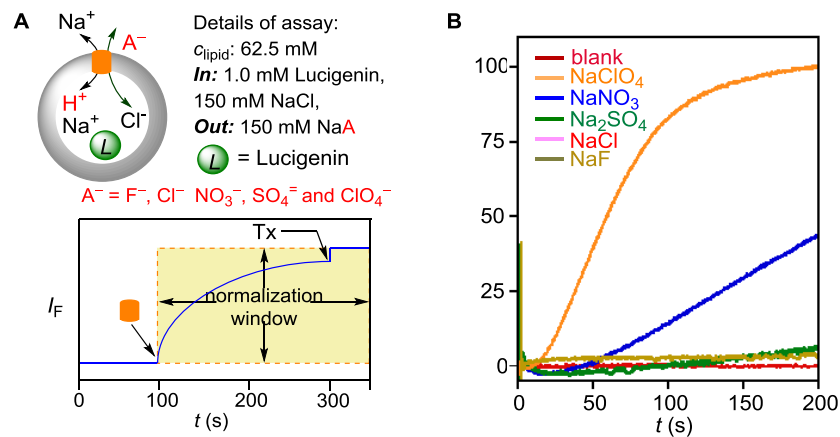


Figure 5.7. Representations of chloride efflux activity across EYPC-LUVs containing lucigenin in 150 mM NaCl (A); Efflux of Cl^- ion across EYPC-LUVs containing lucigenin upon addition of **1c** (20 μM) with intravesicular NaCl and extravesicular Na_mA salt ($\text{A}^- = \text{F}^-, \text{Cl}^-, \text{NO}_3^-, \text{SO}_4^{2-}$ and ClO_4^- ; m = valency of an anion) (B).

acceleration of Cl^- transport rate which was further quantified (Figure 5.8B). The enhanced rate of Cl^- transport in the presence of valinomycin established the $\text{Cl}^-/\text{NO}_3^-$ antiport as the preferred transport mechanism involving **1c**. Numerical analysis of the normalized fluorescence quenching curves provided $r_i = 0.0087 \text{ s}^{-1}$ and $t_{1/2} = 51.9 \text{ s}$ for only **1c**; whereas the combination of **1c** and valinomycin gave $r_i = 0.0208 \text{ s}^{-1}$ and $t_{1/2} = 29.1 \text{ s}$ indicating more than 2.3 fold enhancement in

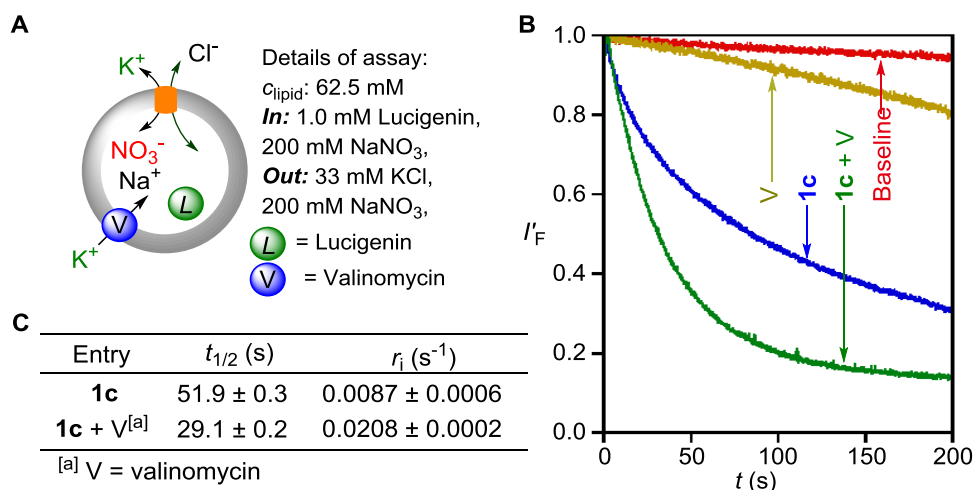


Figure 5.8. Representations of chloride influx activity assay using EYPC-LUVs containing lucigenin in the presence of valinomycin and **1c** (A). Comparison of Cl^- transport activity of **1c** (20 μM) in the presence and the absence of valinomycin (2 μM) (B). Calculated half-life ($t_{1/2}$) and initial rate (r_i) of Cl^- influx for **1c** in the presence and the absence of valinomycin (C).

the Cl^- transport rate (Table 8C). The remarkable improvement of transport rate in the presence of valinomycin clearly indicates the $\text{Cl}^-/\text{NO}_3^-$ antiport mechanism of **1c** which gets accelerated because of the synergistic effect of **1c** and valinomycin.

5.2.5. Planar Lipid Bilayer Conductance Measurements:

To appraise the necessary evidence for ion channel formation, by the most active compound **1c**, electrical conductance across planar lipid bilayer membrane was measured. The planar lipid bilayer, consisting of 1,2-diphytanoyl-*sn*-glycero-3-phosphocholine (DPhPC) lipid, was prepared over the orifice connecting two electrolytic chambers of the instrument. Electrical conductance between two chambers, after applying voltage, describe the information about ion channel formation.²⁶ Significant conduction of ions was observed by adding **1c** ($c = 80 \mu\text{M}$) in the *cis* chamber of the electrolyte solution. The periodic opening and closing events were also observed at different holding potentials corroborating to the ion channel formation at the planar bilayer by **1c** (Figure 5.9). The single channel conductance $G = 79.7 \pm 4.9 \text{ pS}$ and the diameter $d = 4.71 \pm 0.16 \text{ \AA}$ were calculated for the supramolecular ion channel formed by **1c**.

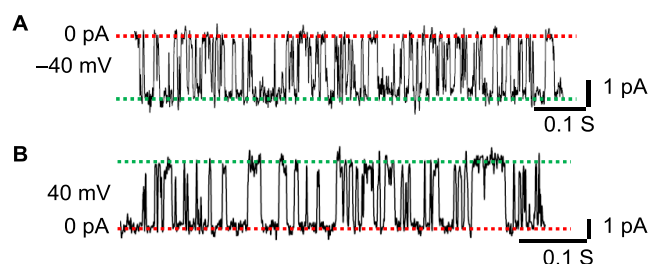


Figure 5.9. Single-channel current traces recorded at -40 mV (**A**) and $+40 \text{ mV}$ (**B**) holding potentials in 1 M symmetrical KCl solution. The baseline current was indicated by 0 pA . The main conductance state is indicated by two dotted lines.

5.2.6. Molecular Modelling of the Ion Channel Formation:

To understand the molecular picture of the nanochannel, we had proposed a model based on the hydrogen bonding network of the bis(diols) system. Alkyl chains were truncated to ethyl for simplicity in the calculation. Semiempirical quantum calculations were performed to obtain the molecular level insight of the supramolecular

architecture. At first, the face-to-face dimeric unit was optimized using Gaussian 09²⁷ software with wB97XD²⁸ functional and 6-31G (d,p) basis set to obtain the rosette structure M_2 . The nanotubular structure was achieved by placing five optimized rosette units on top of each other. This oligomeric assembly was further optimized with MOPAC2012²⁹ software using the PM6-DH+³⁰ method, and the result indicates the formation of the nanochannel $M_{2.5}$ with the hydrophilic interior and hydrophobic exterior, in line with our proposition (Figure 5.10). We calculated the average diameter using the radius of gyration method for the middle layer. The diameter is found to be 6.4 Å. However, the cavity is not circular, giving us different values for major (8.4 Å) and minor (3.8 Å) axes as shown in Figure 5.10. The experimental value (4.7 Å), based on the conductance measurement, is understandably close to the smaller value, i.e., the minor axis value. Hence, the outcome of the molecular modeling study in accordance with the proposed model of ion channel formation.

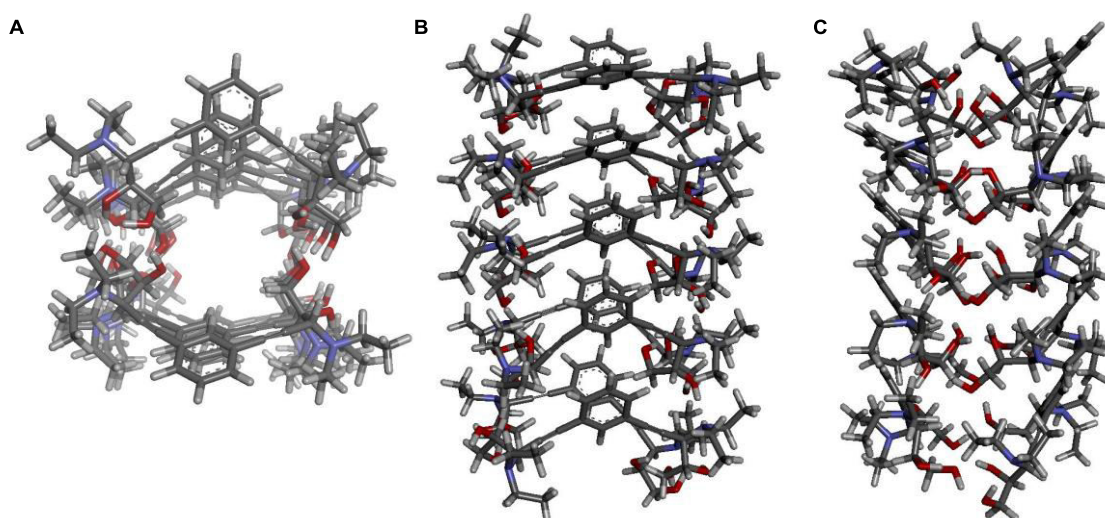


Figure 5.10. Top (A) and side (B-C) view of the optimized structures of ion channel **1d**. Compound **1d** was selected for the optimization for the simplicity of the calculation, as the presence of a lesser number of atoms in this structure of **1d** than others. (This study was carried out in collaboration with Dr. Arnab Mukherjee at IISER Pune.)

5.2.7. Effect of Ion Transport in Biological Systems:

Formation of an efficient artificial ion channel in spherical as well as in planar lipid bilayers prompted us to investigate the ion transport activity of **1c** across the cell membrane. The change in Cl^- concentration in the intracellular matrix was monitored

with a cell permeable chloride selective dye *N*-(ethoxycarbonylmethyl)-6-methoxyquinolinium bromide (MQAE).^{31,32} The characteristic of quenching in fluorescence intensity of MQAE dye in the presence of Cl⁻ ion by diffusion mediated collisional quenching had been used to determine the intracellular chloride concentration. A significant amount of quenching in fluorescence intensity of MQAE ($\lambda_{\text{ex}} = 350$ nm and $\lambda_{\text{em}} = 460$ nm) was encountered upon preincubation of HeLa cells with **1c** in concentration-dependent manner (Figure 5.11). The dose-dependent quenching of fluorescence implies the enhanced chloride concentration at the intracellular matrix, transported through artificial ion channel formed by of **1c**. The differences in mean intensities had appeared to be statistically very significant according to one-way analysis of variance (ANOVA).

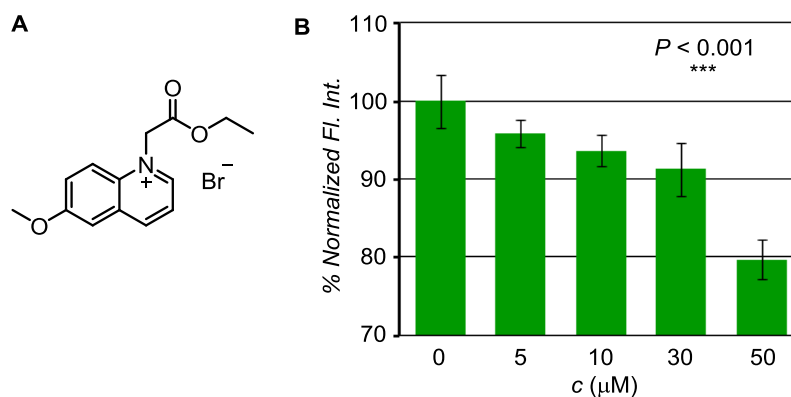


Figure 5.11. The structure of MQAE dye (A); normalized fluorescence intensity of HeLa cells incubated with MQAE (5 mM) for 3 h followed by treatment of **1c** (0 – 50 μM) for 24 h (B).

The successful Cl⁻ transports across the cell membrane emboldened us to investigate the impact of Cl⁻ transport in cell viability. According to few recent studies, the stimulated transport of Cl⁻ can induce apoptosis via disruption of ionic homeostasis of the cell.^{12,14,33,34} At first, the effect of **1c** in cell viability was screened in various cancer (*e.g.* lung adenocarcinoma epithelial A549, human cervical cancer HeLa, human breast cancer MCF 7, and human bone osteosarcoma U2OS,) and normal (*e.g.* mouse fibroblast NIH3T3) cell lines of different origin. A single point screening of cell viability was done by MTT assay, after incubation of **1c** (10 μM) with different cell lines. A considerable amount of cell death was observed upon treatment of **1c** irrespective of cell type and origin (Figure 5.12).

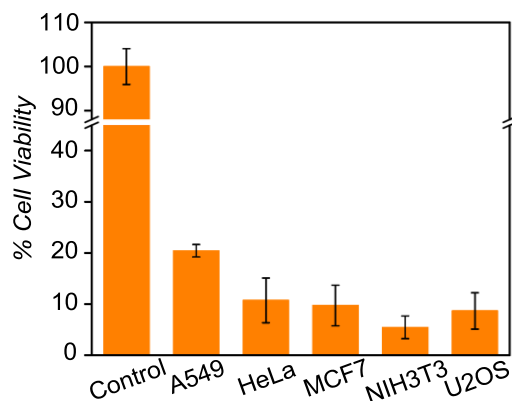


Figure 5.12. Cell viability obtained from single point screening of compounds **1c** (10 μM each) by MTT assay. Cell viability was checked after 24 h treatment of **1c** in various cell lines, from left to right, A549, HeLa, MCF7, NIH3T3 and U2OS.

The Cl^- transport mediated cell death, via the artificial ion channel, was confirmed by subsequent comparing the cell viability in presence and absence of Cl^- ion in the extracellular media. Two different varieties of HBSS (Hanks Balanced Salt Solution) were prepared; with and without Cl^- ion, to be used as extracellular media. The HeLa cells were suspended in two different types of HBSS media, separately, and incubated with **1c** in various concentrations. Significantly higher cell viability was observed for cells suspended in the Cl^- -free HBSS media than those are dispersed in the Cl^- ion-containing buffer (Figure 5.13). The difference in cell viability in presence and absence of Cl^- ion clearly indicates that the cell death is due to the enhanced level of Cl^- ion in the intracellular matrix, transported through artificial ion channel formed by **1c**.

A detailed study had been carried out to evaluate the mode of Cl^- ion transport mediated cell death via either apoptosis or necrosis. In the intrinsic pathway of apoptosis, disruption of mitochondrial membrane potential (MMP) may lead to the release of cytochrome *c* from the intra-mitochondrial space to the cytoplasm. The released cytochrome *c* binds with *Apaf-1* and procaspase 9 to form apoptosome which subsequently releases caspase 9.³⁵ The cleaved caspase 9 triggers the expression of cleaved caspase 3, known to be the executioner caspase, which subsequently undergoes a few consecutive processes to induce apoptosis in the cell.³⁶⁻³⁹ At first the change in mitochondrial membrane potential, as the indication of early stages of apoptosis,

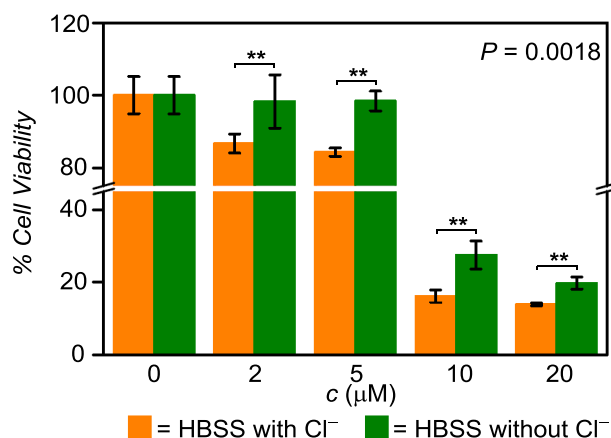


Figure 5.13. MTT assay for comparing cell viability of HeLa cells in presence and absence of Cl⁻ ion in extracellular media (HBSS buffer) upon dose dependent treatment of **1c** (0 – 20 μM) for 24 h.

was monitored with an MMP sensitive probe JC-1. This dye exhibits red fluorescence emission because of *J*-aggregation in the healthy mitochondrial membrane, whereas, depolarization of mitochondrial membrane leads to dispersion of the dye in cytosol resulting green fluorescence emission.^{40,41} Preincubation of HeLa cells with **1c** (0, 5, 10 and 20 μM) followed by treatment with JC-1 dye resulted in the stepwise dose-dependent decrease of red fluorescence with the concurrent increase in green fluorescence (Figure 5.14A–D). The quantification of the pixel intensity ratio (red/green) also suggested that the change in fluorescence is an upshot of the mitochondrial membrane depolarization (Figure 5.14E). The disruption of the ionic homeostasis

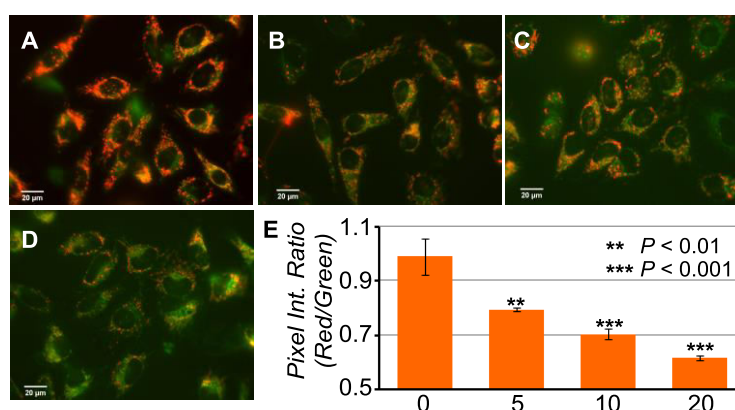


Figure 5.14. Live cell imaging of HeLa cells upon treating with 0 μM (A), 5 μM (B), 10 μM (C), and 20 μM (D) of **1c** for 24 h followed by staining with JC-1 dye. Red and green channel images were merged to create the displayed image. The pixel ratio (red/green) for each images was plotted in the bar graph (E).

of cells, due to the excess transport of Cl^- ion through the artificial anion channels is, therefore, responsible for the change in the membrane potential of mitochondria.

The change in ionic homeostasis of cells also causes an interruption of electron transport chain in the mitochondrial respiratory cycles resulting in the abnormal reactive oxygen species (ROS) production.^{42,43} A ROS-sensitive probe (3-methyl-7-(4,4,5,5-tetramethyl-1,3,2-dioxaborolan-2-yl)-2*H*-chromen-2-one) had been used to determine the change in ROS concentration in the cell. The ROS probe is known to have reaction in presence of ROS which results the highly fluorescent coumarin dye (Figure 5.15A). The emission intensity of that probe had been found to increase with an enhancement in ROS concentration.^{44,45} A concentration dependent enhancement of ROS level was encountered when HeLa cells were incubated with **1c** (0–50 μM) followed by incubation with, an ROS-sensitive probe (Figure 5.15B).

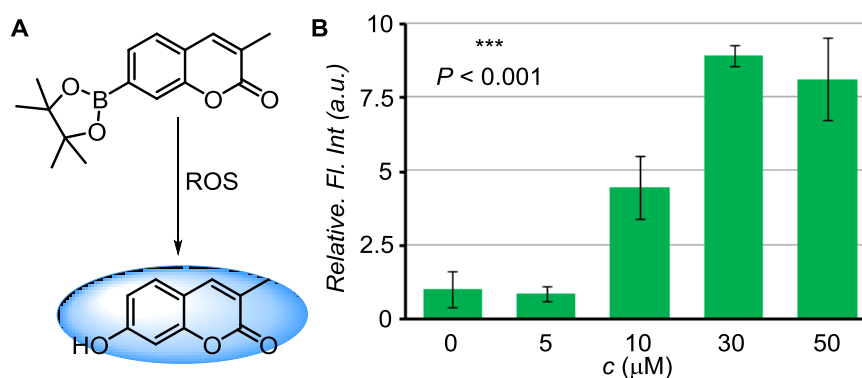


Figure 5.15. The structure of **ROS probe** (A); Measurement of ROS production in HeLa cells upon incubation with different concentration of **1c** (0–50 μM) for 7 h, followed by treatment with the **ROS probe** (100 μM) for 1 h (B). Fluorescence intensities were recorded using plate reader at $\lambda_{\text{em}} = 460 \text{ nm}$ ($\lambda_{\text{ex}} = 315 \text{ nm}$), and normalized with respect to the emission intensity of untreated cells.

Cytochrome *c*, a well-conserved electron transport protein, is a part of the respiratory chain and localized between mitochondrial intermembrane spaces. Release of cytochrome *c* upon apoptotic stimulation may lead to instigate the caspase-dependant apoptotic pathways.⁴⁶⁻⁴⁸ The elevated level of ROS can trigger the opening of mitochondrial permeability transition pore (PTP), mainly formed by natural ion channels present in the mitochondrial membrane, resulting disruption of outer-mitochondrial membrane.⁴⁹⁻⁵¹ On the other hand, enhanced amount of ROS may downregulate the Bcl-

2 and Bcl-xL proteins leading to the opening of mitochondrial PTP.^{49,52,53} Therefore, the release of cytochrome *c* was monitored by immunostaining with a specific antibody. A considerable amount of enhancement on fluorescence intensity and dispersion of the fluorescence signal all over the cytosol was detected upon treatment of **1c** (0, 10 and 20 μM) in HeLa cells for 8 h (Figure 5.16) which signifies the release of cytochrome *c* from mitochondria, endorsed by the change in ionic homeostasis.

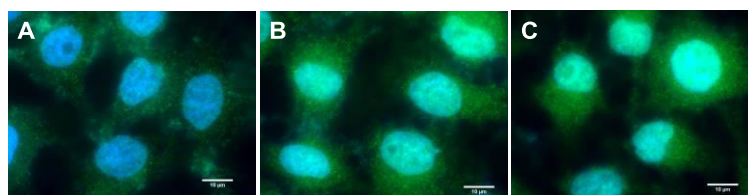


Figure 5.16. HeLa cells treated first with 0 μM (A), 10 μM (B) and 20 μM (C) of **1c** for 8 h, then fixed and analyzed for cytochrome *c* release by immunostaining with cytochrome *c* antibody. Nuclei were stained with Hoechst 33342.

The released cytochrome *c* can initiate the program of apoptotic cell death via provoking a family of caspases.^{38,54-56} In next stage, the expression of caspase family was investigated for the proper understanding of the pathway of mitochondria-dependent apoptosis. The level of cleaved caspase 9 and caspase 3 were examined by immunoblot analysis. A significant amount of enhancement of cleaved caspase 9 and cleaved caspase 3 were observed upon incubation with increasing concentration of **1c** (0 – 20 μM) (Figure 5.17). The enhancements in the levels of caspases were quantified with respect to the GAPDH level. The expression of caspase 9 and caspase 3 confirms the caspase-mediated intrinsic pathway of apoptosis as the pathway of cell death. In addition to that, cleavage of poly(ADP-ribose) polymerase (PARP) by endogenous caspases, is a well-known phenomenon during apoptosis.^{57,58} Cleavage of PARP-1 prevents the futile repair of DNA strand breaks to facilitate the apoptotic process.^{57,59} A significant amount of degradation of full-length PARP-1 (116 kD) with a concomitant increase of cleaved PARP-1 (86 kD) were encountered upon Immunoblot analysis of HeLa cells incubated with various concentration of **1c** (0–20 μM). The activation of cleaved PARP-1 epitomizes as an additional validation of **1c** mediated caspase-dependent apoptosis (Figure 5.17).

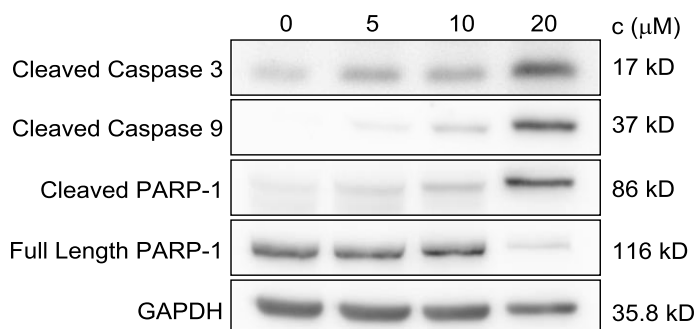


Figure 5.17. Immunoblot assay for cleaved caspase 9, caspase 3 and PARP-1 in HeLa cells, after 24 h incubation with various concentrations (0, 5, 10 and 20 μM) of **1c**. Data were quantified with respect to Glyceraldehyde 3-phosphate dehydrogenase (GAPDH) levels.

On the other hand, apoptosis can also proceed via activation of the p53-mediated pathway. Phosphorylation of Ser-15 position of p53 protein is a well-known pathway of p53 mediated apoptosis program.^{60,61} No phosphorylation step was found on Ser-15 of p53 protein which abolishes the possibility of p53 mediated apoptosis program (Figure 5.18). A cell lysate of a positive control for the P-p53 (Ser-15) antibody was prepared to validate the workability of antibody. Lysate of HeLa cells (2×10^6 cells) for positive control was prepared by treatment of 10 μM camptothecin (CPT) for 16 h.

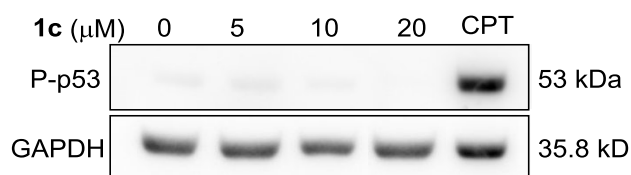


Figure 5.18. Immunoblot assay for P-p53 (Ser-15) in HeLa cells, after 24 h incubation with various concentrations (0, 10, 20 and 40 μM) of **1c** and 16 h incubation with CPT (10 μM).

To confirm the intrinsic pathway of apoptosis as the prime mode of cell death, the cell viability was checked in the presence of caspase inhibitors. Benzyloxycarbonyl-Asp(OMe)-Glu(OMe)-Val-Asp(OMe)-fluoromethylketone(z-DEVD-fmk) and benzyloxycarbonyl-Leu-Glu(OMe)-His-Asp(OMe)-fluoromethylketone (z-LEHD-fmk) are small cell-permeable peptides, known to have an inhibitory action for expression of cleaved caspase 3 and caspase 9 respectively.^{55,62,63} The **1c** mediated caspase-dependent apoptosis can be inhibited by introduction of caspase inhibitors. An extremely significant amount of retention of cell viability was detected upon preincubation of HeLa cells with of z-DEVD-fmk and z-LEHD-fmk followed by treatment of **1c** (Figure 5.19). The

restoring of cell viability, because of inhibition of executioner caspase, strongly supports the prime mode of cell death via the caspase-mediated intrinsic pathway of apoptosis.

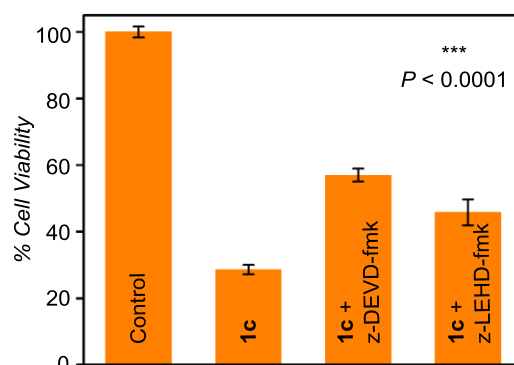


Figure 5.19. HeLa cells were pre-incubated with z-DEVD-fmk or z-LEHD-fmk (100 μ M each) for 3 h followed by incubation with **1c** (20 μ M) for 24 h.

5.3. CONCLUSION:

In summary, we had introduced small bis(diol) molecules for the strategic construction of a supramolecular nanotubular assembly that allows selective transmembrane transport of chloride ions. Formation of the nanotubular structure was achieved by the intermolecular hydrogen bonding interactions from the hydroxyl moieties present at two termini of a molecule. The molecular library of these bis(diol) was designed by varying their logP values. These compounds were synthesized following the Cu(I)-catalyzed aldehyde-amine-alkyne three-component reaction followed by acid catalyzed ketal-deprotection chemistry to obtain free hydroxyl groups. Ion transport across vesicles revealed an excellent alliance of logP value with the transport activity, correlating the Lipinski's rule of lipid membrane permeability. The bis(diol) system favored anion transport with prominent chloride ion selectivity, and the antiport mechanism for the anion transport was established. The transmembrane ion transport process was also operative through ion channel constructed from the self-assembly of bis(diol) molecules, and a computational model for such supramolecular channel was also established.

The bis(diol) system was efficient in delivering Cl^- ions into cells indicated by the increase in the intracellular Cl^- ion level, and the process also resulted in the significant cell death. Change in the mitochondrial membrane potential, subsequent generation of excess ROS and release of cytochrome *c* from mitochondrial

intermembrane spaces were encountered upon disruption of the Cl^- ion homeostasis. The observed cell death was related to the apoptosis process as evident from the expression of proteins of the caspase family namely, caspase 3 and caspase 9. The caspase-mediated apoptosis pathway was further confirmed via monitoring the diminution of ion transport mediated cell death in the presence of caspase inhibitors. Hence, artificial Cl^- channels displaying apoptosis-inducing activity can be a potential tool for treatment in next generation.

5.4. EXPERIMENTAL SECTION:

5.4.1. General Methods:

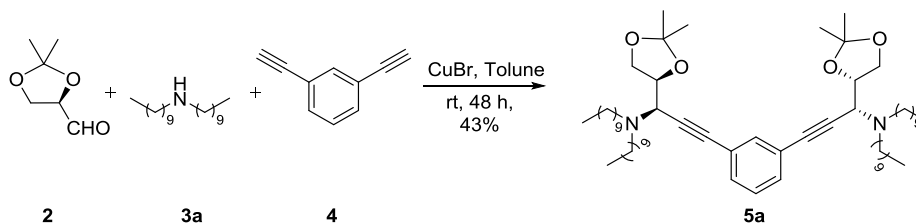
All reagents and solvents for synthesis were purchased commercially and used without further purification. Toluene was pre-dried over activated molecular sieves. Column chromatographies were performed on Merck silica gel (100 – 200 mesh). Thin layer chromatographies (TLCs) were carried out on E. Merck silica gel 60-F254 plates. Egg-yolk phosphatidylcholine (EYPC) and diphytanoylphosphatidylcholine (DPhPC) were obtained from Avanti Polar Lipids as a solution (25 mg/mL in CHCl_3) and solid respectively. HEPES buffer, HPTS, lucigenin, Triton X-100, NaOH and inorganic salts were purchased of molecular biology grade from Sigma. Large unilamellar vesicles (LUVs) were prepared by using mini extruder, equipped with a polycarbonate membrane of 100 nm (or 200 nm) pore size, obtained from Avanti Polar Lipids. MCF7, U2OS, and HeLa cell lines were purchased from European Collection of Cell Cultures (ECACC). A549 and NIH-3T3 cell lines were generous gifts from Dr. Kundan Sengupta (IISER Pune) and Dr. Nagaraj Balasubramanian (IISER Pune) respectively. Dimethyl sulfoxide (DMSO), thiazolyl blue tetrazolium bromide (MTT), and *N*-(ethoxycarbonylmethyl)-6-methoxyquinolinium bromide (MQAE) were purchased from Sigma-Aldrich. 96-Well plates, 24-well plates, 6-well plates, 15 and 50 mL graduated sterile centrifuge tubes and tissue culture flasks with filter cap sterile were purchased from Eppendorf Product Pvt. Ltd. Active, caspase 9, and anti-GAPDH antibodies were purchased from Abcam and Sigma respectively. Cytochrome *c* antibody was purchased from Cell Signaling Technology. Cytochrome *c*, phospho-p53 (Ser-15) and active caspase 3 antibodies were purchased from Cell Signaling Technology. Anti-PARP-1 (Ab-2) Mouse mAb (C-2-10) antibody was purchased from Calbiochem. Anti-rabbit and Anti-mouse IgG HRP-conjugated antibody were obtained from Jackson ImmunoResearch. AlexaFluor-488 was purchased from Invitrogen. Inhibitors for active caspase 3 and caspase 9 were purchased from R & D Systems. The compound 3-methyl-7-(4,4,5,5-tetramethyl-1,3,2-dioxaborolan-2-yl)-2*H*-chromen-2-one (**ROS Probe**) was a generous gift from Dr. Harinath Chakrapani's Laboratory at IISER Pune.

5.4.2. Physical Measurements:

All NMR spectra were recorded on 400 MHz Bruker Ascend™ 400 spectrometer using either residual solvent signal as an internal reference or from internal tetramethylsilane on the δ scale. The chemical shifts (δ) were reported in ppm and coupling constants (J) in Hz. The following abbreviations were used: m (multiplet), s (singlet), d (doublet), t (triplet) dd (doublet of doublet). High-resolution mass spectra were obtained on a MicroMass ESI-TOF MS spectrometer equipped with a Micromass Z-Spray electrospray ionization (ESI) source (Waters Co., Synapt G2, France). Mass spectra were also recorded in Applied Biosystems 4800 Plus MALDI TOF/TOF analyzer. FT-IR spectra were obtained using NICOLET 6700 FT-IR spectrophotometer as KBr disc and reported in ν (cm^{-1}). Fluorescence spectra were recorded from Fluoromax-4 from JobinYvon Edison-equipped with an injector port and a magnetic stirrer. Measurements of pH were done using a Helmer pH meter. All data from fluorescence studies were processed either by KaleidaGraph 3.51 or Origin 8.5 program. Conductance measurement through ion channel was carried out in planar bilayer lipid membrane (BLM) workstation obtained from Warner Instruments, consisting of head-stage and its corresponding amplifier BC-535, 8-pole Bessel filter LPF-8, Axon CNS Digidata 1440A and pClamp 10 software. The conductance data was analyzed in Clampfit 10 software. ChemBio Draw 15 Ultra software was used for drawing structures and processing figures. MTT assay was recorded in a microplate reader (Varioskan Flash). Western blot was visualized in a using ImageQuant LAS 4000 (GE Healthcare). Cell images were taken in were taken using Olympus Inverted IX81 microscope equipped with Hamamatsu Orca R2 camera. Image J software was used for analyzing cell images, and the quantifying amount of protein in immunoblot analysis. GraphPad Prism 6 software was used for statistical analysis.

5.4.3. Synthesis:

Synthesis of N,N' -((1*R*,1'*R*)-(1,3-phenylenebis(1-((*S*)-2,2-dimethyl-1,3-dioxolan-4-yl)prop-2-yn-3,1-diyl))bis(*N*-decyldecan-1-amine) 5a, ($\text{C}_{62}\text{H}_{108}\text{N}_2\text{O}_4$):

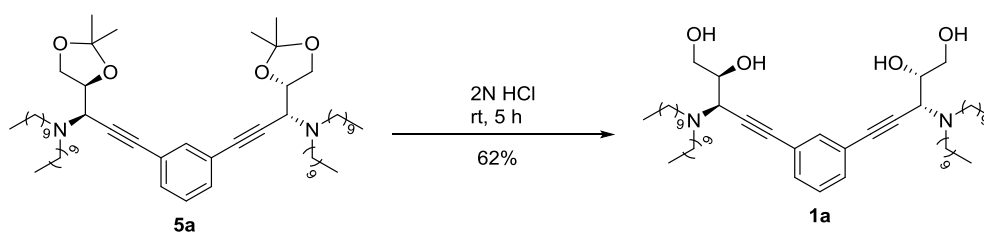


Scheme 5.2. Synthesis of 5a.

Compound 2 was synthesised by a reported protocol.^{20,23} Compound 2 (1.55 g, 11.9 mmol) and amine 3a (3.5 g, 11.9 mmol) was added to 10 mL of dry toluene in a clean and dry 50 mL round-bottom flask. The mixture was stirred for 30 min and then CuBr (56.9 mg, 0.396 mmol), and diethynylbenzene (4, 500 mg, 3.96 mmol) were added to it and stirred at room

temperature for 48 h. After completion of the reaction, monitored by TLC, the reaction mixture was filtered through celite and expected compound was purified by column chromatography, using 10% ethyl acetate in petroleum ether solvent, which yields 890 mg (43%) of compound as pale yellow oil. **NMR (400 MHz, CDCl₃):** δ 7.42 (d, J = 1.4 Hz, 1H), 7.33 (dd, J = 7.2, 1.4 Hz, 2H), 7.23 (dd, J = 8.4, 7.0 Hz, 1H), 4.26 (dd, J = 13.6, 6.9 Hz, 2H), 4.14 (dd, J = 8.3, 6.1 Hz, 2H), 3.96 (dd, J = 8.2, 7.1 Hz, 2H), 3.84 (d, J = 7.4 Hz, 2H), 2.63 – 2.52 (m, 4H), 2.51 – 2.40 (m, 4H), 1.57 – 1.45 (m, 6H), 1.45 (s, 6H), 1.39 (s, 6H), 1.25 (s, 58H), 0.87 (t, J = 6.8 Hz, 12H). **¹³C NMR (100 MHz, CDCl₃):** δ 134.80, 131.54, 128.45, 123.36, 109.83, 85.87, 85.59, 77.16, 76.53, 67.77, 57.86, 52.41, 32.05, 29.81, 29.76, 29.50, 28.35, 27.66, 26.90, 25.84, 22.83, 14.27; **IR:** ν/cm^{-1} 2922, 2854, 1594, 1462, 1373, 1249, 1214, 1154, 1067, 852, 793, 723; **Exact mass (HRMS-ESI):** Calc. for C₆₂H₁₀₈N₂O₄H⁺ (M+ H)⁺: 945.8382; Found: 945.8387.

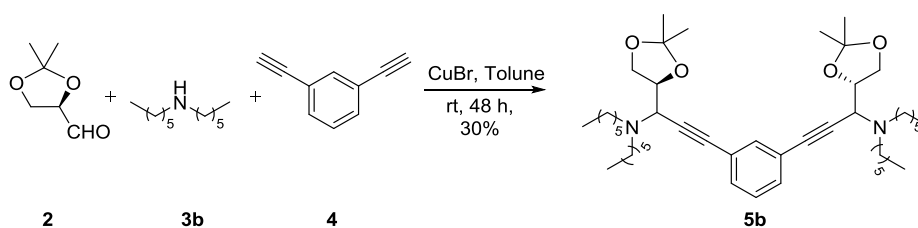
Synthesis of ((2*S*,2'*S*,3*R*,3'*R*)-5,5'-(1,3-phenylene)bis(3-(didecylamino)pent-4-yne-1,2-diol) 1a, (C₅₆H₁₀₀N₂O₄):



Scheme 5.3. Synthesis of **1a**.

In a 25 mL round bottom flask compound **5a** (200 mg, 0.211 mmol) was taken in 5 mL of THF and 2.5 mL of dilute HCl (2 N) was added to it dropwise. The reaction mixture was stirred for 5 h at room temperature. Upon completion of reaction the reaction mixture was neutralized by saturated solution of NaHCO₃ and extracted with CHCl₃. The compound was purified by column chromatography (15% ethyl acetate in petroleum ether) which yields 115 mg (62%) of compound **1a** as colourless oil. **¹H NMR (400 MHz, CDCl₃):** δ 7.45 (s, 1H), 7.38 – 7.33 (m, 2H), 7.28 – 7.22 (m, 1H), 3.98 (dd, J = 11.8, 2.7 Hz, 2H), 3.88 (d, J = 9.0 Hz, 2H), 3.77 – 3.65 (m, 4H), 2.63 (d, J = 32.5 Hz, 8H), 1.55 (s, 8H), 1.26 (s, 57H), 0.87 (t, J = 6.8 Hz, 12H); **¹³C NMR (100 MHz, CDCl₃):** δ 134.97, 131.70, 128.49, 123.22, 86.25, 85.21, 70.45, 63.00, 55.50, 51.63, 32.04, 29.77, 29.73, 29.71, 29.46, 28.40, 27.58, 22.82, 14.24.; **IR:** ν/cm^{-1} 3409, 2923, 2854, 1595, 1463, 1380, 1287, 1193, 1102, 1054, 887, 794, 721; **Exact mass (HRMS-ESI):** Calc. for C₅₆H₁₀₀N₂O₄H⁺ (M+H)⁺: 865.7756; Found: Found: 865.7758.

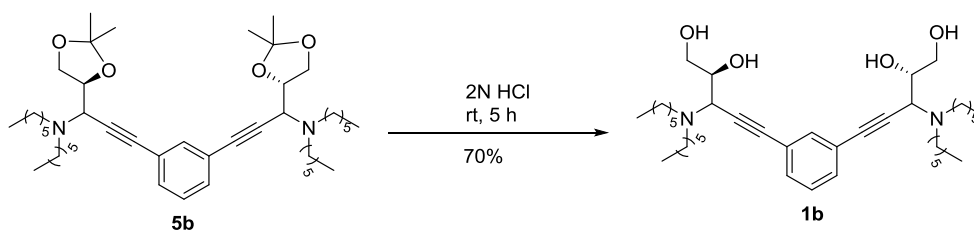
Synthesis of *N,N'*-((1*R*,1'*R*)-1,3-phenylenebis(1-((*S*)-2,2-dimethyl-1,3-dioxolan-4-yl)prop-2-yne-3,1-diyl)bis(*N*-hexylhexan-1-amine) 5b, (C₄₆H₇₆N₂O₄):



Scheme 5.4. Synthesis of **5b**.

Compound **2** (1.55 g, 11.9 mmol) and amine **3b** (2.20 g, 11.9 mmol) was added to 10 mL of dry toluene in a clean and dry 50 mL round-bottom flask. The mixture was stirred for 30 min and then CuBr (56.9 mg, 0.396 mmol), and diethynylbenzene (**4**, 500 mg, 3.96 mmol) were added to it and stirred at room temperature for 48 h. After completion of the reaction, monitored by TLC, the reaction mixture was filtered through celite and expected compound was purified by column chromatography, using 2% ethyl acetate in petroleum ether solvent, which yields 740 mg (30%) of compound as pale yellow oil. **NMR (400 MHz, CDCl₃):** δ 7.42 (t, $J = 1.3$ Hz, 1H), 7.33 (dd, $J = 7.2, 1.4$ Hz, 2H), 7.24 (dd, $J = 8.5, 7.0$ Hz, 1H), 4.26 (dd, $J = 13.6, 6.9$ Hz, 2H), 4.14 (dd, $J = 8.3, 6.2$ Hz, 2H), 3.96 (dd, $J = 8.3, 7.0$ Hz, 2H), 3.84 (d, $J = 7.5$ Hz, 2H), 2.57 (d, $J = 1.6$ Hz, 4H), 2.47 (d, $J = 5.5$ Hz, 4H), 1.58 – 1.42 (m, 14H), 1.40 – 1.20 (m, 33H), 0.88 (dd, $J = 8.0, 5.5$ Hz, 12H). **¹³C NMR (100 MHz, CDCl₃):** δ 134.81, 131.54, 128.47, 123.35, 109.84, 85.83, 85.60, 67.77, 57.86, 52.40, 31.96, 28.27, 27.33, 26.89, 25.83, 22.81, 14.23. **IR:** ν/cm^{-1} 2926, 2858, 1594, 1462, 1374, 1249, 1214, 1155, 1067, 893, 852, 794, 729; **Exact mass (HRMS-ESI):** Calc. for C₄₆H₇₆N₂O₄H⁺ (M+ H)⁺: 721.5878; Found: 721.5874.

Synthesis of (2*S*,2'*S*,3*R*,3'*R*)-5,5'-(1,3-phenylene)bis(3-(didecylamino)pent-4-yne-1,2-diol) **1b, (C₄₀H₆₈N₂O₄):**

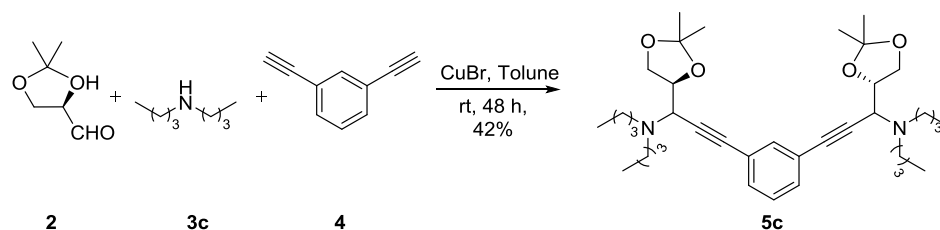


Scheme 5.5. Synthesis of **1b**.

In a 25 mL round bottom flask compound **5b** (200 mg, 0.277 mmol) was taken in 5 mL of THF and 2.5 mL of dilute HCl (2N) was added to it dropwise. The reaction mixture was stirred for 5 h at room temperature. Upon completion of reaction the reaction mixture was neutralized by saturated solution of NaHCO₃ and extracted with CHCl₃. The compound was purified by column chromatography (18% ethyl acetate in petroleum ether) which yields 124 mg (70%) of compound **1b** as colourless oil. **¹H NMR (400 MHz, CDCl₃):** 7.45 (d, $J = 1.5$ Hz, 1H), 7.36 (d, $J = 1.6$ Hz, 1H), 7.35 (d, $J = 1.5$ Hz, 1H), 7.28 – 7.23 (m, 1H), 3.98 (dd, $J = 11.8, 2.7$ Hz,

2H), 3.85 (d, $J = 9.3$ Hz, 2H), 3.77 – 3.60 (m, 4H), 2.72 – 2.49 (m, 8H), 1.53 (d, $J = 4.8$ Hz, 8H), 1.31 (dd, $J = 7.0, 4.6$ Hz, 26H), 0.89 (dd, $J = 8.6, 4.8$ Hz, 12H); ^{13}C NMR (100 MHz, CDCl_3): δ 135.00, 131.69, 128.51, 123.23, 86.25, 85.23, 77.16, 70.43, 63.01, 55.52, 31.90, 28.36, 27.23, 22.77, 14.18.; IR: ν/cm^{-1} 3415, 2924, 2856, 1595, 1463, 1403, 1383, 1285, 1088, 887, 794, 754, 724; HRMS (ESI): Calc. for $\text{C}_{40}\text{H}_{68}\text{N}_2\text{O}_4\text{H}^+$ ($\text{M}+\text{H}$) $^+$: 641.5257; Found: 641.5257.

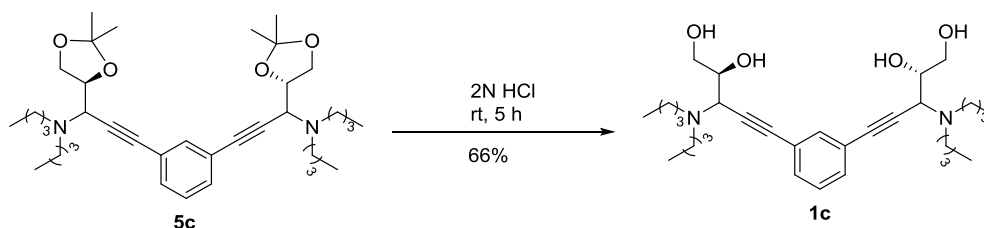
Synthesis of N,N' -((1*R*,1'*R*)1,3-phenylenebis(1-((*S*)-2,2-dimethyl-1,3-dioxolan-4-yl)prop-2-yne-3,1-diyl))bis(*N*-butylbutan-1-amine) 5c, ($\text{C}_{38}\text{H}_{60}\text{N}_2\text{O}_4$):



Scheme 5.6. Synthesis of **5c**.

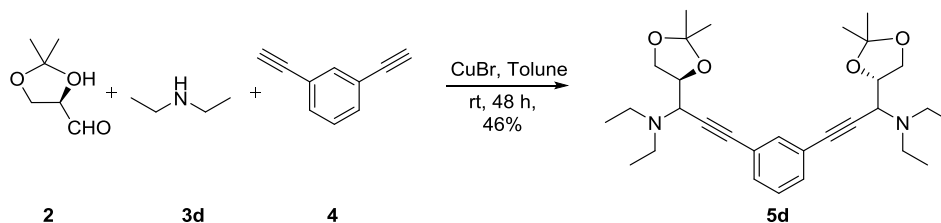
Compound **2** (1.55 g, 11.9 mmol) and amine **3c** (1.58 g, 11.9 mmol) was added to 10 mL of dry toluene in a clean and dry 50 mL round-bottom flask. The mixture was stirred for 30 min and then CuBr (56.9 mg, 0.396 mmol), and diethynylbenzene (**4**, 500 mg, 3.96 mmol) were added to it and stirred at room temperature for 48 h. After completion of the reaction, monitored by TLC, the reaction mixture was filtered through celite and expected compound was purified by column chromatography, using 3% ethyl acetate in petroleum ether solvent, which yields 1.01 gm (42 %) of compound as pale yellow oil. NMR (400 MHz, CDCl_3): δ 7.43 (t, $J = 1.3$ Hz, 1H), 7.36 – 7.30 (m, 2H), 7.25 – 7.20 (m, 1H), 4.26 (dd, $J = 13.6, 6.9$ Hz, 2H), 4.14 (dd, $J = 8.3, 6.2$ Hz, 2H), 3.97 (dd, $J = 8.2, 6.9$ Hz, 2H), 3.84 (d, $J = 7.4$ Hz, 2H), 2.65 – 2.53 (m, 4H), 2.52 – 2.41 (m, 4H), 1.53 – 1.42 (m, 14H), 1.40 – 1.27 (m, 14H), 0.92 (t, $J = 7.3$ Hz, 12H). ^{13}C NMR (100 MHz, CDCl_3): δ 134.85, 131.51, 128.49, 123.38, 109.82, 85.91, 85.58, 77.16, 67.75, 57.85, 52.10, 30.53, 26.91, 25.85, 20.81, 14.26. IR: ν/cm^{-1} 2953, 2867, 1593, 1373, 1301, 1214, 1156, 1065, 853, 793, 733; Exact mass (MALDI): Calc. for $\text{C}_{38}\text{H}_{60}\text{N}_2\text{O}_4\text{H}^+$ ($\text{M}+\text{H}$) $^+$: 609.4626; Found: 609.4834.

Synthesis of (2*S*,2'*S*,3*R*,3'*R*)-5,5'-(1,3-phenylene)bis(3-(dibutylamino)pent-4-yne-1,2-diol), 1c, ($\text{C}_{32}\text{H}_{52}\text{N}_2\text{O}_4$):



Scheme 5.7. Synthesis of **1c**.

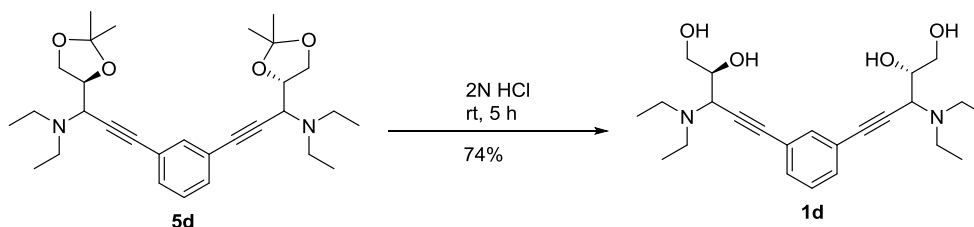
In a 25 mL round bottom flask compound **5c** (200 mg, 0.328 mmol) was taken in 5 mL of THF and 2.5 mL of dilute HCl (2N) was added to it dropwise. The reaction mixture was stirred for 5 h at room temperature. Upon completion of reaction the reaction mixture was neutralized by saturated solution of NaHCO₃ and extracted with CHCl₃. The compound was purified by column chromatography (18% ethyl acetate in petroleum ether) which yields 115 mg (66%) of compound **1c** as colourless oil. ¹H NMR (400 MHz, CDCl₃): δ 7.47 (s, 1H), 7.37 (dd, *J* = 8.5, 1.2 Hz, 2H), 7.29 (d, *J* = 1.3 Hz, 1H), 4.00 (dd, *J* = 11.8, 2.8 Hz, 2H), 3.84 – 3.71 (m, 4H), 3.66 (t, *J* = 6.4 Hz, 2H), 2.70 – 2.48 (m, 8H), 1.59 – 1.23 (m, 20H), 0.96 (t, *J* = 7.3 Hz, 12H).; ¹³C NMR (100 MHz, CDCl₃): δ 135.03, 131.74, 128.56, 123.13, 86.40, 84.96, 70.42, 63.00, 55.57, 51.41, 30.41, 29.84, 20.72, 14.17.; IR: ν/cm⁻¹ 3406, 2954, 2926, 1644, 1594, 1464, 1404, 1285, 1105, 1055, 887, 844, 795, 733; Exact mass (HRMS): Calc. for C₃₂H₅₂N₂O₄H⁺ (M+H)⁺: 529.4005; Found: 529.3998.

Synthesis of (1*R*,1'*R*)-3,3'-(1,3-phenylene)bis(1-((*S*)-2,2-dimethyl-1,3-dioxolan-4-yl)-*N,N*-diethylprop-2-yn-1-amine) 5d, (C₃₀H₄₄N₂O₄):**Scheme 5.8.** Synthesis of **5d**.

Compound **2** (1.55 gm, 11.9 mmol) and amine **3d** (868 mg, 11.9 mmol) was added to 10 mL of dry toluene in a clean and dry 50 mL round-bottom flask. The mixture was stirred for 30 min and then CuBr (56.9 mg, 0.396 mmol), and diethynylbenzene (**4**, 500 mg, 3.96 mmol) were added to it and stirred at room temperature for 48 h. After completion of the reaction, monitored by TLC, the reaction mixture was filtered through celite and expected compound was purified by column chromatography, using 10% ethyl acetate in petroleum ether solvent, which yields 904.1 mg (46 %) of compound as pale yellow oil. NMR (400 MHz, CDCl₃): δ 7.41 (d, *J* = 1.4 Hz, 1H), 7.32 (dd, *J* = 7.2, 1.5 Hz, 2H), 7.23 (dd, *J* = 8.3, 7.0 Hz, 1H), 4.29 (dd, *J* = 14.1, 6.9 Hz, 2H), 4.15 (dd, *J* = 8.4, 6.2 Hz, 2H), 3.95 (dd, *J* = 8.4, 7.0 Hz, 2H), 3.85 (d, *J* = 7.8 Hz, 2H), 2.83 – 2.69 (m, 4H), 2.56 (dq, *J* = 14.0, 7.0 Hz, 4H), 1.46 (s, 6H), 1.39 (s, 6H), 1.13 (t, *J* = 7.2 Hz, 12H). ¹³C NMR (100 MHz, CDCl₃): δ 134.77, 131.55, 128.49, 123.30, 110.08, 85.73, 77.16, 76.29, 67.90, 57.45, 45.55, 26.92, 25.84, 13.41. IR: ν/cm⁻¹ 2983, 2924, 1632, 1462, 1376, 1253,

1214, 1155, 1060, 909, 852, 726; **Exact mass (HRMS-ESI):** Calc. for $C_{30}H_{44}N_2O_4H^+$ ($M+H$)⁺: 497.3374; Found: 497.3365.

Synthesis of (2*S*,2'*S*,3*R*,3'*R*)-5,5'-(1,3-phenylene)bis(3-(diethylamino)pent-4-yne-1,2-diol), 1d, (C₂₄H₃₆N₂O₄):



Scheme 5.9. Synthesis of **1d**.

In a 25 mL round bottom flask compound **5d** (200 mg, 0.402 mmol) was taken in 5 mL of THF and 2.5 mL of dilute HCl (2N) was added to it dropwise. The reaction mixture was stirred for 5 h at room temperature. Upon completion of reaction the reaction mixture was neutralized by saturated solution of NaHCO₃ and extracted with CHCl₃. The compound was purified by column chromatography (2.5 % MeOH in CHCl₃) which yields 120.7 mg (74%) of compound **1d** as colourless oil. **¹H NMR (400 MHz, CDCl₃):** δ 7.43 (s, 1H), 7.34 (d, *J* = 7.7 Hz, 2H), 7.29 – 7.20 (m, 1H), 3.98 (dd, *J* = 11.8, 2.4 Hz, 2H), 3.80 (d, *J* = 9.9 Hz, 2H), 3.72 (dd, *J* = 11.8, 2.7 Hz, 2H), 3.64 (d, *J* = 9.8 Hz, 2H), 2.75 (dq, *J* = 14.6, 7.3 Hz, 4H), 2.59 (td, *J* = 13.6, 6.8 Hz, 4H), 1.13 (t, *J* = 7.1 Hz, 12H); **¹³C NMR (100 MHz, CDCl₃/ CD₃OD (5:1)):** δ 134.92, 132.25, 128.71, 122.07, 70.38, 62.66, 55.48, 45.92, 29.60, 11.76; **IR:** ν/cm^{-1} 3356, 2967, 2925, 1641, 1467, 1393, 1291, 1108, 1050, 908, 797, 728; **HRMS (ESI):** Calc. for $C_{24}H_{36}N_2O_4H^+$ ($M+H$)⁺: 417.2748; Found: 417.2753

5.4.4. Ion Transport Experiments:

A. Ion-transporting activity studies across EYPC-LUV Δ HPTS: Ion transport and ion selectivity studies were performed following the similar procedure described in previous chapters.

B. Preferential Ion Selectivity Assay (FCCP) Assay: FCCP assay was performed following the similar procedure described in previous chapter.

C. Chloride transport activity across EYPC-LUVs Δ lucigenin:

Buffer and stock solution preparation: Solid NaNO₃ and NaCl were dissolved, in appropriate quantity, in Milli-Q water to get 200 mM NaNO₃ and 2 M NaCl solution. Stock solutions of all channel-forming compounds were prepared in HPLC grade CH₃CN/MeOH (2:3).

Preparation of EYPC-LUVs Δ lucigenin: In a clean and dry small round bottomed flask 1 mL egg yolk phosphatidylcholine (EYPC, 25 mg/mL stock in CHCl_3) was added. The solution was dried by purging of nitrogen with continuous rotation to form a transparent thin film of EYPC. The transparent film was kept under high vacuum for 6 h to remove all trace of CHCl_3 at room temperature. The resulting film was hydrated with 1 mL buffer (1 mM lucigenin, 200 mM NaNO_3) for 1 h with 5-6 times occasional vortexing and subjected to freeze-thaw cycle (≥ 12 times). Extrusions were performed 19 times (must be an odd number) by a Mini-extruder with a polycarbonate membrane of pore size 200 nm (Avanti). Extravesicular dyes were removed by gel filtration (using Sephadex G-50) with 200 mM NaNO_3 , and diluted to 3 mL to get EYPC-LUVs Δ lucigenin: inside: 1 mM lucigenin, 200 mM NaNO_3 , outside: 200 mM NaNO_3 .

Chloride transport activity: In a clean and dry fluorescence cuvette, 1950 μL of NaNO_3 solution (200 mM NaNO_3) was added followed by addition of 50 μL of EYPC-LUVs Δ lucigenin. The cuvette was placed in the fluorescence instrument in slowly stirring condition by a magnetic stirrer equipped with the instrument (at $t = 0$ s). The time course of lucigenin fluorescence emission intensity, F_t was observed at $\lambda_{\text{em}} = 535$ nm ($\lambda_{\text{ex}} = 450$ nm). 33.3 μL of 2 M NaCl was added to the cuvette at $t = 25$ s to create the chloride gradient between the intra and extra vesicular system. Channel forming compound were added at $t = 100$ s in different concentration and finally 25 μL of 10% Triton X-100 was added at $t = 300$ s to lyse those vesicles resulting destruction of chloride gradient (Figure 5.5).

Fluorescence intensities (F_t) were normalized to fractional emission intensity I_F using Equation 5.5:

$$I'_F = [(F_t - F_0) / (F_0 - F_\infty)] \times 100 \quad \text{Equation 5.5}$$

where, F_0 = Fluorescence intensity just before the compound addition (at 0 s). F_∞ = Fluorescence intensity at saturation after complete leakage (at 320 s). F_t = Fluorescence intensity at time t .

For data analysis and comparison, time (X-axis) was normalized to the point of transporter addition (*i.e.* $t = 100$ s was normalized to $t = 0$ s) and end point of the experiment (*i.e.* $t = 350$ s was normalized to $t = 250$ s).

D. Effect of extravesicular cation on Cl^- transport in EYPC-LUVs Δ lucigenin:

The involvement of cations in the transport process was evaluated by the lucigenin based assay. The preparation of solutions and vesicles are similar as described in section VII.C. In assay condition the chloride salt of various cation ($\text{M}^+ = \text{Li}^+, \text{Na}^+, \text{K}^+, \text{Rb}^+$ and Cs^+) were added to evaluate the contribution of cation in transport process.

Cation transport activity: In a clean and dry fluorescence cuvette 1950 μL of NaNO_3 solution (200 mM) was added followed by addition of 50 μL of EYPC-LUVs Δ lucigenin. The cuvette was placed in the fluorescence instrument in slow stirring condition by a magnetic stirrer equipped with the instrument (at $t = 0$ s). The time course of lucigenin fluorescence emission intensity, F_t was observed at $\lambda_{\text{em}} = 535$ nm ($\lambda_{\text{ex}} = 450$ nm). 33.3 μL of 2 M MCl ($\text{M}^+ = \text{Li}^+, \text{Na}^+, \text{K}^+, \text{Rb}^+$ and Cs^+) was added to the cuvette at $t = 25$ second to create the chloride gradient between the intra and extra-vesicular system. Channel forming compounds were added at $t = 100$ s in different concentration and finally 25 μL of 10% Triton X-100 was added at $t = 300$ s to lyse those vesicles resulting destruction of chloride gradient.

E. Effect of extravesicular anion on Cl^- efflux in EYPC-LUVs Δ lucigenin:

The chloride efflux was monitored in the form of fluorescence enhancement. Change in the rate of transport upon changing external anion gave the conformation of antiport mechanism.

Preparation of EYPC-LUVs Δ lucigenin: Vesicles were prepared according to the same procedure as stated above by keeping 150 mM NaCl in intravesicular matrix in stead of NaNO_3 solution.⁹

Antiport activity: In a clean and dry fluorescence cuvette 1950 μL of Na_mA solution (150 mM; $\text{A}^- = \text{F}^-, \text{ClO}_4^-, \text{NO}_3^-, \text{SO}_4^{2-}, \text{Cl}^-$; $m =$ valency of an anion) was added followed by addition of 50 μL of EYPC-LUVs Δ lucigenin. The cuvette was placed in fluorescence instrument in slowly stirring condition by a magnetic stirrer equipped with the instrument (at $t = 0$ s). The time course of lucigenin fluorescence emission intensity, F_t was observed at $\lambda_{\text{em}} = 535$ nm ($\lambda_{\text{ex}} = 450$ nm). Transporter molecules were added at $t = 100$ s in different concentration and finally 25 μL of 10% Triton X-100 was added at $t = 300$ s to lyse those vesicles resulting destruction of chloride gradient.

F. Preferential transport mechanism by lucigenin assay:

The direct experimental insight of preferential ion transporting mechanism for **1c** was obtained by lucigenin assay in the presence of valinomycin. Vesicles containing lucigenin and NaNO_3 were prepared and suspended in KCl solution, and the ion transport rate of **1c** was monitored in the absence and presence of valinomycin. The significant enhancement in the rate of transport presence of valinomycin indicates the antiport mechanism as a preferential transport mechanism (Figure 5.8).

Preparation of EYPC-LUVs Δ lucigenin: Vesicles were prepared according to the same procedure as stated above by keeping 200 mM NaNO_3 in intravesicular matrix.⁹

Antiport activity: In a clean and dry fluorescence cuvette 1950 μL of NaNO_3 solution was added followed by addition of 50 μL of EYPC-LUVs Δ lucigenin. The cuvette was placed in fluorescence instrument in slowly stirring condition by a magnetic stirrer equipped with the instrument (at $t = 0$ s). The time course of lucigenin fluorescence emission intensity, F_t was observed at $\lambda_{\text{em}} = 535$ nm ($\lambda_{\text{ex}} = 450$ nm). 33.3 μL of 2 M KCl was added to the cuvette at $t = 25$ s to create the chloride gradient between the intra and extra-vesicular system. Valinomycin (2.5 μM) was added to the cuvette at 50 s. After that **1c** (20 μM) was added at $t = 100$ s and finally at $t = 300$ s 25 μL of 10% Triton X-100 was added to lyse those vesicles resulting destruction of chloride gradient.

5.4.5. Evidence of Ion Channel Formation:

Planar Bilayer Conductance Measurements: Bilayer membrane (BLM) was formed across an aperture of 150 μm diameter in a polystyrene cup (Warner Instrument, USA) with lipid diphytanoylphosphatidylcholine (DPhPC; Avanti Polar Lipids), dissolved in *n*-decane (20 mg/mL). Both *cis* and *trans* compartments were filled with symmetrical solution, containing 1 M KCl. The *cis* compartment was held at virtual ground, and the *trans* chamber was connected to the BC 535 head-stage (Warner Instrument, USA) via matched Ag-AgCl electrodes. Derivative **1c** was added to the *cis* chamber, and the solution was stirred with magnetic stirrer. It formed channels within 30 minutes, as observed by the distinct channel opening and closing events at different voltages. Currents were low-pass filtered at 1 kHz and digitized at 5 kHz using pClamp9 software (Molecular Probes, USA) and an analog-to-digital converter (Digidata 1440A, Molecular Devices). Positive clamping potentials refer potentials with respect to the ground, and positive currents are presented as upward deflections from the base line (0 pA). The software pClamp 9 was used for data acquisition and analysis. I-V curve was generated from the BLM, containing multiple channels using a voltage ramp from -80 mV to $+80$ mV (for 40 s time duration).

The effective channel diameter was calculated from the single channel conductance value, by using equation 5.6.

$$1/g = (l + \pi d/4)(4\rho/\pi d^2)$$

Equation 5.6

Where, g = corrected conductance (obtained by multiplying measured single channel conductance with the Sansom's correction factor), l length of the ion channel (34 Å), and ρ = resistivity of the recording solution ($\rho = 10.1 \Omega \cdot \text{cm}$).

5.4.6. Molecular Modeling Studies:

To design the model of the ion channel we had optimized the monomer-dimer using Gaussian 09²⁷ software with wB97XD²⁸ functional and 6-31G (d,p) basis set in the vacuum. The oligomeric structure of channel was further optimized with MOPAC2012¹⁹ software package using PM6-DH+³⁰ methods.

5.4.7. Biological studies:

A. Cell culture protocol:

All cell lines were grown in High Glucose Dulbecco's Modified Eagle Medium (DMEM; Invitrogen or Lonza) containing 10% fetal bovine serum (FBS; Invitrogen), 2 mM L-glutamine (Invitrogen) and 100 units/mL penicillin-streptomycin (Invitrogen). Cells were maintained in 100 mm tissue culture treated dishes (Corning) at 37 °C in humidified 5% CO₂ incubator (Thermo Scientific).

B. Measurement of intracellular Cl⁻ concentrations: Time-dependent influx data of Cl⁻ were measured in HeLa cells by using chloride selective cell permeable fluorescent dye *N*-(ethoxycarbonylmethyl)-6-methoxyquinolinium bromide (MQAE). Cells were suspended in a 96-well flat bottom tissue culture treated plates (Corning) at a density of 10⁴ cells/well (per 100 μL) and incubated at 37 °C, 5% CO₂ for 14 h. MQAE was added to each well by maintaining final concentration as 5 mM for 3 h. Extracellular dye was removed by washing with PBS and compound **1c** was added in DMEM at various concentrations and cells were incubated for 24 h. The MQAE fluorescence was measured using a fluorescence microplate reader ($\lambda_{\text{ex}} = 350$ nm and $\lambda_{\text{em}} = 460$ nm) (Figure 5.11). Fluorescence intensities were normalized with respect to the emission intensity of untreated cells. Each bar represents the mean intensity of three independent experiments, and the differences in mean intensities are statistically significant according to one-way analysis of variance (ANOVA).

C. MTT-based cytotoxicity assay: Cells were dispersed in a 96-well flat bottom tissue culture treated plates (Corning) at a density of 10⁴ cells/well (per 100 μL) and incubated at 37 °C in a 5% CO₂ incubator for 14 h. Compound **1c** was added to each well in different concentration by maintaining the maximum amount of DMSO at 1 μL and incubated for 24 h. DMEM solution containing compounds in each well were replaced with 100 μL of MTT-DMEM mixture (0.5 mg MTT/mL of DMEM) and incubated for 4 h in identical condition. After 4 h, MTT solution was removed and 100 μL of DMSO was added to each well to dissolve the formazan crystals. The absorbance was recorded in a microplate reader (Varioskan Flash) at the wavelength of 570 nm. All experiments were performed in triplicate, and the relative cell viability (%) was expressed as a percentage about the untreated cells.

D. Chloride mediated cell death studies:

HBSS buffer solution. Hank's balanced salt solution (HBSS with Cl^-) was prepared with the following compositions: 136.9 mM NaCl, 5.5 mM KCl, 0.34 mM Na_2HPO_4 , 0.44 mM KH_2PO_4 , 0.81 mM MgSO_4 , 1.25 mM CaCl_2 , 5.5 mM D-glucose, 4.2 mM NaHCO_3 and 10 mM HEPES (pH 7.4). Chloride free HBSS was prepared by mixing 136.9 mM Na-gluconate, 5.5 mM K-gluconate, 0.34 mM Na_2HPO_4 , 0.44 mM KH_2PO_4 , 0.81 mM MgSO_4 , 1.25 mM Ca-gluconate, 5.5 mM D-glucose, 4.2 mM NaHCO_3 and 10 mM HEPES (pH 7.4).

Cells were dispersed in a 96-well flat bottom tissue culture treated plates (Corning) at a density of 10^4 cells/well (per 100 μL) and incubated at 37 °C in 5% CO_2 for 14 h. Cellular media was replaced by HBSS buffer (either with Cl^- or without Cl^-) containing 10% FBS. Compound **1c** were added to each well in different concentration by maintaining the maximum amount of DMSO at 1 μL and incubated for 24 h. HBSS buffer solution of compounds in each well was replaced by 100 μL of MTT-HBSS mixture (0.5 mg MTT/mL of HBSS) and incubated for 4 h in identical condition. Excess MTT solution was removed after 4 h and 100 μL of DMSO was added to each well to dissolve the formazan crystals. The absorbance was recorded in a microplate reader (Varioskan Flash) at the wavelength of 570 nm (Figure 5.13). Each bar represents the mean intensity of three independent experiments, and the differences in mean intensities are statistically very significant ($P < 0.01$) according to one-way analysis of variance (ANOVA).

E. Mitochondrial membrane depolarization: The HeLa cells were seeded in glass bottom 35 mm dishes at the concentration of 0.75×10^5 cells per plate. Cells were incubated with 0, 5, 10 and 20 μM of **1c** for 24 h. After that cells were washed thoroughly and incubated with JC-1 at the final concentration of 1 $\mu\text{g}/\text{mL}$ for 30 min. Fluorescence images were acquired after washing with PBS in both red and green channel (Figure 5.14). A bar diagram was plotted by calculating the ratio of pixel intensities (red/green) from 7 different images of each set of cells. One way ANOVA analysis of seven replicate images show the statistically significant ($P < 0.01 - 0.001$) mean difference in the ratio of pixel intensity.

F. Measurement of ROS level: Cells were dispersed in a 96-well flat bottom tissue culture treated plates (Corning) at density of 1.5×10^4 cells/well (per 100 μL) and incubated at 37 °C in a 5% CO_2 incubator for 14 h. Compound **1c** was added to each well in different concentration (0–50 μM) by maintaining the maximum amount of DMSO at 1 μL and incubated for 7 h. 3-methyl-7-(4,4,5,5-tetramethyl-1,3,2-dioxaborolan-2-yl)-2H-chromen-2-one (**ROS probe**)^{44,45} was added to the each well at final concentration 50 μM and incubated further for 1 h. The fluorescence was recorded in a microplate reader (Varioskan Flash) at the wavelength of $\lambda_{\text{em}} =$

460 nm ($\lambda_{\text{ex}} = 315$ nm) (Figure 5.15). All experiments were performed in triplicate, and the relative emission intensity was normalized with respect to the untreated cell. Each bar represents the mean intensity of three independent experiments, and the differences in mean intensity are found to be statistically significant ($P < 0.001$) according to one-way analysis of variance (ANOVA).

G. Immunofluorescence analysis for cytochrome *c* release: Cells were seeded at a density of 1×10^5 cells per well on top of glass coverslips (Micro-Aid, India). Following **1c** (0, 10 and 20 μM) treatment, cells were fixed using 4% formalin (Macron Chemicals) and were permeabilized using 0.5% Triton X-100 for 10 min at 4 °C. Cells were blocked with 10% (v/v) FBS (Invitrogen), stained with primary antibody (cytochrome *c* antibody) and then incubated with secondary antibody (goat anti-rabbit AlexaFluor-488). Cells were then counterstained with 0.5 $\mu\text{g}/\text{mL}$ Hoechst 33342 and mounted on glass slides (Micro-Aid, India). Cell images were taken using Olympus Inverted IX81 microscope equipped with Hamamatsu Orca R2 camera. Microscopy images were captured using 100X oil-immersion objective (Figure 5.16).

H. Immunoblot analysis: Cells were seeded at a density of 6×10^5 cells per well in 6-well tissue culture treated plates (Corning) and maintained at 37 °C for 16 h. Cells were then treated with **1c** by direct addition of the drug to the culture medium for 24 h at different concentration (0, 5, 10 and 20 μM). Control cells were treated with an equivalent volume of DMSO. After 24 h treatment, medium containing **1c** was aspirated, and cells were washed once with 1X phosphate buffered saline (PBS; PAN-Biotech GmbH). Cells were lysed in sample buffer containing 60 mM Tris (pH 6.8), 6% glycerol, 2% sodium dodecyl sulfate (SDS), 0.1 M dithiothreitol (DTT) and 0.006% bromophenol blue and lysates were stored at -40 °C.

Cell lysates were resolved using sodium dodecyl sulfate polyacrylamide gel electrophoresis (SDS-PAGE) and transferred to Immobilon-P polyvinylidene difluoride (PVDF) membrane (Millipore). Blocking was performed in 5% (w/v) skimmed milk (SACO Foods, USA) prepared in 1X Tris-buffered saline containing 0.1% Tween 20 (1X TBS-T) for 1 h at room temperature. Blots were incubated for 3 h at room temperature (or for 16 h at 4 °C) in primary antibody solution. Following washes, blots were incubated with peroxidase-conjugated secondary antibody solution prepared in 5% (w/v) skimmed milk in 1X TBS-T for 1 h at room temperature following which blots were developed using Immobilon Western Detection Reagent kit (Millipore) and visualized using ImageQuant LAS 4000 (GE Healthcare).

I. Caspase Inhibitor Activity:

Inhibitor for caspase-3: Benzyloxycarbonyl-Asp(OMe)-Glu(OMe)-Val-Asp(OMe)-fluoromethylketone (z-DEVD-fmk).

Inhibitor for caspase-9: Benzyloxycarbonyl-Leu-Glu(OMe)-His-Asp(OMe)-fluoromethylketone (z-LEHD-fmk).

Cell viability was checked via MTT assay according to the similar procedure as stated above. HeLa cells were preincubated with caspase inhibitors (100 μ M each) followed by incubation with **1c** (20 μ M) for 24 h (Figure 19). The bar diagram represents the mean intensity of three independent experiments and the differences in mean intensities are statistically significant ($P < 0.0001$), in each case, according to one-way analysis of variance (ANOVA).

5.4.8. NMR Spectra:

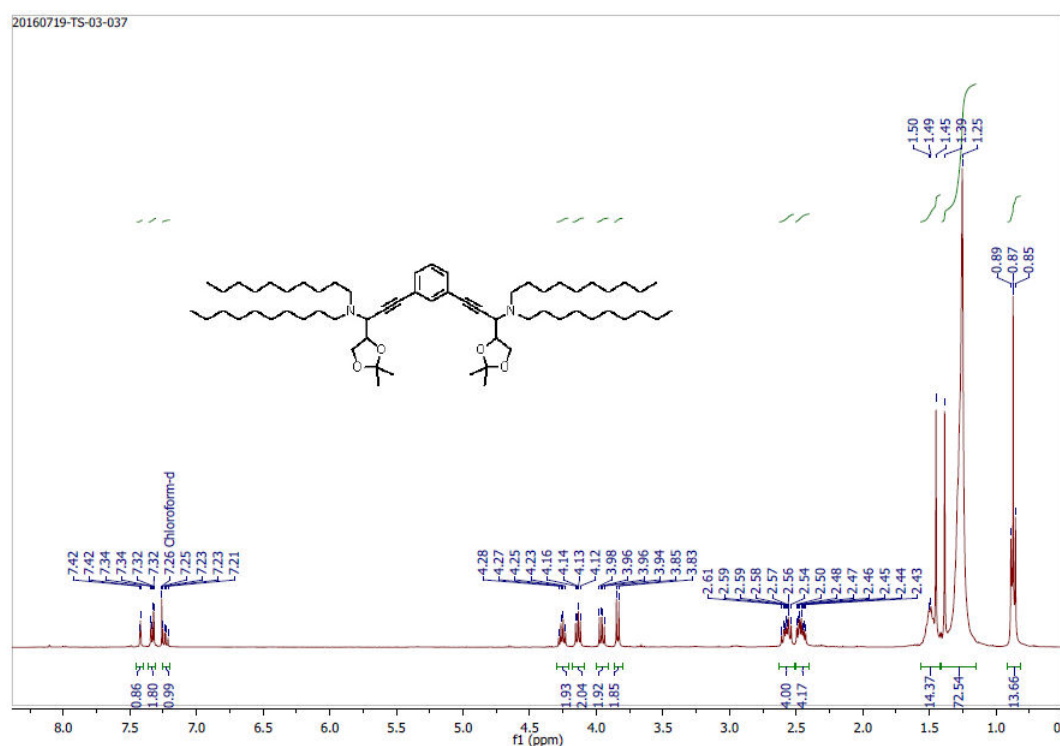


Figure 5.20. ^1H NMR spectrum of **5a**.

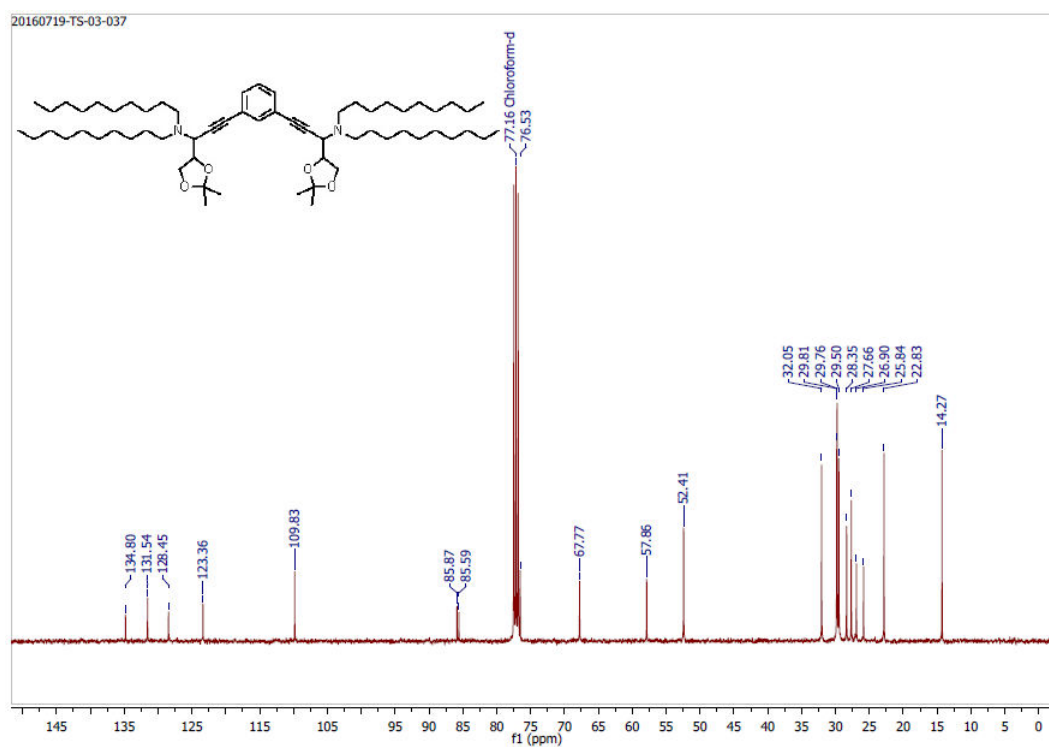


Figure 5.21. ^{13}C NMR spectrum of 5a.

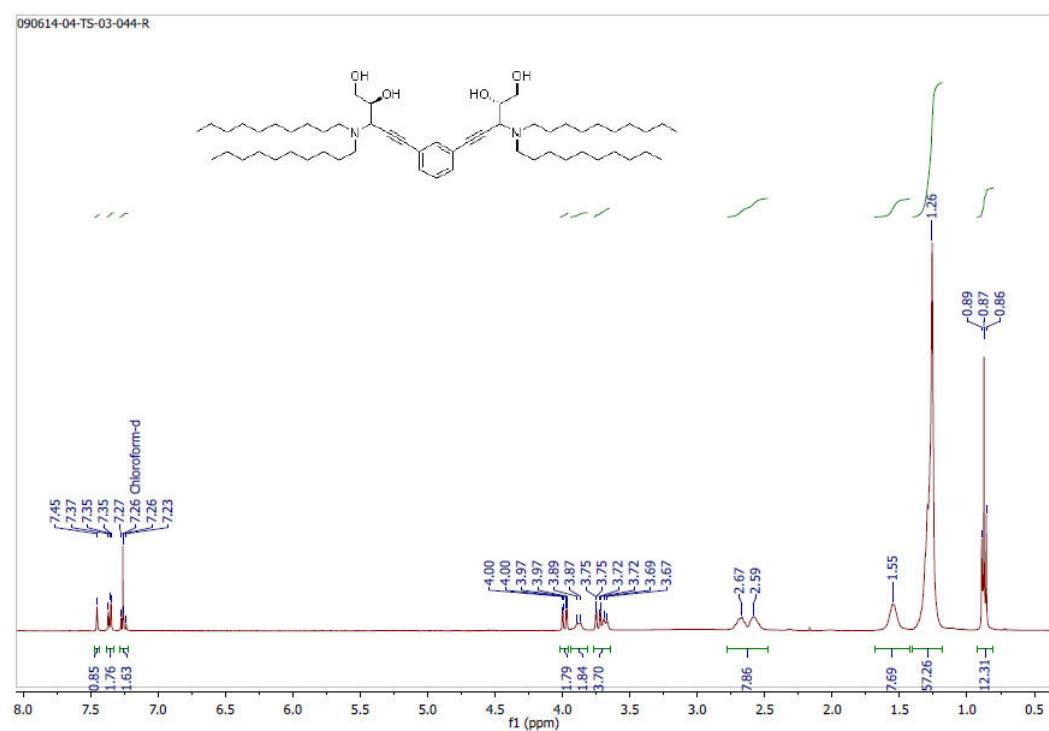


Figure 5.22. ^1H NMR spectrum of 1a.

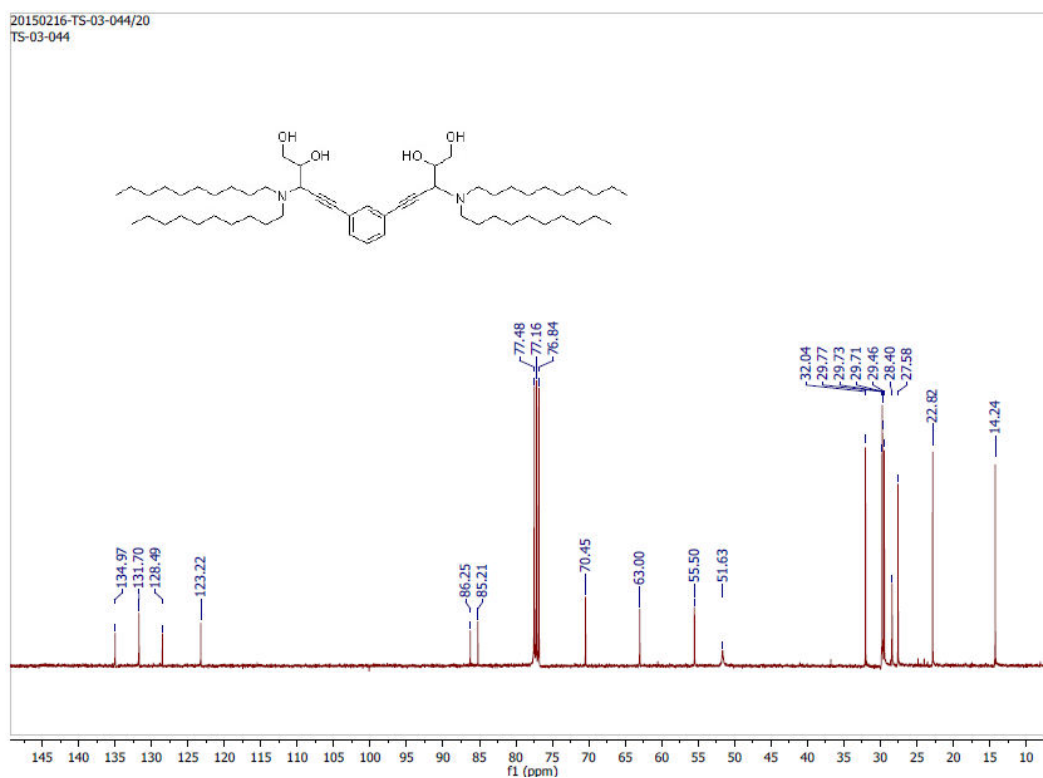


Figure 5.23. ^{13}C NMR spectrum of **1a**.

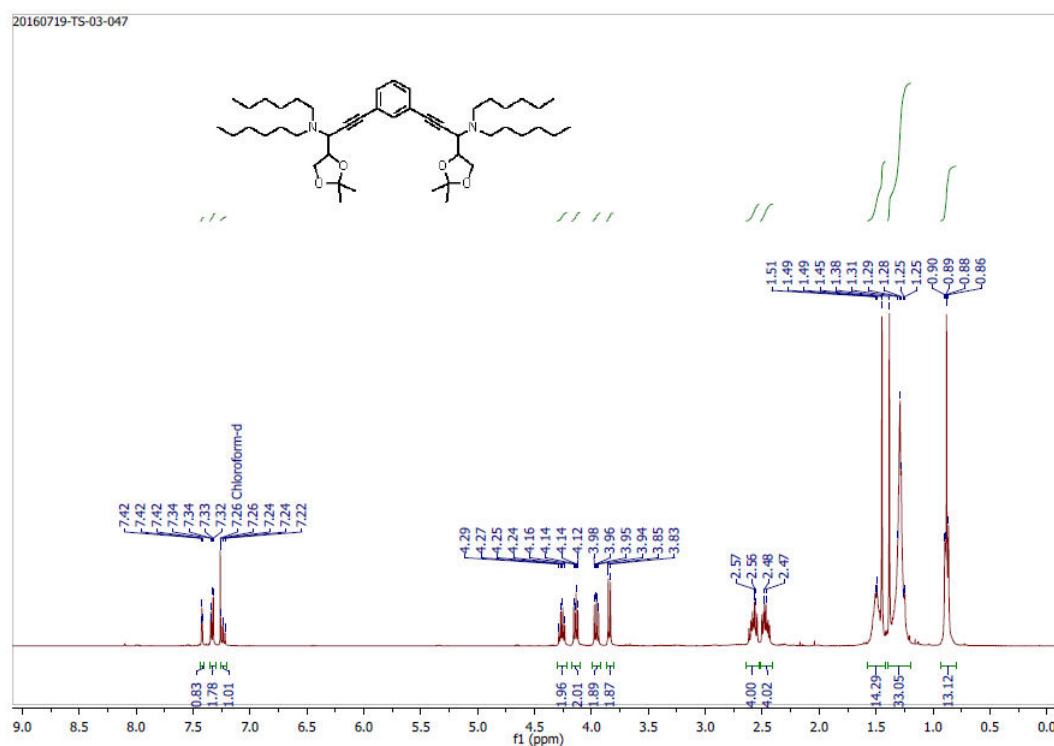


Figure 5.24. ^1H NMR spectrum of **5b**.

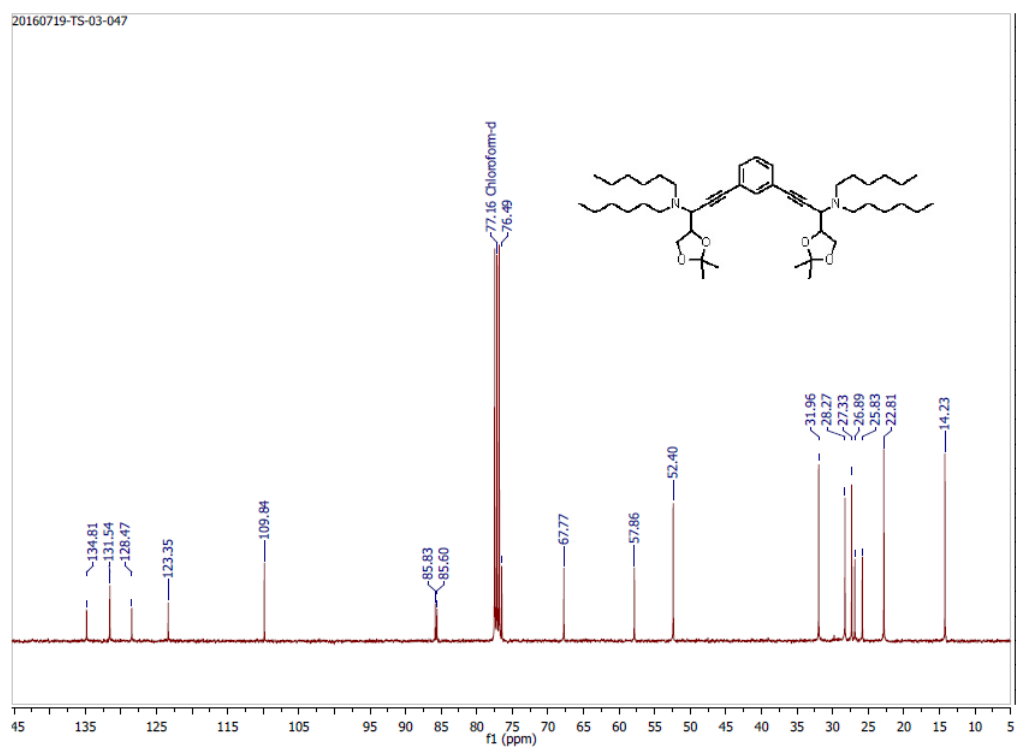


Figure 5.25. ^{13}C NMR spectrum of **5b**.

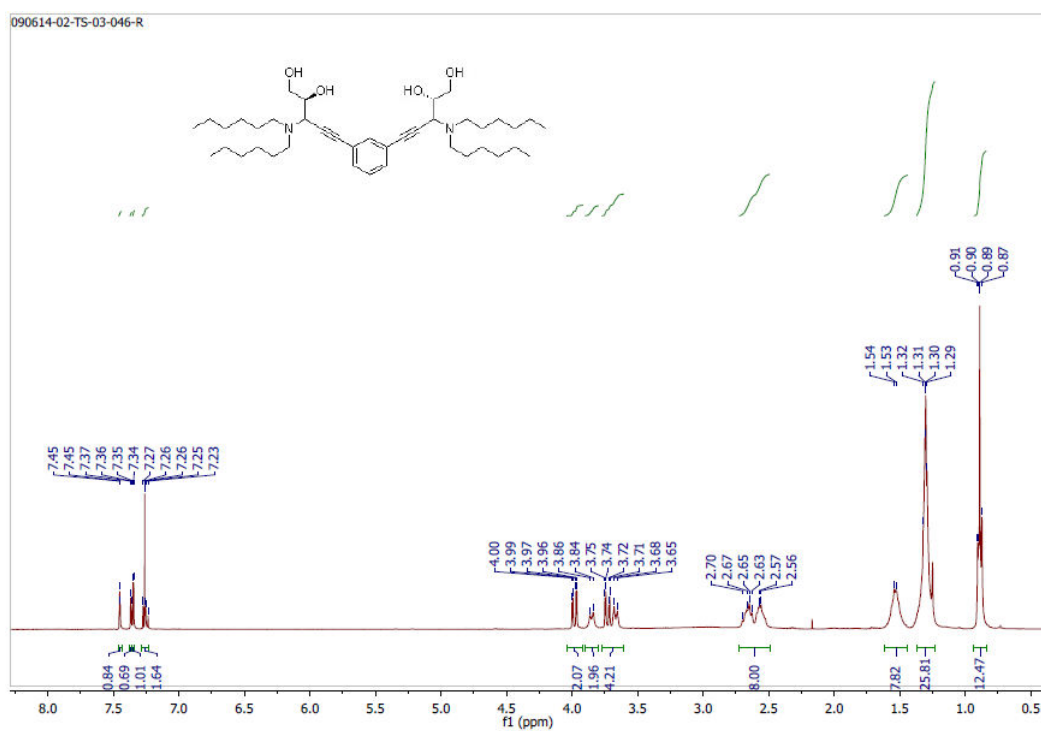


Figure 5.26. ^1H NMR spectrum of **1b**.

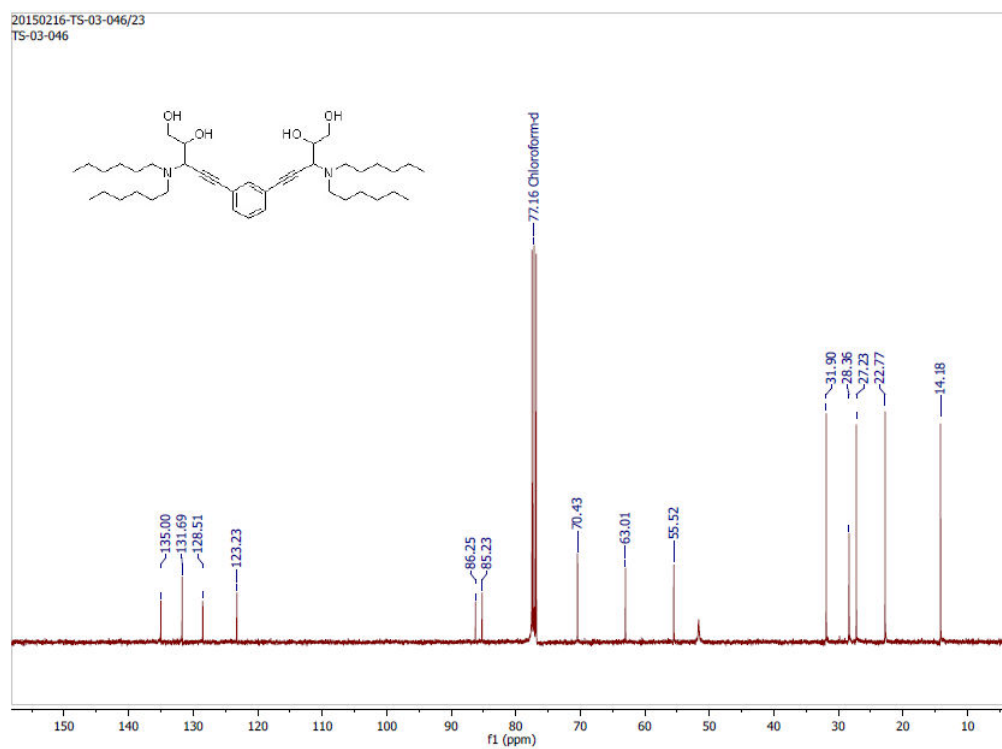


Figure 5.27. ^{13}C NMR spectrum of **1b**.

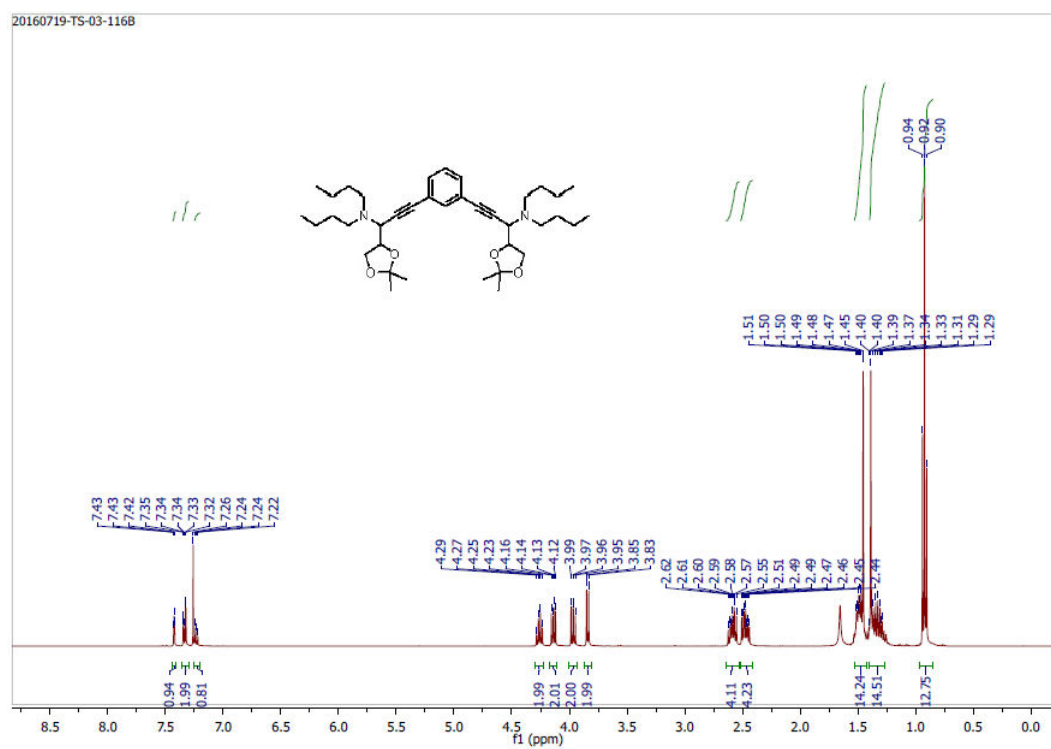


Figure 5.28. ^1H NMR spectrum of **5c**.

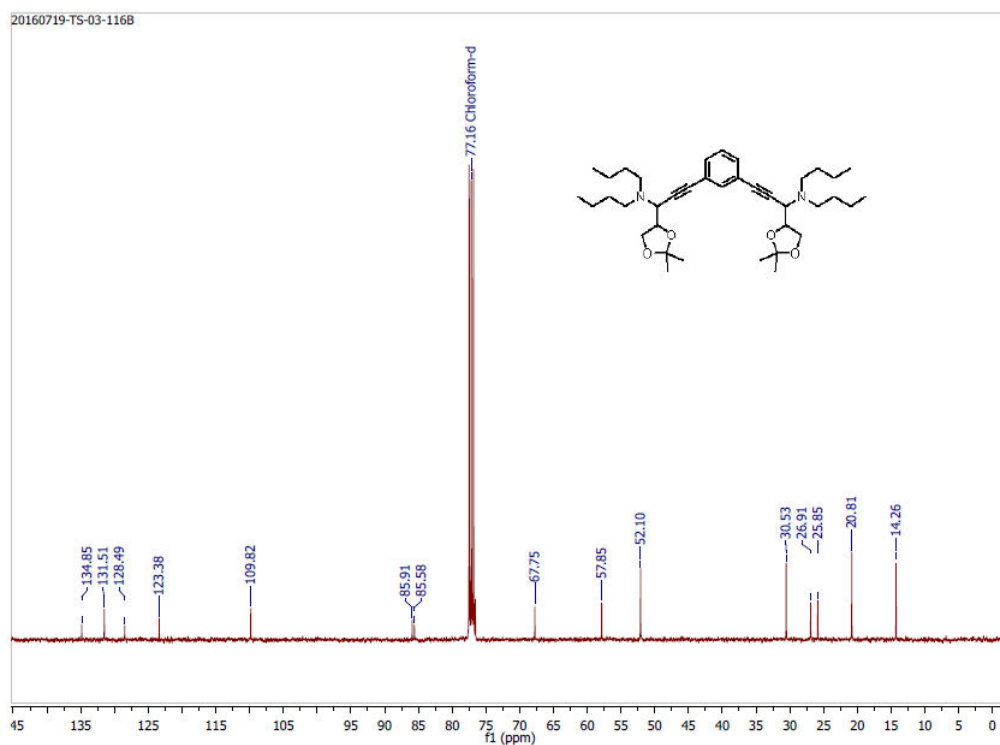


Figure 5.29. ^{13}C NMR spectrum of 5c.

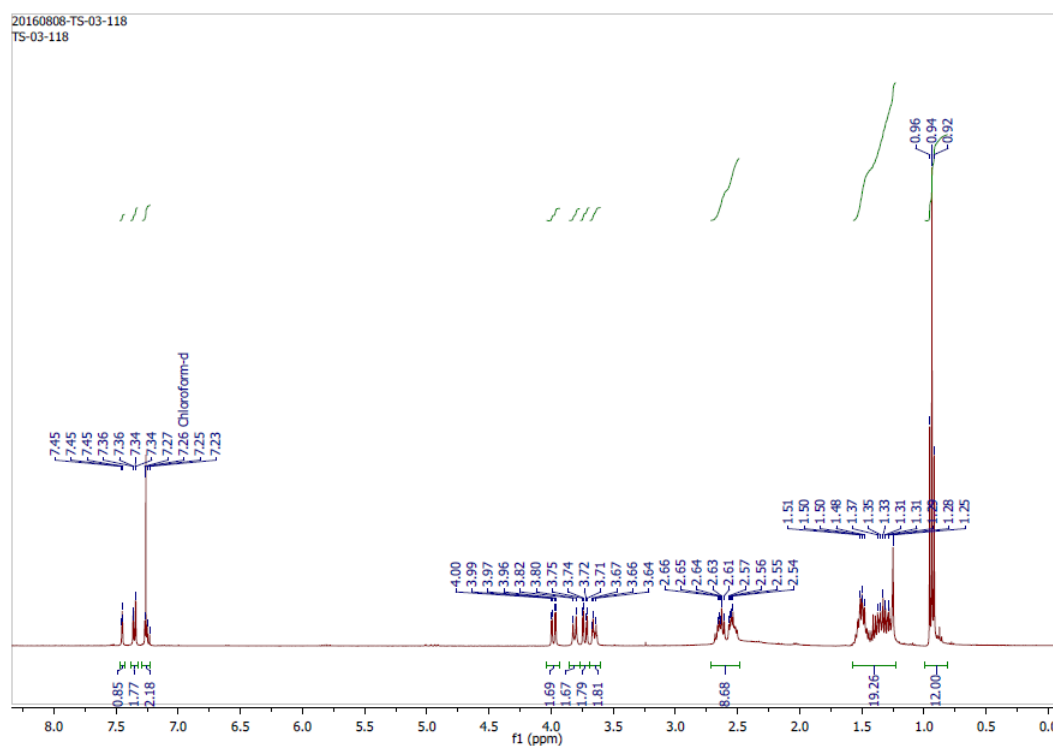


Figure 30. ^1H NMR spectrum of 1c.

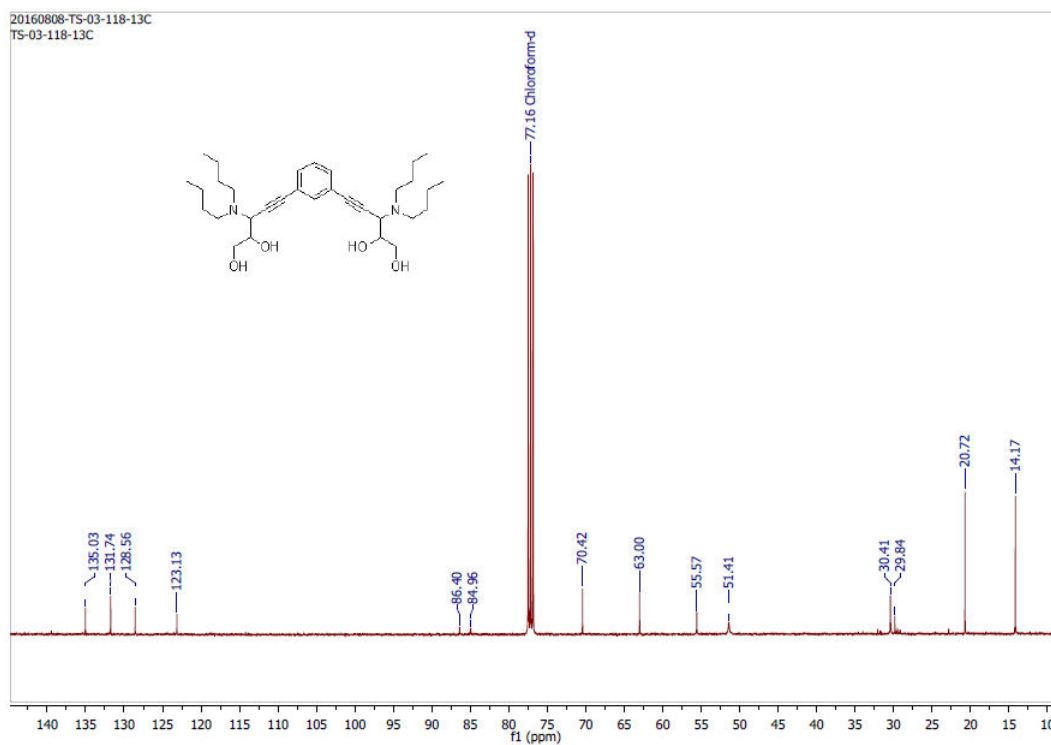


Figure 5.31. ^{13}C NMR spectrum of 1c.

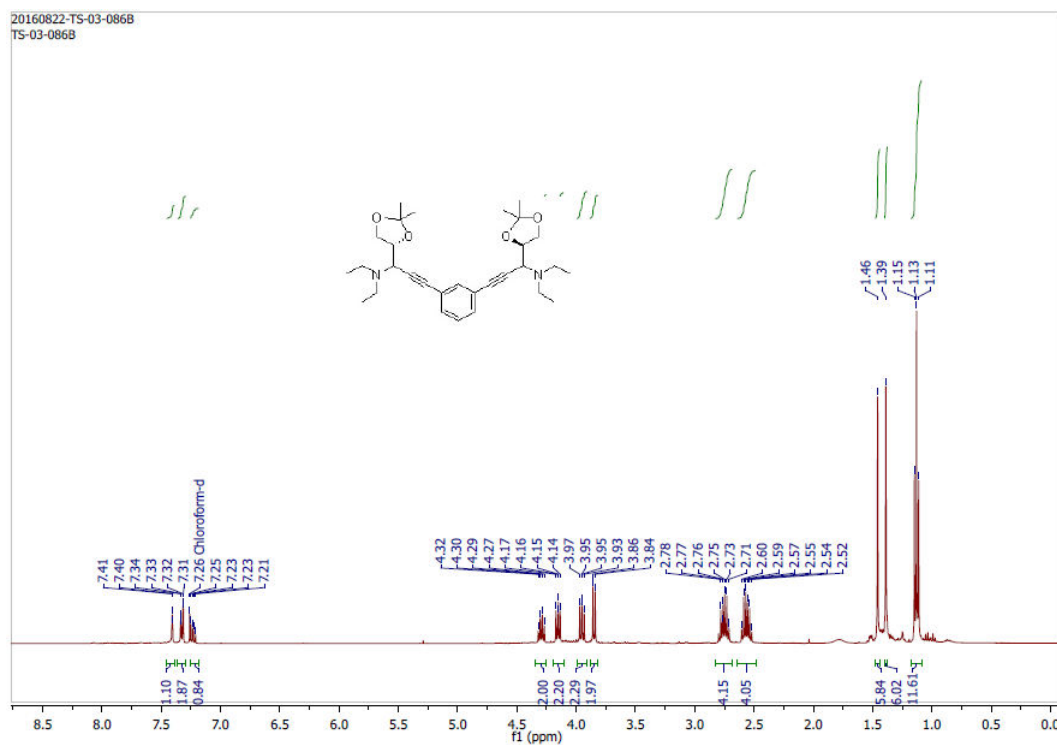


Figure 5.32. ^1H NMR spectrum of 5d.

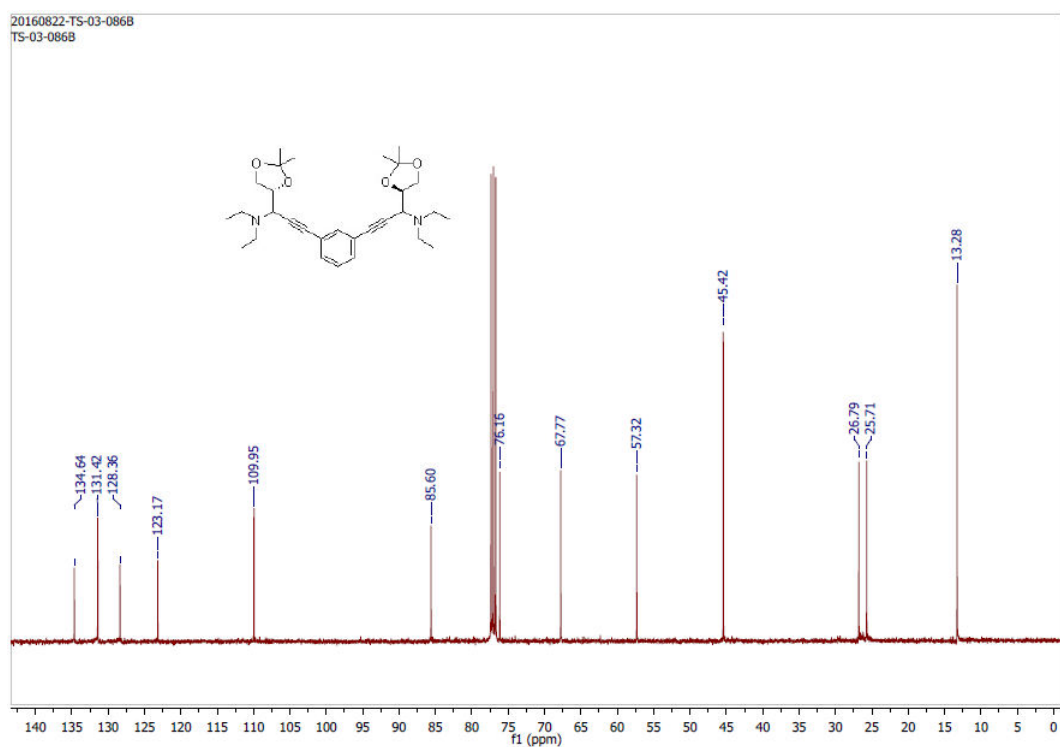


Figure 5.33. ^{13}C NMR spectrum of **5d**.

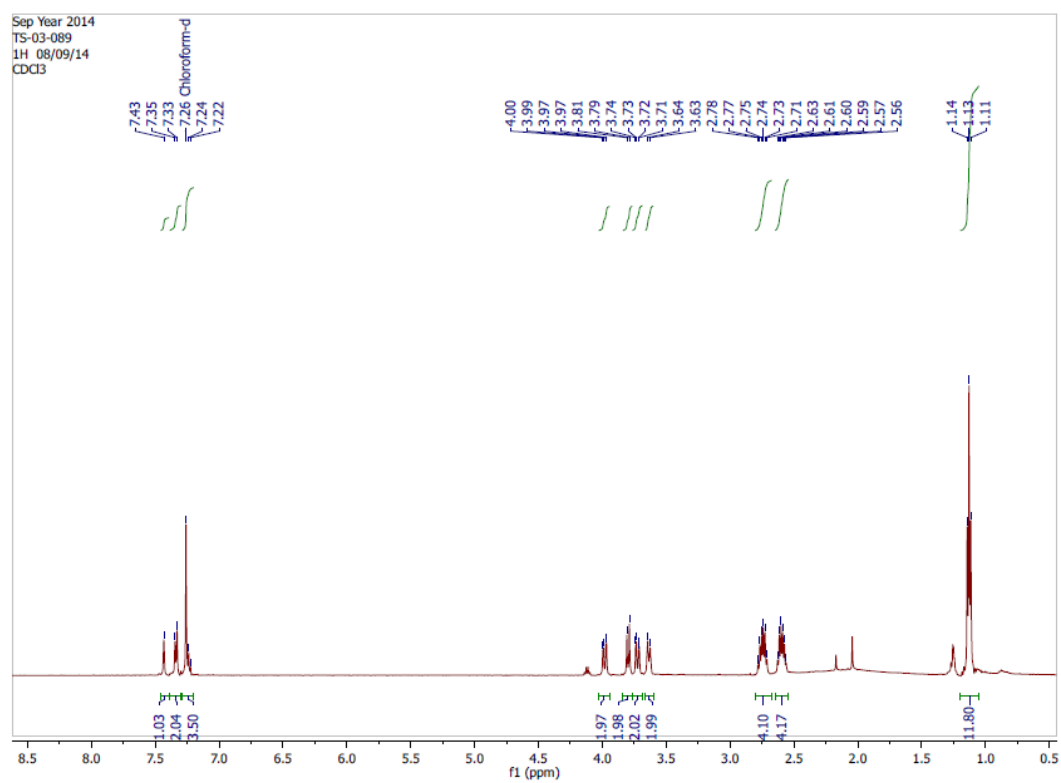


Figure 5.34. ^1H NMR spectrum of **1d**.

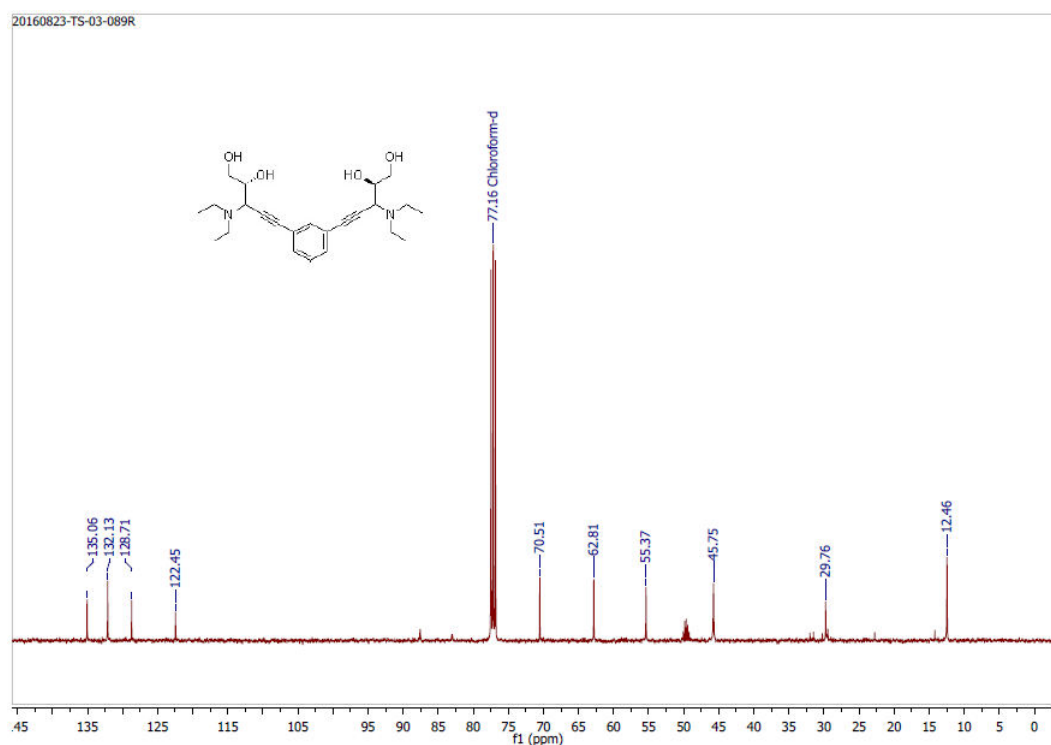


Figure 5.35. ^{13}C NMR spectrum of **1d**.

5.5. REFERENCE:

- (1) Broughman, J. R.; Shank, L. P.; Takeguchi, W.; Schultz, B. D.; Iwamoto, T.; Mitchell, K. E.; Tomich, J. M. *Biochemistry* **2002**, *41*, 7350.
- (2) Tomich, J. M.; Bukovnik, U.; Layman, J.; Schultz, B. D. *Cystic Fibrosis: Renewed Hopes through Research* **2012**, 291.
- (3) Leevy, W. M.; Donato, G. M.; Ferdani, R.; Goldman, W. E.; Schlesinger, P. H.; Gokel, G. W. *J. Am. Chem. Soc.* **2002**, *124*, 9022.
- (4) Leevy, W. M.; Gokel, M. R.; Hughes-Strange, G. B.; Schlesinger, P. H.; Gokel, G. W. *New J. Chem.* **2005**, *29*, 205.
- (5) Fernandez-Lopez, S.; Kim, H.-S.; Chol, E. C.; Delgado, M.; Granja, J. R.; Khasanov, A.; Kraehenbuehl, K.; Long, G.; Weinberger, D. A.; Wilcoxon, K. M.; Ghadiri, M. R. *Nature* **2001**, *414*, 329.
- (6) Leevy, W. M.; Gammon, S. T.; Levchenko, T.; Daranciang, D. D.; Murillo, O.; Torchilin, V.; Piwnica-Worms, D.; Huettner, J. E.; Gokel, G. W. *Org. Biomol. Chem.* **2005**, *3*, 3544.
- (7) Boudreault, P.-L.; Arseneault, M.; Otis, F.; Voyer, N. *Chem. Commun.* **2008**, 2118.
- (8) Smith, B. A.; Daschbach, M. M.; Gammon, S. T.; Xiao, S.; Chapman, S. E.; Hudson, C.; Suckow, M.; Piwnica-Worms, D.; Gokel, G. W.; Leevy, W. M. *Chem. Commun.* **2011**, 47, 7977.

- (9) Busschaert, N.; Wenzel, M.; Light, M. E.; Iglesias-Hernández, P.; Pérez-Tomás, R.; Gale, P. A. *J. Am. Chem. Soc.* **2011**, *133*, 14136.
- (10) Moore, S. J.; Wenzel, M.; Light, M. E.; Morley, R.; Bradberry, S. J.; Gomez-Iglesias, P.; Soto-Cerrato, V.; Perez-Tomas, R.; Gale, P. A. *Chem. Sci.* **2012**, *3*, 2501.
- (11) Moore, S. J.; Haynes, C. J. E.; Gonzalez, J.; Sutton, J. L.; Brooks, S. J.; Light, M. E.; Herniman, J.; Langley, G. J.; Soto-Cerrato, V.; Perez-Tomas, R.; Marques, I.; Costa, P. J.; Felix, V.; Gale, P. A. *Chem. Sci.* **2013**, *4*, 103.
- (12) Ko, S.-K.; Kim, S. K.; Share, A.; Lynch, V. M.; Park, J.; Namkung, W.; Van Rossom, W.; Busschaert, N.; Gale, P. A.; Sessler, J. L.; Shin, I. *Nat. Chem.* **2014**, *6*, 885.
- (13) Soto-Cerrato, V.; Manuel-Manresa, P.; Hernando, E.; Calabuig-Fariñas, S.; Martinez-Romero, A.; Fernandez Dueñas, V.; Sahlholm, K.; Knopfel, T.; Garcia-Valverde, M.; Rodilla, A. M.; Jantus-Lewintre, E.; Farras, R.; Ciruela, F.; Perez-Tomas, R.; Quesada, R. *J. Am. Chem. Soc.* **2015**, *137*, 15892.
- (14) Saha, T.; Hossain, M. S.; Saha, D.; Lahiri, M.; Talukdar, P. *J. Am. Chem. Soc.* **2016**, *138*, 7558.
- (15) Saggiomo, V.; Otto, S.; Marques, I.; Felix, V.; Torroba, T.; Quesada, R. *Chem. Commun.* **2012**, *48*, 5274.
- (16) Haynes, C. J. E.; Moore, S. J.; Hiscock, J. R.; Marques, I.; Costa, P. J.; Felix, V.; Gale, P. A. *Chem. Sci.* **2012**, *3*, 1436.
- (17) Busschaert, N.; Bradberry, S. J.; Wenzel, M.; Haynes, C. J. E.; Hiscock, J. R.; Kirby, I. L.; Karagiannidis, L. E.; Moore, S. J.; Wells, N. J.; Herniman, J.; Langley, G. J.; Horton, P. N.; Light, M. E.; Marques, I.; Costa, P. J.; Felix, V.; Frey, J. G.; Gale, P. A. *Chem. Sci.* **2013**, *4*, 3036.
- (18) Lipinski, C. A.; Lombardo, F.; Dominy, B. W.; Feeney, P. J. *Adv. Drug Deliv. Rev.* **1997**, *23*, 3.
- (19) Marvin 5.8.0, 2012, ChemAxon (<http://www.chemaxon.com>).
- (20) Deshmukh, S. C.; Roy, A.; Talukdar, P. *Org. Biomol. Chem.* **2012**, *10*, 7536.
- (21) Deshmukh, S. C.; Talukdar, P. *J. Org. Chem.* **2014**, *79*, 11215.
- (22) Saha, T.; Dasari, S.; Tewari, D.; Prathap, A.; Sureshan, K. M.; Bera, A. K.; Mukherjee, A.; Talukdar, P. *J. Am. Chem. Soc.* **2014**, *136*, 14128.
- (23) Sugisaki, Claudia H.; Ruland, Y.; Baltas, M. *Eur. J. Org. Chem.* **2003**, *2003*, 672.
- (24) Benz, R.; McLaughlin, S. *Biophys. J.* **1983**, *41*, 381.
- (25) Biwersi, J.; Tulk, B.; Verkman, A. S. *Anal. Biochem.* **1994**, *219*, 139.
- (26) Ishida, H.; Qi, Z.; Sokabe, M.; Donowaki, K.; Inoue, Y. *J. Org. Chem.* **2001**, *66*, 2978.
- (27) Frisch M. J., Trucks G. W., Schlegel H. B., Scuseria G. E., Robb M. A., Cheeseman J. R., Scalmani G., Barone V., Mennucci B., Petersson G. A., Nakatsuji H., Caricato M., Li X., Hratchian H. P., Izmaylov A. F., Bloino J., Zheng G., Sonnenberg J. L., Hada M., Ehara

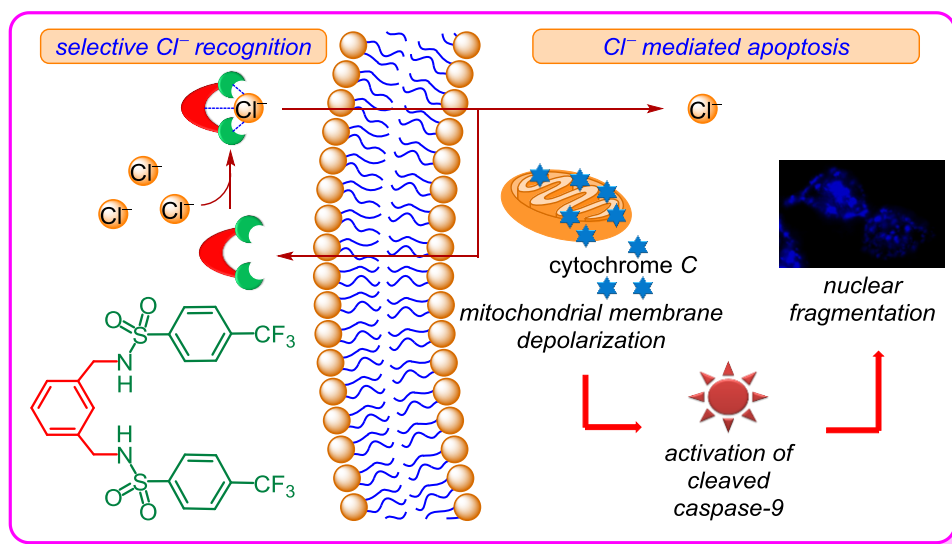
- M., Toyota K., Fukuda R., Hasegawa J., Ishida M., Nakajima T., Honda Y., Kitao O., Nakai H., Vreven T., Montgomery J. A., Jr., Peralta J. E., Ogliaro F., Bearpark M., Heyd J. J., Brothers E., Kudin K. N., Staroverov V. N., Keith T., Kobayashi R., Normand J., Raghavachari K., Rendell A., Burant J. C., Iyengar S. S., Tomasi J., Cossi M., Rega N., Millam J. M., Klene M., Knox J. E., Cross J. B., Bakken V., Adamo C., Jaramillo J., Gomperts R., Stratmann R. E., Yazyev O., Austin A. J., Cammi R., Pomelli C., Ochterski J. W., Martin R. L., Morokuma K., Zakrzewski V. G., Voth G. A., Salvador P., Dannenberg J. J., Dapprich S., Daniels A. D., Farkas O., Foresman J. B., Ortiz J. V., Cioslowski J., and Fox D. J. Gaussian 09, Revision B.01, Gaussian, Inc., Wallingford CT, **2010**.
- (28) Chai, J.-D.; Head-Gordon, M. *Phys. Chem. Chem. Phys.* **2008**, *10*, 6615.
- (29) J. J. P. Stewart, *MOPAC2012*, Stewart Computational Chemistry, Colorado Springs, CO, USA, 2012.
- (30) Korth, M. *J. Chem. Theory Comput.* **2010**, *6*, 3808.
- (31) Verkman, A. S. *Am. J. Physiol. Cell Physiol.* **1990**, *259*, C375.
- (32) Zhu, Y.; Parsons, S. P.; Huizinga, J. D. *Neurogastroenterol. Motil.* **2010**, *22*, 704.
- (33) Tsukimoto, M.; Harada, H.; Ikari, A.; Takagi, K. *J. Biol. Chem.* **2005**, *280*, 2653.
- (34) Yu, L.; Jiang, X. H.; Zhou, Z.; Tsang, L. L.; Yu, M. K.; Chung, Y. W.; Zhang, X. H.; Wang, A. M.; Tang, H.; Chan, H. C. *PLoS One* **2011**, *6*, e17322.
- (35) Ly, J. D.; Grubb, D. R.; Lawen, A. *Apoptosis* **2003**, *8*, 115.
- (36) Chu, Z.-L.; Pio, F.; Xie, Z.; Welsh, K.; Krajewska, M.; Krajewski, S.; Godzik, A.; Reed, J. C. *J. Biol. Chem.* **2001**, *276*, 9239.
- (37) Drušković, M.; Šuput, D.; Milisav, I. *Croatian Med. J.* **2006**, *47*, 832.
- (38) Ashkenazi, A. *Nat Rev Drug Discov.* **2008**, *7*, 1001.
- (39) Loreto, C.; La Rocca, G.; Anzalone, R.; Caltabiano, R.; Vespasiani, G.; Castorina, S.; Ralph, D. J.; Celtek, S.; Musumeci, G.; Giunta, S.; Djinovic, R.; Basic, D.; Sansalone, S. *BioMed Res. Int.* **2014**, *2014*, 10.
- (40) Smiley, S. T.; Reers, M.; Mottola-Hartshorn, C.; Lin, M.; Chen, A.; Smith, T. W.; Steele, G. D.; Chen, L. B. *Proc. Nat. Acad. Sci.* **1991**, *88*, 3671.
- (41) Cossarizza, A.; Baccaranicontri, M.; Kalashnikova, G.; Franceschi, C. *Biochem. Biophys. Res. Commun.* **1993**, *197*, 40.
- (42) Sabharwal, S. S.; Schumacker, P. T. *Nat. Rev. Cancer* **2014**, *14*, 709.
- (43) Sena, Laura A.; Chandel, Navdeep S. *Molecular Cell* **2012**, *48*, 158.
- (44) Khodade, V. S.; Kulkarni, A.; Gupta, A. S.; Sengupta, K.; Chakrapani, H. *Org. Lett.* **2016**, *18*, 1274.
- (45) Kim, E.-J.; Bhuniya, S.; Lee, H.; Kim, H. M.; Cheong, C.; Maiti, S.; Hong, K. S.; Kim, J. S. *J. Am. Chem. Soc.* **2014**, *136*, 13888.

- (46) Liu, X.; Kim, C. N.; Yang, J.; Jemmerson, R.; Wang, X. *Cell* **1996**, *86*, 147.
- (47) Li, P.; Nijhawan, D.; Budihardjo, I.; Srinivasula, S. M.; Ahmad, M.; Alnemri, E. S.; Wang, X. *Cell* **1997**, *91*, 479.
- (48) Jiang, X.; Wang, X. *Annu. Rev. Biochem.* **2004**, *73*, 87.
- (49) Herrera, B.; Álvarez, A. M.; SÁNchez, A.; FernÁNdez, M.; Roncero, C.; Benito, M.; Fabregat, I. *FASEB J.* **2001**, *15*, 741.
- (50) Madesh, M.; Hajnoczky, G. *J. Cell Biol.* **2001**, *155*, 1003.
- (51) Skulachev, V. P. *Apoptosis* **2006**, *11*, 473.
- (52) Cook, S. A.; Sugden, P. H.; Clerk, A. *Circulation Res.* **1999**, *85*, 940.
- (53) Tsujimoto, Y.; Shimizu, S. *Apoptosis* **2007**, *12*, 835.
- (54) Cullen, S. P.; Martin, S. J. *Cell Death Differ.* **2003**, *16*, 935.
- (55) Wu, J.; Liu, T.; Xie, J.; Xin, F.; Guo, L. *Cell. Mol. Life Sci.* **2006**, *63*, 949.
- (56) McIlwain, D. R.; Berger, T.; Mak, T. W. *Cold Spring Harb. Perspect. Biol.* **2013**, *5*.
- (57) Boulares, A. H.; Yakovlev, A. G.; Ivanova, V.; Stoica, B. A.; Wang, G.; Iyer, S.; Smulson, M. *J. Biol. Chem.* **1999**, *274*, 22932.
- (58) Park, S.-H.; Choi, Y. P.; Park, J.; Share, A.; Francesconi, O.; Nativi, C.; Namkung, W.; Sessler, J. L.; Roelens, S.; Shin, I. *Chem. Sci.* **2015**, *6*, 7284.
- (59) Curtin, N. J. *Nat. Rev. Cancer* **2012**, *12*, 801.
- (60) Milczarek, G. J.; Martinez, J.; Bowden, G. T. *Life Sci.* **1996**, *60*, 1.
- (61) Haupt, S.; Berger, M.; Goldberg, Z.; Haupt, Y. *J. Cell Sci.* **2003**, *116*, 4077.
- (62) Ekert, P. G.; Silke, J.; Vaux, D. L. *Cell Death Differ.* **1999**, *6*, 1081.
- (63) Shah, N.; Asch, R. J.; Lysholm, A. S.; LeBien, T. W. *Blood* **2004**, *104*, 2873.

End of Chapter 5

Chapter 6

Chloride-Mediated Apoptosis-Inducing Activity of Bis(sulfonamide) Anionophores



6.1. INTRODUCTION:

In addition to the ion channels, ion carriers are widely found in natural systems to perform the crucial task of transmembrane transport of ions. Ion carriers are relatively small biomolecules, which can travel across the lipid membrane after successive complexation with ions followed by the release of the same on the opposite side of the membrane (Figure 6.1). These are small proteins or small molecular cargos which are made up of hydrophilic binding pocket with specific ion recognition sites and a rigid hydrophobic scaffold to achieve favorable interaction while diffusing through the membrane.

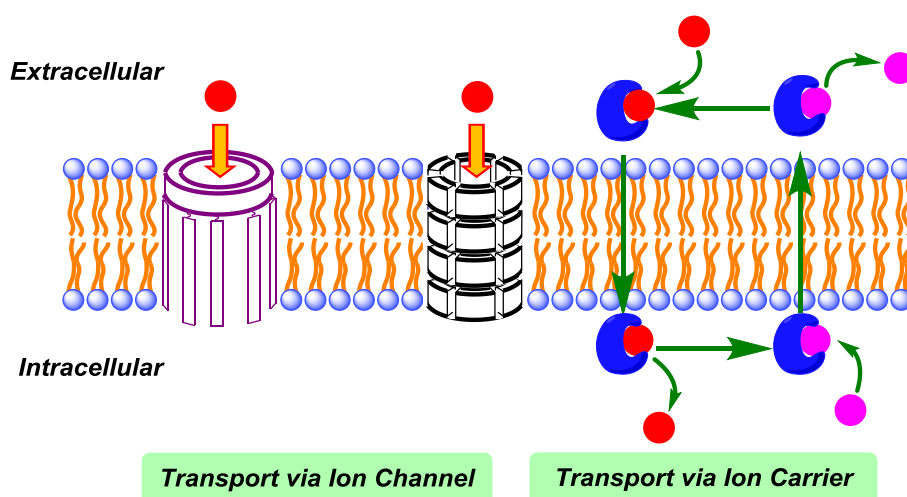


Figure 6.1. Representation of ion transport mechanism by ion channel and ion carrier.

The synthetic ion carriers have gained immense potential in integrating a palliative care approach in several life-threatening diseases, including cystic fibrosis, cancer, etc. Prodigiosin¹ is a natural Cl^- carrier that functions as an anion exchanger via either H^+/Cl^- symport or Cl^-/anion antiport mechanism.² Ion transport properties of prodigiosin and its synthetic analogs are also linked to their anticancer activities.^{3,4} Among diverse synthetic anionophores, classes of urea/thiourea,⁵⁻⁷ calix[4]pyrrole⁸ derivatives and tambjamine analogs⁹ were also reported for their anticancer activities. These molecules either change the intracellular pH or disrupt the cellular ionic homeostasis which triggers the apoptosis-inducing pathway.

Various strategies have been incorporated to design synthetic ion carriers which comprise of rigid scaffold connected to multiple ion binding sites. The lipophilic scaffolds commonly so far used are, cholapods,¹⁰⁻¹³ *trans*-decaline,¹⁴ calyx[4]pyrrole, its fluorinated, and triazole analogues,¹⁵⁻¹⁷ tripodal tris(aminoethyl)amine (tren),¹⁸ squaramides,^{19,20} cyclohexane,²¹ and cyanoguanidines.²² Few examples of scaffolds related to prodigiosin structure are also found in the literature.^{1,9} Various functional motifs have been used for coordinating anions with a host via hydrogen bonding interactions, among them urea, thiourea,^{5-7,14,20,23-27} amide groups,^{8,28} etc. (for structures of ion carriers see Figure 1.12 and 1.13). In this chapter, we demonstrate bis(sulfonamides) as a new class of low molecular weight Cl⁻ transporters. The study provides thoughtful insight into the correlation between structure, lipophilicity, anion recognition, and anion transport activity. Transport of Cl⁻ into the cells by these anionophores facilitates the activation of caspase-dependent apoptotic pathways.

Sulfonamide was envisaged as a better scaffold for anion recognition compared to the carboxylic amide,^{29,30} due to the higher acidity of the N–H protons.^{31,32} The *m*-xylenediamine was selected as the rigid core, and the *para*-substituent of each arylsulfonyl group was varied to tune the lipophilicity and anion binding properties of bis(sulfonamide) derivatives. According to


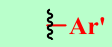
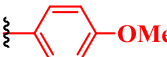
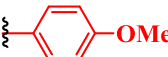
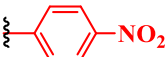
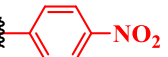
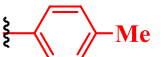
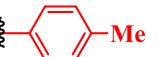
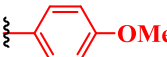
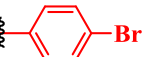
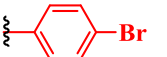
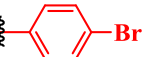
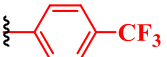
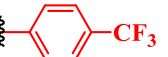
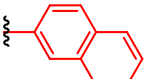
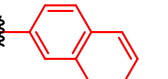
Entry			logP	pK _{a1}
1a			2.77	10.17
1b			2.96	9.97
1c			4.11	10.36
1d			3.69	10.15
1e			4.62	10.13
1f			4.84	10.10
1g			5.06	10.23
2	-	-	5.33	13.23

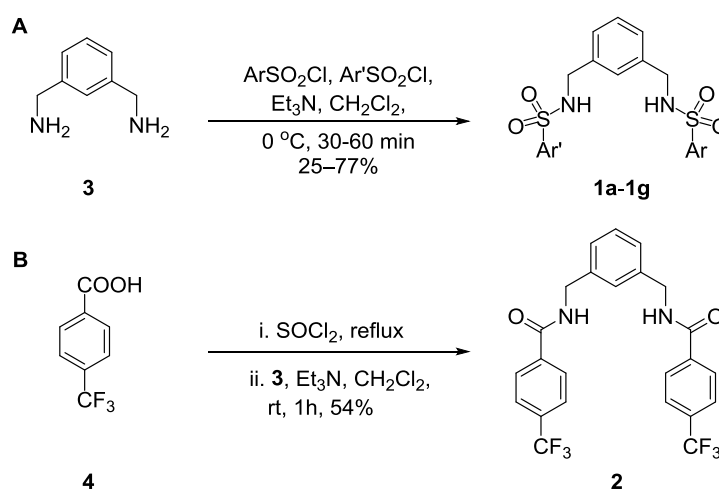
Table 6.1. Structures, logP values and pK_a values of N–H protons of designed transporters **1a–1g** and **2**.

Lipinski's rule,³³ the structural modulation, based on lipophilicity, was expected to influence the membrane permeability of designed molecules and thereby, a variation in the ion transport activity was envisaged. The logP values of all designed molecules were calculated (*i.e.* logP = 2.77, 2.96, 4.11, 3.69, 3.62, 4.84 and 5.06 for **1a–1g**, respectively) using the calculator plugins of MarvinSketch program (Table 6.1).³⁴ The anion binding properties were also varied by considering electron affinity of respective *para*-substituent which is again reflected in the p*K*_{a1} value of sulfonamide N–H protons (calculated by MarvinSketch program; Table 6.3). A bis(carboxylic amide) derivative **2** was designed to evaluate the importance of the sulfonamide groups in the anion recognition process.

6.2. RESULTS AND DISCUSSIONS:

6.2.1. Synthesis:

Compounds **1a–1g** were synthesized from commercially available *m*-xylenediamine **3** by treating with corresponding sulfonyl chloride derivatives (Scheme 6.1). Compound **2** on the other hand, was synthesized from 4-(trifluoromethyl)benzoic acid **4** by treating with SOCl₂ followed by addition of **3**. All compounds were purified by column chromatography, and characterized by ¹H NMR, ¹³C NMR, HRMS, IR and melting point (see experimental section for detailed reaction condition and characterization).



Scheme 6.1. Synthesis of bis(sulfonamide) derivatives **1a–1g** (A) and bis(carboxylic amide) derivative **2** (B).

6.2.2. Anion Binding Studies:

The anion binding to the receptor is the primary criteria for a functional ion carrier. At first, Cl^- ion binding properties of **1a–1g** and **2** were investigated by ^1H NMR titrations in either CD_3CN (for **1a**, **1b**, **1c**, **1f**, **1g** and **2**) or CDCl_3 (for **1d** and **1e**), selected based on compatibility. Upon stepwise addition of tetrabutylammonium chloride (TBACl) to compounds **1a–1g**, downfield shifts of H_a , H_b and H_c signals and upfield shifts of H_d protons were observed (Figure 6.2A). These data indicate the presence of $\text{C-H}_a\cdots\text{Cl}^-$, $\text{N-H}_b\cdots\text{Cl}^-$ and $\text{C-H}_c\cdots\text{Cl}^-$ interactions with the anion. For calculating stoichiometry and binding constant, the change in chemical shift ($\Delta\delta$) of H_a proton was monitored rather than the $\Delta\delta$ of H_b proton due to the line broadening of the H_b proton upon addition of excess TBACl. When the receptor **1f** and TBACl were mixed in CD_3CN by varying mole fraction (κ) of the receptor, and the $\Delta\delta$ of H_a proton was monitored (Figure 6.2B), the maximum interaction was observed at $\kappa = 0.5$ indicating 1:1 complexation between **1f** and Cl^- . The δ of the H_a proton from figure 6.4A was plotted against the increasing concentration

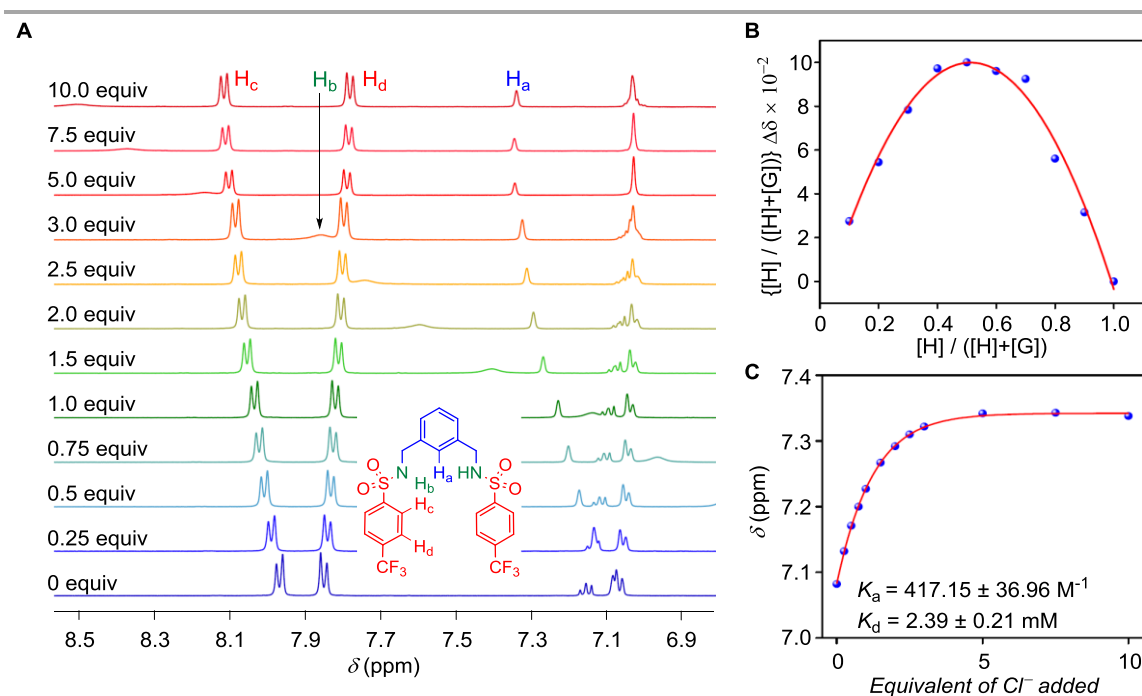


Figure 6.2. Partial ^1H NMR (400 MHz, 298 K) spectral change of **1f** in CD_3CN upon stepwise addition of TBACl (0 – 10 equiv) (**A**); Job's plot obtained from ^1H NMR titration spectra for **1f** with TBACl in CD_3CN by varying mole fraction of **1f** (**B**). The plot of the concentration of TBACl versus δ of H_a **1f** (**C**), fitted to 1:1 binding model of WinEQNMR2 program.

of TBACl (Figure 6.2C) and the association constant for the complexation of **1f** with Cl^- was calculated by fitting the dose-response curve to the 1:1 binding model of WinEQNMR2 program.³⁵ The dissociation constants, K_d , for **1f** appeared to be 2.39 ± 0.21 mM.

$$\delta_{cal} = \sum_{m=1}^{m=i} \sum_{n=0}^{n=j} \frac{\delta_{mn} \beta_{mn} m [M]^m [L]^n}{[M]_{total}}$$

Equation 6.1

where, M represents the free, uncomplexed receptor and L is the ligand; δ_{calc} , is the weighted average of the chemical shifts of the various M -containing species present, $M_m L_n$, and i and j represent the maximum values of m and n respectively.

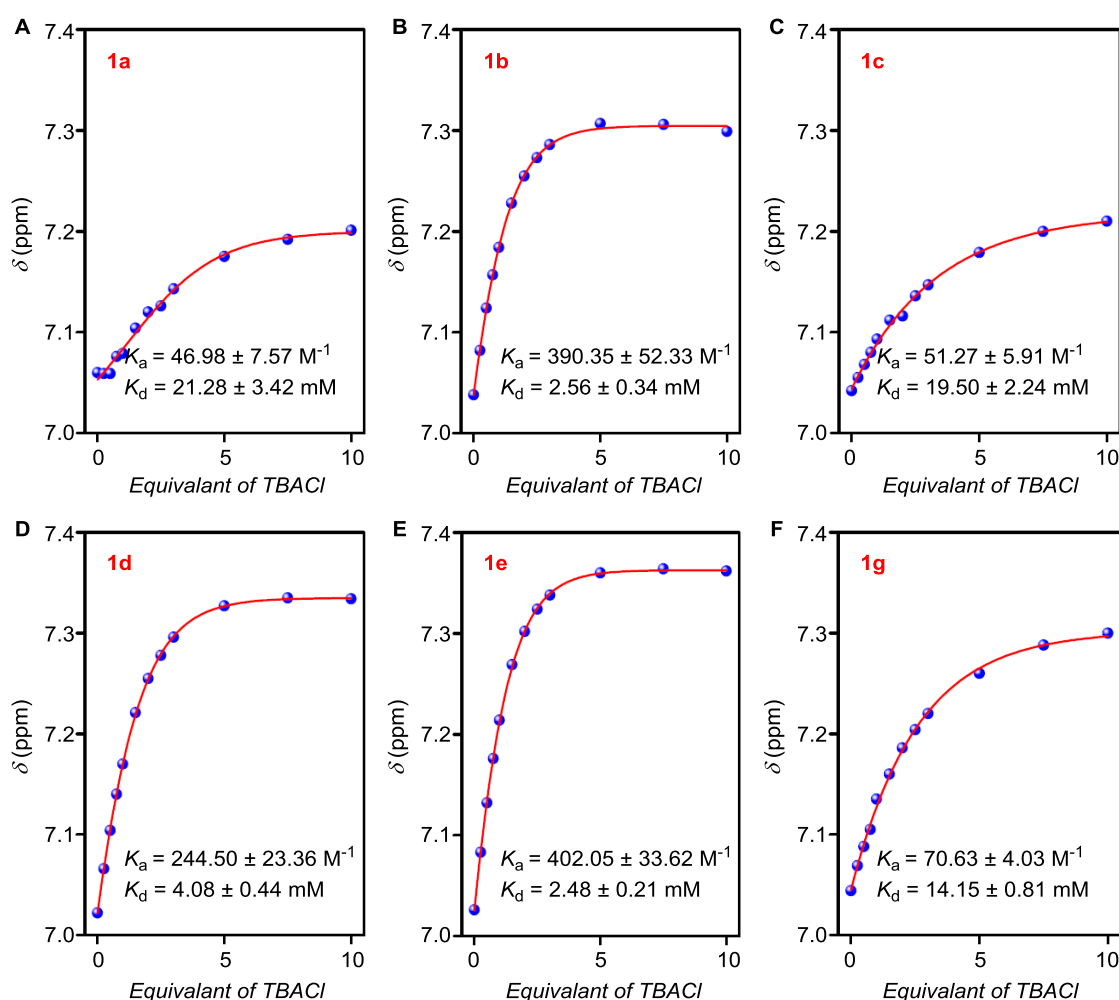


Figure 6.3. The plot of concentration of TBACl versus δ of H_a for **1a** (A), **1b** (B), **1c** (C), **1d** (D), **1e** (E), and **1g** (G), fitted to 1:1 binding model of WinEQNMR2 program.

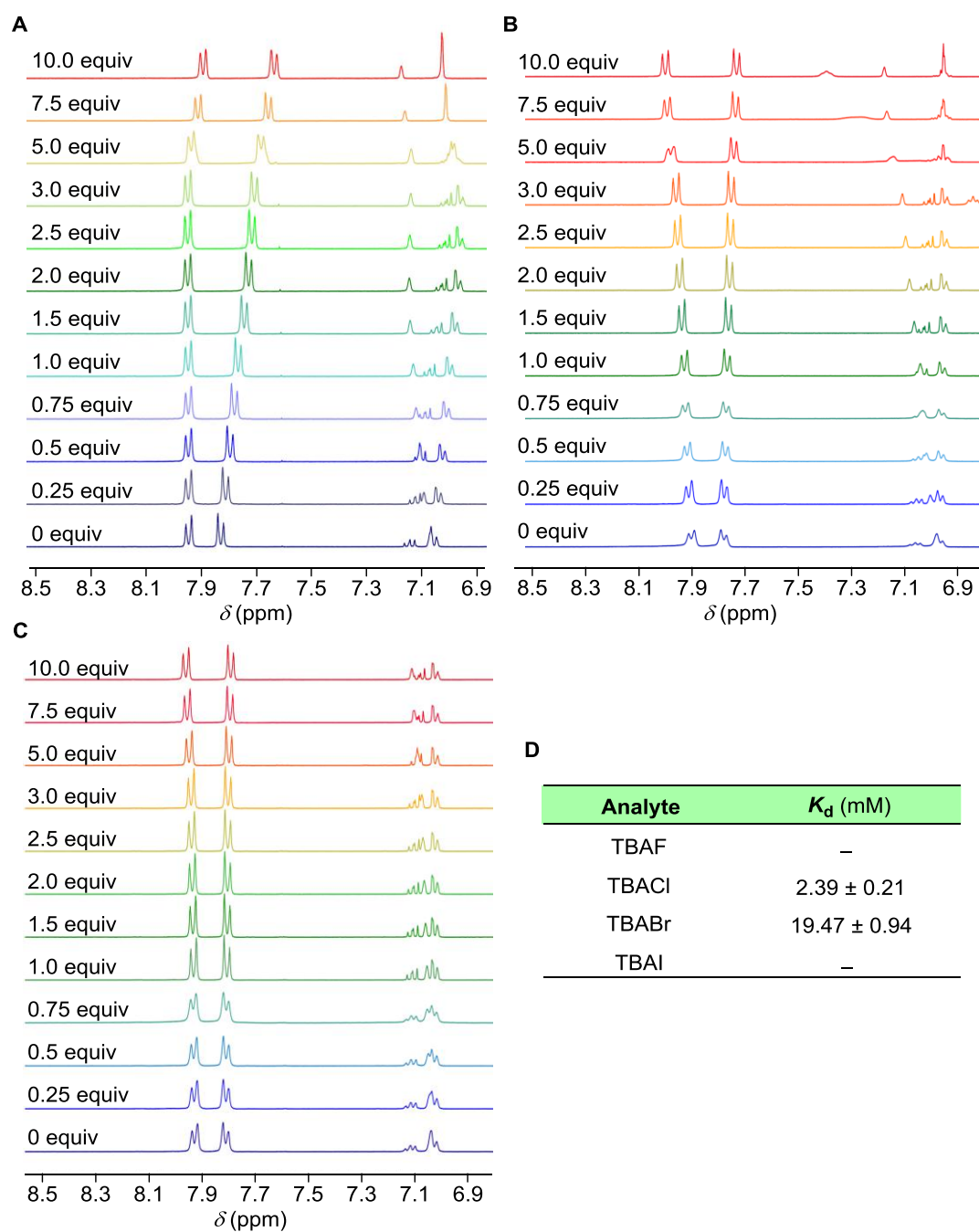


Figure 6.4. ^1H NMR titration spectra for **1f** with stepwise addition of TBAF (A), TBABr (B) and TBAI (C) in CD_3CN . The equivalents of added TBAF, TBABr and TBAI are shown on the spectra. Table of calculated dissociation constant values from those titrations (D). In case of TBAF and TBAI the change in chemical shift is not significant, which gave error in further calculation of binding constant, implies absence of binding of F^- and I^- with **1f**.

The Cl^- ion recognition studies for other receptor, **1a**, **1b**, **1c**, and **1g** provided the dissociation constants, $K_d = 21.28 \pm 3.42$, 2.56 ± 0.34 , 19.50 ± 2.24 , and 14.15 ± 0.81 mM, respectively. Similarly, Cl^- ion binding studies with **1d** and **1e** in CDCl_3 provided

$K_d = 4.08 \pm 0.44$ and 2.48 ± 0.20 M, respectively. Therefore, an electron withdrawing group on Ar/Ar' moieties increase the acidity of sulfonamide N–H proton, and this is responsible for better Cl^- ion binding (Figure 6.3 and Table 6.2). Though the difference between calculated $\text{p}K_{a1}$ values is very small, a significant amount of contribution in anion binding from the electron withdrawing power of the substituent was observed.

The significant ion binding of **1f** prompted us to investigate the selectivity for anion recognition. Halide ion binding studies by **1f** provided the sequence: Cl^- ($K_d = 2.39 \pm 0.21$ M) > Br^- ($K_d = 19.47 \pm 0.94$ M) > $\text{I}^- \sim \text{F}^-$ ($K_d =$ not determined) confirming better Cl^- ion recognition by binding the bis(sulfonamide) receptor (Figure 6.4). It is noteworthy that the ^1H NMR titration of compound **2** with TBACl did not provide any significant change of proton chemical shift suggesting poor Cl^- ion binding by the bis(carboxylic amide) derivative. This observation was corroborated to the higher acidities of sulfonamide N–H protons ($\text{p}K_{a1} = 10.10$) of **1f** compared to the carboxylic amide N–H protons ($\text{p}K_{a1} = 13.23$) of **2**.

6.2.3. Anion Binding Model:

A. Molecular Dynamics Simulation:

To obtain the theoretical insight about the geometry of [**1f** + Cl^-] complex, initial structures were generated by using CONFLEX 7 program.^{36,37} Initial conformations for density functional theory (DFT) calculations were predicted by using MMFF94s force field of the software. First seven conformations, obtained according to their decreasing Boltzmann population percentages (Figure 6.5), were selected for further geometry optimization studies.

The **conf-1** and **conf-2** were placed in the same class because of very similar conformation. Similarly, **conf-3**, **conf-4** and **conf-5** were identified as another class. The **conf-6** and **conf-7** were identified as third and fourth classes, respectively. Subsequently, **conf-1**, **conf-3**, **conf-6** and **conf-7** were optimized by Gaussian 09 program package³⁸ using B3LYP functional and 6-311G++(d,p) basis set.³⁹ The polarization continuum model (PCM) was used to incorporate the effect of chloroform as the solvent in the calculations. The optimizations of

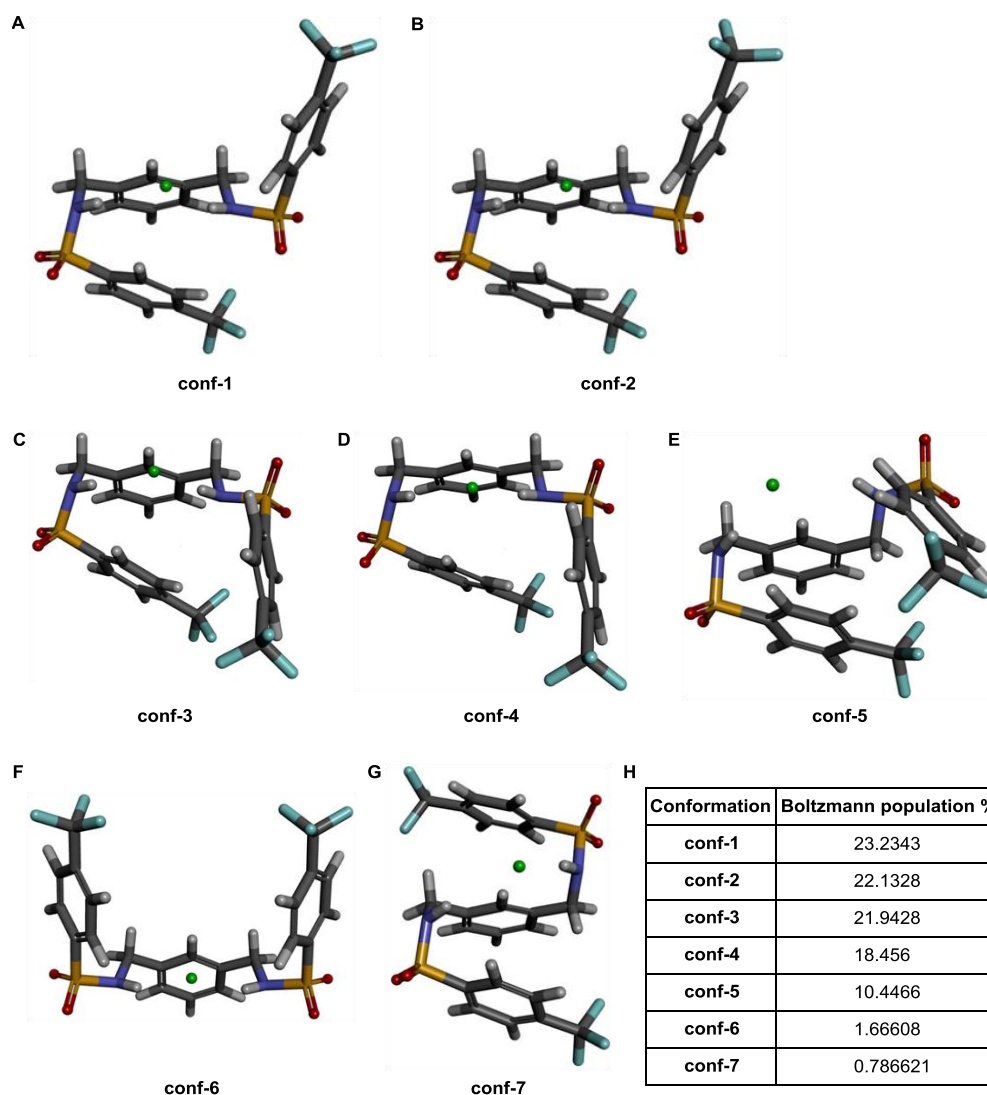


Figure 6.5. Initial geometries, **conf-1** – **conf-7** of $[1f+Cl^-]$, optimized by CONFLEX 7 software using MMFF94s force field (A - G). Boltzmann populations of conformations **conf-1** – **conf-7** are also provided (H). Conformations with Boltzmann population lower than 0.05% were not considered.

conf-1 and **conf-3** resulted in identical structure as shown in Figure 6.6.A. Optimizations of **conf-6** and **conf-7** resulted in separate structures figure 6.8B and 6.8C, respectively. The free energies of these two conformations (*i.e.*, the structures presented in Figure 6.6.B and 6.6.C) were 0.13 and 0.76 kcal/mol higher compared to that presented in Figure 6.6.A. Therefore, the most stable conformation (*i.e.* the structure presented in Figure 6.6.A) was considered as the final optimized structure of the $[1f+Cl^-]$ complex in the solution.

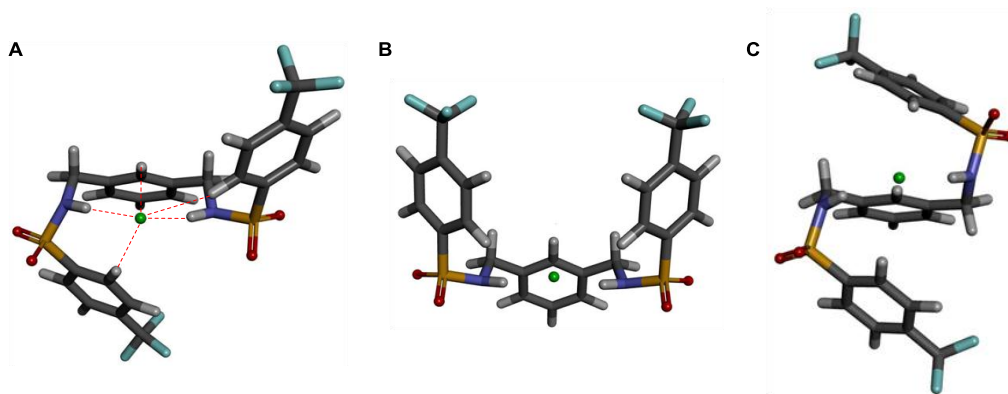


Figure 6.6. The geometry optimized structures of $[1f+Cl^-]$, resulted from **conf-1** and **conf-3** (A), **conf-6** (B) and **conf-7** (C). The conformation presented in (A) exhibit lowest free energy hence most stable.

B. Mass Spectrometric Study:

This optimized structure also correlates to the noncovalent interactions (*i.e.* two $N-H\cdots Cl^-$, and three $C-H\cdots Cl^-$ interactions) those observed in NMR titration studies. On the other hand, the direct experimental evidence of anion recognition of **1f** was obtained from the

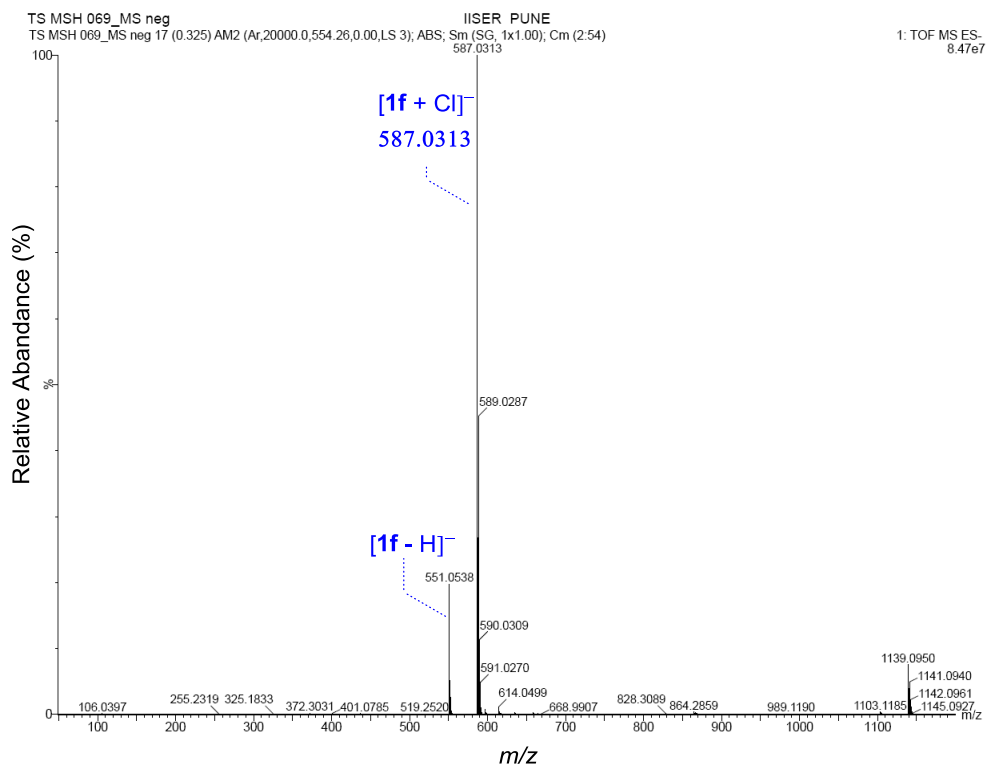


Figure 6.7. ESI-MS spectrum obtained by injecting the solution containing 1:1 mixture of **1f** and TBACl in CH_3CN showing the characteristics signal of $[1f+Cl^-]$ complex.

electrospray ionization-mass spectrometric (ESI-MS) study. A sample was prepared in CH_3CN by mixing **1f** and TBACl in 1:1 molar ratio, and electrosprayed under as mild as possible ionization conditions. The mass spectrometric data provided peaks at $m/z = 587.0313$ and 589.0287 , which correspond to the $[\mathbf{1f}+\text{Cl}^-]$ complex in the solution state (Figure 6.7).

6.2.4. Ion Transport Activity:

Anion recognition properties of bis(sulfonamide) compounds **1a–1g** encouraged us to evaluate their ion transport activity across large unilamellar vesicles (in EYPC-LUVs \supset HPTS). All synthetic receptors **1a–1g** exhibited significant fluorescence intensity enhancement indicating transport of ions across the LUVs. Comparison of ion transport activity at identical concentration $c = 10 \mu\text{M}$ provided the activity sequence: **1f** > **1e** > **1g** > **1d** > **1c** > **1b** > **1a** (Figure 6.8A). On the other hand, ion transport activity of the bis(carboxylic amide) **2** was negligible compared to **1f** (Figure 6.8B). In spite of identical aromatic moieties and comparable logP values ($\log P = 4.84$ and 5.33 for **1f** and **2**, respectively), the higher acidity of sulfonamide N–H proton was crucial for better anion binding by **1f**.

The dose-response plots of bis(sulfonamides) **1a–1f** (Figure 6.9) provided $EC_{50} = 26.56 \pm 1.13$, 17.18 ± 0.77 , 15.84 ± 0.23 , 10.26 ± 0.42 , 8.19 ± 0.11 and $5.89 \pm 0.15 \mu\text{M}$, respectively (Table 6.2). EC_{50} calculation could not be performed on **1g** due to the precipitation observed at

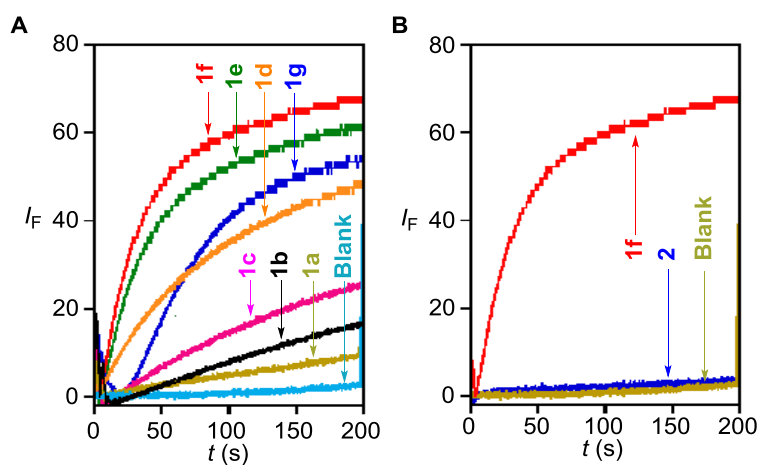


Figure 6.8. Comparison of ion transport activities of bis(sulfonamide) derivatives **1a–1g** ($10 \mu\text{M}$ each) across EYPC-LUVs \supset HPTS (A). Comparison of ion transport activities of **1f** ($10 \mu\text{M}$) and **2** ($10 \mu\text{M}$) across EYPC-LUVs \supset HPTS (B).

higher concentrations of the compound upon its addition in the buffer. The lowest activity of **1a** was primarily correlated to its poor anion binding ability ($K_d = 21.28 \pm 3.42$). In addition to this, low $\log P = 2.77$ of **1a** also contribute to its preferential distribution in the aqueous media over permeation through the hydrophobic lipid bilayer membranes. Compound **1c** with better Cl^- binding ability ($K_d = 19.50 \pm 2.24$ mM) and permeability ($\log P = 4.11$) compared to **1a** displayed higher transport activity. Although, the binding of **1b** with Cl^- is much higher than **1c**, the lower $\log P$ value of the nitro-substituted derivative restricts its membrane permeation which results in the poor ion transport property. Similarly, higher ion transport activity of the compound **1e** was corroborated to its better anion binding ability than **1d**, even if having close $\log P$ values. The effect of permeability ($\log P = 4.84$) and anion binding ($K_d = 2.39 \pm 0.21$ mM) was most significant for **1f** which provided the lowest value of $EC_{50} = 5.89$ μM . Despite of having low

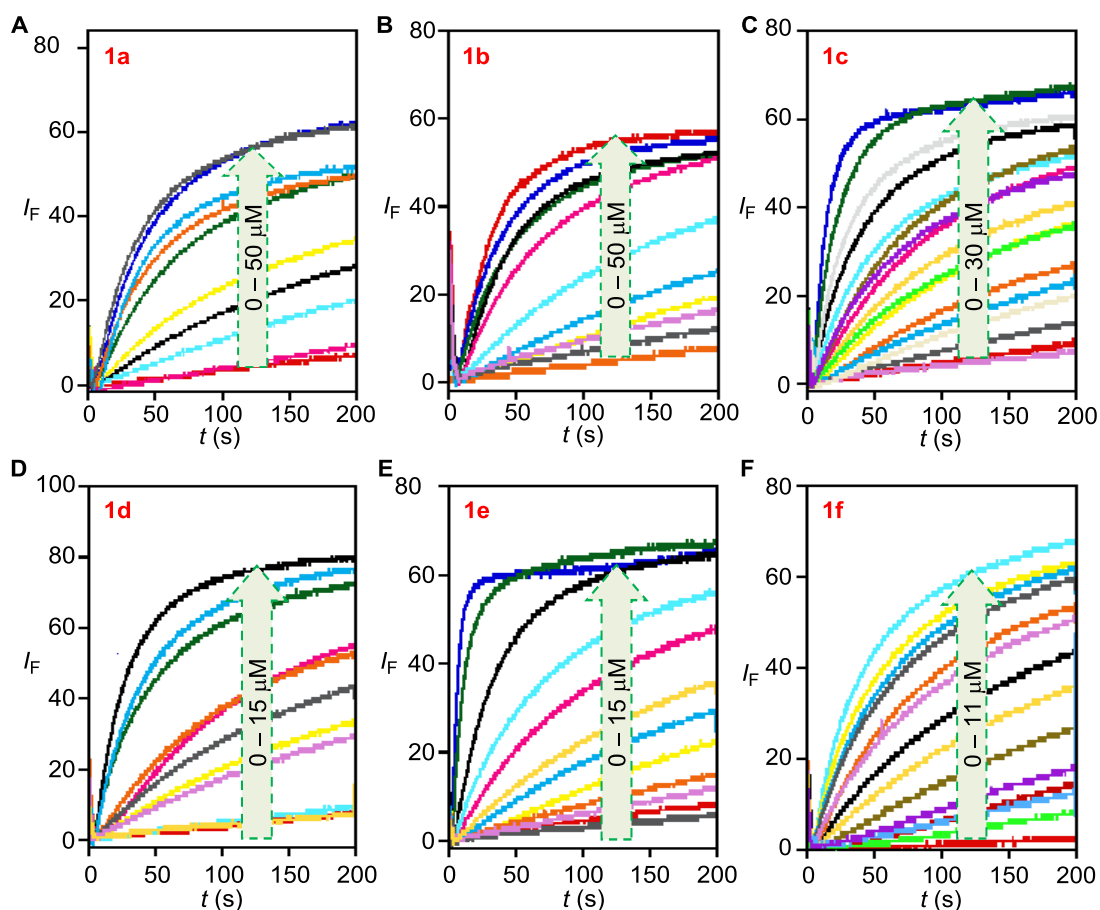


Figure 6.9. Concentration-dependent ion transport activity of **1a** (A), **1b** (B), **1c** (C), **1d** (D), **1e** (E), and **1f** (F), across EYPC-LUVs \supset HPTS.

anion binding property ($K_d = 14.15 \pm 0.81$ M), appreciably high ion transport activity was observed for compound **1g**. This result can be justified from the highest logP value (logP = 5.06) among all bis(sulfonamide) compounds. However, the solubility of the compound **1g** in the aqueous solution was compromised because of its hydrophobic nature. This comparison indicates that, anion recognition is the primary criteria for an ion transporter but the rate of transport is controlled by the lipophilicity i.e., the ease of membrane penetration of the molecule.

Table 6.2. Experimentally determined K_d and EC_{50} values for **1a–1g** and **2**.

Compound	logP	K_d (mM)	EC_{50} (μ M)
1a	2.77	$21.28 \pm 3.42^{[a]}$	26.56 ± 1.13
1b	2.96	$2.56 \pm 0.34^{[a]}$	17.18 ± 0.77
1c	4.11	$19.50 \pm 2.24^{[a]}$	15.84 ± 0.23
1d	3.69	$4.08 \pm 0.44^{[b]}$	10.26 ± 0.42
1e	3.62	$2.48 \pm 0.20^{[b]}$	8.19 ± 0.11
1f	4.84	$2.39 \pm 0.21^{[a]}$	5.89 ± 0.15
1g	5.06	$14.15 \pm 0.81^{[a]}$	ND ^[c]
2	5.33	ND ^{[a],[c]}	ND ^[c]

^[a] K_d values were determined in CD_3CN . ^[b] K_d values were determined in $CDCl_3$. ^[c] ND = could not be determined.

6.2.5. Ion Selectivity Studies:

The top three active compounds **1d–1f** was used further to investigate the selectivity and the mechanism of ion transport.. The difference in ion transport activity in EYPC-LUVs Δ HPTS upon changing extravesicular anions implies the involvement of anions in the transport process. For compound **1f** ($c = 6 \mu$ M), an activity sequence: $Cl^- \gg SCN^- > OAc^- > F^- > ClO_4^- \geq I^- > NO_3^- > Br^-$ was observed (Figure 6.10C). The observed Cl^- ion selectivity of **1f** rationalized by the strong binding of the ion in the cavity of the bis(sulfonamide) molecule. Lower transport activities for other anions indicate poor binding due to the mismatch of their sizes with the binding pocket of the bis(sulfonamide). The little-enhanced activity observed for I^- compared to Br^- may be because of the higher membrane permeation of more hydrophobic I^- anion.⁴⁰ Variation

of monovalent cations in the extravesicular buffer provided marginally enhanced ion transport activities for K^+ , Rb^+ and Cs^+ compared to Li^+ and Na^+ (Figure 6.10F). In the absence of any of ditopic binding motif in **1f**, the observations suggest the possibility of cation recognition as an alternate binding motif in the molecular cavity.⁴¹ Anion selectivity studies for **1d** and **1e** also inferred excellent transport of Cl^- ion (Figure 6.10A,B and 6.10D,E).

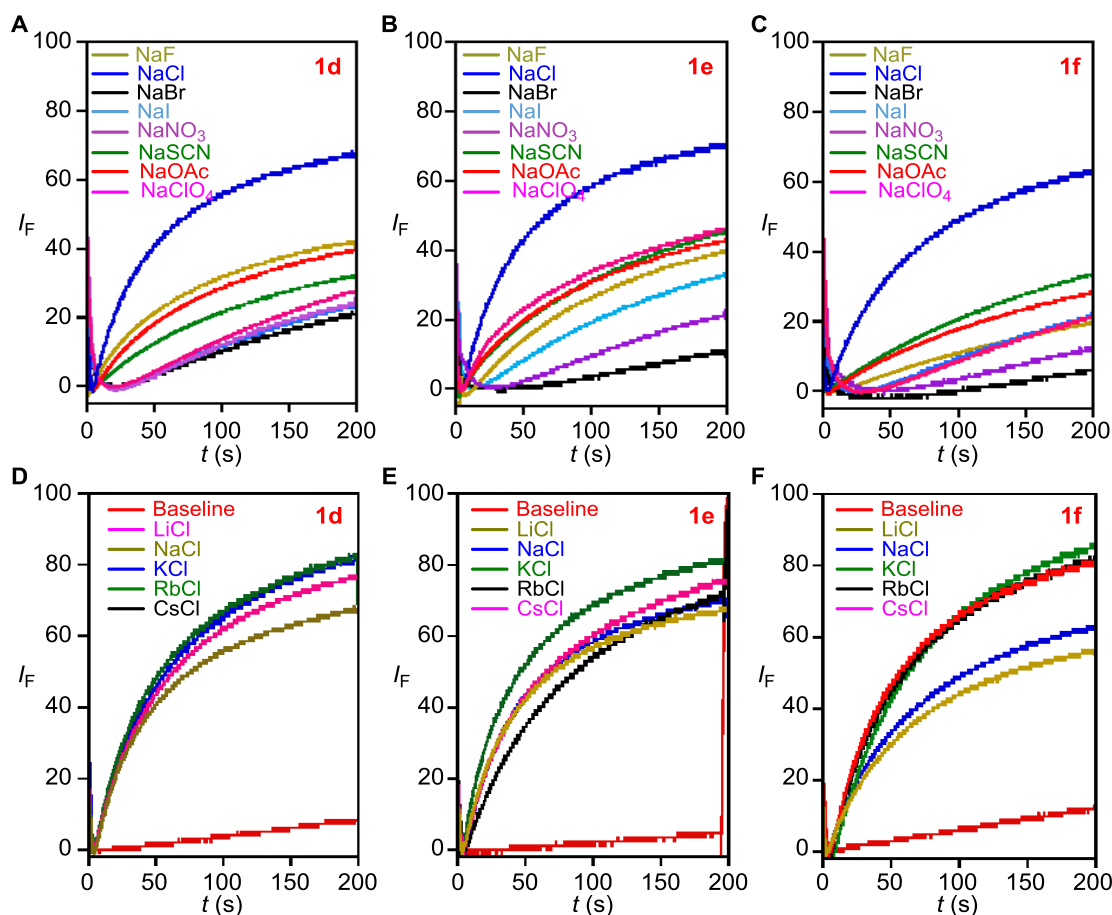


Figure 6.10. Anion selectivity (A-C) of **1d** (10 μ M), **1e** (8 μ M) and **1f** (6 μ M) determined from the ion transport studies across EYPC-LUVs \supset HPTS. Cation selectivity of the same (D-F).

6.2.6. Chloride Ion Transport Study:

In the next stage, Cl^- ion transport activities of **1d–1f** across LUVs were investigated in details by monitoring the fluorescence intensity of intravesicular lucigenin dye at $\lambda_{em} = 535$ nm ($\lambda_{ex} = 450$ nm).⁴² EYPC/cholesterol-LUVs \supset lucigenin were prepared with 7:3 EYPC/cholesterol by entrapping lucigenin dye and $NaNO_3$ (200 mM) and assay was performed as described in previous chapter. A sharp quenching in

fluorescence, observed upon addition of **1f**, confirmed the Cl^- transport activity of the compound (Figure 6.11A). Compounds **1e** and **1d** also displayed quenching of lucigenin fluorescence in the presence of extravesicular NaCl (Figure 6.12B), and the observed trend of Cl^- transport activity **1f** > **1e** > **1d** resembles that obtained from HPTS assays (Figure 6.11B).

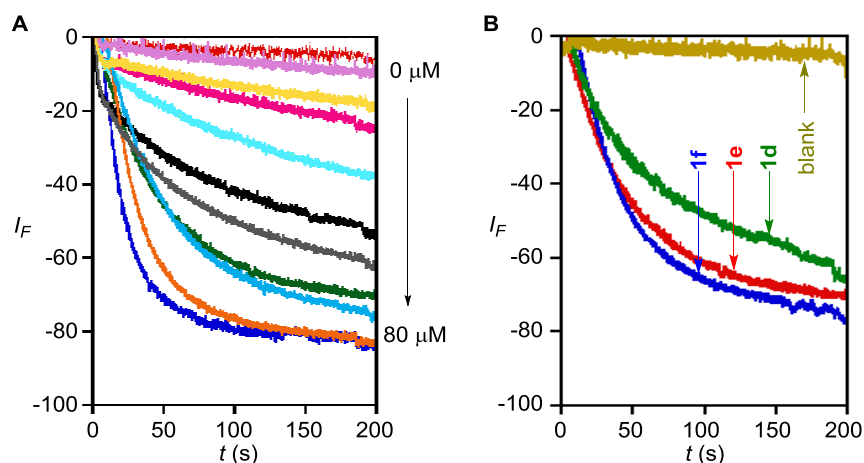


Figure 6.11. Cl^- ion influx across EYPC/cholesterol-LUVs \supset lucigenin upon addition of **1f** (0–80 μM) (A). Comparison of Cl^- influx across EYPC/cholesterol-LUVs \supset lucigenin for **1d**, **1e** and **1f** (60 μM each) (B).

Numerical analysis of the activity profiles (Figure 6.11B) was done to get the quantitative data of Cl^- ion transport across EYPC/cholesterol-LUVs \supset lucigenin. At first, the normalized fluorescence quenching curves were fitted to the single exponential decay function (Equation 6.2) and then the half-life ($t_{1/2}$) was calculated by using Equation 6.3. Similarly, the initial rate (r_i) was estimated by fitting the dose-response curve to a double exponential decay function (Equation 6.4 and 6.6). Double exponential decay curves were fitted to the plot to get better regression factor. An increase in initial rate (r_i) with a concomitant decrease in half-life ($t_{1/2}$) was encountered while moving from compound **1d**, **1e** to **1f** (Table 6.3).

Half-lives ($t_{1/2}$) of transport activities were obtained by fitting of fluorescence quenching curves to a single exponential decay function (Equation 6.2 and then calculating half-lives by use of Equation 6.3).

$$I/I_0 = a + be^{-ct} \quad \text{Equation 6.2}$$

$$t_{1/2} = 0.693/c \quad \text{Equation 6.3}$$

To obtain the initial rate for the transport process the fluorescence quenching curve was fitted with the double exponential decay equation,

$$I/I_0 = y_0 - a.e^{(-bt)} + c.e^{(-dt)} \quad \text{Equation 6.4}$$

Differentiating according to t gives:

$$\partial y/\partial t = a.b.e^{(-bt)} + b.d.e^{(-bt)} \quad \text{Equation 6.5}$$

The initial rate r_i (at $t = 0$ s) gives:

$$r_i = \partial y/\partial t_{t=0} = a.b + c.d \quad \text{Equation 6.6}$$

Double exponential decay equation was used to calculate the initial rate because of better regression factor (R^2).

Table 6.3: Determination of half-lives ($t_{1/2}$) and initial rates (r_i) of Cl^- ion influx across EYPC/cholesterol-LUVs \Rightarrow lucigenin by **1d–1f** (60 μM each).

Compound	$t_{1/2}$ (s)	r_i (s^{-1})
1d	32.36 ± 0.10	0.0165 ± 0.0014
1e	26.04 ± 0.09	0.0232 ± 0.0026
1f	17.86 ± 0.05	0.0335 ± 0.0087

6.2.7. Ion Transport Mechanism:

In the aforesaid lucigenin experiments, either $\text{Cl}^-/\text{NO}_3^-$ antiport or Cl^-/Na^+ symport was considered as the probable mechanism for the ion transport pathway. Therefore, experiments were carried out by varying either the cations or the anions in the extravesicular media to identify the correct mechanism. To evaluate the presence of a symport process, vesicles containing lucigenin in NaNO_3 were suspended in extravesicular MCl ($\text{M}^+ = \text{Li}^+, \text{Na}^+, \text{K}^+, \text{Rb}^+$ and Cs^+) salt solution. The addition of **1f** displayed small differences in the transport rates which rule out the possibility of Cl^-/Na^+ symport mechanism (Figure 6.12A). On the other hand, the variation of extravesicular of Na_mA ($\text{A}^- = \text{F}^-, \text{ClO}_4^-, \text{NO}_3^-, \text{SO}_4^{2-}, \text{Cl}^-$; m = valency of an anion) with iso-osmolar intravesicular NaCl provided remarkable differences in Cl^- efflux rates upon addition of **1f** (Figure 6.12B). These experiments suggest that the Cl^-/A^- antiport is the effective ion transport process.

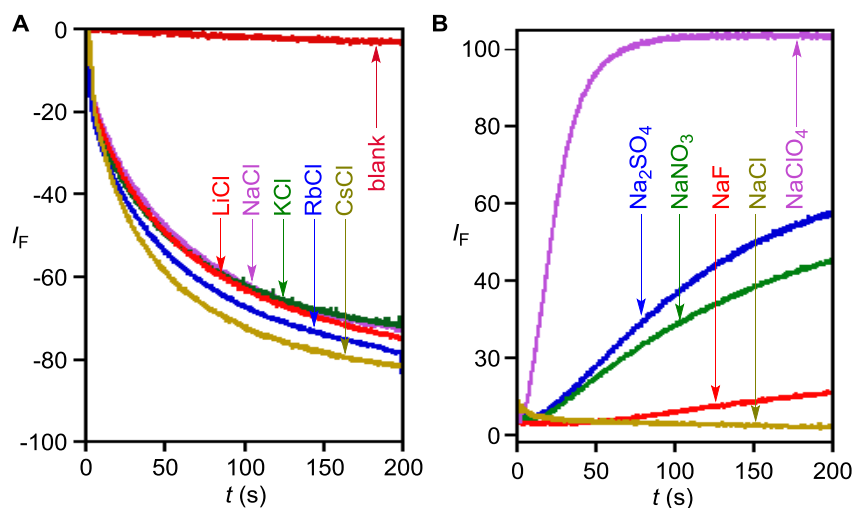


Figure 6.12. Influx of Cl^- ion across EYPC/cholesterol-LUVs \Rightarrow lucigenin upon addition of **1f** (60 μM) with intravesicular NaNO_3 and extravesicular MCl ($\text{M}^+ = \text{Li}^+, \text{Na}^+, \text{K}^+, \text{Rb}^+$ and Cs^+) (A). Exflux of Cl^- ion across EYPC/cholesterol-LUVs \Rightarrow lucigenin upon addition of **1f** (40 μM) with intravesicular NaCl and extravesicular Na_mA salt ($\text{A}^- = \text{F}^-, \text{Cl}^-, \text{NO}_3^-, \text{SO}_4^{2-}$ and ClO_4^- ; $m =$ valency of an anion) (B).

Finally, in pursuit to obtain direct experimental insight of preferential transport mechanism of **1f**, valinomycin (V), a K^+ selective transporter, was used. EYPC/cholesterol-LUVs \Rightarrow lucigenin with intravesicular NaNO_3 were suspended in the KCl solution, and ion transport rate of **1f** was monitored in absence and in the presence of valinomycin. A significant enhancement in the rate of transport of **1f** was observed in the presence of valinomycin (Figure 6.13A). Numerical analysis of the normalized fluorescence quenching curves provided $r_1 = 0.0120 \pm 0.0004 \text{ s}^{-1}$ and $t_{1/2} = 47.04 \pm 0.14 \text{ s}$ for only **1f**; whereas the combination of **1f** and valinomycin gave $r_1 = 0.1333 \pm 0.0007 \text{ s}^{-1}$ and $t_{1/2} = 5.83 \pm 0.02 \text{ s}$ indicating more than 11-fold enhancement in the Cl^- transport rate. The remarkable improvement of transport rate in the presence of valinomycin clearly indicates the $\text{Cl}^-/\text{NO}_3^-$ antiport mechanism of **1f** which gets accelerated because of the synergistic effect of **1f** and valinomycin.

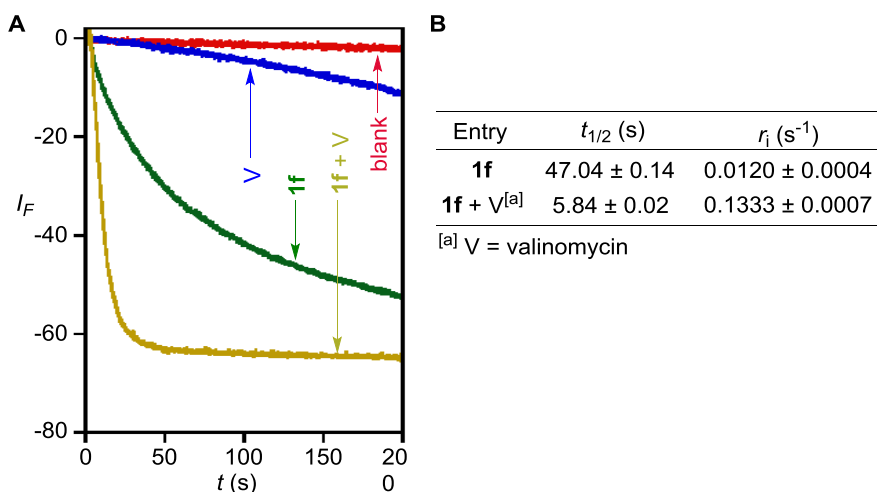


Figure 6.13. Comparison of Cl^- transport activity of **1f** (40 μM) in the presence and the absence of valinomycin (2.5 μM) (A). Calculated half-life ($t_{1/2}$) and initial rate (r_i) of Cl^- influx for **1f** in the presence and the absence of valinomycin (B).

6.2.8. Evidence of Carrier Mechanism:

The required evidence of ion transport through carrier mechanism was obtained by the classic U-tube experiment.^{5,16,20,43} In this experiment the mimic of lipid membrane was established by an organic phase, separating two aqueous phases (Figure 6.14A). The large dimension of organic phase restricts the movement of ions from one aqueous layer to the other whereas; ion carriers can easily act as a vehicle by overcoming the organic phase barrier. The possibility of ion channel formation in this system is impractical as the nanochannel cannot span through the long (~ 10 cm) hydrophobic layer (Figure 6.14A). In this experiment, equimolar NaCl and NaNO_3 were added to the aqueous phase of the donor and receiver phase respectively and concentration of Cl^- in the receiver phase was monitored by chloride ion selective electrode (ISE). Remarkable enhancement in Cl^- level was observed in the receiver aqueous phase only when **1f** was taken in the organic phase (Figure 6.14B). This result confirms the Cl^- transport of **1f** by carrier mechanism.

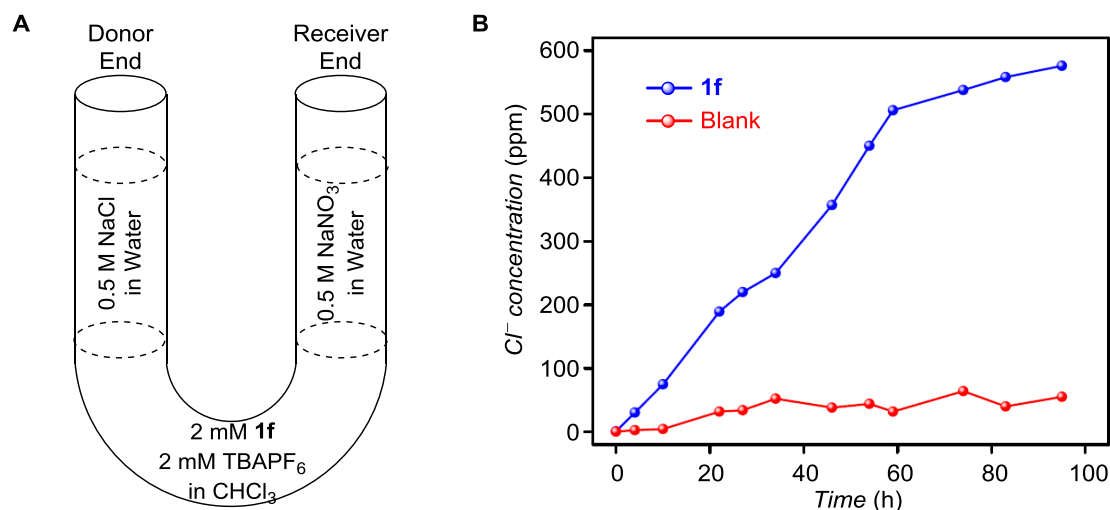


Figure 6.14. Schematic representation of U-tube experiment (A). Concentration of Cl⁻ in the aqueous phase of receiver end of U-tube as the function of time (B). Data were recorded in presence and absence of **1f** in the organic phase.

6.2.9. Effect of Ion Transport in Biological Systems:

The excellent Cl⁻ transport activity of designed bis(sulfonamide) derivatives **1a–1f** prompted us to explore their bio-applicability. Literature reports have demonstrated that dysregulation of ionic homeostasis, via the influx of Cl⁻ ion into cells, can induce apoptosis.^{8,44,45} At first, the viability of various cancer (*e.g.* human breast cancer, MCF-7; human bone osteosarcoma, U2OS; human cervical cancer, HeLa; and lung adenocarcinoma epithelial, A549) and normal (*e.g.* mouse fibroblast NIH3T3) cell lines were screened for compounds **1a–1f** and **2**. A single point screening was done by MTT assay with these compounds (20 μM each). The maximum cell death was observed for the most efficient anionophore **1f** while the least active bis(carboxylic amide) derivative **2** caused minimum cell death (Figure 6.15A). Overall, the differences in cell viability were inversely proportional to the ion transport abilities of these molecules. This data indicates the direct correlation of ion transport and cell death. The dose-dependent cell viability studies for compounds **1e** and **1f** provided $IC_{50} = 56.9\text{--}14.6\ \mu\text{M}$ (Figure 6.15B) and $IC_{50} = 12.2\text{--}7.5\ \mu\text{M}$ (Figure 6.15C), respectively depending on cell line used. The compound **1f** was selected to perform the further studies because of its least IC_{50} values in the cell viability experiments.

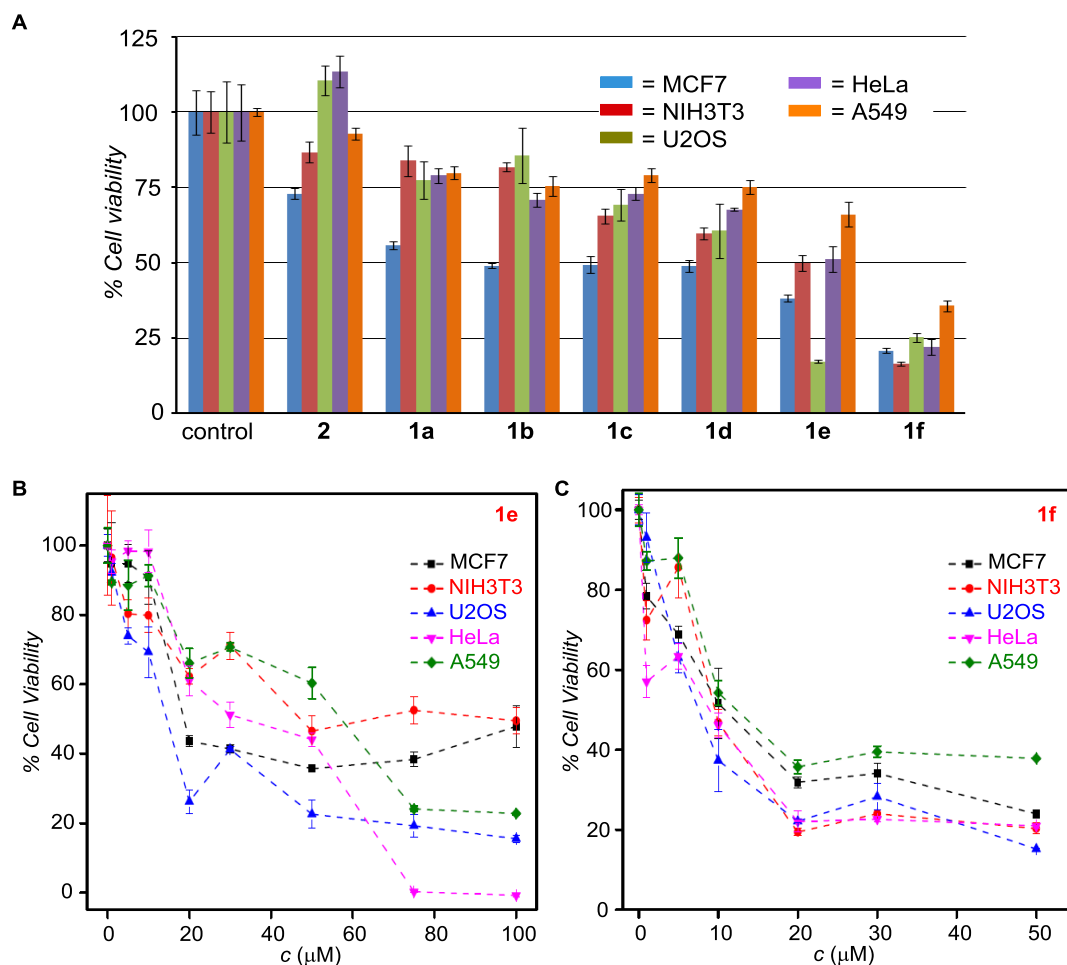


Figure 6.15. Cell viability obtained from single point screening of compounds **1a–1f** and **2** (20 μM each) by MTT assay. Cell viability was checked after 24 h treatment of each compound in various cell lines, from left to right, MCF7, NIH3T3, U2OS, HeLa and A549. Each bar diagram represents mean cell viability, calculated from three independent experiments (A). Compound **1g** was excluded because of the precipitation in higher concentration. Cell viability obtained from MTT assay upon dose dependent treatment of **1e** (B) and **1f** (C) for 24 h in various cell lines.

The direct evidence of Cl^- ion transport into the live cells upon treatment with **1f** was obtained by using MQAE, a Cl^- selective dye ($\lambda_{\text{ex}} = 350 \text{ nm}$ and $\lambda_{\text{em}} = 460 \text{ nm}$), that gives quenching of fluorescence in the presence of the ion.^{46,47} A remarkable stepwise quenching of fluorescence was observed upon post incubation of either HeLa (Figure 6.16A) or MCF7 (Figure 6.16B) cells with **1f** (0 – 50 μM). The gradual quenching of MQAE fluorescence indicates a concentration-dependent influx of Cl^- ions in the intracellular matrix facilitated by the transporter molecule.

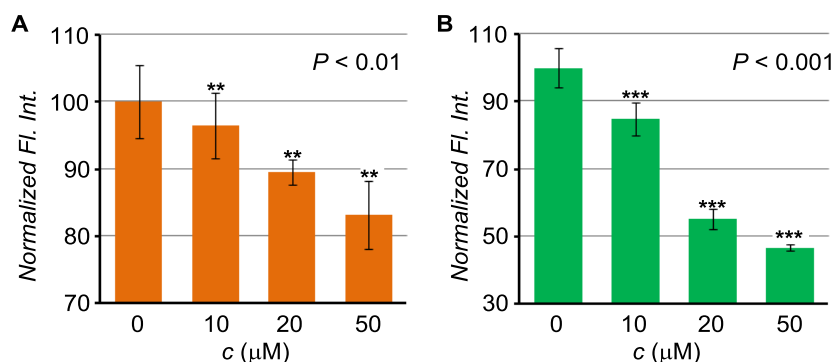


Figure 6.16. Normalized fluorescence intensity of HeLa (A) and MCF7 (B) cells incubated with MQAE (5 mM) for 3 h followed by treatment of **1f** (0 – 50 μM) for 24 h. Fluorescence intensities were recorded by the plate reader at $\lambda_{\text{em}} = 460$ nm ($\lambda_{\text{ex}} = 350$ nm), and normalized with respect to the fluorescence intensity of untreated cells. Each bar represents the mean intensity of three independent experiments, and the differences in mean intensity are statistically significant ($P < 0.01$ for HeLa and $P < 0.001$ for MCF7) according to one-way analysis of variance (ANOVA).

The correlation between the enhanced Cl^- ion level in the intracellular matrix and the death of either HeLa or MCF7 cells was evaluated by altering the Cl^- ion concentration in the extracellular matrix. HBSS (Hank's balanced salt solution) buffers of two different salt compositions (with and without Cl^- ions) were prepared, and cells were suspended separately in these buffers. Then, both sets of cells were treated separately with **1f** (0 – 20 μM) for 24 h and the cell viability between the sets was compared. Remarkably higher viability was observed for cells suspended in Cl^- ion free HBSS than those dispersed in the HBSS buffer containing the ion (Figure 6.17). These results confirm that the enhanced level of intracellular Cl^- ion, transported by **1f**, is potentially related to the amount of cell death. Such Cl^- ion mediated cell death is known to trigger the apoptotic pathways in live cells.^{8,9,44,48}

A number of experiments were carried out to establish the appropriate apoptotic pathway. In the intrinsic pathway of apoptosis, disruption of mitochondrial membrane potential (MMP) induces the release of cytochrome *c* from mitochondria to cytosol.^{49,50} Released cytochrome *c* subsequently binds to the *Apaf-1* to form apoptosome. Then the cytochrome *c*/*Apaf-1* complex activates caspase-9, which further activates multiple pathways, including activation of caspase-3, to induce apoptosis.⁵¹⁻⁵⁴ Therefore, the process of apoptosis can be monitored at several stages, such as, (a) by monitoring the

mitochondrial membrane potential (MMP) and cytochrome *c* release as a pre-apoptotic symptom, (b) by monitoring proteins of the caspase family, and (c) by observing the nuclear fragmentation of the cells.

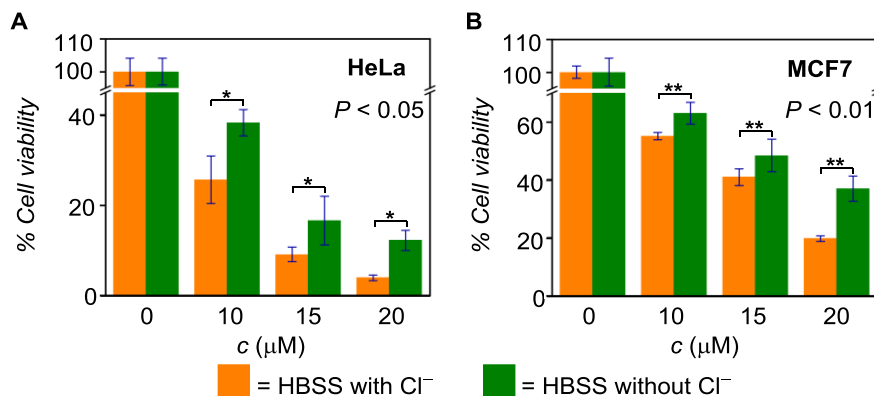


Figure 6.17. Comparison of HeLa cell viability in Cl⁻ containing and Cl⁻ free HBSS buffer upon dose dependent treatment of **1f** (0 – 20 μM) for 24 h (A). Similar studies were done with MCF7 cells (B). The differences in mean intensities (three independent experiments) are statistically significant ($P < 0.05$ for HeLa and $P < 0.01$ for MCF7) according to one-way analysis of variance (ANOVA).

The collapse of MMP, observed during the early stages of apoptosis, can be monitored by using JC-1, a membrane potential sensitive fluorescent probe.^{55,56} This dye exhibits intense red fluorescence when present in the mitochondrial membrane of healthy cells due to the formation of *J*-aggregate. The disruption of MMP does not allow the dye to stay in the membrane resulting in its dispersion in the cytosol. In the cytoplasm, the JC-1 dye exhibits green fluorescence due to the loss of aggregation. When HeLa cells were treated with **1f** (0–20 μM) for 24 h followed by staining with JC-1, a stepwise decrease in the red fluorescence with concomitant enhancement of the green fluorescence was observed (Figure 6.18A–C). Subsequently, the ratio of pixel intensities (*i.e.* red/green) was calculated from the live cell images of the stained cells (Figure 6.18D). The decrease in the ratio of pixel intensities can be correlated to the disruption of MMP upon treatment of **1f**.

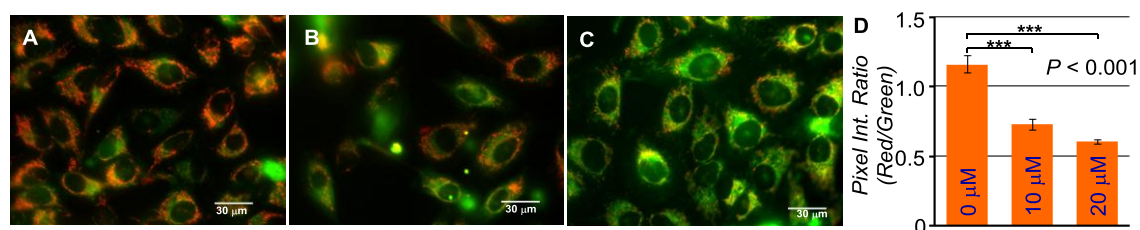


Figure 6.18. Live cell imaging of HeLa cells upon treating with 0 μM (A), 10 μM (B) and 20 μM (C) of **1f** for 24 h followed by staining with JC-1 dye. Each image was generated by merging the images obtained from red and green channels. The bar graph (D) represents the ratio of pixel intensities (red/green) for each set of cells. One way ANOVA analysis of seven replicate images show the statistically significant ($P < 0.001$) mean difference in the ratio of pixel intensity.

Cytochrome *c* is a well conserved electron-transport protein and confined between mitochondrial intermembrane spaces. Apoptotic stimulation triggers the release of cytochrome *c* from mitochondria which subsequently instigate the caspase-dependant apoptotic pathway.⁵⁷⁻⁵⁹ HeLa cells were incubated with increasing concentration of **1f** (0, 10 and 20 μM) for 8 h and immunostaining analysis was done with cytochrome *c* antibody. The release of cytochrome *c* was monitored by an enhancement in emission intensity which further diffused upon treatment of higher dose. The release of cytochrome *c* upon ion transport endorses the induction of mitochondrial-dependent apoptosis by **1f** (Figure 6.19).

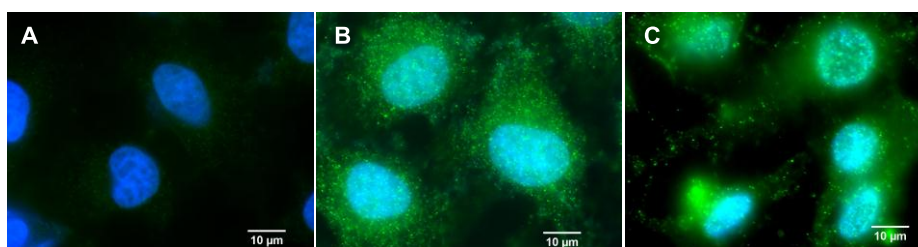


Figure 6.19. HeLa cells are treated with 0 μM (A), 10 μM (B) and 20 μM (C) of **1f** for 8 h, then fixed and analyzed for cytochrome *c* release by immunostaining with cytochrome *c* antibody. DMSO was used as negative control, and the nuclei were stained with Hoechst 33342.

It is already established that mitochondria-dependent apoptotic pathway can proceed via activation of family of caspases.^{53,60-62} In the next step, for a better understanding of ion transporter induced caspase cascade, the activation of initiator caspase-9 and the executioner caspase-3 were investigated. Immunoblot assay was

performed on HeLa cells upon treatment with **1f** (0 – 40 μM) for 24 h by using appropriate primary antibodies. A dose-dependent enhancement of the amount of activated caspase-9 and caspase-3 with simultaneous degradation of procaspase-3 indicates the caspase-dependent intrinsic pathway of the apoptosis program (Figure 6.20). The enhancement of caspase-3 and 9 was quantified with respect to the amount of GAPDH present in the respective set of cells (Figure 6.20B-D).

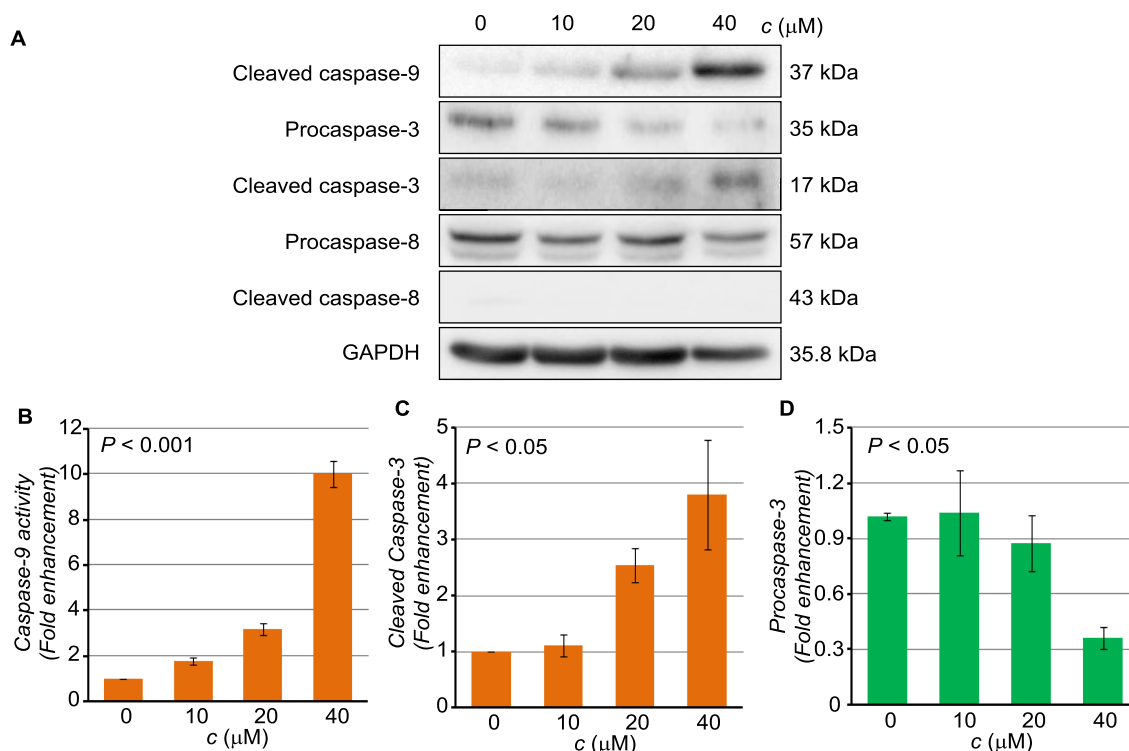


Figure 6.20. Immunoblot assay for active caspase-9, caspase-3 and caspase-8 in HeLa cells, after 24 h incubation with various concentrations (0, 10, 20 and 40 μM) of **1f** (A). Quantification of immunoblot analysis for cleaved caspase-9 (B), Cleaved caspase-3 (C) and procaspase-3 (D).

On the other hand, apoptosis can also be initiated via an extrinsic pathway involving caspase-8.^{53,63} No such activation of caspase-8, and no degradation of procaspase-8 ruled out the possibility of the extrinsic pathway of apoptosis program (6.20A). Similarly, apoptosis can also proceed via activation of the p53 mediated pathway.⁶⁴ Phosphorylation at the Ser-15 position of the p53 protein is a common phenomenon in p53 mediated apoptosis pathway.⁶⁵ Absence of phosphorylation at the Ser-15 position of p53 protein, monitored by immunoblot assay, eliminate the possibility of p53 mediated apoptosis program (Figure 6.21). A cell lysate of a positive control for the P-p53 (Ser-15) antibody was prepared to validate the workability of antibody. Lysate

of HeLa cells (2×10^6 cells) for positive control was prepared by treatment of $10 \mu\text{M}$ camptothecin (CPT) for 16 h.

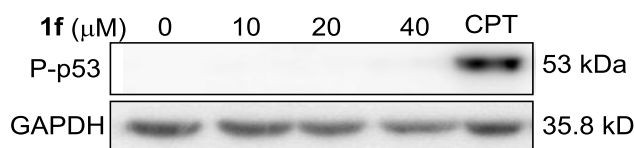


Figure 6.21. Immunoblot assay for P-p53 (Ser-15) in HeLa cells, after 24 h incubation with various concentrations (0, 10, 20 and $40 \mu\text{M}$) of **1f** and 16 h incubation with CPT ($10 \mu\text{M}$).

Moreover, to elucidate the caspase-dependent intrinsic pathway of apoptosis, cell viability was screened in the presence of caspase inhibitors. The small polypeptide derivatives, Benzyloxycarbonyl-Asp(OMe)-Glu(OMe)-Val-Asp(OMe)-fluoromethylketone (z-DEVD-fmk), and Benzyloxycarbonyl-Leu-Glu(OMe)-His-Asp(OMe)-fluoromethylketone (z-LEHD-fmk) are known cell permeable, irreversible inhibitors for caspase-3 and caspase-9, respectively, which can inhibit the caspase dependent apoptotic pathway of cell.^{61,66,67} Almost negligible amount of caspase-3 and caspase-9 activation was observed in immunoblot assay, upon preincubation of HeLa

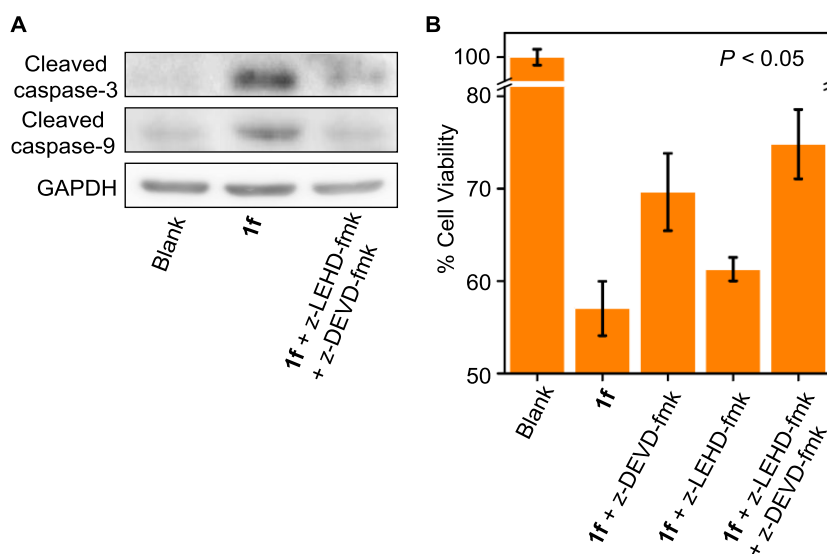


Figure 6.22. Immunoblot analysis of HeLa cells preincubated with z-DEVD-fmk and/or z-LEHD-fmk ($50 \mu\text{M}$ each) for 3 h followed by incubation with **1f** ($20 \mu\text{M}$) for 24 h (A). The difference in cell viability upon treatment with **1f** and caspase inhibitors measured by MTT assay. Cells were preincubated with z-DEVD-fmk and/or z-LEHD-fmk ($50 \mu\text{M}$) for 3 h followed by incubation with **1f** ($10 \mu\text{M}$) for 24 h (B).

cells with z-DEVD-fmk and z-LEHD-fmk (50 μ M each) followed by treatment of **1f** (20 μ M) for 24 h (Figure 6.22A). Similarly, in MTT assay, a significant increase in cell viability was encountered upon treatment of **1f** when cells were preincubated with caspase inhibitors (Figure 6.22B). This enhanced cell viability can be correlated to the protection process of cells from ion transporters by inhibition of caspase-dependent intrinsic pathway of apoptosis program.

Apoptosis can also be characterized by distinct changes in cellular morphology, including membrane blebbing, chromatin condensation, the appearance of membrane-associated apoptotic bodies, internucleosomal DNA fragmentation, as well as by cleavage of poly(ADP-ribose) polymerase (PARP).^{5,68,69} Nuclear condensation, fragmentation, and formation of apoptotic bodies can be identified by Hoechst 33342, a fluorescent nuclear staining dye. HeLa cells were treated with **1f** (20 μ M) for 24 h and then, stained with the dye. A significant change in nuclear morphology was observed in treated HeLa cells compared to untreated ones (Figure 6.23A). The appearance of nuclear condensation and fragmentation indicates apoptotic cell death.

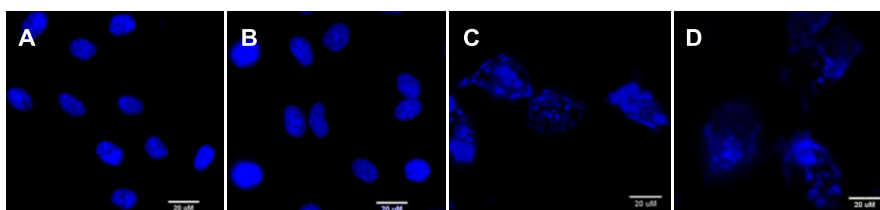


Figure 6.23. Live cell imaging of HeLa cells stained with Hoechst 33342. Typical oval nuclei in control (untreated) cells (**A** and **B**), fragmented nuclei of cells after 24 h treatment with **1f** (20 μ M) (**C** and **D**).

It is also well-known that PARP cleavage, by endogenous caspases, serves to prevent futile repair of DNA strand breaks during the apoptotic program.^{68,70} An appearance of cleaved PARP-1 (86 kD) with concomitant degradation of full-length PARP-1 (116 kD) was observed upon treatment of HeLa cells with **1f** (40 μ M) for 24 h (Figure 6.24). The activation of cleaved PARP-1 by endogenous caspase substrate can be considered as an additional validation of caspase-mediated apoptosis.

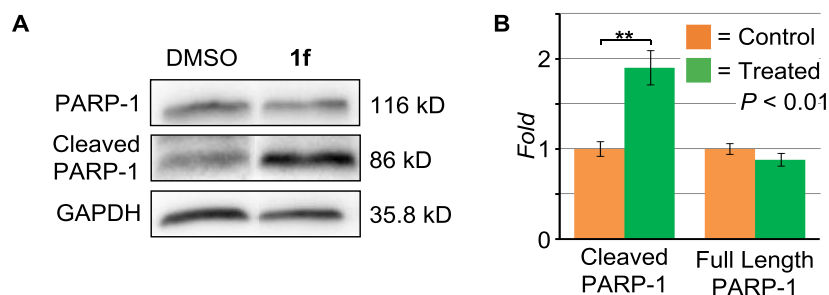


Figure 6.24. The expression of cleaved PARP-1 and degradation of full-length PARP-1 in HeLa cells, after 24 h incubation with **1f** (40 μM), determined by immunoblot analysis (**A**). Statistically, significant difference in cleaved PARP-1 expression was observed upon applying unpaired *t*-test on three replicate data (**B**).

Finally, to establish the relation between the change in ionic homeostasis and induction of apoptosis, reactive oxygen species (ROS) level of cells were measured. It is well known in the literature that ROS level of a cell can be effected by the change in ionic homeostasis via interruption of the respiratory chain in mitochondria.^{71,72} ROS level in HeLa cells was measured fluorometrically by using a ROS-sensitive probe, 3-methyl-7-(4,4,5,5-tetramethyl-1,3,2-dioxaborolan-2-yl)-2H-chromen-2-one (**ROS probe**).^{73,74} An enhancement of ROS level was observed when HeLa cells were incubated with increasing concentration of **1f** (0 – 100 μM) for 8 h (Figure 6.25A). Furthermore, a significantly higher enhancement in ROS level was observed when media with Cl^- was used as an external buffer (HBSS buffer with Cl^-) than Cl^- free media (Cl^-

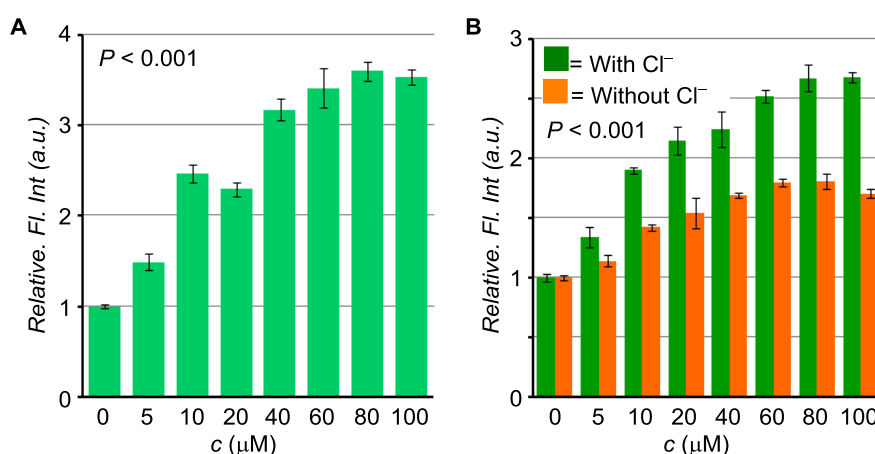


Figure 6.25. Measurement of ROS production in HeLa cells upon incubation with varied concentration of **1f** (0 – 100 μM) for 7 h, followed by treatment with the ROS probe (50 μM) for 1 h in the same solution (**A**). Comparison of ROS production in HeLa cells in absence and presence of Cl^- ion (HBSS buffer with and without Cl^- ion) in extracellular media (**B**).

free HBSS buffer) (Figure 6.25B). Thus, the Cl^- dependent enhancement of ROS level signifies the ion transport mediated ROS production in HeLa cells upon incubation with **1f**. The enhanced level of ROS instigates the opening of mitochondrial permeability transition pore which results in the leakage of cytochrome *c* from mitochondria *i.e.* the induction of intrinsic apoptotic pathway.⁷⁵⁻⁷⁸

6.3. CONCLUSION:

We described bis(sulfonamides) as efficient artificial anionophores for selective Cl^- ion transport. These anion transporters were synthesized by reacting the 1,3-phenylenedimethanamine core with arylsulfonyl chlorides to create a molecular library of variable sulfonamide N–H proton acidity, and lipophilicity. $^1\text{H-NMR}$ titrations confirmed strong anion binding when an electron withdrawing group is connected at the *para*-position of the aryl group. The bis(sulfonamide) system displayed strongest binding with Cl^- ion compared to other halides, and a 1:1 binding model was established with Cl^- ion. Anion recognition of the system was also much stronger compared to the corresponding bis(carboxylic amide) derivative. Transmembrane ion transport studies confirmed the compound with appropriate lipophilicity and strong anion binding ability is the most efficient transporter. Selective transport of Cl^- ion and Cl^- /anion antiport mechanism across large unilamellar vesicles were also confirmed by several fluorescent-based assays.

MTT assay indicated an inverse correlation between cell viability and ion transport activity of bis(sulfonamides) derivatives. The elevated intracellular Cl^- ion level and the Cl^- mediated cell death were also confirmed. The disruption of ionic homeostasis of cells led to the change in the mitochondrial membrane potential which subsequently initiate the release of cytochrome *c* from mitochondrial intermembrane spaces to the cytosol. The mitochondria-dependent intrinsic apoptotic pathway of cell death was confirmed by expression of a family of caspases and cleaved PARP-1. The change in the nuclear morphology was also observed as a postapoptotic symptom. The caspase-9 and caspase-3 dependent intrinsic pathway of apoptosis were further confirmed by monitoring transporter mediated cell death in the presence of caspase inhibitors. Finally, the induction of apoptosis mechanism by ion transport involving excessive production of ROS was demonstrated. Hence, artificial Cl^- transporters as

apoptosis inducing agents, via disrupting ionic homeostasis of the cell, could be a potential therapeutic tool for cancer treatment in next generation.

6.4. EXPERIMENTAL SECTION:

6.4.1. General Methods:

All reagents and solvents for synthesis were purchased commercially and used without further purification. Dichloromethane (CH_2Cl_2) was pre-dried over calcium hydride and then distilled. Column chromatographies were performed on Merck silica gel (100 – 200 mesh). Thin layer chromatographies (TLCs) were carried out with E. Merck silica gel 60-F254 plates. Egg yolk phosphatidylcholine (EYPC) and dipalmitoylphosphatidylcholine (DPPC) were obtained from Avanti Polar Lipids as a solution in CHCl_3 (25 mg/mL). HEPES buffer, HPTS, lucigenin, Triton X-100, NaOH and inorganic salts were purchased of molecular biology grade from Sigma. Large unilamellar vesicles (LUVs) were prepared by using mini extruder, equipped with a polycarbonate membrane of 100 nm pore size, obtained from Avanti Polar Lipids. MCF7 and HeLa cell line was purchased from European Collection of Cell Cultures (ECACC). A549 and NIH-3T3 cell lines were generous gifts from Dr. Kundan Sengupta (IISER Pune) and Dr. Nagaraj Balasubramanian (IISER Pune). Dimethyl sulfoxide (DMSO), thiazolyl blue tetrazolium bromide (MTT), and *N*-(ethoxycarbonylmethyl)-6-methoxyquinolinium bromide (MQAE) were purchased from Sigma-Aldrich. 96-Well plates, 6-well plates, 15 and 50 mL graduated sterile centrifuge tubes and tissue culture flasks with filter cap sterile were purchased from Eppendorf Product Pvt. Ltd. Active caspase-3, caspase-9, anti-GAPDH antibody were purchased from Cell Signaling Technology, Abcam and Sigma respectively. Cytochrome *c*, phospho-p53 (Ser-15) and active caspase-8 antibody were purchased from Cell Signaling Technology. Anti-PARP-1 (Ab-2) Mouse mAb (C-2-10) antibody was purchased from Calbiochem. Anti-rabbit and Anti-mouse IgG HRP-conjugated antibody were obtained from Jackson ImmunoResearch. AlexaFluor-488 was purchased from Invitrogen. Inhibitors for caspase-3 and caspase-8 were purchased from R & D Systems. The compound 3-methyl-7-(4,4,5,5-tetramethyl-1,3,2-dioxaborolan-2-yl)-2H-chromen-2-one (**ROS Probe**) was a generous gift from Dr. Harinath Chakrapani's Laboratory at IISER Pune.

6.4.2. Physical Measurements:

All NMR spectra were recorded either on 500 MHz Bruker, or 400 MHz Bruker AscendTM 400 spectrometer using either residual solvent signals as an internal reference or from internal tetramethylsilane on the δ scale. The chemical shifts (δ) were reported in ppm and coupling constants (*J*) in Hz. The following abbreviations were used: m (multiplet), s (singlet), d (doublet), t (triplet) dd (doublet of doublet). High-resolution mass spectra were obtained from a MicroMass ESI-TOF MS spectrometer equipped with a Micromass Z-Spray electrospray

ionization (ESI) source (Waters Co., Synapt G2, France). FT-IR spectra were obtained using NICOLET 6700 FT-IR spectrophotometer as KBr disc and reported in ν (cm^{-1}). Melting points were measured using a VEEGO Melting point apparatus. All melting points were measured in open glass capillary, and values are uncorrected. Fluorescence spectra were recorded from Fluoromax-4 from JobinYvon Edison equipped with an injector port and a magnetic stirrer. Measurements of pH were done using a Helmer pH meter. All data from fluorescence studies were processed either by KaleidaGraph 3.51 or Origin 8.5 program. ChemBio Draw 15 Ultra software was used for drawing structures and processing figures. MTT assay was recorded in a microplate reader (Varioskan Flash). Westernblot was visualized in a using ImageQuant LAS 4000 (GE Healthcare). Cell images were taken in were taken using Olympus Inverted IX81 microscope equipped with Hamamatsu Orca R2 camera. Image *J* software was used for analyzing cell images, and the quantifying amount of protein in immunoblot analysis. GraphPad Prism 6 software was used for statistical analysis.

6.4.3. Synthesis:

A. Synthesis of *N,N'*-(1,3-phenylenebis(methylene))bis(4-methoxybenzenesulfonamide) **1a**, ($\text{C}_{22}\text{H}_{24}\text{N}_2\text{O}_6\text{S}_2$):

In a 50 mL round bottom flask *m*-xylylenediamine **3** (0.19 mL, 1.5 mmol) and Et_3N (0.45 mL, 3.3 mmol) were dissolved in dry CH_2Cl_2 (5 mL). To the reaction mixture, a solution of 4-methoxybenzene-1-sulfonyl chloride **5a** (619.9 mg, 3.0 mmol) in dry CH_2Cl_2 (3 mL) was added dropwise at 0 °C. The reaction mixture was stirred at 0 °C for 30 min. After completion of the reaction, the reaction mixture was filtered. The filtrate was evaporated under reduced pressure to obtain a residue which was purified by column chromatography over silica gel (Eluent: 2% MeOH in CHCl_3) to furnish the pure **1a** (520 mg, 73%) as a off white solid. ^1H NMR (400 MHz, CD_3CN): δ 7.76 – 7.70 (m, 4H), 7.20 – 7.16 (t, $J = 8.0$ Hz, 1H), 7.10 – 6.99 (m, 7H), 5.86 (t, $J = 6.3$ Hz, 2H), 3.96 (d, $J = 6.6$ Hz, 4H), 3.85 (s, 6H); ^{13}C NMR (100 MHz, CD_3CN): δ 163.84, 138.65, 133.14, 130.04, 129.51, 128.20, 127.84, 115.24, 56.50, 47.45; IR: ν/cm^{-1} 3861, 3744, 3681, 3648, 2377, 2306, 1744, 1700, 1651, 1539, 1508, 1330, 1259, 1157, 1097, 1025; HRMS (ESI): Calc. for $\text{C}_{22}\text{H}_{24}\text{N}_2\text{O}_6\text{S}_2\text{H}^+$ ($\text{M} + \text{H}$) $^+$: 477.1155; Found: 477.1162; M.P.: 147 °C.

B. Synthesis of *N,N'*-(1,3-phenylenebis(methylene))bis(4-nitrobenzenesulfonamide) **1b**, ($\text{C}_{20}\text{H}_{18}\text{N}_4\text{O}_8\text{S}_2$):

In a 50 mL round bottom flask *m*-xylylenediamine **3** (0.19 mL, 1.5 mmol) and Et_3N (0.45 mL, 3.3 mmol) were dissolved in dry CH_2Cl_2 (5 mL). To the reaction mixture, a solution of 4-nitrobenzenesulfonyl chloride **5b** (664.8 mg, 3.0 mmol) in dry CH_2Cl_2 (3 mL) was added dropwise at 0 °C. The reaction mixture was stirred at 0 °C for 30 min. After completion of the

reaction, the reaction mixture was filtered. The filtrate was evaporated under reduced pressure to obtain a yellow residue, which was purified by column chromatography over silica gel (Eluent: 2% MeOH in CHCl₃) to furnish the pure **1b** (245 mg, 32%) as a off white solid. **¹H NMR (400 MHz, CD₃CN):** δ 8.28 (d, *J* = 9.0 Hz, 4H), 7.95 (d, *J* = 9.0 Hz, 4H), 7.15 – 7.08 (m, 1H), 7.03 (d, *J* = 7.9 Hz, 3H), 6.29 (s, 2H), 4.05 (s, 4H); **¹³C NMR (100 MHz, CD₃CN):** δ 151.10, 147.29, 138.19, 129.66, 129.23, 128.31, 128.06, 125.32, 47.44; **IR:** *v*/cm⁻¹ 3863, 3829, 3746, 3647, 3610, 3564, 1743, 1683, 1647, 1534, 1350, 1166, 1095; **HRMS (ESI):** Calc. for C₂₀H₁₈N₄O₈S₂Na⁺ (M+Na)⁺: 529.0463; Found: 529.0465; **M.P.:** 157 °C.

C. Synthesis of *N,N'*-(1,3-phenylenebis(methylene))bis(4-methylbenzenesulfonamide) **1c, (C₂₂H₂₄N₂O₄S₂):**

In a 50 mL round bottom flask *m*-xylylenediamine **3** (0.19 mL, 1.5 mmol) and Et₃N (0.45 mL, 3.3 mmol) were dissolved in dry CH₂Cl₂ (5 mL). To the reaction mixture, a solution of 4-toluenesulfonyl chloride **5c** (0.94 g, 3.3 mmol) in dry CH₂Cl₂ (3 mL) was added dropwise at 0 °C. The reaction mixture was stirred at 0 °C for 30 min. After completion of the reaction, the reaction mixture was filtered. The filtrate was evaporated under reduced pressure to obtain a residue which was purified by column chromatography over silica gel (Eluent: 1% MeOH in CHCl₃) to furnish the pure **1c** (300 mg, 45%) as a off white solid. **¹H NMR (400 MHz, CDCl₃):** δ 7.73 (d, *J* = 8.3 Hz, 4H), 7.30 (d, *J* = 7.9 Hz, 4H), 7.21 – 7.15 (m, 1H), 7.11 – 7.07 (m, 2H), 7.03 (s, 1H), 4.82 (t, *J* = 6.3 Hz, 2H), 4.03 (d, *J* = 6.3 Hz, 4H), 2.43 (s, 6H). **¹³C NMR (100 MHz, CD₃CN):** δ 144.53, 138.65, 138.60, 130.67, 129.52, 128.18, 127.91, 127.85, 47.46, 21.52. **IR:** *v*/cm⁻¹ 3837, 3744, 3648, 3607, 3489, 1329, 1161, 1094, 1063. **HRMS (ESI):** Calc. for C₂₂H₂₄N₂O₄S₂H⁺ (M+H)⁺: 445.1255; Found: 445.1254. **M.P.:** 154 °C.

D. Synthesis of 4-bromo-*N*-(3-(((4-methoxyphenyl)sulfonamido)methyl)benzyl)benzenesulfonamide **1d, (C₂₁H₂₁BrN₂O₅S₂):**

In a 50 mL round bottom flask *m*-xylylenediamine **3** (0.193 mL, 1.469 mmol) and Et₃N (0.450 mL, 3.232 mmol) were dissolved in dry CH₂Cl₂ (4.9 mL). To the reaction mixture, a solution of 4-methoxybenzenesulfonyl chloride **5a** (303 mg, 1.46 mmol) and 4-bromobenzenesulfonyl chloride **5d** (375.3 mg, 1.46 mmol) in dry CH₂Cl₂ (3 mL) was added dropwise at 0 °C. The reaction mixture was stirred at 0 °C for 30 min. After completion of the reaction, reaction mixture was filtered. The filtrate was evaporated under reduced pressure to obtain a residue which was purified by column chromatography over silica gel (Eluent: 9% EtOAc in CHCl₃) to furnish the pure **1d** (220 mg, 28.5%) as a off white solid. **¹H NMR (400 MHz, CD₃CN):** δ 7.77 – 7.71 (m, 2H), 7.66 (s, 4H), 7.17 (t, *J* = 7.6 Hz, 1H), 7.10 – 6.99 (m, 5H), 6.07 (s, 1H), 5.86 (t, *J* = 6.2 Hz, 1H), 4.01 (d, *J* = 6.0 Hz, 2H), 3.95 (d, *J* = 6.6 Hz, 2H), 3.86 (s, 3H); **¹³C NMR (100 MHz, CD₃CN):** δ 163.86, 140.88, 138.70, 138.29, 133.25, 133.13, 130.06, 129.70, 129.55, 128.23, 127.89, 127.66, 115.26, 56.51, 47.49, 47.42; **IR:** *v*/cm⁻¹ 3859,

3745, 3679, 3648, 3616, 2376, 2309, 1744, 1699, 1650, 1513, 1460, 1333, 1159; **HRMS (ESI)**: Calc. for $C_{21}H_{21}BrN_2O_5S_2H^+$ $[M+H]^+$: 525.0153; Found: 525.0149; **M.P.**: 148 °C.

E. Synthesis of *N,N'*-(1,3-phenylenebis(methylene))bis(4-bromobenzenesulfonamide) **1e, ($C_{20}H_{18}Br_2N_2O_4S_2$):**

In a 50 mL round bottom flask *m*-xylylenediamine **3** (0.19 mL, 1.46 mmol) and Et_3N (0.45 mL, 3.3 mmol) were dissolved in dry CH_2Cl_2 (5 mL). To the reaction mixture, a solution of 4-bromobenzenesulfonyl chloride **5d** (750.7 mg, 3.0 mmol) in dry CH_2Cl_2 (3 mL) was added dropwise at 0 °C. The reaction mixture was stirred at 0 °C for 30 min. After completion of the reaction, the reaction mixture was filtered. Filtrate was evaporated under reduced pressure to obtain yellow residue, which was purified by column chromatography over silica gel (Eluent: 1% MeOH in $CHCl_3$) to furnish the pure **1e** (206 mg, 24%) as a off white solid. **1H NMR (400 MHz, DMSO- d_6)**: δ 8.26 (t, $J = 6.3$ Hz, 2H), 7.81 – 7.75 (m, 4H), 7.72 – 7.66 (m, 4H), 7.17 (t, $J = 7.7$ Hz, 1H), 7.07 (d, $J = 7.5$ Hz, 3H), 3.92 (d, $J = 6.3$ Hz, 4H); **^{13}C NMR (100 MHz, DMSO- d_6)**: δ 139.98, 137.35, 132.14, 128.50, 128.18, 126.84, 126.46, 126.05, 45.98; **IR**: ν/cm^{-1} 3862, 3751, 3733, 3690, 3647, 36069, 3244, 1796, 1744, 1685, 1510, 1335, 1164, 1093, 1066, 1009; **HRMS (ESI)**: Calc. for $C_{20}H_{19}Br_2N_2O_4S_2^+$ $(M+H)^+$: 574.9127; Found: 574.9135; **M.P.**: 171 °C.

F. Synthesis of *N,N'*-(1,3-phenylenebis(methylene))bis(4-(trifluoromethyl)benzenesulfonamide) **1f, ($C_{22}H_{18}F_6N_2O_4S_2$):**

In a 50 mL round bottom flask *m*-xylylenediamine **3** (0.029 mL, 0.22 mmol) and Et_3N (0.067 mL, 0.48 mmol) were dissolved in dry CH_2Cl_2 (0.75 mL). To the reaction mixture, a solution of 4-(trifluoromethyl)benzenesulfonyl chloride **5e** (107.6 mg, 0.44 mmol) in dry CH_2Cl_2 (0.44 mL) was added dropwise at 0 °C. The reaction mixture was stirred at 0 °C for 30 min. After completion of the reaction, reaction mixture was filtered the. The filtrate was evaporated under reduced pressure to obtain a residue which was purified by column chromatography over silica gel (Eluent: 1% MeOH in $CHCl_3$) to furnish pure **1f** (40 mg, 33 %) as a off white solid. **1H NMR (400 MHz, CD_3CN)**: δ 7.93 (d, $J = 8.2$ Hz, 4H), 7.81 (d, $J = 8.3$ Hz, 4H), 7.12 (dd, $J = 8.6, 6.7$ Hz, 1H), 7.03 (d, $J = 8.0$ Hz, 3H), 6.22 (s, 2H), 4.02 (d, $J = 4.8$ Hz, 4H). **^{13}C NMR (101 MHz, CD_3CN)**: δ 145.44, 138.20, 129.59, 128.64, 128.33, 128.00, 127.28, 127.25, 127.21, 127.17, 47.43; **IR**: ν/cm^{-1} 3863, 3742, 3678, 3648, 3616, 2308, 1744, 1699, 1651, 1541, 1517, 1460, 1327, 1170, 1136, 1063; **HRMS (ESI)**: Calc. for $C_{22}H_{18}F_6N_2O_4S_2Na^+$ $(M+Na)^+$: 575.0509; Found: 575.0499; **M.P.**: 187 °C.

G. Synthesis of *N,N'*-(1,3-phenylenebis(methylene))bis(naphthalene-2-sulfonamide) **1g, ($C_{28}H_{24}N_2O_4S_2$):**

In a 50 mL round bottom flask *m*-xylylenediamine **3** (0.194 mL, 1.5 mmol) and Et_3N (0.630 mL, 4.5 mmol) were dissolved in dry CH_2Cl_2 (6 mL). To the reaction mixture, a solution of of

naphthalene-2-sulfonyl chloride **5g** (730 mg, 3.23 mmol) in dry CH₂Cl₂ (2 mL) was added dropwise at 0 °C. The reaction mixture was stirred at 0 °C for 1 h. After completion of the reaction, solvent was evaporated under reduced pressure to obtain a residue which was purified by column chromatography over silica gel (Eluent: 1% MeOH in CHCl₃) to furnish pure **1g** (600 mg, 77 %) as a off white solid. **¹H NMR (400 MHz, CD₃CN):** δ 8.35 (d, *J* = 1.4 Hz, 2H), 8.06 – 7.92 (m, 6H), 7.75 (dd, *J* = 8.6, 1.9 Hz, 2H), 7.69 – 7.59 (m, 4H), 7.06 (dd, *J* = 8.3, 6.8 Hz, 1H), 7.00 – 6.94 (m, 2H), 6.91 (s, 1H), 6.00 (t, *J* = 6.4 Hz, 2H), 3.88 (d, *J* = 6.5 Hz, 4H). **¹³C NMR (101 MHz, CD₃CN):** δ 138.34, 135.61, 133.06, 130.35, 130.14, 129.76, 129.36, 129.04, 128.80, 128.52, 128.16, 127.81, 123.27, 47.36. **IR:** *v*/cm⁻¹ 3265, 1431, 1314, 1145, 1055, 862; **HRMS (ESI):** Calc. for C₂₈H₂₄N₂O₄S₂Na⁺ (M+Na)⁺: 539.10759; Found: 539.1067; **M.P.:** 139 °C.

H. Synthesis of *N,N'*-(1,3-phenylenebis(methylene))bis(4-(trifluoromethyl)benzamide) **2**, (C₂₄H₁₈F₆N₂O₂):

In a 50 mL round bottom flask 4-(trifluoromethyl) benzoic acid **4** (0.2 g, 1.05 mmol) was dissolved in SOCl₂ (5 mL) and refluxed overnight. Excess SOCl₂ was evaporated under reduced pressure to get 4-(trifluoromethyl)benzoyl chloride.

In a 50 mL round bottom flask *m*-xylylenediamine **3** (65.9 μL, 0.5 mmol) and Et₃N (0.342 mL, 2.5 mmol) was dissolved in dry CH₂Cl₂ (2 mL). To the reaction mixture, a solution of freshly prepared 4-(trifluoromethyl)benzoyl chloride in dry CH₂Cl₂ (3 mL) was added dropwise at 0 °C. The reaction mixture was stirred at 0 °C for 1 h. After completion of the reaction, reaction mixture was filtered, and filtrate was evaporated under reduced pressure to obtain residue which was purified by column chromatography over silica gel (Eluent: 0.5% MeOH in CHCl₃) to furnish the pure **2** (130 mg, 54%) as a off white solid. **¹H NMR (400 MHz, CD₃CN):** δ 7.93 (d, *J* = 8.2 Hz, 4H), 7.72 (d, *J* = 8.2 Hz, 4H), 7.64 (s, 2H), 7.33 (s, 1H), 7.32 – 7.28 (m, 1H), 7.24 (d, *J* = 7.6 Hz, 2H), 4.56 (d, *J* = 6.1 Hz, 4H); **¹³C NMR (101 MHz, DMSO)** δ 165.04, 139.46, 138.08, 131.26, 130.94, 128.28, 128.10, 125.73, 125.55, 125.29, 125.25, 122.55, 42.60; **IR:** *v*/cm⁻¹ 3852, 3745, 3648, 3614, 3306, 2312, 1744, 1699, 1647, 1541, 1323, 1115, 1066, 1014; **HRMS (ESI):** Calc. for C₂₄H₁₈F₆N₂O₂H⁺ (M+H)⁺: 481.1350, Found: 481.1353; **M.P.:** 232 °C.

6.4.4. Anion Recognition by ¹H NMR Titration:

¹H NMR titrations were carried out in Bruker 500 MHz or 400 MHz spectrometer at room temperature and calibrated to the residual solvent peak in CD₃CN (δ = 1.94 ppm) or CDCl₃ (δ = 7.26 ppm). Titrations were performed by the addition of aliquots of tetrabutylammonium chloride (TBACl) (0.3 M in CD₃CN or CDCl₃) to the solution of receptor (~ 0.006 M) in CD₃CN or CDCl₃. Both TBA-salt and receptor were dried under high vacuum prior to use. All NMR data

were processed in MestReNova 6 software, and the change in chemical shift was plotted and fitted to the 1:1 binding model using WinEQNMR2 program.³⁵

Stoichiometry of anion binding by Job's plot analysis:

Stock solutions of **1f** and TBACl (30.1 mM each) were prepared separately and mixed in a specific ratio in 10 different samples according to Table 6.4.

Table 6.4. Calculation and Result table for Job's plot analysis.

Sample No	[H] ^a (mM)	[G] ^b (mM)	[H] + [G] (mM)	[H]/([H]+[G])	δ of proton H _a	$\Delta\delta$	[H]/([H+G])* $\Delta\delta$
1f-J1	3.01	27.09	30.1	0.1	7.311	0.275	0.0275
1f-J2	6.02	24.08	30.1	0.2	7.308	0.272	0.0544
1f-J3	9.03	21.07	30.1	0.3	7.297	0.261	0.0783
1f-J4	12.04	18.06	30.1	0.4	7.279	0.243	0.0972
1f-J5	15.05	15.05	30.1	0.5	7.236	0.2	0.1
1f-J6	18.06	12.04	30.1	0.6	7.196	0.16	0.096
1f-J7	21.07	9.03	30.1	0.7	7.168	0.132	0.0924
1f-J8	24.08	6.02	30.1	0.8	7.106	0.07	0.056
1f-J9	27.09	3.01	30.1	0.9	7.071	0.035	0.0315
1f-J10	30.1	0	30.1	1	7.036	0	0

^a [H] = Conc. of **1f**, ^b [G] = Conc. of TBACl.

6.4.5. Ion Transport Experiments:

Ion transport activity through the liposomal membrane was done according to the previous chapter.

6.4.6. Evidence of Carrier Mechanism:

U-tube Experiment:

The U-tube experiments were carried out in a U-shaped glass tube, partially filled with CHCl₃ as the organic phase. Two aqueous layers were created at the donor and receiver end of the tube. 0.5 M NaCl and equimolar NaNO₃ were placed at the donor and receiver end, respectively. It has been assumed that ion channel connecting two aqueous layers is not favourable as the long organic layer. 2 mM of TBAPF₆ was added in the organic phase to maintain the ion balance. Delivery of Cl⁻ ion to the receiver aqueous layer was monitored in the absence and presence of **1f** (2 mM). The experiments were carried out at room temperature under a slow stirring condition in the organic phase. The concentration (ppm) of Cl⁻ in the receiving phase was measured by chloride ion selective electrode (ISE).

A glass made U-shaped tube of 1 cm diameter has been used for this assay. The volume of organic layer is 14 mL and each aqueous layer contains 7 mL of salt solution. The stirring rate has been kept in between 150-200 rpm.

6.4.7. Biological Studies:

A. Cell culture protocol:

All cell lines were grown in High Glucose Dulbecco's Modified Eagle Medium (DMEM; Invitrogen or Lonza) containing 10% fetal bovine serum (FBS; Invitrogen), 2 mM L-glutamine (Invitrogen) and 100 units/mL penicillin-streptomycin (Invitrogen). Cells were maintained in 100 mm tissue culture treated dishes (Corning) at 37 °C in humidified 5% CO₂ incubator (Thermo Scientific).

B. MTT-based cytotoxicity assay:

Cells were dispersed in a 96-well flat bottom tissue culture treated plates (Corning) at a density of 10⁴ cells/well (per 100 μL) and incubated at 37 °C in a 5% CO₂ incubator for 16 h. Compounds were added to each well in different concentrations by maintaining the maximum amount of DMSO at 2 μL and incubated for 24 h. DMEM solution containing compounds in each well were replaced with 110 μL of MTT-DMEM mixture (0.5 mg MTT/mL of DMEM) and incubated for 4 h in identical condition. After 4 h, MTT solution was removed and 100 μL of DMSO was added to each well to dissolve the formazan crystals. The absorbance was recorded in a microplate reader (Varioskan Flash) at the wavelength of 570 nm. All experiments were performed in quadruplicate, and the relative cell viability (%) was expressed as a percentage relative to the untreated cells.

Table S3: IC₅₀ values of **1e** and **1f**.

	1e (μM)	1f (μM)
MCF7	18.7	11.2
NIH3T3	47.1	99.7
U2OS	14.6	7.5
HeLa	32.4	8.9
A549	56.9	12.2

C. Measurement of intracellular Cl⁻ concentrations: Time-dependent influx data of Cl⁻ were measured in HeLa and MCF7 cells by using chloride selective cell permeable fluorescent dye *N*-(ethoxycarbonylmethyl)-6-methoxyquinolinium bromide (MQAE). Cells were seeded in a 96-

well flat bottom tissue culture treated plates (Corning) at density of 10^4 cells/well (per 100 μ L) and incubated at 37 °C, 5% CO₂ for 16 h. MQAE was added to each well by maintaining final concentration as 5 mM for 3.5 h. Extracellular dye was removed by washing with PBS and compound **1f** was added in DMEM at various concentrations and cells were incubated for 24 h. The MQAE fluorescence was measured using a fluorescence microplate reader ($\lambda_{\text{ex}} = 350$ nm and $\lambda_{\text{em}} = 460$ nm).

D. Chloride mediated cell death studies.

HBSS buffer solution. Hank's balanced salt solution (HBSS with Cl⁻) was prepared with the following compositions: 136.9 mM NaCl, 5.5 mM KCl, 0.34 mM Na₂HPO₄, 0.44 mM KH₂PO₄, 0.81 mM MgSO₄, 1.25 mM CaCl₂, 5.5 mM D-glucose, 4.2 mM NaHCO₃ and 10 mM HEPES (pH 7.4). Chloride free HBSS was prepared by mixing 136.9 mM Na-gluconate, 5.5 mM K-gluconate, 0.34 mM Na₂HPO₄, 0.44 mM KH₂PO₄, 0.81 mM MgSO₄, 1.25 mM Ca-gluconate, 5.5 mM D-glucose, 4.2 mM NaHCO₃ and 10 mM HEPES (pH 7.4).

Cells were dispersed in a 96-well flat bottom tissue culture treated plates (Corning) at a density of 10^4 cells/well (per 100 μ L) and incubated at 37 °C in 5% CO₂ for 16 h. Cellular media was replaced by HBSS buffer (either with Cl⁻ or without Cl⁻) containing 10% FBS. Compounds were added to each well in different concentration by maintaining the maximum amount of DMSO at 2 μ L and incubated for 24 h. HBSS buffer solution of compounds in each well was replaced by 110 μ L of MTT-DMEM mixture (0.5 mg MTT/mL of DMEM) and incubated for 4 h in identical condition. Remaining MTT solution was removed after 4 h and 100 μ L of DMSO was added to each well to dissolve the formazan crystals. The absorbance was recorded in a microplate reader (Varioskan Flash) at the wavelength of 570 nm.

E. Immunofluorescence analysis for cytochrome *c* release:

Cells were seeded at a density of 1×10^5 cells per well on top of glass cover slips (Micro-Aid, India). Following **1f** treatment, cells were fixed using 4% formalin (Macron Chemicals) and were permeabilised using 0.5% Triton X-100 for 10 min at 4 °C. Cells were blocked with 10% (v/v) FBS (Invitrogen), stained with primary antibody (cytochrome *c* antibody) and then incubated with secondary antibody (goat anti-rabbit AlexaFluor-488). Cells were then counterstained with 0.5 μ g/mL Hoechst 33342 and mounted on glass slides (Micro-Aid, India). Cell images were taken in were taken using Olympus Inverted IX81 microscope equipped with Hamamatsu Orca R2 camera. Microscopy images were captured using 100X oil-immersion objective.

F. Immunoblot analysis:

Cells were seeded at a density of 6×10^5 cells per well in 6-well tissue culture treated plates (Corning) and maintained at 37 °C for 16 h. Cells were then treated with **1f** by direct addition of

the drug to the culture medium for 24 h at different concentration (0, 10, 20 and 40 μM). Control cells were treated with an equivalent volume of DMSO. After 24 h treatment, medium containing **1f** was aspirated, and cells were washed once with 1X phosphate buffered saline (PBS; PAN-Biotech GmbH). Cells were lysed in sample buffer containing 60 mM Tris (pH 6.8), 6% glycerol, 2% sodium dodecyl sulfate (SDS), 0.1 M dithiothreitol (DTT) and 0.006% bromophenol blue and lysates were stored at $-40\text{ }^{\circ}\text{C}$.

Cell lysates were resolved using sodium dodecyl sulfate polyacrylamide gel electrophoresis (SDS-PAGE) and transferred to Immobilon-P polyvinylidene difluoride (PVDF) membrane (Millipore). Blocking was performed in 5% (w/v) skimmed milk (SACO Foods, USA) prepared in 1X Tris-buffered saline containing 0.1% Tween 20 (1X TBS-T) for 1 h at room temperature. Blots were incubated for 3 h at room temperature (or for 16 h at $4\text{ }^{\circ}\text{C}$) in primary antibody solution. Following washes, blots were incubated with peroxidase-conjugated secondary antibody solution prepared in 5% (w/v) skimmed milk in 1X TBS-T for 1 h at room temperature following which blots were developed using Immobilon Western Detection Reagent kit (Millipore) and visualized using ImageQuant LAS 4000 (GE Healthcare).

G. Caspase Inhibitor Activity:

Inhibitor for caspase-3: Benzyloxycarbonyl-Asp(OMe)-Glu(OMe)-Val-Asp(OMe)-fluoromethylketone (z-DEVD-fmk).

Inhibitor for caspase-9: Benzyloxycarbonyl-Leu-Glu(OMe)-His-Asp(OMe)-fluoromethylketone (z-LEHD-fmk).

Immunoblot analysis: Cells were seeded at a density of 6×10^5 cells per well in 6-well tissue culture treated plates (Corning) and maintained at $37\text{ }^{\circ}\text{C}$ for 16 h. One set of cells were then treated with z-DEVD-fmk and z-LEHD-fmk ($50\text{ }\mu\text{M}$ each) for 3 h. Then each set of cells were incubated with **1f** for 24 h at different concentration ($20\text{ }\mu\text{M}$). Control cells were treated with an equivalent volume of DMSO. After 24 h treatment, medium containing **1f** was aspirated, and cells were washed once with 1X phosphate buffered saline (PBS; PAN-Biotech GmbH). Cells were lysed in sample buffer containing 60 mM Tris (pH 6.8), 6% glycerol, 2% sodium dodecyl sulfate (SDS), 0.1 M dithiothreitol (DTT) and 0.006% bromophenol blue and lysates were stored at $-40\text{ }^{\circ}\text{C}$. Remaining procedure of gel electrophoresis was done according to the same protocol as stated above.

MTT assay: MTT assay was performed as stated above. Cells were preincubated with caspase inhibitors ($50\text{ }\mu\text{M}$ each) followed by incubation with **1f** ($10\text{ }\mu\text{M}$) for 24 h. Each bar represents the mean intensity of three independent experiments, and the differences in mean intensity are

statistically significant ($P < 0.05$), in each case, according to one-way analysis of variance (ANOVA).

H. Nuclear fragmentation by live cell imaging:

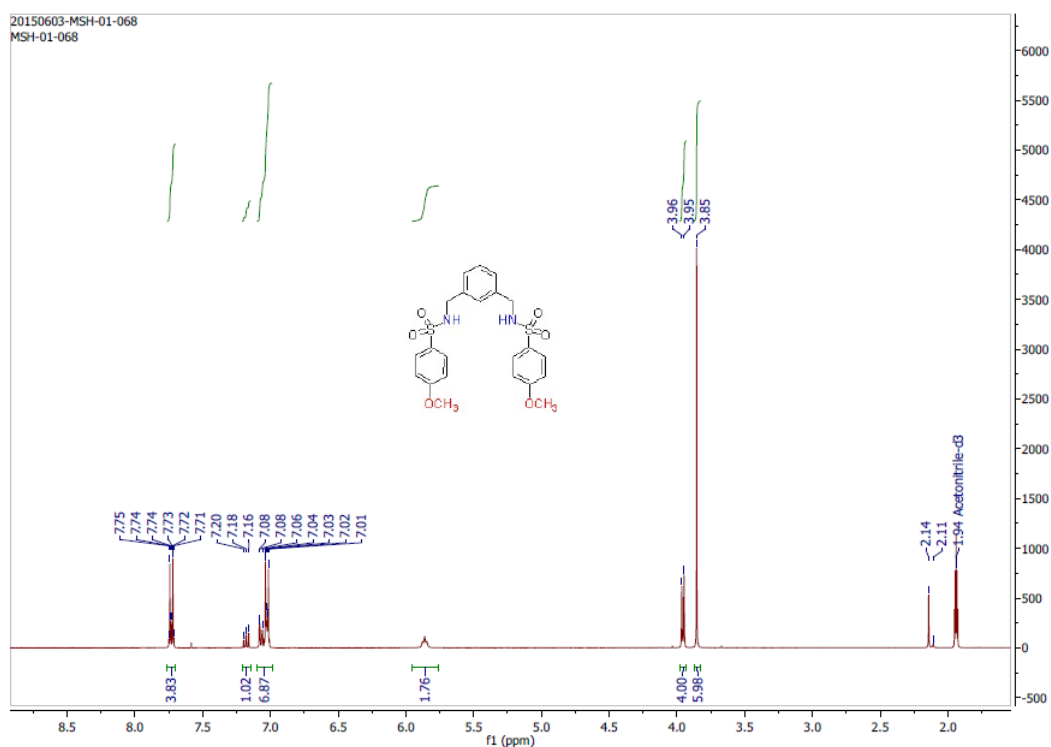
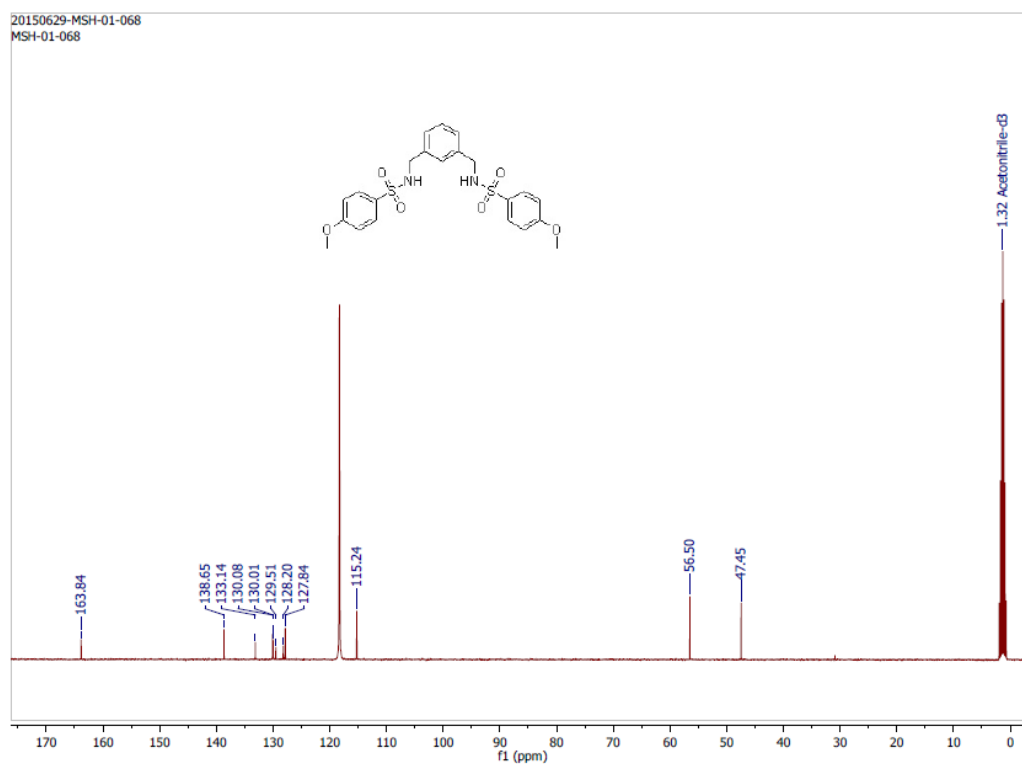
The HeLa cells were seeded in glass bottom 35 mm dishes at the concentration of 0.75×10^5 cells per plate. Cells were incubated with 20 μM of **1f** for 24 h. After that cells were washed thoroughly and incubated with Hoechst 33342 for 15 min. Fluorescence images were acquired after washing with PBS (Figure 16).

I. Measurement of ROS level:

Cells were dispersed in a 96-well flat bottom tissue culture treated plates (Corning) at density of 1.5×10^4 cells/well (per 100 μL) and incubated at 37 $^\circ\text{C}$ in a 5% CO_2 incubator for 16 h. Compounds were added to each well in different concentration by maintaining the maximum amount of DMSO at 2 μL and incubated for 7 h. 3-methyl-7-(4,4,5,5-tetramethyl-1,3,2-dioxaborolan-2-yl)-2H-chromen-2-one (**ROS probe**)^{73,74} was added to the each well at final concentration 50 μM and incubated further for 1 h. Fluorescence intensities were recorded from the plate reader at $\lambda_{\text{em}} = 460 \text{ nm}$ ($\lambda_{\text{ex}} = 315 \text{ nm}$), and normalized with respect to the fluorescence intensity of untreated cells. Each bar represents the mean intensity of three independent experiments, and the differences in mean intensity are statistically significant ($P < 0.001$), in each case, according to one-way analysis of variance (ANOVA).

In another set of experiment, external media was replaced with HBSS buffer and the enhancement in fluorescence intensity was compared with Cl^- free HBSS buffer. Gradual increase in fluorescence was observed in case of Cl^- containing HBSS buffer. But, Cl^- free buffer showed very less enhancement in the fluorescence intensity *i.e.* less production of ROS in absence of Cl^- .

6.4.8. NMR Spectra:

Figure 6.36. ^1H NMR spectrum of 1a.Figure 6.37. ^{13}C NMR spectrum of 1a.

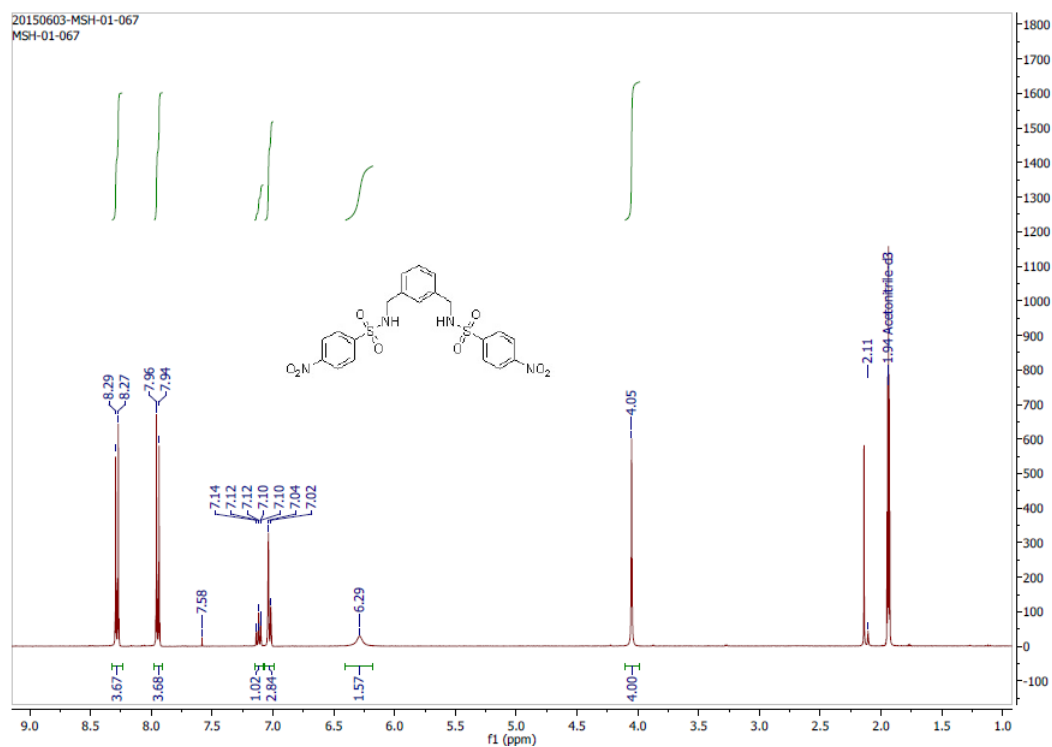


Figure 6.38. ^1H NMR spectrum of **1b**.

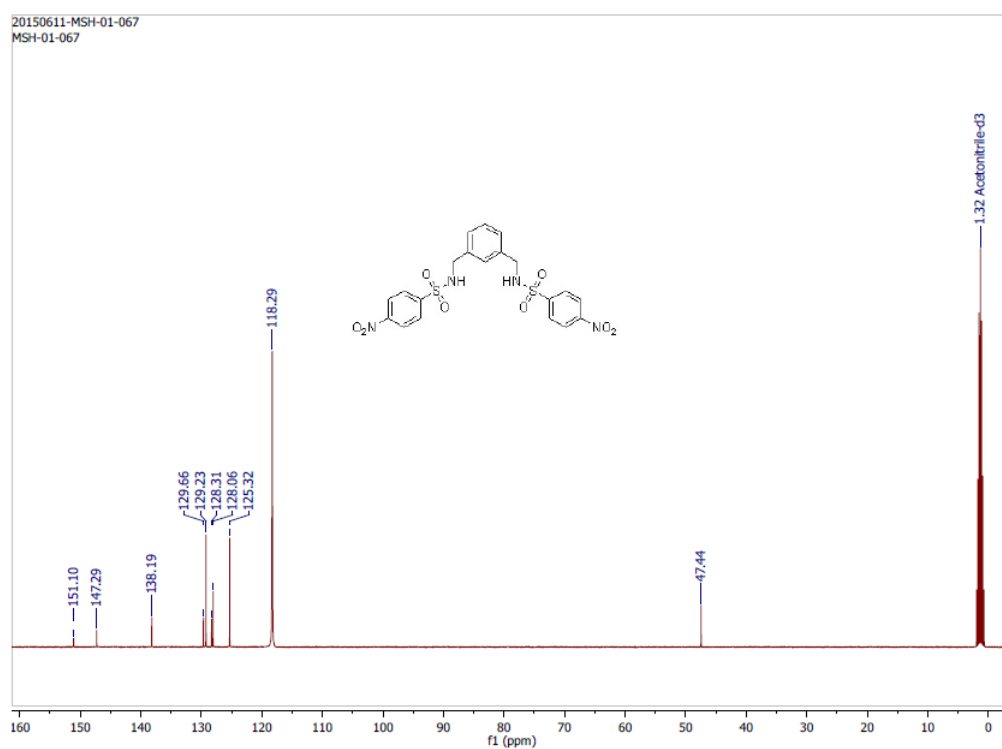


Figure 6.39. ^{13}C NMR spectrum of **1b**.

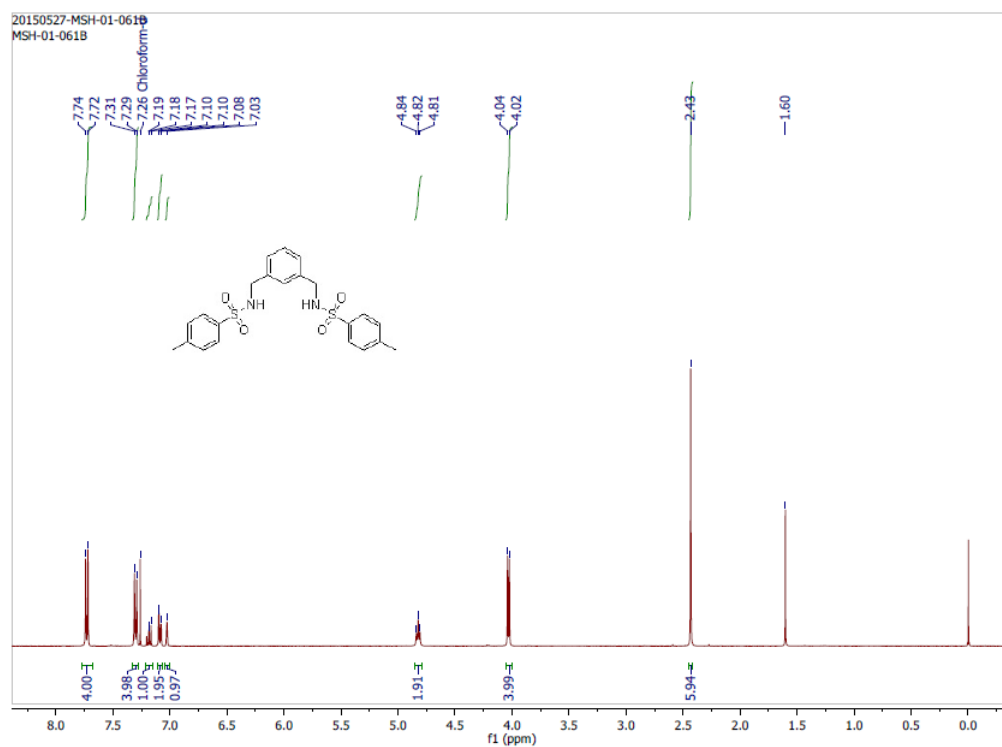


Figure 6.40. ^1H NMR spectrum of **1c**.

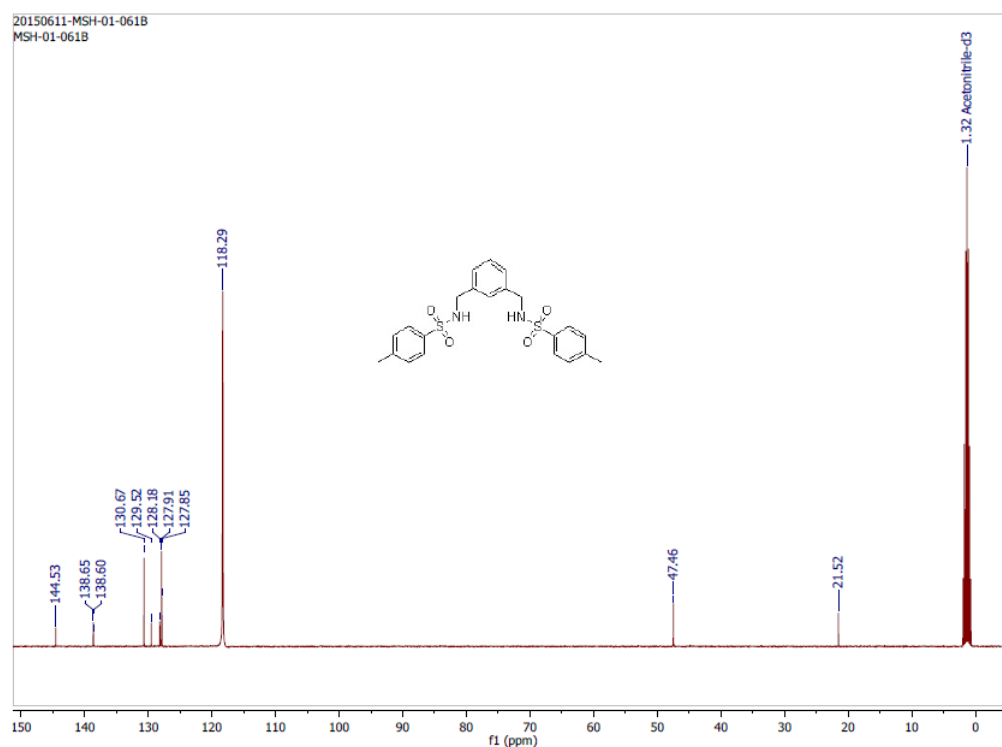


Figure 6.41. ^{13}C NMR spectrum of **1c**.

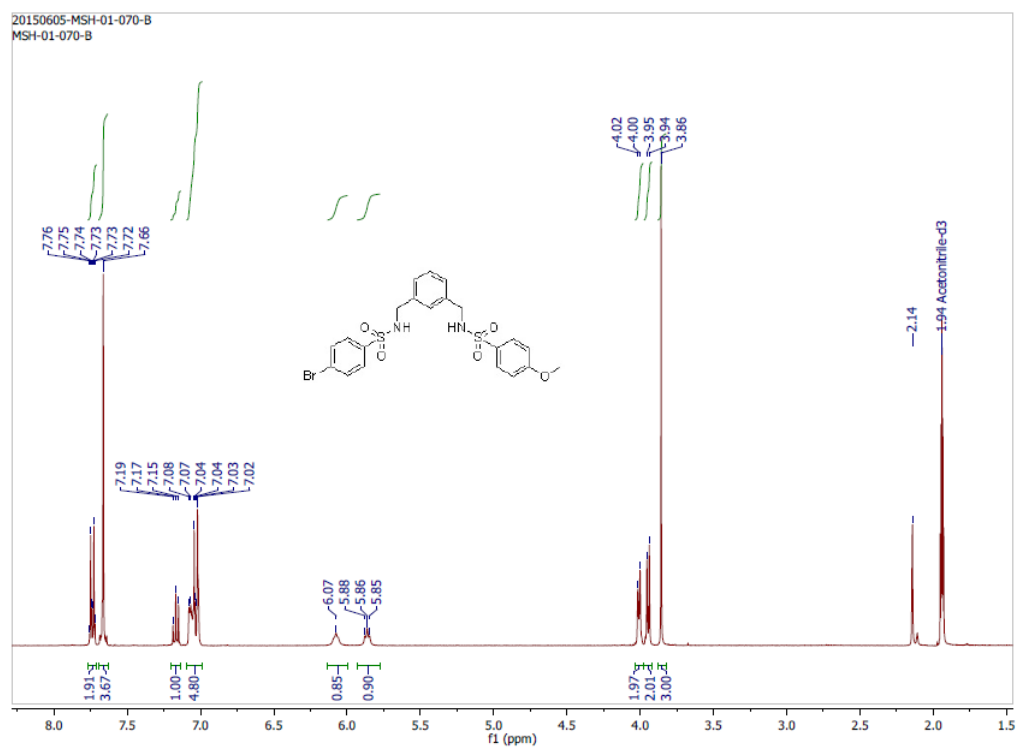


Figure 6.42. ^1H NMR spectrum of **1d**.

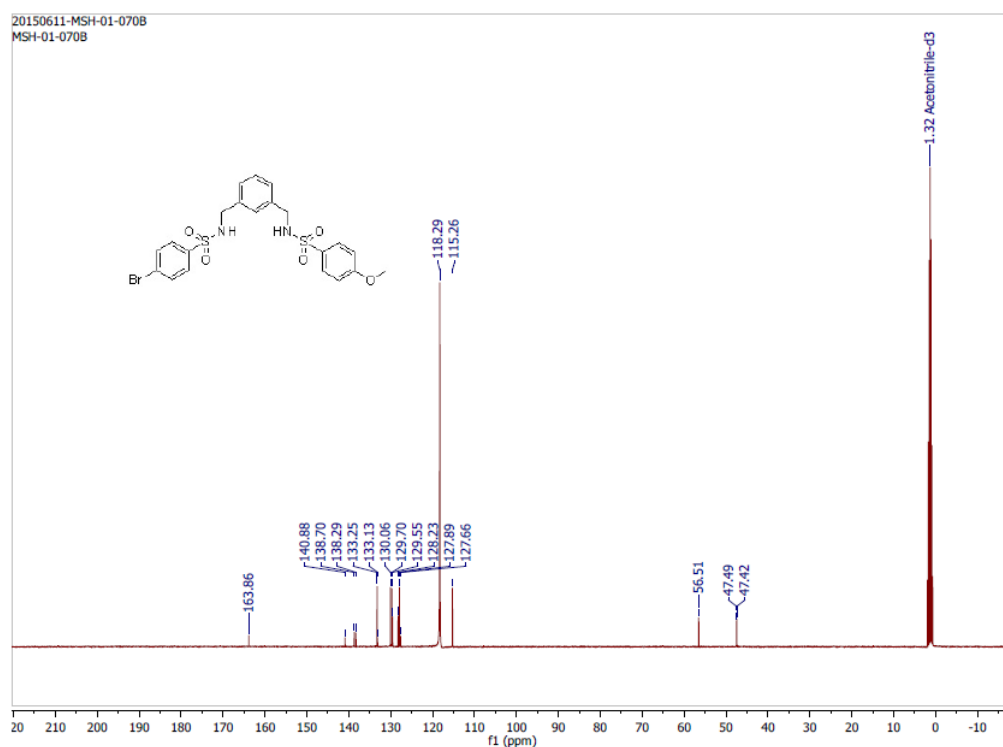


Figure 6.43. ^{13}C NMR spectrum of **1d**.

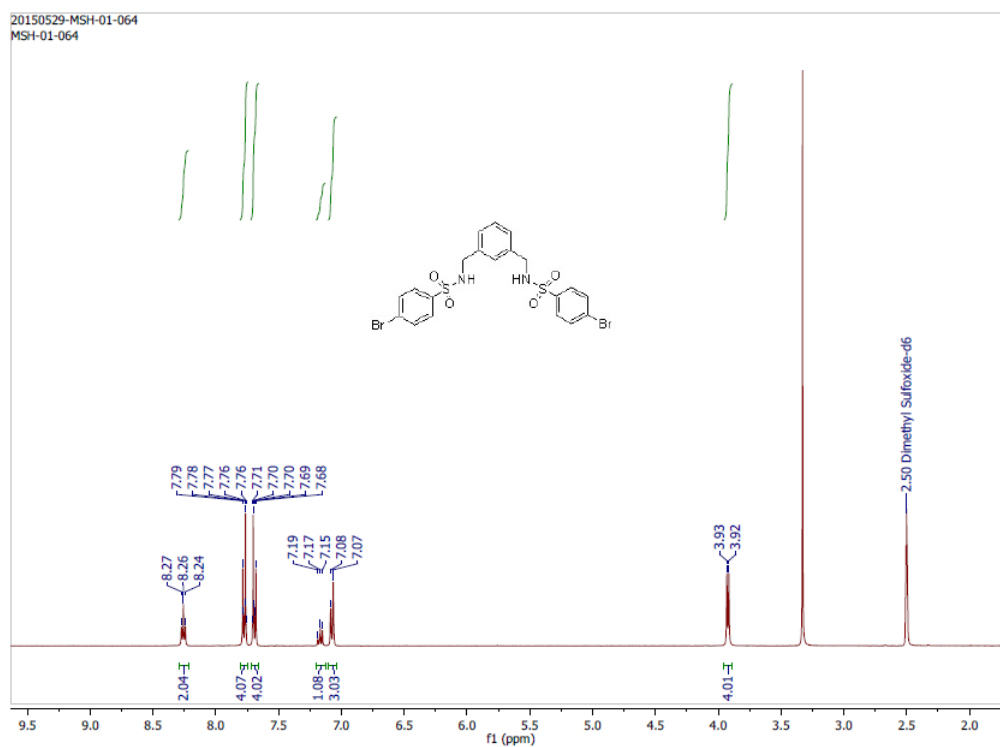


Figure 6.44. ^1H NMR spectrum of **1e**.

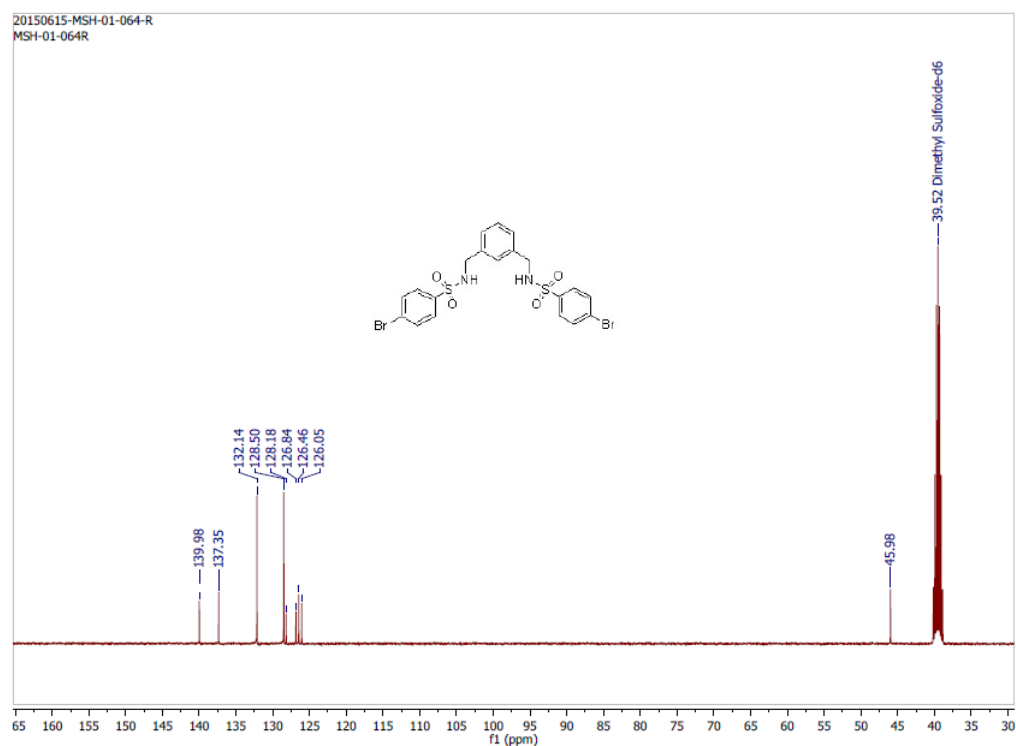


Figure 6.45. ^{13}C NMR spectrum of **1e**.

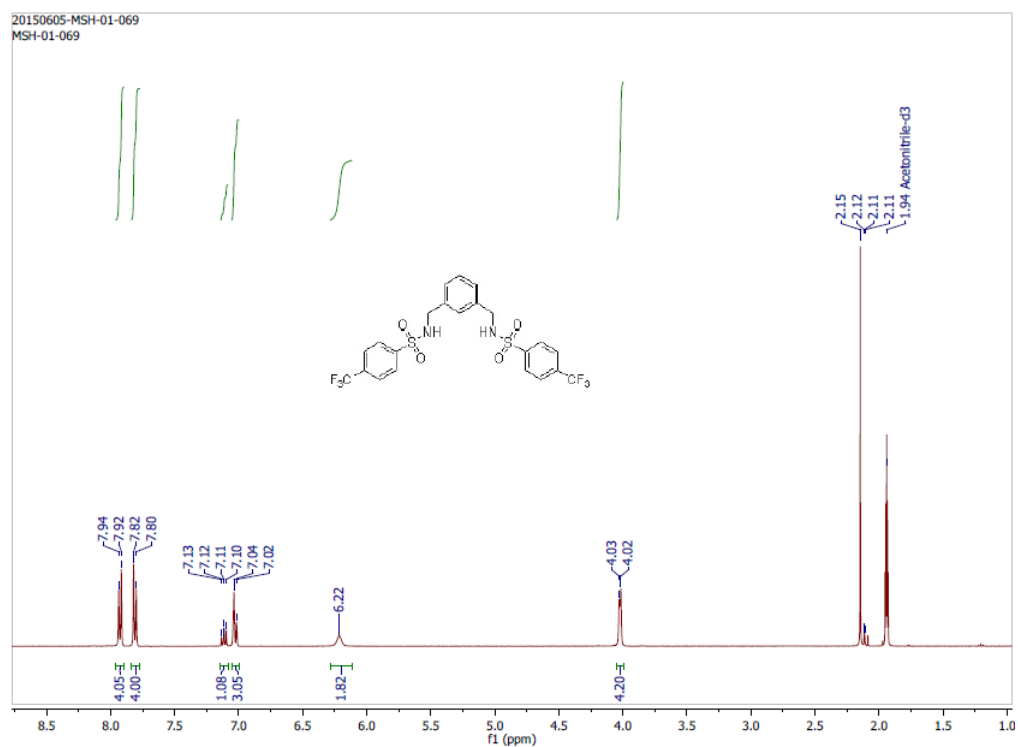


Figure 6.46. ^1H NMR spectrum of **1f**.

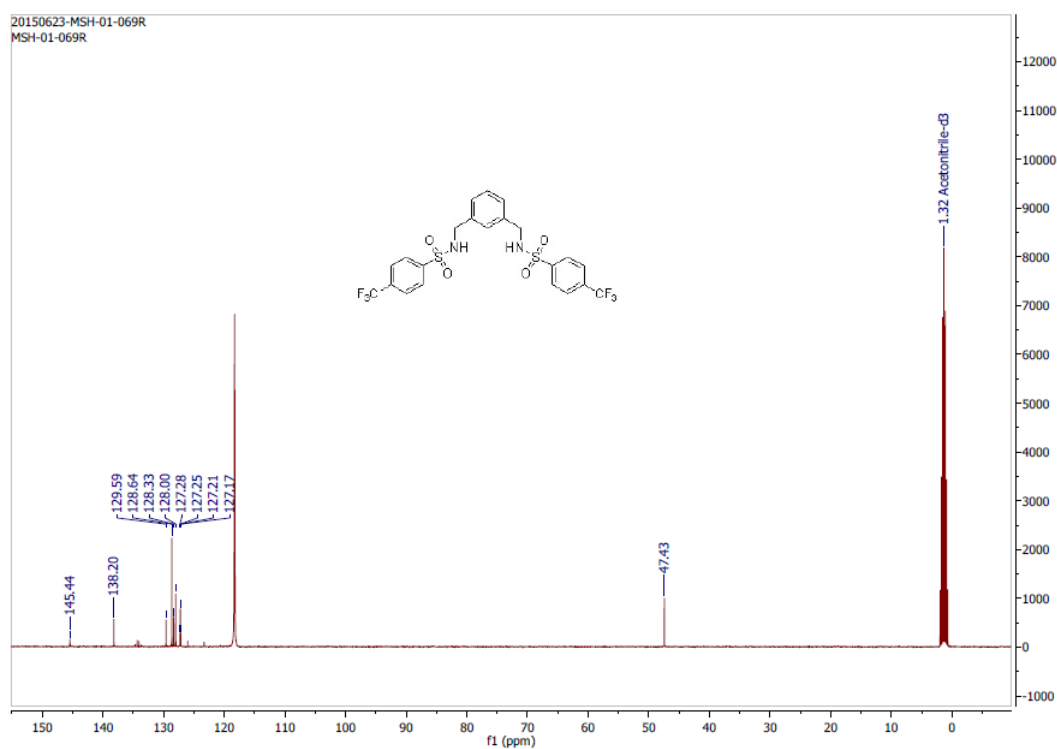


Figure 6.47. ^{13}C NMR spectrum of **1f**.

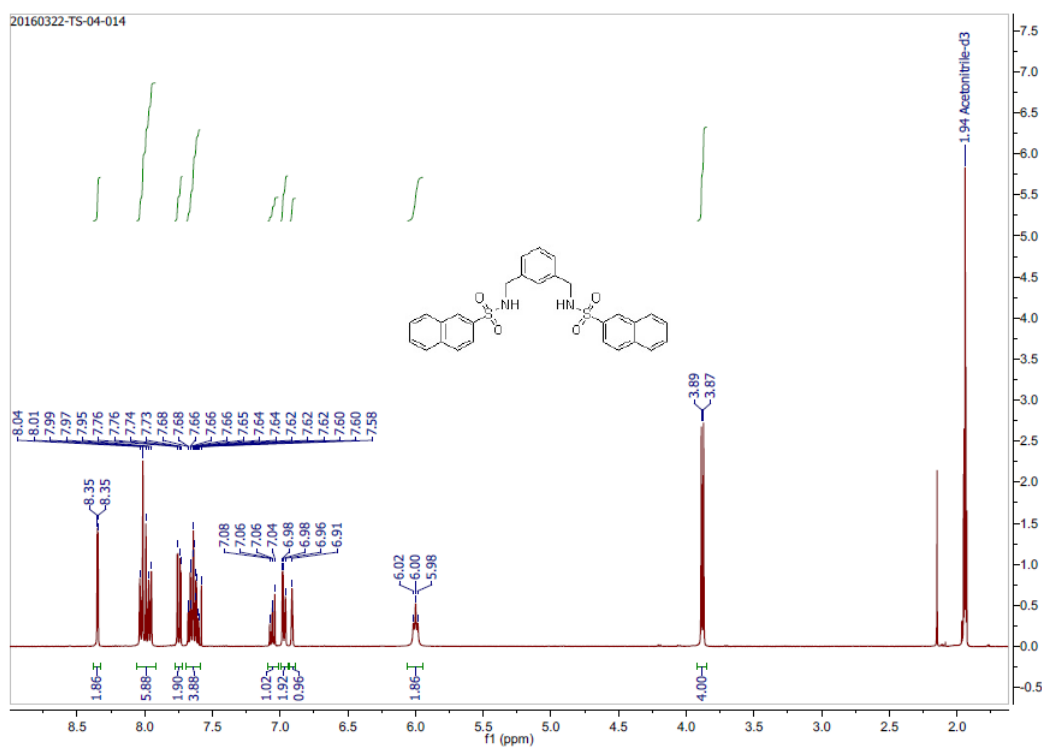


Figure 6.48. ¹H NMR spectrum of 1g.

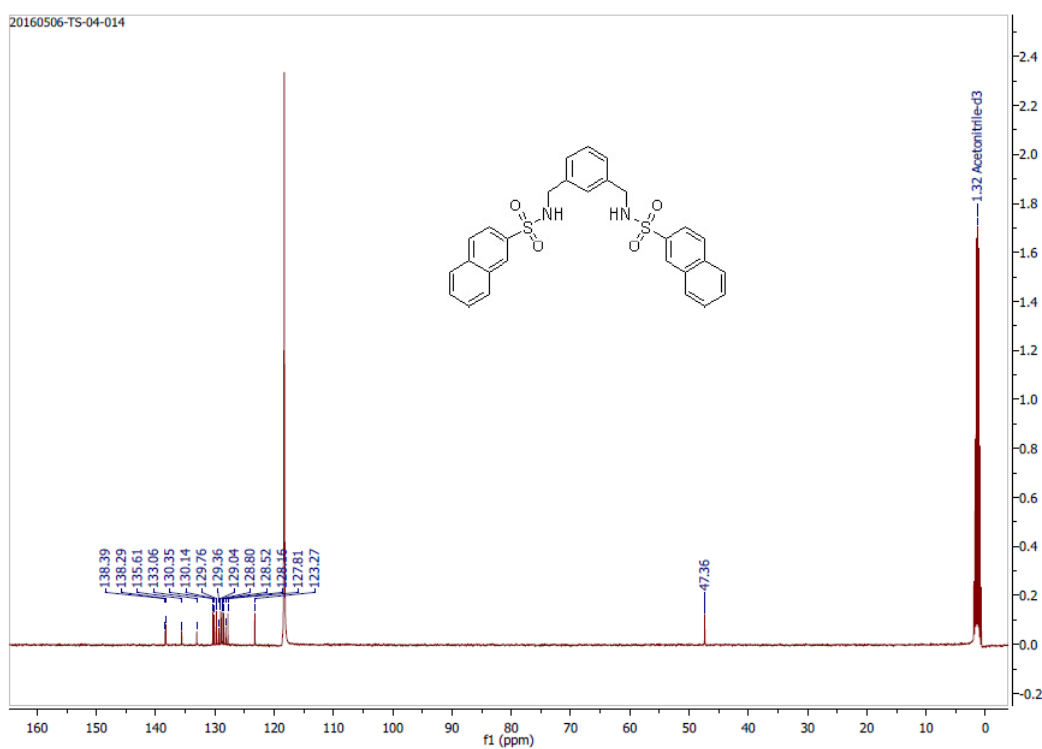


Figure 6.49. ¹³C NMR spectrum of 1g.

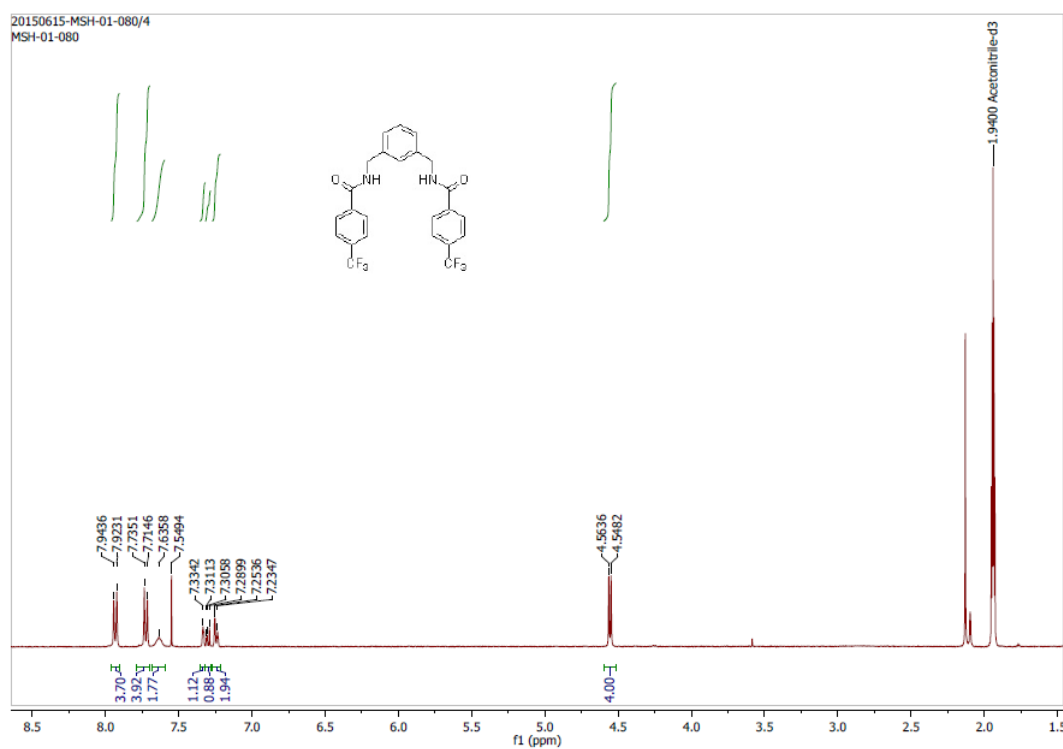


Figure 6.50. ^1H NMR spectrum of **2**.

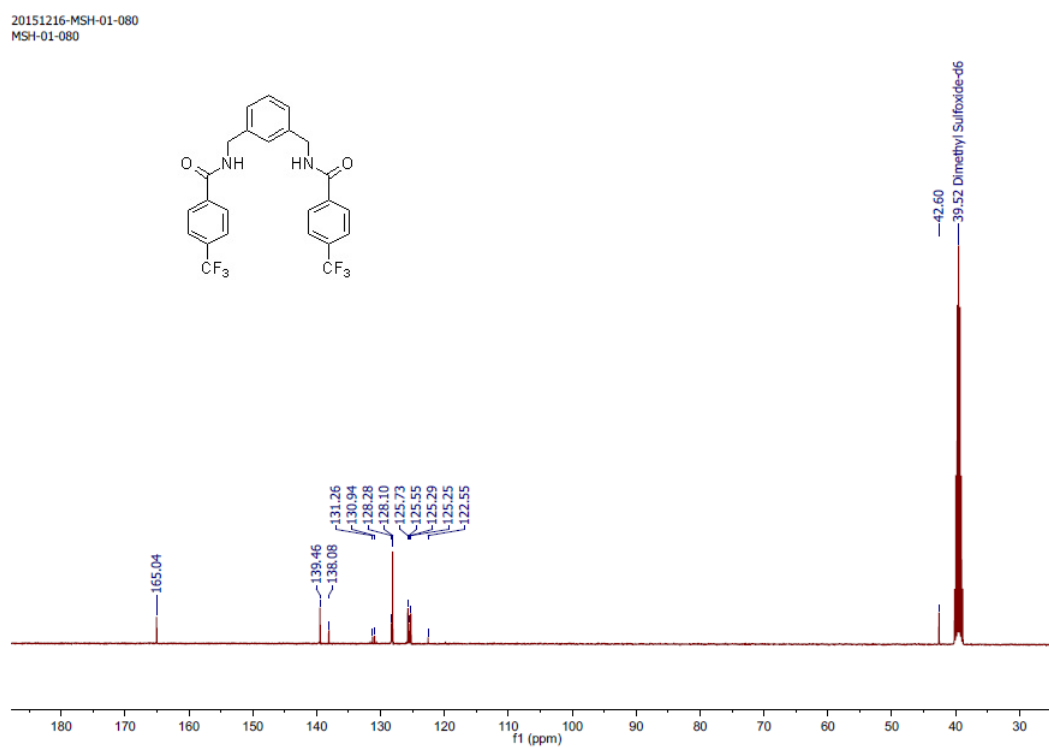


Figure 6.51. ^{13}C NMR spectrum of **2**.

6.5. REFERENCE:

- (1) Fuerstner, A. *Angew. Chem., Int. Ed.* **2003**, *42*, 3582.
- (2) Seganish, J. L.; Davis, J. T. *Chem. Commun.* **2005**, 5781.
- (3) Sessler, J. L.; Eller, L. R.; Cho, W.-S.; Nicolaou, S.; Aguilar, A.; Lee, J. T.; Lynch, V. M.; Magda, D. J. *Angew. Chem., Int. Ed.* **2005**, *44*, 5989.
- (4) Marchal, E.; Rastogi, S.; Thompson, A.; Davis, J. T. *Org. Biomol. Chem.* **2014**, *12*, 7515.
- (5) Busschaert, N.; Wenzel, M.; Light, M. E.; Iglesias-Hernández, P.; Pérez-Tomás, R.; Gale, P. A. *J. Am. Chem. Soc.* **2011**, *133*, 14136.
- (6) Moore, S. J.; Wenzel, M.; Light, M. E.; Morley, R.; Bradberry, S. J.; Gomez-Iglesias, P.; Soto-Cerrato, V.; Perez-Tomas, R.; Gale, P. A. *Chem. Sci.* **2012**, *3*, 2501.
- (7) Moore, S. J.; Haynes, C. J. E.; Gonzalez, J.; Sutton, J. L.; Brooks, S. J.; Light, M. E.; Herniman, J.; Langley, G. J.; Soto-Cerrato, V.; Perez-Tomas, R.; Marques, I.; Costa, P. J.; Felix, V.; Gale, P. A. *Chem. Sci.* **2013**, *4*, 103.
- (8) Ko, S.-K.; Kim, S. K.; Share, A.; Lynch, V. M.; Park, J.; Namkung, W.; Van Rossom, W.; Busschaert, N.; Gale, P. A.; Sessler, J. L.; Shin, I. *Nat. Chem.* **2014**, *6*, 885.
- (9) Soto-Cerrato, V.; Manuel-Manresa, P.; Hernando, E.; Calabuig-Fariñas, S.; Martínez-Romero, A.; Fernández-Dueñas, V.; Sahlholm, K.; Knöpfel, T.; García-Valverde, M.; Rodilla, A. M.; Jantus-Lewintre, E.; Farràs, R.; Ciruela, F.; Pérez-Tomás, R.; Quesada, R. *J. Am. Chem. Soc.* **2015**, *137*, 15892.
- (10) McNally, B. A.; Koulov, A. V.; Smith, B. D.; Joos, J.-B.; Davis, A. P. *Chem. Commun.* **2005**, 1087.
- (11) Davis, A. P.; Joos, J.-B. *Coord. Chem. Rev.* **2003**, *240*, 143.
- (12) Davis, A. P. *Coord. Chem. Rev.* **2006**, *250*, 2939.
- (13) McNally, B. A.; Koulov, A. V.; Lambert, T. N.; Smith, B. D.; Joos, J.-B.; Sisson, A. L.; Clare, J. P.; Sgarlata, V.; Judd, L. W.; Magro, G.; Davis, A. P. *Chem. Eur. J.* **2008**, *14*, 9599.
- (14) Hussain, S.; Brotherhood, P. R.; Judd, L. W.; Davis, A. P. *J. Am. Chem. Soc.* **2011**, *133*, 1614.
- (15) Tong, C. C.; Quesada, R.; Sessler, J. L.; Gale, P. A. *Chem. Commun.* **2008**, 6321.
- (16) Gale, P. A.; Tong, C. C.; Haynes, C. J. E.; Adeosun, O.; Gross, D. E.; Karnas, E.; Sedenberg, E. M.; Quesada, R.; Sessler, J. L. *J. Am. Chem. Soc.* **2010**, *132*, 3240.
- (17) Fisher, M. G.; Gale, P. A.; Hiscock, J. R.; Hursthouse, M. B.; Light, M. E.; Schmidtchen, F. P.; Tong, C. C. *Chem. Commun.* **2009**, 3017.
- (18) Busschaert, N.; Gale, P. A.; Haynes, C. J. E.; Light, M. E.; Moore, S. J.; Tong, C. C.; Davis, J. T.; Harrell, W. A., Jr. *Chem. Commun.* **2010**, *46*, 6252.

- (19) Santacroce, P. V.; Davis, J. T.; Light, M. E.; Gale, P. A.; Iglesias-Sanchez, J. C.; Prados, P.; Quesada, R. *J. Am. Chem. Soc.* **2007**, *129*, 1886.
- (20) Busschaert, N.; Kirby, I. L.; Young, S.; Coles, S. J.; Horton, P. N.; Light, M. E.; Gale, P. A. *Angew. Chem., Int. Ed.* **2012**, *51*, 4426.
- (21) Cooper, J. A.; Street, S. T. G.; Davis, A. P. *Angew. Chem., Int. Ed.* **2014**, *53*, 5609.
- (22) Wenzel, M.; Light, M. E.; Davis, A. P.; Gale, P. A. *Chem. Commun.* **2011**, *47*, 7641.
- (23) Andrews, N. J.; Haynes, C. J. E.; Light, M. E.; Moore, S. J.; Tong, C. C.; Davis, J. T.; Harrell Jr, W. A.; Gale, P. A. *Chem. Sci.* **2011**, *2*, 256.
- (24) Valkenier, H.; Judd, L. W.; Li, H.; Hussain, S.; Sheppard, D. N.; Davis, A. P. *J. Am. Chem. Soc.* **2014**, *136*, 12507.
- (25) Busschaert, N.; Bradberry, S. J.; Wenzel, M.; Haynes, C. J. E.; Hiscock, J. R.; Kirby, I. L.; Karagiannidis, L. E.; Moore, S. J.; Wells, N. J.; Herniman, J.; Langley, G. J.; Horton, P. N.; Light, M. E.; Marques, I.; Costa, P. J.; Felix, V.; Frey, J. G.; Gale, P. A. *Chem. Sci.* **2013**, *4*, 3036.
- (26) Valkenier, H.; Haynes, C. J. E.; Herniman, J.; Gale, P. A.; Davis, A. P. *Chem. Sci.* **2014**, *5*, 1128.
- (27) Lee, J. H.; Lee, J. H.; Choi, Y. R.; Kang, P.; Choi, M.-G.; Jeong, K.-S. *J. Org. Chem.* **2014**, *79*, 6403.
- (28) Winstanley, K. J.; Allen, S. J.; Smith, D. K. *Chem. Commun.* **2009**, 4299.
- (29) Berryman, O. B.; Hof, F.; Hynes, M. J.; Johnson, D. W. *Chem. Commun.* **2006**, 506.
- (30) Mammoliti, O.; Allasia, S.; Dixon, S.; Kilburn, J. D. *Tetrahedron* **2009**, *65*, 2184.
- (31) Huang, X.-Y.; Wang, H.-J.; Shi, J. *J. Phys. Chem. A* **2010**, *114*, 1068.
- (32) <http://www.chem.wisc.edu/areas/reich/pkatable/index.htm>.
- (33) Lipinski, C. A.; Lombardo, F.; Dominy, B. W.; Feeney, P. J. *Adv. Drug Deliv. Rev.* **1997**, *23*, 3.
- (34) Marvin 5.8.0, ChemAxon, 2012 (<http://www.chemaxon.com>).
- (35) Hynes, M. J. *J. Chem. Soc., Dalton Trans.* **1993**, 311.
- (36) Goto, H.; Obata, S.; Nakayama, N.; Ohta, K. CONFLEX 7, CONFLEX Corporation: Tokyo, Japan, 2012.
- (37) Goto, H.; Osawa, E. *J. Am. Chem. Soc.* **1989**, *111*, 8950.
- (38) Frisch, M. J., Trucks, G. W., Schlegel, H. B., Scuseria, G. E., Robb, M. A., Cheeseman, J. R., Scalmani, G., Barone, V., Mennucci, B., Petersson, G. A., Nakatsuji, H., Caricato, M., Li, X., Hratchian, H. P., Izmaylov, A. F., Bloino, J., Zheng, G., Sonnenberg, J. L., Hada, M., Ehara, M., Toyota, K., Fukuda, R., Hasegawa, J., Ishida, M., Nakajima, T., Honda, Y., Kitao, O., Nakai, H., Vreven, T., Montgomery, J. A., Jr., Peralta, J. E., Ogliaro, F., Bearpark, M., Heyd, J. J., Brothers, E., Kudin, K. N., Staroverov, V. N., Keith, T., Kobayashi, R., Normand, J., Raghavachari, K., Rendell, A., Burant, J. C., Iyengar, S. S.,

- Tomasi, J., Cossi, M., Rega, N., Millam, J. M., Klene, M., Knox, J. E., Cross, J. B., Bakken, V., Adamo, C., Jaramillo, J., Gomperts, R., Stratmann, R. E., Yazyev, O., Austin, A. J., Cammi, R., Pomelli, C., Ochterski, J. W., Martin, R. L., Morokuma, K., Zakrzewski, V. G., Voth, G. A., Salvador, P., Dannenberg, J. J., Dapprich, S., Daniels, A. D., Farkas, O., Foresman, J. B., Ortiz, J. V., Cioslowski, J., Fox, D. J. Gaussian 09, Revision B.01; Gaussian, Inc.: Wallingford, CT, 2010.
- (39) Foster, J. P.; Weinhold, F. *J. Am. Chem. Soc.* **1980**, *102*, 7211.
- (40) Madhavan, N.; Robert, E. C.; Gin, M. S. *Angew. Chem., Int. Ed.* **2005**, *44*, 7584.
- (41) Bochenska, M.; Biernat, J. F.; Topolski, M.; Bradshaw, J. S.; Bruening, R. L.; Izatt, R. M.; Dalley, N. K. *J. Inclusion Phenom. Mol. Recognit. Chem.*, **1989**, *7*, 599.
- (42) Biwersi, J.; Tulk, B.; Verkman, A. S. *Anal. Biochem.* **1994**, *219*, 139.
- (43) Milano, D.; Benedetti, B.; Boccalon, M.; Brugnara, A.; Iengo, E.; Tecilla, P. *Chem. Commun.* **2014**, *50*, 9157.
- (44) Tsukimoto, M.; Harada, H.; Ikari, A.; Takagi, K. *J. Biol. Chem.* **2005**, *280*, 2653.
- (45) Yu, L.; Jiang, X. H.; Zhou, Z.; Tsang, L. L.; Yu, M. K.; Chung, Y. W.; Zhang, X. H.; Wang, A. M.; Tang, H.; Chan, H. C. *PLoS One* **2011**, *6*, e17322.
- (46) Verkman, A. S. *Am. J. Physiol. Cell Physiol.* **1990**, *259*, C375.
- (47) Zhu, Y.; Parsons, S. P.; Huizinga, J. D. *Neurogastroenterology & Motility* **2010**, *22*, 704.
- (48) Van Rossom, W.; Asby, D. J.; Tavassoli, A.; Gale, P. A. *Org. Biomol. Chem.* **2016**, *14*, 2645.
- (49) Gottlieb, E.; Armour, S. M.; Harris, M. H.; Thompson, C. B. *Cell Death Differ.* **2003**, *10*, 709.
- (50) Ly, J. D.; Grubb, D. R.; Lawen, A. *Apoptosis* **2003**, *8*, 115.
- (51) Chu, Z.-L.; Pio, F.; Xie, Z.; Welsh, K.; Krajewska, M.; Krajewski, S.; Godzik, A.; Reed, J. C. *J. Biol. Chem.* **2001**, *276*, 9239.
- (52) Drušković, M.; Šuput, D.; Milisav, I. *Croat. Med. J.* **2006**, *47*, 832.
- (53) Ashkenazi, A. *Nat. Rev. Drug Discov.* **2008**, *7*, 1001.
- (54) Loreto, C.; La Rocca, G.; Anzalone, R.; Caltabiano, R.; Vespasiani, G.; Castorina, S.; Ralph, D. J.; Celtek, S.; Musumeci, G.; Giunta, S.; Djinovic, R.; Basic, D.; Sansalone, S. *BioMed Res. Int.* **2014**, *2014*, 10.
- (55) Smiley, S. T.; Reers, M.; Mottola-Hartshorn, C.; Lin, M.; Chen, A.; Smith, T. W.; Steele, G. D.; Chen, L. B. *Proc. Nat. Acad. Sci.* **1991**, *88*, 3671.
- (56) Cossarizza, A.; Baccaranicontri, M.; Kalashnikova, G.; Franceschi, C. *Biochem. Biophys. Res. Commun.* **1993**, *197*, 40.
- (57) Liu, X.; Kim, C. N.; Yang, J.; Jemmerson, R.; Wang, X. *Cell* **1996**, *86*, 147.
- (58) Li, P.; Nijhawan, D.; Budihardjo, I.; Srinivasula, S. M.; Ahmad, M.; Alnemri, E. S.; Wang, X. *Cell* **1997**, *91*, 479.

- (59) Jiang, X.; Wang, X. *Annu. Rev. Biochem.* **2004**, *73*, 87.
- (60) Cullen, S. P.; Martin, S. J. *Cell Death Differ.* **2009**, *16*, 935.
- (61) Wu, J.; Liu, T.; Xie, J.; Xin, F.; Guo, L. *Cell. Mole. Life Sci.* **2006**, *63*, 949.
- (62) McIlwain, D. R.; Berger, T.; Mak, T. W. *Cold Spring Harbor Perspect. Biol.* **2013**, *5*.
- (63) de Vries, E. G. E.; Gietema, J. A.; de Jong, S. *Clin. Cancer Res.* **2006**, *12*, 2390.
- (64) Haupt, S.; Berger, M.; Goldberg, Z.; Haupt, Y. *J. Cell Sci.* **2003**, *116*, 4077.
- (65) Milczarek, G. J.; Martinez, J.; Bowden, G. T. *Life Sci.* **1996**, *60*, 1.
- (66) Ekert, P. G.; Silke, J.; Vaux, D. L. *Cell Death Differ.* **1999**, *6*, 1081.
- (67) Shah, N.; Asch, R. J.; Lysholm, A. S.; LeBien, T. W. *Blood* **2004**, *104*, 2873.
- (68) Boulares, A. H.; Yakovlev, A. G.; Ivanova, V.; Stoica, B. A.; Wang, G.; Iyer, S.; Smulson, M. *J. Biol. Chem.* **1999**, *274*, 22932.
- (69) Park, S.-H.; Choi, Y. P.; Park, J.; Share, A.; Francesconi, O.; Nativi, C.; Namkung, W.; Sessler, J. L.; Roelens, S.; Shin, I. *Chem. Sci.* **2015**, *6*, 7284.
- (70) Curtin, N. J. *Nat. Rev. Cancer* **2012**, *12*, 801.
- (71) O'Rourke, B.; Cortassa, S.; Aon, M. A. *Physiology* **2005**, *20*, 303.
- (72) Zhao, W.; Lu, M.; Zhang, Q. *Mol. Med. Rep.* **2015**, *12*, 8041.
- (73) Khodade, V. S.; Kulkarni, A.; Gupta, A. S.; Sengupta, K.; Chakrapani, H. *Org. Lett.* **2016**, *18*, 1274.
- (74) Kim, E.-J.; Bhuniya, S.; Lee, H.; Kim, H. M.; Cheong, C.; Maiti, S.; Hong, K. S.; Kim, J. S. *J. Am. Chem. Soc.* **2014**, *136*, 13888.
- (75) Simon, H. U.; Haj-Yehia, A.; Levi-Schaffer, F. *Apoptosis*, *5*, 415.
- (76) Tsujimoto, Y.; Shimizu, S. *Apoptosis* **2006**, *12*, 835.
- (77) Circu, M. L.; Aw, T. Y. *Free Radical Biol. Med.* **2010**, *48*, 749.
- (78) Herrera, B.; Álvarez, A. M.; Sánchez, A.; Fernández, M.; Roncero, C.; Benito, M.; Fabregat, I. *FASEB J.* **2001**, *15*, 741.

End of Chapter 6

❖ Overall Conclusion:

In the overall conclusion, I can state that the fundamental objective of my doctoral research was to introduce artificial ion transport systems and to explore its application in the biomedical arena. The thesis deals with the design, synthesis, and characterization of biomimetic artificial ion channels and ion carriers which have shown a remarkable biological application in the line of future therapeutics. The ion transport activity, ion selectivity, lipophilic correlation with the transport activity and the bioapplicability are the main focus of my doctoral research. Apoptosis inducing activity because of chloride ion transport in live cells by ion carrier and ion channel could be a potential therapeutic tool for cancer treatment in the next generation. However, a careful and smart optimization related to structure and the activity of those ion transporting agents are required for the direct biomedical application. The study related to the bioactivity is still in early stage and 'miles to go' before it reaches to the humanity as a therapeutic agent.

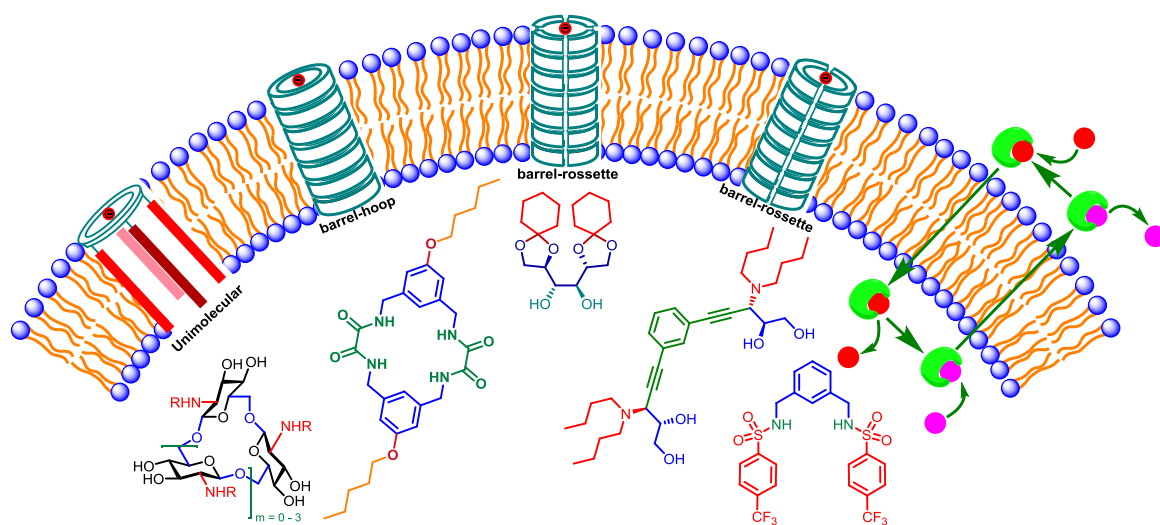


Figure: Schematic illustration of ion transporting agent discussed in the thesis.

End of the Thesis

❖ *Research Publications (Included in Thesis):*

1. *Chloride Transport through Supramolecular Barrel-Rosette Ion Channels: Lipophilic Control and Apoptosis-Inducing Activity.*

Tanmoy Saha, Amitosh Gautam, Arnab Mukherjee, Mayurika Lahiri, and Pinaki Talukdar*

Journal of the American Chemical Society **2016**, 138, 16443.

2. *Self-Assembly of Bis(oxalyl amide) Macrocycles as Transmembrane Barrel-Hoop Anion Channel*

Tanmoy Saha, Pratyush Kumar Mishra and Pinaki Talukdar*.

Manuscript Submitted

3. *Chloride-Mediated Apoptosis-Inducing Activity of Bis(sulfonamide) Anionophores.*

Tanmoy Saha, Munshi Sahid Hossain, Debasis Saha, Mayurika Lahiri, and Pinaki Talukdar.*

Journal of the American Chemical Society **2016**, 138, 7558–7567.

4. *Hopping mediated anion transport through a mannitol-based rosette ion channel.*

Tanmoy Saha, Sathish Dasari, Debanjan Tewari, Annamalai Prathap, Kana M. Sureshan, Amal K. Bera,* Arnab Mukherjee,* and Pinaki Talukdar.*

Journal of the American Chemical Society **2014**, 136, 14128-14135.

5. *Cyclo-oligo-(1->6)- β -D-glucosamine based artificial channels for tunable transmembrane ion transport.*

Tanmoy Saha, Arundhati Roy, Marina L. Gening, Denis V. Titov, Alexey G. Gerbst, Yury E. Tsvetkov, Nikolay E. Nifantiev* and Pinaki Talukdar.*

Chemical Communications **2014**, 50, 5514-5516.

❖ *Research Publication (Not Included in Thesis):*

6. *Trimodal Control of Ion Transport Activity on Cyclo-Oligo-(1→6)-β-D-Glucosamine Based Artificial Ion Transport Systems.*
Arundhati Roy,[†] **Tanmoy Saha**,[†] Marina L. Gening, Denis V. Titov, Alexey G. Gerbst, Yury E. Tsvetkov, Nikolay E. Nifantiev* and Pinaki Talukdar.*
Chemistry A-European Journal **2015**, *21*, 17445–17452. († Equal contribution)
7. *Performance Comparison of Two Cascade Reaction Models in Fluorescence off–on Detection of Hydrogen Sulfide.*
Tanmoy Saha, Dnyaneshwar Kand and Pinaki Talukdar.*
RSC Advances **2015**, *5*, 1438-1446.
8. *Lysosome Targeting Fluorescence Probe for Imaging Intracellular Thiols.*
Dnyaneshwar Kand,[†] **Tanmoy Saha**,[†] Mayurika Lahiri, Pinaki Talukdar.*
Organic & Biomolecular Chemistry **2015**, *13*, 8163 -8168. († Equal contribution)
9. *In vitro sensing of Cu⁺ through a green fluorescence rise of pyranine.*
Tanmoy Saha, Abhigyan Sengupta, Partha Hazra, Pinaki Talukdar.*
Photochemical & Photobiological Sciences **2014**, *13*, 1427-1433.
10. *BODIPY based "click on" fluorogenic dyes: Application in live cell imaging.*
Dinesh Pratapsinh Chauhan,[†] **Tanmoy Saha**,[†] Mayurika Lahiri, Pinaki Talukdar.*
Tetrahedron Letters **2014**, *55*, 244-247. († Equal contribution)
11. *A colorimetric and fluorometric BODIPY probe for rapid, selective detection of H₂S and its application in live cell imaging.*
Tanmoy Saha,[†] Dnyaneshwar Kand,[†] and Pinaki Talukdar.*
Organic & Biomolecular Chemistry **2013**, *11*, 8166 – 8170. († Equal contribution)
12. *Hydrogen Sulfide Mediated Cascade Reaction Forming an Iminocoumarin: Applications in Fluorescent Probe Development and Live-Cell Imaging.*
Pratryush Kumar Mishra, **Tanmoy Saha**, Pinaki Talukdar.*
Organic & Biomolecular Chemistry **2015**, *13*, 7430-7436.

13. *Turn-On Fluorescent Probe Designed for Fluoride Ion Sensing in Aqueous Media.*
Arundhati Roy, **Tanmoy Saha**, Pinaki Talukdar.*
Tetrahedron Letters **2015**, 56, 4975 – 4979.
14. *Structural Imposition on Off-On Response of Naphthalimide Based Probes for Selective Thiophenol Sensing.*
Dnyaneshwar Kand, Prashant Sahebrao Mandal, **Tanmoy Saha**, Pinaki Talukdar.*
RSC Advances **2014**, 4, 59579-59586.
15. *Metal-Organic Framework Based Highly Selective Fluorescence Turn-On Probe for Hydrogen Sulphide.*
Sanjog S. Nagarkar, **Tanmoy Saha**, Aamod V. Desai, Pinaki Talukdar*, Sujit K. Ghosh.*
Scientific Reports **2014**, 4, 7053.
16. *Cascade reactions based fluorescent probe for rapid and selective fluoride ion detection.*
Arundhati Roy, Dnyaneshwar Kand, **Tanmoy Saha** and Pinaki Talukdar.*
Chemical Communications **2014**, 50, 5510-5513.
17. *Pink fluorescence emitting fluoride ion sensor: Investigation of the cascade sensing mechanism and bioimaging applications.*
Arundhati Roy, Dnyaneshwar Kand, **Tanmoy Saha** and Pinaki Talukdar.*
RSC Advances **2014**, 4, 33890-33896.
18. *Fluorescent Off-On NBD probe for fluoride sensing: Theoretical validation and experimental studies.*
Arundhati Roy, Avdhoot Datar, Dnyaneshwar Kand, **Tanmoy Saha** and Pinaki Talukdar.*
Organic & Biomolecular Chemistry **2014**, 12, 2143-2149.

-
19. *Off-on type fluorescent NBD-probe for selective sensing of cysteine and homocysteine over glutathione.*
Dnyaneshwar Kand, **Tanmoy Saha**, Pinaki Talukdar.*
Sensors and Actuators B: Chemical **2014**, 196, 440–449.
20. *Linear and cyclic oligo- β -(1 \rightarrow 6)-D-glucosamines: Synthesis, conformations, and applications for design of a vaccine and oligodentate glycoconjugates.*
Marina L. Gening, Yury E. Tsvetkov, Denis V. Titov, Alexey G. Gerbst, Olga N. Yudina, Alexey A. Grachev, Alexander S. Shashkov, Sébastien Vidal, Anne Imberty, **Tanmoy Saha**, Dnyaneshwar Kand, Pinaki Talukdar, Gerald B. Pier, and Nikolay E. Nifantiev.*
Pure and Applied Chemistry **2013**, 85, 1879-1891.
21. *BODIPY based colorimetric fluorescent probe for selective thiophenol detection: Theoretical and experimental studies.*
Dnyaneshwar Kand, Pratyush Kumar Mishra, **Tanmoy Saha**, Mayurika Lahiri and Pinaki Talukdar.*
Analyst **2012**, 137, 3921-3924.